2008

Segmented field electron conformal therapy planning algorithm

David Jaquet Perrin
Louisiana State University and Agricultural and Mechanical College, david.j.perrin@gmail.com

SEGMENTED FIELD ELECTRON CONFORMAL THERAPY PLANNING ALGORITHM

A Thesis

Submitted to the Graduate Faculty of the
Louisiana State University and
Agricultural and Mechanical College
in partial fulfillment of the
requirements for the Degree of
Master of Science

in

The Department of Physics & Astronomy

by
David Jaquet Perrin
B.S. Louisiana State University, 2005
December 2008

Acknowledgements

I thank the members of my thesis committee for all of their assistance and guidance, particularly Dr. Kenneth Hogstrom for his thoughts and time throughout the project and Dr. Kenneth Matthews for his help with image processing in IDL. I thank Dr. Dennis Cheek for his insight into the inner workings of Pinnacle^3, without which the patient plans would've been extremely more difficult. I thank the entire staff at Mary Bird Perkins Cancer Center, both for treating me not just as a student but as a fellow team member and for answering my random questions whenever I randomly had them.

I thank my parents, David and Brenda Perrin, for supporting me throughout my many years of education, even through the multiple field changes. I thank my girlfriend, Lara, for helping to keep me sane the past few years and for the occasional neck rub. I thank Andrew Morrow for the periodic good-hearted argument about things that don't really matter and coding suggestions. I thank Sarah Lewis, Yvonne Thomas, April Quillen, and Davelyn Zachary for all their help in getting things scheduled over the years.

Finally, thanks to LSU Medical Physics and Health Physics program, the Health Physics Society Richard J Burk, Jr. Fellowship, and Varian Medical Systems, Inc. for financial support.

Table of Contents

List of Tables

List of Figures

Abstract

Purpose: Segmented-field electron conformal therapy (SFECT) is rarely used, or if used, used sub optimally, primarily due to inadequate tools for its planning. The development of SFECT planning tools could help begin to bring electron therapy to the same level of sophistication as x-ray and proton therapy, resulting in greater consideration by radiation oncologists. The purpose of this work was to develop a forward planning algorithm that will improve segmentation of the SFECT treatment field. It was hypothesized that a forward planning algorithm can produce segmented-field ECT fields that improve dose conformity as the number of beam energies is increased from one to five using the Varian beam set (6, 9, 12, 16, and 20 MeV).

Methods: A planning algorithm that allowed each field segment to have its own energy, shape, size, and weighting was developed. The planning algorithm developed an initial plan and then went through several iterations of re-planning based on the dose distributions of each previous plan in order to converge the 90% dose surface to the distal PTV surface. The planning algorithm was used to develop SFECT plans for six hypothetical PTVs and two head and neck patient PTVs. These plans were compared to single-energy plans developed by the same planning algorithm.

Results: Conformity improved little beyond allowing three energies due to energy overlap and field-size restrictions. For the hypothetical PTVs, non-PTV treated to 90% of the prescribed dose was reduced compared to the single-energy plans, resulting in improved dose conformity, supporting the hypothesis. The improved conformity came at the expense of increased dose heterogeneity within the PTV. One of the patient plans improved in conformity, supporting the hypothesis and indicating the planning algorithm has the potential to plan patient cases. The other patient case did not improve in conformity and therefore did not support the hypothesis.

Conclusion: The planning algorithm was successful in developing plans that improved conformity while still treating the PTV to prescription dose. The planning algorithm has the potential to plan patient SFECT treatments. Future improvements to the algorithm may improve its ability to plan patient cases.

Chapter 1. Introduction

1.1 Background and Significance

1.1.1 Electron Conformal Therapy

Electron beam therapy can be preferable in cases of superficial tumors (depth of 6 cm or less) due to its high surface dose and rapid dose fall-off at depth relative to X-ray therapy. As such, electrons have long been used to treat malignancies found in the skin (e.g. nose, eyelid, ear), lips, upper respiratory system, digestive tract, salivary glands, neck regions, chest-wall, and breast, as well as provide dose boost to surgical scars, post-surgical tumor beds, and lymph nodes (Tapley 1976).

Electron conformal therapy (ECT) uses one or more electron energies to contain the planning target volume (PTV) in the 90% (of given dose) dose surface, while achieving as homogeneous a dose as possible (e.g., 90-100%) and delivering minimal dose to underlying critical structures and normal tissues (Hogstrom *et. al.* 2003). Therefore, the patients that will benefit the most from ECT are those with malignancies with nearby or underlying critical structures. ECT has been used to treat sarcomas of the paraspinal muscles (Low *et. al.* 1995), post-mastectomy chest walls (Zackrisson and Karlsson 1996, Perkins *et. al.* 2001), and diseases of the head and neck (Zackrisson and Karlsson 1996, Kudchadker *et. al.* 2002a, 2003). Modulated electron therapy (MET) can be delivered with ECT by using both energy modulation and intensity modulation (Hogstrom *et. al.* 2003). Energy modulation can be used to conform the dose surface to both the proximal and distal PTV surfaces in the direction of the electron beam's central-axis. Intensity modulation can be used to improve conformity of the dose surface to the lateral PTV surface in the direction perpendicular to the electron beam's central-axis.

The two primary methods for delivering MET, bolus ECT and segmented-field ECT, are shown in Figure 1. Bolus ECT uses machinable wax milled to match the patient's anatomy on

one side and to conform the 90% dose surface to the distal PTV surface on the other side. Hogstrom *et. al.*(2003) defined segmented-field electron conformal therapy (SFECT) as 'the utilization of multiple abutted electron field segments, each having a common virtual source position but each having its own energy and weight, so as to conform the therapeutic dose surface (e.g., 90% of given dose) to the PTV.' Thus, SFECT allows for energy modulation by allowing each segment its own energy and intensity modulation by allowing each segment its own number of monitor units (MUs). Relative to a conventional single field segment, single energy dose plan, both bolus ECT and SFECT increase the dose inhomogeneity (e.g., $D_{90\text{-}10}$) in the PTV. The increase in PTV dose inhomogeneity is due to the loss of side-scatter equilibrium created by the irregular proximal surface of the bolus (Kudchadker *et. al.* 2002b) for bolus ECT and is due to abutted field segments of different energies having different penumbra widths for SFECT (Richert *et. al.* 2007).

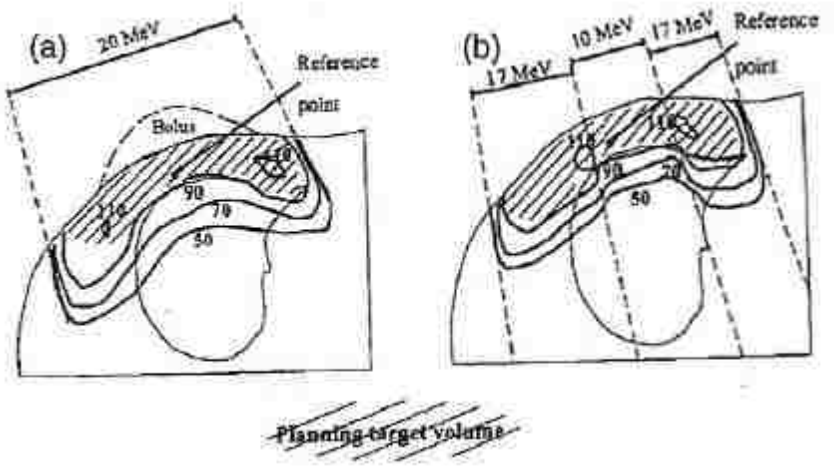

Figure 1: (a) Transverse section of bolus ECT dose distribution using a single 20 MeV field. Hot spots under edges of bolus are due to the gradient of the bolus material. (b) Transverse section of SFECT dose distribution using three fields. Hot spots are due to abutment of field segments of differing energies. The reference point was used for normalization (100%) just outside abutting edges. [Zackrisson and Karlsson 1996]

Bolus ECT has several advantages over SFECT. Algorithms exist for the design of bolus for use in planning bolus ECT (Low *et. al.*1992), while SFECT plans currently must use a best

guess approach to planning, as no such planning algorithm exists. Bolus ECT has been used at M. D. Anderson Cancer Center for more than a decade, and its use in the clinic has been well documented (Low *et. al.* 1995, Perkins *et. al.* 2001, Kudchadker *et. al.* 2002a, 2003). Bolus can be milled to 1-mm accuracy providing nearly continuous energy modulation equivalent to energy steps of 0.2 MeV compared to the coarse 3-5 MeV energy steps that would be used with SFECT. Since SFECT requires multiple field segments, bolus ECT requires significantly less total MUs, possibly resulting in less bremsstrahlung dose to the patient. Lastly, if the PTV extends very close to the surface, bolus ECT delivers a higher surface dose due to dose buildup in the bolus where as a SFECT plan may require constant thickness bolus in order to completely treat the PTV. However, SFECT can be preferable to bolus ECT; its primary advantage over bolus ECT is its sharper dose fall off past the PTV. This is because bolus ECT must use the maximum energy needed over the entire treatment area, whereas SFECT uses only the energy needed for each individual segment.

In addition to bolus ECT and SFECT, ECT can be delivered using modulated electron radiotherapy (MERT). MERT allows each beam its own energy and intensity pattern and has been the focus of many recent studies (Ma *et. al.* 2000, 2003, Lee *et. al.* 2001, Olofsson *et. al.* 2004, Al-Yahya *et. al.* 2005). Intensity is modulated within each individual beam, similar to IMRT, rather than just allowing each field segment its own MUs as in SFECT. Additionally, MERT allows multiple beams at single point, again similar to IMRT. The delivery of MERT differs from the delivery of SFECT in that it requires a multi-leaf collimator (MLC), whereas SFECT can be delivered using Cerrobend cutouts or an electron MLC (eMLC).

1.1.2 Segmented-Field Electron Conformal Therapy

It is possible that SFECT could produce dose distributions superior to X-ray Intensity Modulated Radiation Therapy (IMRT) when treating superficial tumors with critical healthy

tissues beneath, as in the chest wall and the head and neck regions. Due to the slow falloff of X-ray dose with depth, X-ray IMRT typically delivers low dose to a large volume of normal tissue, likely greater than from SFECT. Ashenafi (2006) showed a significant reduction in secondary cancer complication probability (SCCP) in the ipsilateral and total lung, contralateral breast, and normal tissue for post-mastectomy radiotherapy treatments using conventional electron beam techniques as compared to IMRT delivered with the TomoTherapy Hi-Art system. Therefore, the use of SFECT, as opposed to IMRT, could result in a decreased normal tissue complication probability (NTCP) and also possibly lower risk of radiation-induced secondary cancers.

Presently, SFECT is rarely used, or if used, used sub optimally, due to (1) inadequate tools for its delivery, (2) dose inhomogeneity caused by abutting field segments of differing energy, and (3) inadequate tools for its planning. The delivery of SFECT is a challenge, requiring the use of either multiple Cerrobend cutouts or a multi-leaf collimator (MLC). Richert *et al.* (2007) showed that currently-available computer controlled hot wire technology was sufficiently accurate (<0.3 mm). Furthermore, abutted field segments of different energies have unequal penumbra, which leads to hot spots up to 110% and cold spots as low as 80% (Zackrisson and Karlsson 1996). Richert *et al.* (2007) investigated a method of penumbra matching by using energy dependent source to collimator distances (SCD). They showed that by using the variable SCD method that hot and cold spots could be reduced to a clinically acceptable 105% and 85%. However, the method of variable SCD requires a modified electron applicator not currently provided by manufacturers.

Alternatively, the photon MLCs (xMLC) available on most treatment machines are unacceptable for use as an eMLC except at greatly reduced SSD (Klein *et al.* 2008). With the exception of the MM50 race-track microtron (Zackrisson and Karlsson 1996), the xMLCs are insufficient eMLCs because (1) the downstream edges are too far from the isocenter, (2) the

heads of the machines contain air, causing significant electron scattering, and (3) the virtual sources are large because the beams are broadened by dual scattering foil systems (Hogstrom *et al.* 2004). Therefore, separate eMLCs have been investigated by several groups (Lee *et al.* 2000, Ma *et al.* 2000, Ravindran *et al.* 2002, Hogstrom *et al.* 2004, Gauer *et al.* 2006). Hogstrom *et al.* (2004) proposed and are developing a retractable eMLC, which would create an accessory-less machine. Gauer *et al.* (2006) have developed an eMLC, built by 3D Line Medical Systems, with two interchangeable holders providing two different surface to collimator air gaps.

Lastly, there is currently no algorithm for optimizing the treatment fields used by SFECT. Current planning uses a best guess approach, manually determining the best energy for each section and then arbitrarily deciding the edges of each segment. This method is difficult, in part due to 3D planning system manufacturers' not including a beam's eye view of PTV depth, such as the one shown in Figure 2. Olofsson *et al.* (2004) demonstrated an inverse planning technique using mixed energies in a single beamlet. However, their method is not widely clinically viable as it requires the use of an eMLC not available on most LINACs.

Therefore, while eMLCs and other methods have been shown to be feasible, they cannot perform optimally without better SFECT treatment field design. The development of SFECT planning tools could help bring electron therapy to a similar level of sophistication as x-ray and proton therapy, resulting in greater consideration by radiation oncologists. Efficient SFECT planning tools would allow the radiation oncologist to more easily determine the best plan, whether it's SFECT, X-ray IMRT, or a combination of the two, for a specific patient. The purpose of this work is to develop a forward planning algorithm that will improve segmentation of the SFECT treatment field.

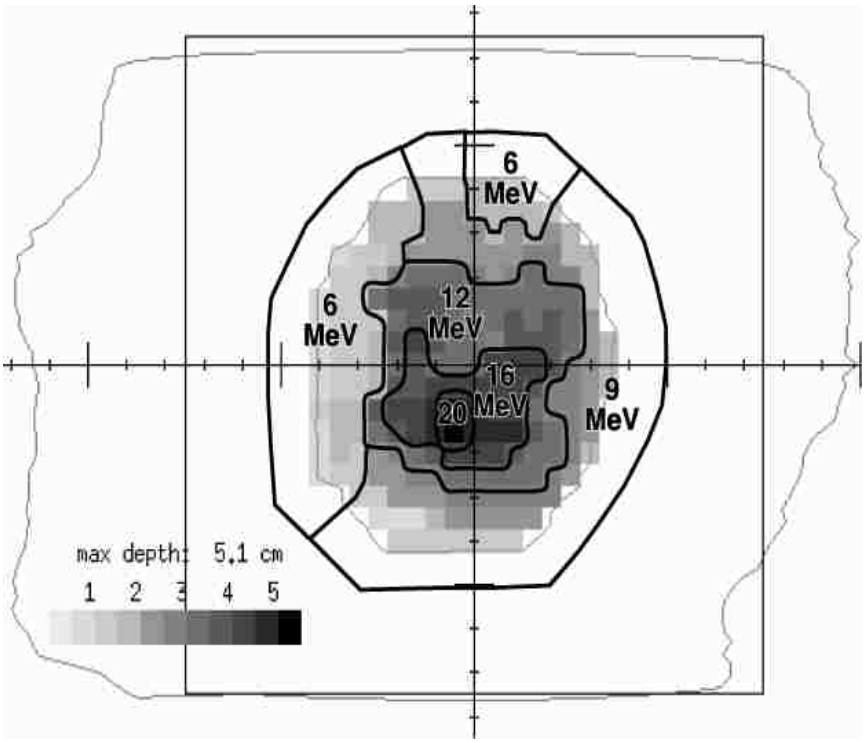

Figure 2: A beam's eye view of PTV distal depth allows for manual energy segmentation. However, such tools do not currently exist in commercial planning systems. [Starkschall et al., 1994]

1.2 Hypothesis

The hypothesis of the present work was that a forward planning algorithm can produce segmented-field ECT fields that improve dose conformity as the number of beam energies is increased from one to five using the Varian beam set (6, 9, 12, 16, and 20 MeV).

1.3 Aims

Specific aims were:

Aim 1: Implementation of a Pencil Beam Algorithm. The Hogstrom pencil beam algorithm will be coded for a flat water phantom to calculate the dose distributions needed by the forward planning algorithm, and dose calculation will be shown equivalent to those in the Phillips Pinnacle[3] treatment planning system (TPS).

Aim 2: Develop Field Segmentation Algorithm. An iterative, forward planning algorithm for designing segmented-field ECT fields will be developed. The algorithm will develop an initial plan and then go through several iterations of re-planning based on the dose distributions of each previous plan. The algorithm will allow each segment to have its own shape, size, and weighting. Simple segmented-field ECT planning tools will be developed for use with the planning algorithm.

Aim 3: Utilization of Algorithm to Compare Impact of Number of Energies. The planning algorithm will allow selection of the maximum number of energies allowed in the plan. Plans will be generated with each of the allowed number of energies for six hypothetical PTVs and compared using multiple metrics.

Aim 4: Demonstrate Use of Algorithm on Patient Data. Two patients, one with a head and neck disease treated with electrons and one with a head and neck disease treated with IMRT, but suitable for SFECT, will be chosen to assess the planning algorithm's potential to plan SFECT fields to non-flat, heterogeneous targets. A plan for each of the allowed number of energies will be generated and exported to the Pinnacle v7.4f TPS for dose calculation. The SFECT plans will be compared to each other for improvement in conformity.

Chapter 2. Methods and Materials

2.1 Aim 1: Implementation of a Pencil Beam Algorithm

The field segmentation algorithm discussed in Aim 2 required calculated dose distributions. In lieu of exporting the segmented fields into the Pinnacle v7.4f treatment planning system and importing the calculated dose distribution back into the field segmentation algorithm at each step of the optimization, the dose calculation was imbedded. The Hogstrom PBA was coded to mimic the PBA used by Pinnacle v7.4f as much as possible for a flat water phantom. Because our implementation used the same input data, beam parameters for our institution's Varian 2100EX in Pinnacle v7.4f were used.

2.1.1 Pencil Beam Theory

The 1D version of the Hogstrom *et al.*(1981) pencil beam algorithm (PBA) described by Starkschall *et al.*(1991) was coded for a flat water phantom. The PBA models multiple Coulomb scattering by using Fermi-Eyges theory (Eyges 1948). Each pencil beam was defined at the bottom of the applicator's secondary Cerrobend insert, having an initial Gaussian projected angular spread with a root mean square (RMS) projected scattering angle σ. Physical principles not modeled by the PBA were accounted for by forcing calculated to equal inputted, measured central-axis percent depth dose. Beam non-uniformity can be accounted for using measured beam profiles; however, a uniform beam was assumed in the present work.

The coded PBA calculated the total dose, D, to points on a 3D grid. Dose at (X, Y, Z) was calculated by summing the dose contribution from each energy segment of the field, i.e.,

$$D(X,Y,Z) = \sum_{n=1}^{\#\ of\ segments} D_n(X,Y,Z). \quad (1)$$

Dose for each segment was partitioned into electron and photon dose components, i.e.,

$$D_n(X,Y,Z) = D_n^e(X,Y,Z) + D_n^\gamma(X,Y,Z), \quad (2)$$

where $D_n^e(X,Y,Z)$ and $D_n^\gamma(X,Y,Z)$ were the electron and photon contamination contribution to the dose at the point (X, Y, Z) from the nth segment.

2.1.2 Electron Dose Model

The electron contribution to the dose at the point (X, Y, Z) was the sum of the dose due to all pencil beams (i, j) within the aperture of the Cerrobend insert, calculated according to Hogstrom *et al.* (1981),

$$D_n^e(X,Y,Z) = \sum_i \sum_j \frac{1}{2\pi\sigma^2}\left(\int_{X_i-\frac{\Delta X}{2}}^{X_i+\frac{\Delta X}{2}}\int_{Y_j-\frac{\Delta Y}{2}}^{Y_j+\frac{\Delta Y}{2}} exp\left(-\left(\frac{\left(X-X'\left(\frac{SSD+Z}{SCD}\right)\right)^2+\left(Y-Y'\left(\frac{SSD+Z}{SCD}\right)\right)^2}{2\sigma^2}\right)\right)dY'dX'\right) * OAR\left(\sqrt{X_i^2+Y_j^2}\right) * D_{CA}^{\infty}(Z) * \left(\frac{SSD_{ref}+Z}{SSD+Z}\right)^2, \quad (3)$$

where: (1) σ is the RMS of the projected angle distribution at depth Z in water; (2) pencil beams were centered at (X_i, Y_j) and were ΔX by ΔY wide, defined at the level of the collimator; (3) SSD equaled the reference SSD_{ref} of 100-cm for all pencil beams, as the PBA was coded for a flat water phantom; (4) the source to collimator distance, SCD, was the same for all pencil beams within a segment, but may have changed between segments for the variable SCD dose calculations; (5) off-axis ratios (OAR) were the relative pencil beams weights at a radial off-axis distance $(X_i^2+Y_j^2)^{1/2}$; and (6) D_{CA}^{∞}, the calculation of which is discussed in Section 2.1.5 below, was the percent depth dose due to electrons for a broad beam (side scatter equilibrium) as determined from central-axis percent depth dose data measured at SSD_{ref} (100-cm) for the rectangle circumscribing the field segment.

The beam sigma, σ, at depth Z in water was calculated by

$$\sigma^2(Z) = \sigma_{\theta_x}^2 * (Z+L_0)^2 + FMCS * \sigma_{MCS}^2(Z), \quad (4)$$

where σ_{θ_x}(radians) is the RMS spread of the projected angle distribution of the beam at the downstream plane of the collimator, L_0 is the air gap (drift distance) between the water surface and the collimator, FMCS is a water scatter correction factor, and σ_{MCS} is the RMS spread of the projected angular distribution at depth Z (due to multiple coulomb scattering in the water). The parameters σ_{θ_x}, L_0, and FMCS were taken from the Pinnacle v7.4f beam model, and σ_{MCS}^2 was given by:

$$\sigma_{MCS}^2(Z) = a_2(Z) = \frac{1}{2}\int_0^Z T\left(E_p(Z')\right)\,(Z - Z')^2\,dZ', \tag{5}$$

where $T(E_p(Z))$ is the linear angular scattering power in water evaluated for the most probable energy at depth Z, $E_p(Z)$. $E_p(Z)$ was calculated using Harder's equation (ICRU 1984),

$$E_p(Z) = E_p(0) * (1 - \frac{Z}{R_p}), \tag{6}$$

where $E_p(0)$ is the most probable energy at the surface and R_p is the practical range of the beam, both taken from the Pinnacle v7.4f beam model. The multiple Coulomb scattering term, $a_2(Z)$, was determined using the recursion relations given by Hogstrom (1987):

$$a_0(Z_i) = a_0(Z_{i-1}) + \frac{\Delta Z}{2} * T(E_p(Z_i)) \tag{7a}$$

$$a_1(Z_i) = a_1(Z_{i-1}) + \Delta Z * a_0(Z_{i-1}) + \frac{(\Delta Z)^2}{4} * T(E_p(Z_i)) \tag{7b}$$

$$a_2(Z_i) = a_2(Z_{i-1}) + 2\Delta Z * a_1(Z_{i-1}) + (\Delta Z)^2 * a_0(Z_{i-1}) + \frac{(\Delta Z)^3}{6} * T(E_p(Z_i)), \tag{7c}$$

where $a_0(Z_0 = 0) = a_1(Z_0) = a_2(Z_0) = 0$, ΔZ is difference between Z_i and Z_{i-1}. $T(E_p(Z_i))$ for water was calculated by

$$T_{H_2O}\left(E_p(Z_i)\right) = [(\frac{T}{\rho})_H\left(E_p(Z_i)\right) * p_H + (\frac{T}{\rho})_O\left(E_p(Z_i)\right) * p_O] * \rho_{H_2O}, \tag{8}$$

where $(T/\rho)_H$ and $(T/\rho)_O$ are the mass angular scattering powers of hydrogen and oxygen from Table 2.6 of ICRU 35, p_H and p_O are the weight fractions of hydrogen (11.2%) and oxygen (88.8%) in water from Table 2.1b of ICRU 35, and ρ_{H_2O} (1.00) is the density of water. The (T/ρ)

values have been modified to approximately account for electron-electron (Möller) scattering by replacing Z^2 with Z(Z+1) in Eq. 2.8 of ICRU 35, accomplished here by multiplying (T/ρ) by (Z+1)/Z, where Z is the atomic number of the individual element.

For the variable SCD dose calculations, the beam energy-specific air gaps were used for L_0, and σ_{θ_x} was modified to account for the new SCDs by (Richert *et al.* 2007):

$$\sigma_{\theta_x}^2(SCD) = \sigma_{\theta_x}^2(SCD_{std})\ \frac{SCD}{SCD_{std}}, \tag{9}$$

where SCD_{std} is the standard source to collimator distance, 95-cm in our work, and SCD is the beam energy-specific source to collimator distance. The energy specific air gaps, SCDs, and modified σ_{θ_x}s are found in Table 1 below.

Table 1: Beam parameters used in the coded PBA for variable SCD dose calculations. Note that Richert *et al.* (2007) used the physical distances for L_0, not the determined distances described in Section 2.1.4

	6 MeV	9 MeV	12 MeV	16 MeV	20 MeV
L_0 (cm)	5	7.5	11.5	17.5	19.5
SCD (cm)	95	92.5	88.5	82.5	80.5
σ_{θ_x} (radians)	0.0655	0.0479	0.0343	0.027	0.0235

2.1.3 Photon Contamination Model

The use of a scattering foil in the LINAC head to flatten the electron beam produces forward peaked bremsstrahlung radiation which creates photon contamination dose. The photon contamination dose from beam segment n to a voxel center at (X, Y, Z), $D_n^{\gamma}(X,Y,Z)$, was calculated by

$$D_n^{\gamma}(X,Y,Z) = \%DD^{\gamma}(Z) * OAR^{\gamma}(X,Y,Z) * f(X,Y), \tag{10}$$

where $\%DD^{\gamma}(Z)$ is the central-axis photon percent depth dose, OAR^{γ}(X, Y, Z) is the ratio of photon dose at (X, Y, Z) to that at (0, 0, Z), and f(X,Y) is an insert transmission factor which adjusts the photon contamination dose passing through the Cerrobend insert, determined by

$$f(X,Y) = \begin{cases} 0.0, & (X,Y) \notin \text{cone} \\ 0.6, & \notin \text{aperture } n, \in \text{cone} \\ 1.0, & \in \text{aperture } n \end{cases}. \quad (11)$$

It was assumed that the dose 1 cm past the practical range (R_p) was due entirely to photon contamination. The photon dose component was given by

$$\%DD^{\gamma}(Z) = \begin{cases} \%DD(R_p + 1\ cm) * \left(\frac{100\ cm + R_p + 1\ cm}{100\ cm + Z}\right)^2, & Z \leq R_p + 1\ cm \\ \%DD(Z), & Z > R_p + 1\ cm \end{cases}. \quad (12)$$

An example of a 20 MeV central-axis photon %DD calculated from a measured 20 MeV central-axis %DD curve is shown in Figure 3.

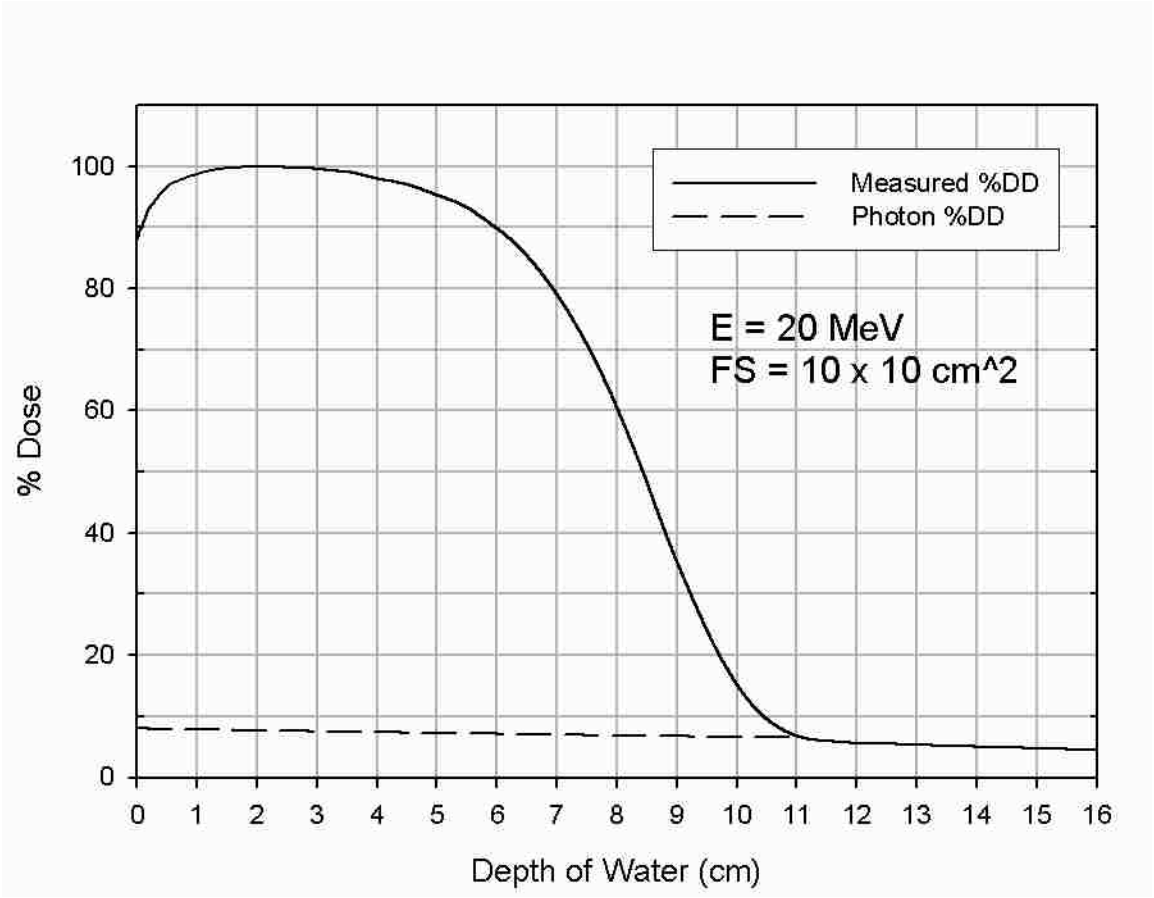

Figure 3: Measured central-axis percent depth dose curves for a 10x10 cm^2 20 MeV beam from our institution's Varian 21EX and a photon central-axis percent depth dose curve calculated from the measured curve using equation (12).

2.1.4 Beam Model Parameters

My beam model utilized the standard beam parameters as the Hogstrom PBA model summarized by Hogstrom and Steadham (1996). These included:

1. Most probable electron energy at the surface, $E_p(0)$: This was determined from the measured R_p of the beam by

$$E_p(0)(MeV) = 0.722 + 1.919\ R_p\ (cm). \quad (13)$$

2. Virtual SSD (cm): The model required the virtual source to surface distance determined according to Hogstrom *et al.* (1981), along with the nominal source to surface distance (100 cm).
3. RMS spread of the projected angle distribution of the beam σ_{θ_x}(radians): This was defined at the downstream plane of the collimator and was due to the dual scattering foil system and scatter in air.
4. Drift distance (air gap) between the surface and collimator, L_0: This and σ_{θ_x} were determined from in-air profiles at various SSDs using the method described in Hogstrom *et al.* (1981, 1984).
5. Central-axis depth-dose data: This was measured for a set of square fields, with field sizes chosen to allow accurate interpolation of depth-dose data for intermediate square sizes.
6. Off-axis ratios (OARs): The ratio of dose at (X, Y, Z) to that at (0, 0, Z) was measured for the set of square fields along the X-axis to model beam nonuniformity. Hogstrom and Steadham (1996) recommended measuring OARs at several depths less than R_p, as beam nonuniformity may be non-uniform with depth, and one depth several cm past R_p to obtain the OAR of the photon contamination dose. However, at depths less than R_p,

Pinnacle 7.4f stores only OARs measured at half the depth of the central-axis distal 90% (R_{90}) and assumes beam nonuniformity does not vary with depth.

7. Water scatter correction factor, FMCS: This was used to adjust the penumbral width of the dose distribution due to scatter in the patient. The value of FMCS, which typically ranges in value from 1.2 to 1.4, was adjusted to obtain a good fit between measured and calculated distributions in the penumbral regions greater than R_{90}.

The previously described model parameters had been determined and verified according to the recommendations of Hogstrom and Steadham (1996) for our institution's Varian 2100EX by a medical physicist at the time of machine commissioning and input into the Pinnacle v7.4f treatment planning system. The beam parameters for our institution's Varian 21EX in the Pinnacle v7.4f treatment planning system, found below in Table 2, were used in our coded PBA to closely mimic the Pinnacle v7.4f model. Also, the OARs less than R_p are typically close 1, hence OARs less than R_p were assumed to be 1 in my model, while the measured values were used for OARs deeper than R_p.

Table 2: Beams parameters for our institution's Varian 21EX from the Pinnacle 7.4f treatment planning system used in the coded PBA. Note that E_p varies from equation (13) because Pinnacle allows fine tuning of E_p if the user desires, though it is not recommended.

	6 MeV	9 MeV	12 MeV	16 MeV	20 MeV
R_p	2.9	4.0	5.8	7.7	10.1
$E_p(0)$	6.4	9.0	12.6	16.5	20.4
Virtual SSD	100	100	100	100	100
Actual SSD	100	100	100	100	100
σ_{θ_x}	0.0655	0.0485	0.0355	0.029	0.0255
L_0	7	7	7	7	7
FMCS	1.2	1.2	1.2	1.2	1.2

2.1.5 Determination of %DD and Output Factors

The pencil beam algorithm takes as input a measured central-axis percent depth-dose curve for a rectangular field. In the case of irregularly shaped field segments, the rectangle that most closely approximates the irregular segment shape was determined. First, a rectangle that

completely circumscribes the segment was drawn around the field, then the segment was rotated by 1 degree and a new rectangle was drawn. This iteration was repeated through 180 degrees, and the rectangle with the least area was selected, as demonstrated in Figure 4.

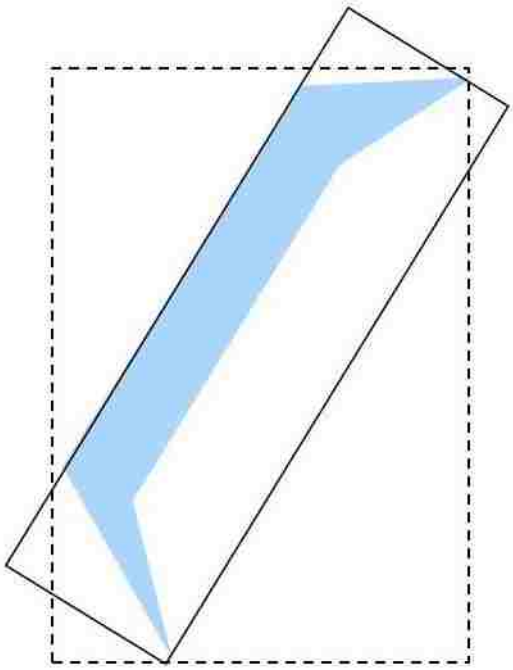

Figure 4: Example of approximating rectangle determination. Plotted in the reference frame of the irregular segment (shaded area), the dashed line is the first rectangle drawn, while the solid line is the best fitting rectangle.

Once the best approximating rectangle was determined, the %DD for the rectangle was determined using the square root method of Hogstrom *et al.* (1981),

$$\%DD^{WX\otimes WY}(Z) = \sqrt{\%DD^{WX\otimes WX}(Z) * \%DD^{WY\otimes WY}(Z)}, \quad (14)$$

where WX and WY are the width and height of rectangle. $\%DD^{WX\otimes WY}$ was then normalized to its own maximum by

$$\%DD^{WX\otimes WY}(Z) = \frac{\%DD^{WX\otimes WY}(Z)}{\%DD^{WX\otimes WY}(R_{100})} * 100\%. \quad (15)$$

The square %DDs ($\%DD^{WX\otimes WX}$, $\%DD^{WY\otimes WY}$) were linearly interpolated from a set of %DD for measured square fields. Measured %DD curves from a Varian 21EX for all measured

square field sizes up to the equilibrium field (2x2 cm^2, 3x3 cm^2, 4x4 cm^2, 6x6 cm^2, 8x8 cm^2) for all electron energies (6,9,12,16,and 20 MeV) were utilized for this purpose. While Pinnacle linearly interpolates between the measured %DD curves, it was believed more accurate to interpolate between curves that had been normalized to a common dose. Hence it was assumed that, due to the lack of side-scatter from build-up material, that all field sizes should have the same dose at the water surface. As surface dose is difficult to measure, a small amount (0.25 cm) of build-up was allowed, and the %DD curves for all field sizes for an energy were normalized by

$$\%DD'^{W\otimes W}(Z) = \%DD^{W\otimes W}(Z) * \frac{\%DD^{Weq\otimes Weq}(0.25)}{\%DD^{W\otimes W}(0.25)}. \quad (16)$$

$\%DD'^{WX\otimes WX}$ and $\%DD'^{WY\otimes WY}$ were then linearly interpolated from these curves, as seen in Figure 5, which originated from the measured %DD curves in Figure 6. $\%DD'^{WX\otimes WY}$ was calculated using the above square root method, including normalizing $\%DD'^{WX\otimes WY}$ to its own maximum dose.

The dose contribution due to photon contamination, determined in Section 2.1.3, was removed from the total %DD curve by

$$\%DD^{WX\otimes WY,e}(Z) = \%DD^{WX\otimes WY,total}(Z) - \%DD^{\gamma}(Z). \quad (17)$$

An example of the final central-axis $\%DD^e$ for a 20 MeV 10x10 cm^2 field is seen below in Figure 7. In the event that $\%DD^e$ was less than 0, it was set to 0 to avoid negative dose. Finally, D_{CA}^{∞} was determined by

$$D_{CA}^{\infty}(Z) = \%DD^{WX\otimes WY,e}(Z) * \left[\text{erf}\left(\frac{WX}{2\sqrt{2}\sigma}\frac{SSD+Z}{SSD}\right)\text{erf}\left(\frac{WY}{2\sqrt{2}\sigma}\frac{SSD+Z}{SSD}\right)\right]^{-1}. \quad (18)$$

The output factor (OF) of the rectangular field was similarly determined. The measured OFs from a Varian 21EX for all field sizes using a 25 cm x 25 cm cone were obtained for all energies. The required $OF^{WX\otimes WX}$ and $OF^{WY\otimes WY}$ were interpolated from the measured OFs, and

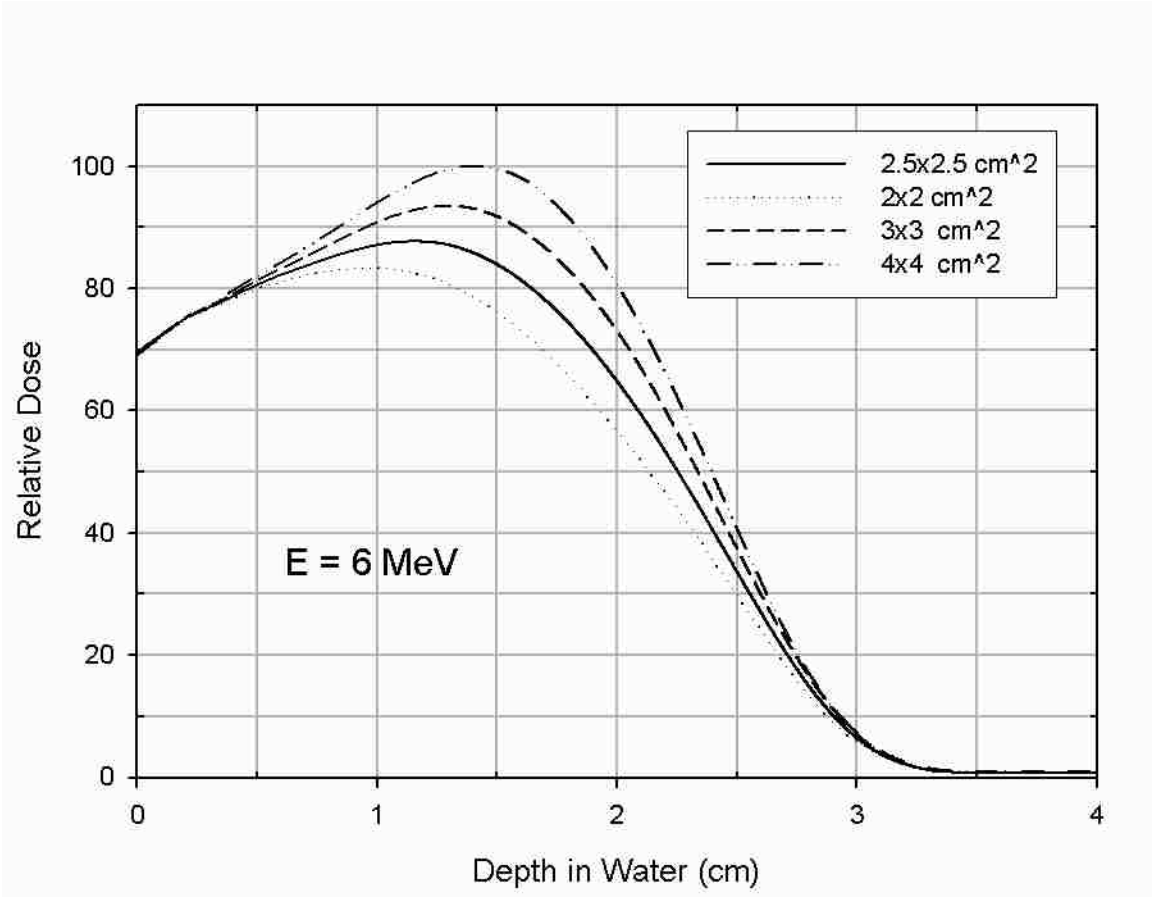

Figure 5: Measured central-axis relative dose versus depth curves for our institution's Varian 21EX at 6 MeV created by normalizing the measured percent depth dose curves (2x2, 3x3, and 4x4 cm^2) to the dose at 0.25 cm depth of the 4x4 cm^2 field. Subsequently, the 2.5x2.5 cm^2 curve is linearly interpolated.

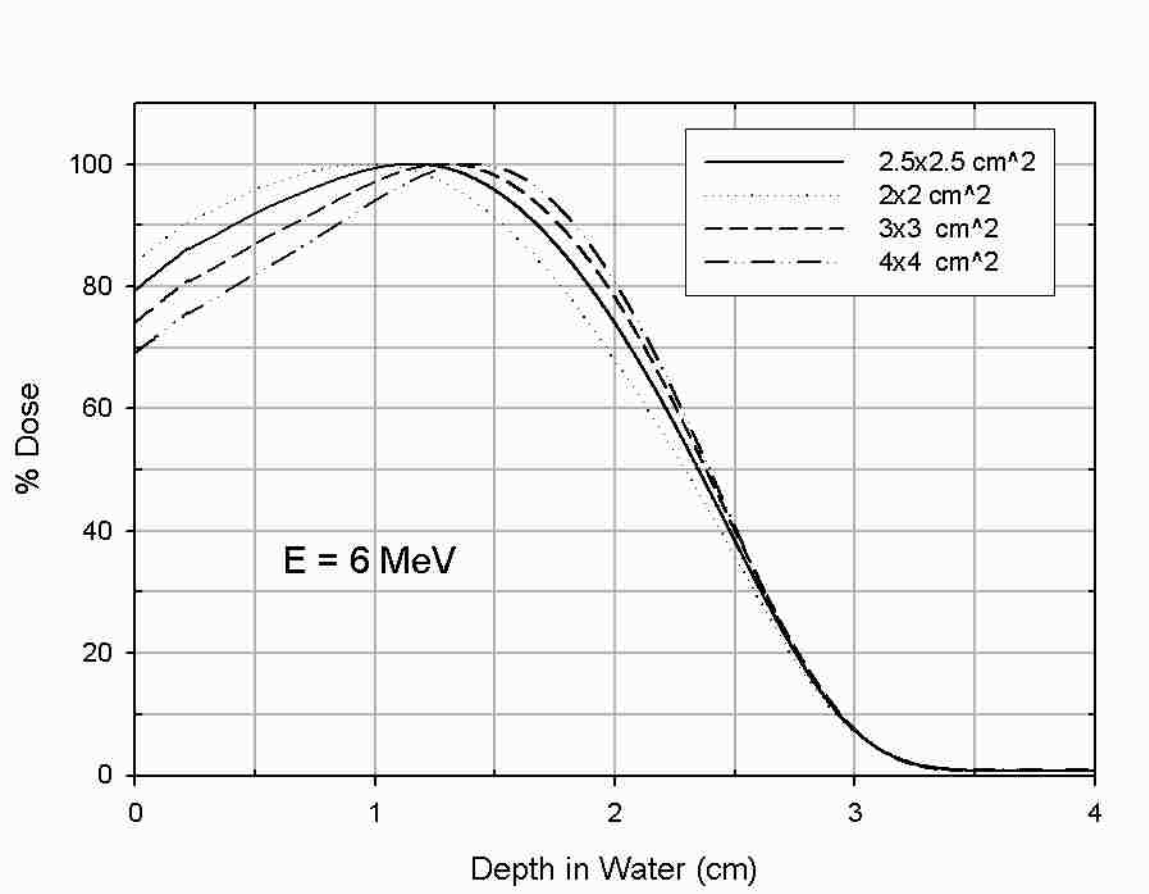

Figure 6: Measured central-axis percent depth curves (2x2, 3x3, and 4x4 cm^2) for our institution's Varian 21EX at 6 MeV. The 2.5x2.5 cm^2 curve is from the interpolated depth dose curve.

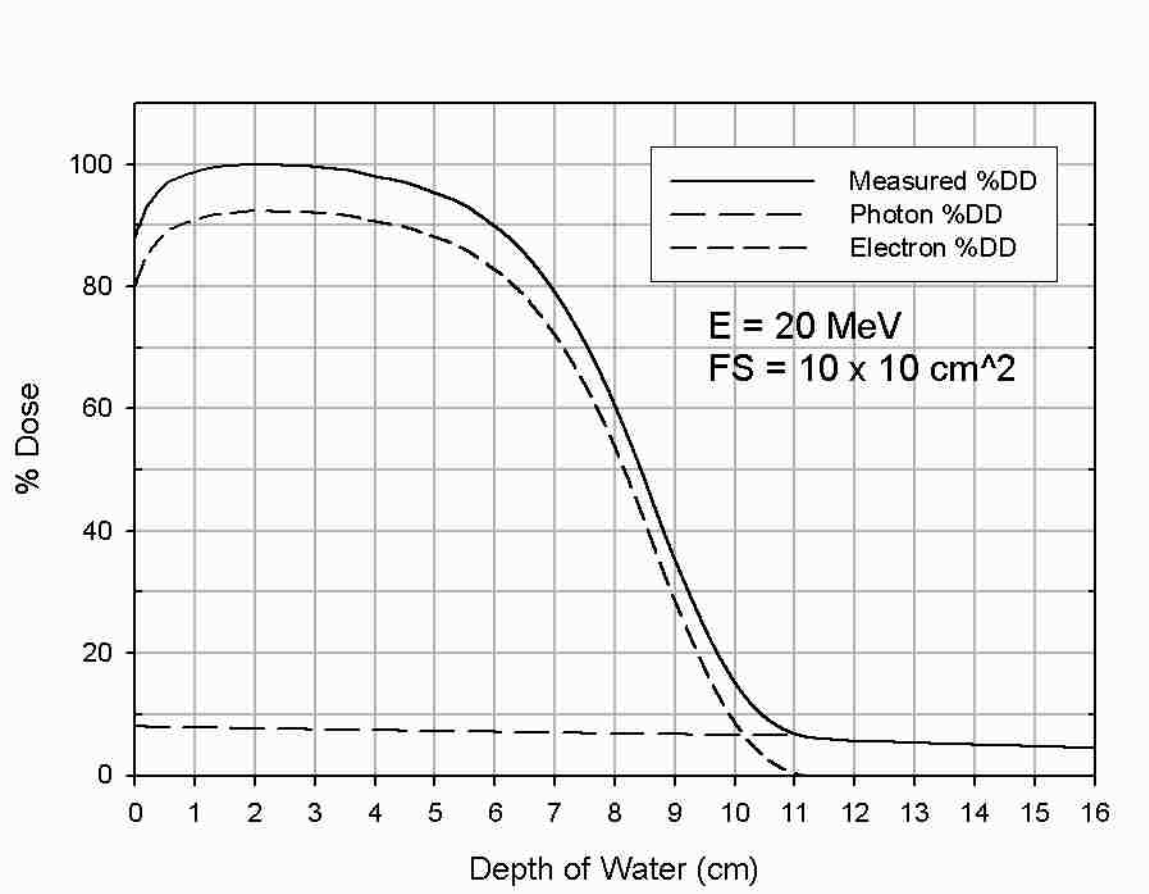

Figure 7: Measured central-axis percent depth dose curves for a 10x10 cm^2 20 MeV beam from our institution's Varian 21EX. The photon central-axis percent depth dose curve calculated from the measured curve is subtracted from the measured curve to produce the electron central-axis percent depth dose curve.

$OF^{WX\otimes WY}$ was determined according to Mills *et al.* (1982), which was shown true for applicators by Shiu *et al.* (1994),

$$OF^{WX\otimes WY} = \sqrt{OF^{WX\otimes WX} * OF^{WY\otimes WY}}. \quad (19)$$

2.1.6 Optimization of Calculation Times

The dose calculation was coded in IDL on a Dell Inspiron 2200 laptop with a 1.4 GHz Intel Celeron processor and 256 MB of RAM running Windows XP. Several of the suggestions of Starkschall *et al.* (1991) to reduce the time of calculation of the PBA were implemented. All beam sigmas from Section 2.1.4 were precalculated. The error functions were precalculated from -4 to 4 in 0.001 increments and stored in an array. In the dose calculation, the argument of

the error function was calculated and multiplied by 10^3, which allowed direct indexing of the error function array. Lateral cut-off distances (how far away from the center of the pencil beam dose was calculated) were set at $\pm 3\sigma$ from the pencil beam in both the x and y directions. Because the pencil beams were approximately Gaussian, restricting contribution of a pencil beam to surrounding dose points to only the pixels that fall within this square accounted for nearly (99.46%) the entire dose from the pencil beams to a point. Since the calculation was in a flat, water phantom, it was sufficient to normalize each dose array to its own (central-axis) maximum rather than normalize each pencil beam by 0.9946^{-1}. Depth cut-off distances were set at 1 cm past R_p for each energy. The electron contribution to the dose should be zero past this depth and thus only the dose from the photon contamination, as discussed in Section 2.1.3, was computed past this depth for each energy. Finally, as the planning algorithm did not account for organs at risk, any dose deeper than the R_p for 20 MeV was not needed by the algorithm. Therefore, the PBA only calculated dose at depths shallower than 14 cm, a few centimeters deeper than the R_p of the 20 MeV beam.

2.1.7 Validation of Dose Calculation

The dose algorithm and the beam model and input data were verified by comparing dose distributions calculated by my coded PBA to dose distributions calculated by Pinnacle v7.4f. Dose distributions were compared for a set of measured square field input data measured at 100-cm SSD and for a square field at an extended SSD of 110-cm. Results of these comparisons are found in Section 3.1 and Appendix C.

2.2 Aim 2: Develop Field Segmentation Algorithm

The goal of Aim 2 was to develop a clinically useful forward planning algorithm for determining the energy, shape, and weight of multiple abutted field segments used in SFECT that conforms the distal 90% isodose surface to the PTV while minimizing the treatment of normal

tissue. R_{90} primarily depends on the energy of the beam, the field size (for regular shaped fields, e.g. square or circular), and the source-to-surface distance (SSD). As beam energy increases, R_{90} moves deeper, as seen in Figure 8 for a 10x10 cm^2 field. As square field size increases, electronic equilibrium is approached, and R_{90} moves deeper as more electrons are able to scatter into the central-axis, as seen in Figure 9. Once electronic equilibrium is reached, further increasing of the field size has an insignificant effect on the central-axis percent depth-dose curve. Increasing SSD has a small impact on central-axis percent depth dose primarily from hardening of the energy spectra, causing R_{90} to move deeper, due to the decrease in electrons scattered off the edge of the applicator and x-ray collimators reaching central-axis (Shiu *et al.* 1994), as seen in Figure 10.

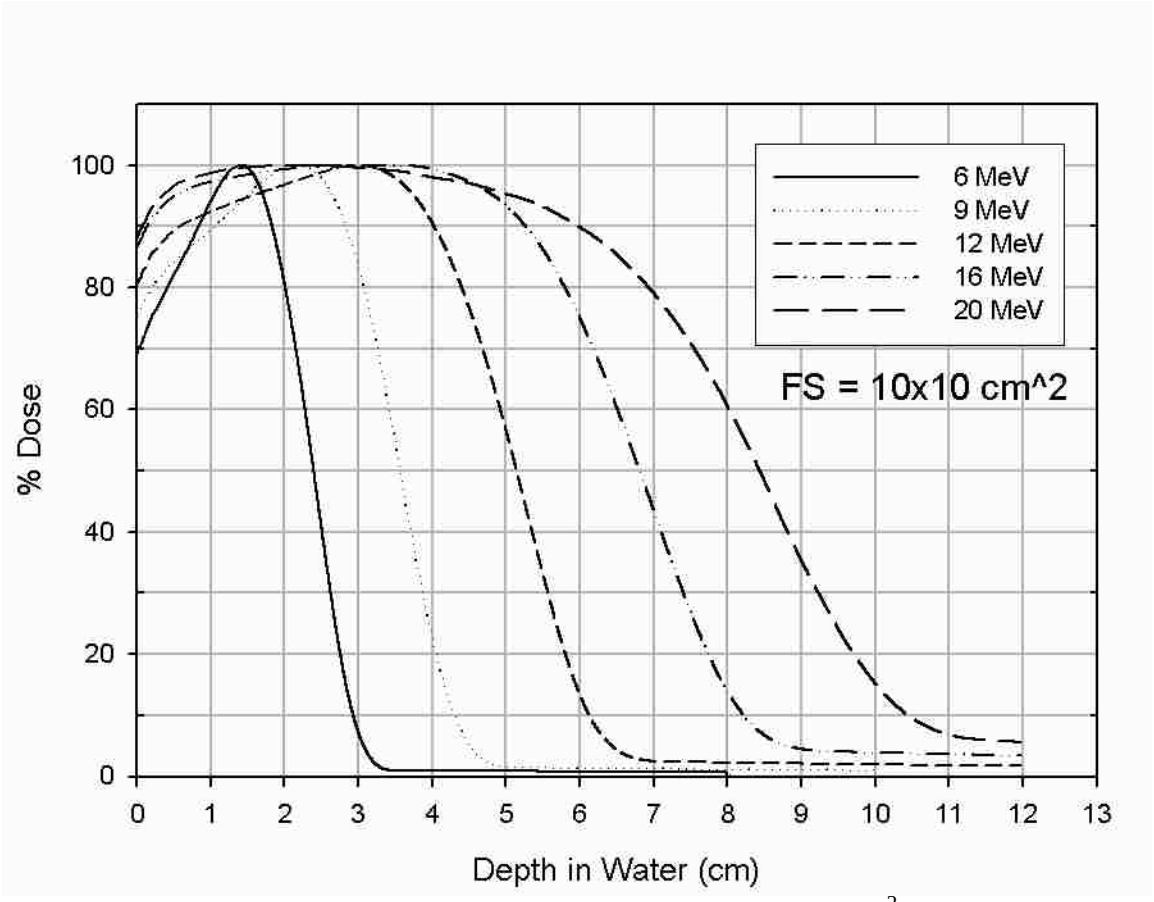

Figure 8: Measured central-axis percent depth dose curves for 10x10 cm^2 fields at 100 SSD of varying energies from our institution's Varian 21EX demonstrating increase of 90% dose depth with increasing energy.

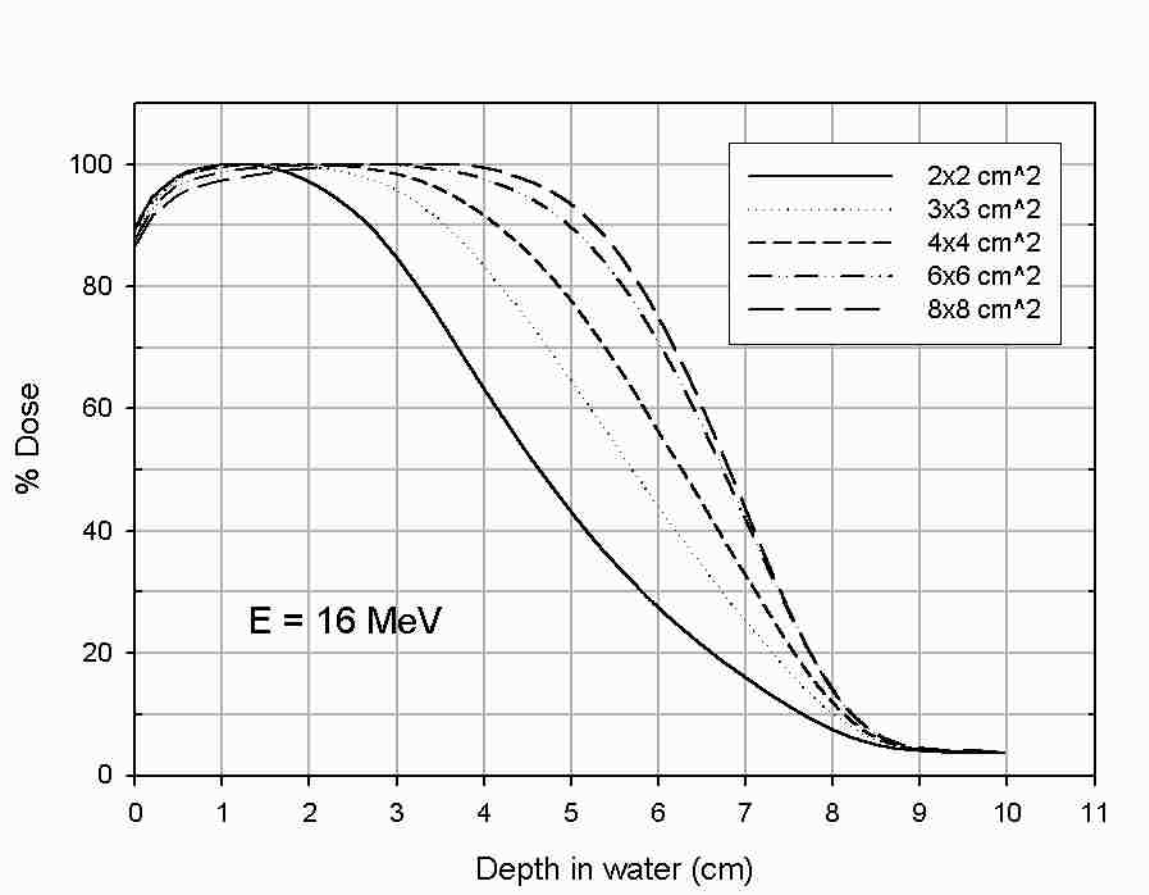

Figure 9: Measured central-axis percent depth dose curves from our institution's Varian 21EX for a 16 MeV beam at 100 SSD of varying field sizes demonstrating increase of 90% dose depth with increasing field size. Electronic equilibrium is reached for the 8x8 cm^2 field.

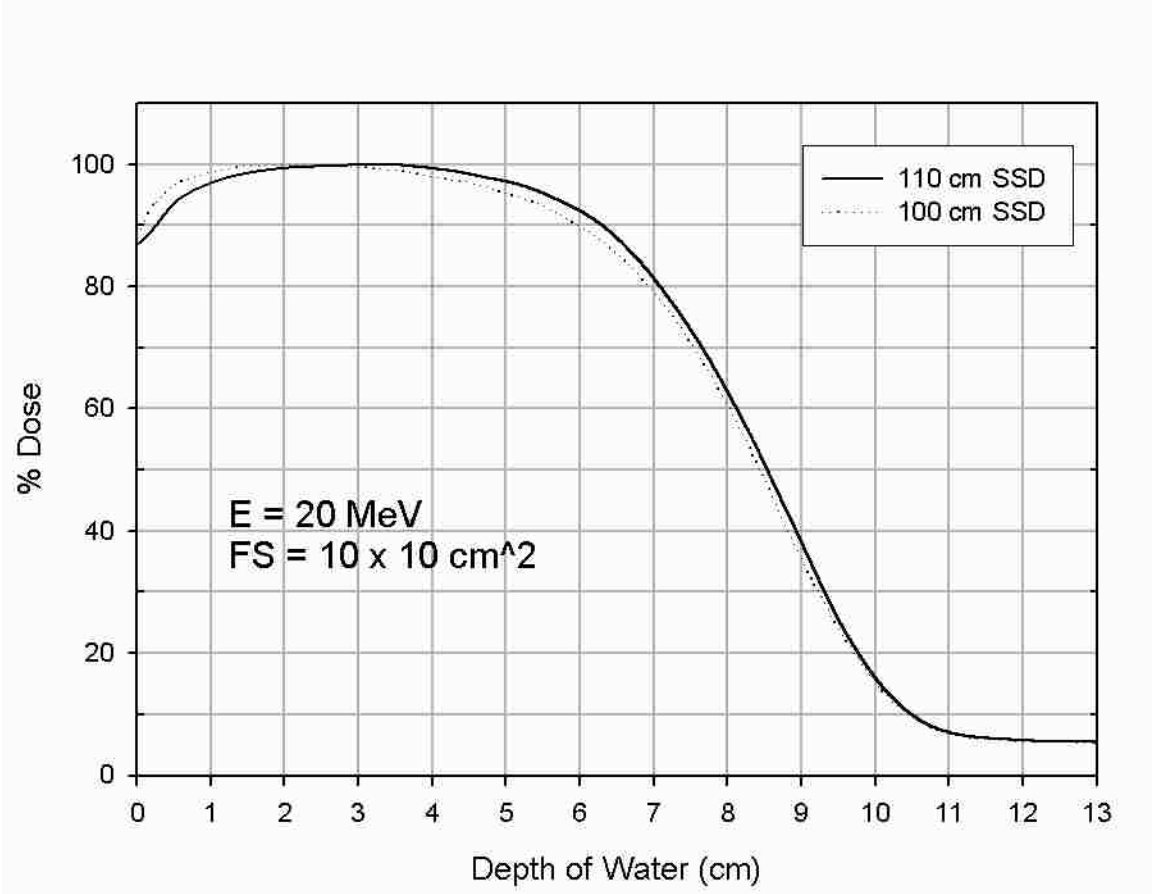

Figure 10: Measured central-axis percent depth dose curves for a 10x10 cm^2 20 MeV beam from our institution's Varian 21EX at 100 cm SSD and 110 cm SSD demonstrating increase of 90% dose depth with increasing SSD.

In the case of SFECT, the 90% isodose surface of the entire plan also depends on the weighting (number of monitor units, MUs) of the individual segments. The number of MUs has no effect on the 90% isodose in a conventional single-beam treatment because the normalization point is within the beam, so an increase in MUs scales the entire dose equally. In SFECT, however, since there are multiple field segments, but only a single normalization point, changing the MUs of one segment will slightly affect the composite field's 90% isodose, as its total dose is changing at a different rate than the dose of the normalization point. Additionally, the composite dose distribution is impacted by contribution of photon dose through the collimator.

The developed field segmentation algorithm addressed the energy, field segment size and shape, and segment weighting. These were the factors that most affect the depth of the 90%

isodose surface, as change in SSD has a very minimal effect except in extreme cases. They were also the factors that were most easily modified for each segment. While changing the SSD for each segment is easily calculated, it would dramatically increase treatment time as the patient would have to be moved for each different segment. So, due to its minimal effect and increase in time, SSD optimization was not considered and an SSD of 100 cm was always used. The largest cone size clinically available, 25 cm x 25 cm, was used in the planning as it will accommodate all PTVs that could be treated without repositioning the patient or gantry. Finally, the algorithm was capable of designing SFECT plans for use with both standard SCD (SSCD) and variable SCD (VSCD) methods.

The described planning algorithm was coded in IDL. It takes as input the Pinnacle v7.4f file containing the PTV and surface contours (plan.roi), the file containing the location of the planned beam isocenter (plan.points), and the file containing the selected gantry position (plan.trial). If the files containing the isocenter and gantry angle were missing, the algorithm assumed an isocenter located in the center of the top surface and a gantry position of 180° (beam pointed directly to the floor). The PTVs described in Section 2.3.1 were created to exact dimensions by modifying the plan.roi file outside of Pinnacle v7.4f and then using Pinnacle v7.4f's contouring tools to copy the modified slice to the remaining slices. The resulting plan.roi files were then used for testing of the planning algorithm.

2.2.1 Step 1: Initial Energy Segmentation of Fields

A BEV of distal PTV depth in the direction of the beam, similar to the one seen in Figure 11, was created with a pixel size of 0.25x0.25 cm^2, defined at 100 SSD. This pixel size was chosen because the default voxel size for a Pinnacle v7.4f water phantom is 0.25x0.25x0.25 cm^3, and consistency with Pinnacle v7.4f models, as much as possible, was desired. A parallel beam, rather than the fan beam geometry used by the PBA to calculate dose, was assumed in the

creation of the BEV of distal PTV depth. The use of parallel geometry in this step was accounted for in planning by the use of a virtual PTV, discussed in Section 2.2.5.

Step 1 of the algorithm was to determine for each pixel of the BEV in which a parallel line through it intersects the PTV the minimum energy such that R_{90}(E, 10-cm Ø field) was greater than the depth to distal surface of the PTV, as demonstrated in Figure 12. If the depth to the distal PTV surface for a pixel was deeper than that of R_{90} for the maximum beam energy (20 MeV), the energy for that pixel was set to the maximum energy (20 MeV). Depth-dose curves (measured for use in Mary Bird Perkins Cancer Center (MBPCC) clinic) from a Varian 21EX for 10x10 cm^2 equilibrium field sizes for all electron energies (6,9,12,16, and 20 MeV) were obtained for this purpose. The square field data was converted to circular field data using pencil beam theory (derivation in Appendix A). The R_{90} values for the equilibrium field size, both square and circular, for all energies are found in Table 3.

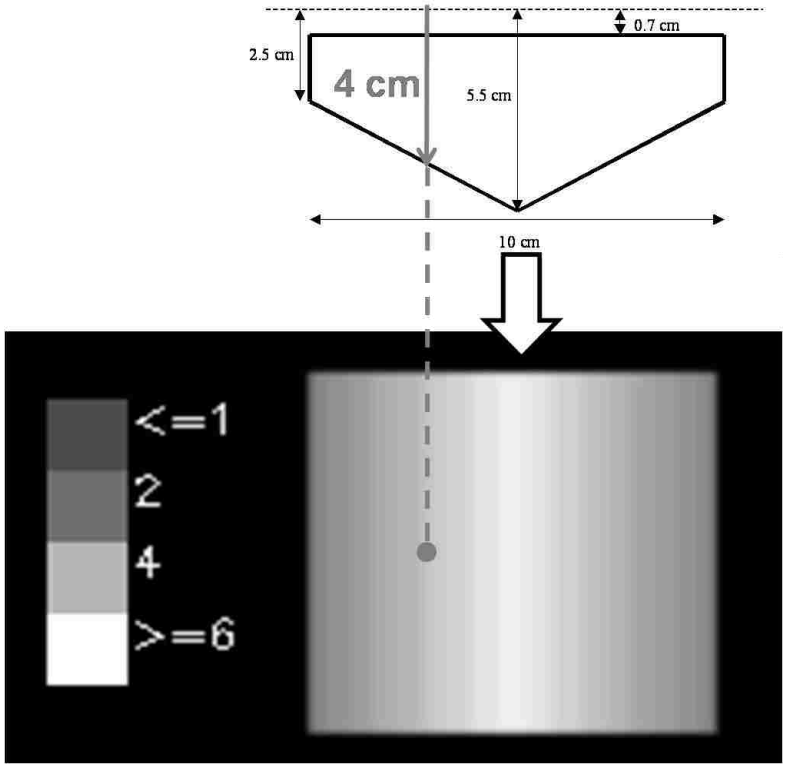

Figure 11: Beam's eye view of distal PTV depth using the pentagon PTV described in Section 2.3.1. The BEV is shaded with the deeper areas being brighter.

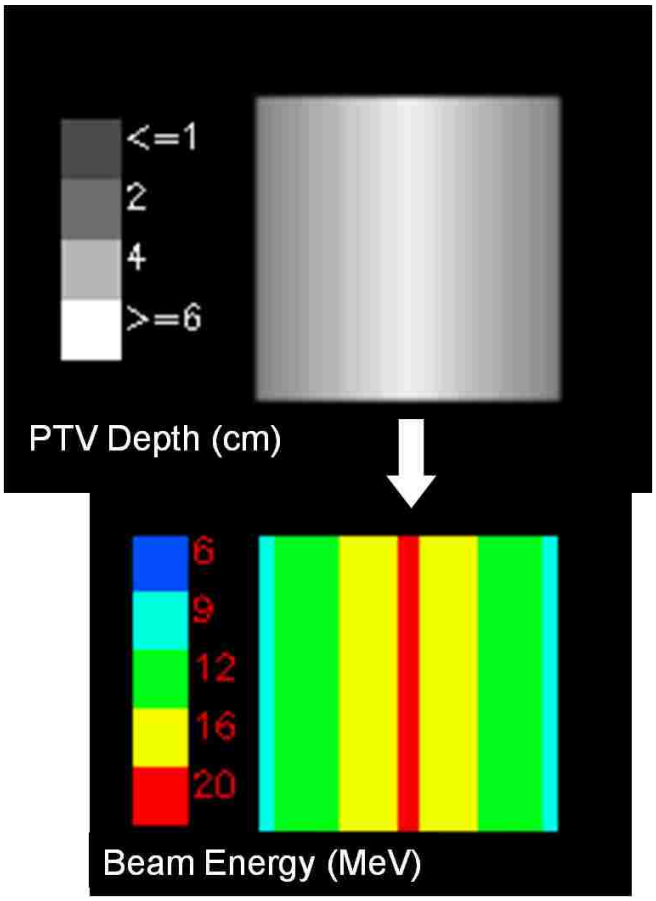

Figure 12: Overlay on the BEV of the pentagon PTV of the minimum energy required to treat R_{90} to the distal PTV surface. Each pixel of the BEV is labeled with the minimum energy for which R_{90} would reach the distal PTV surface if a 10-cm diameter circular field were used around the pixel.

Table 3: R_{90} depth in water (cm) of square and circular equilibrium (Eq.) field sizes.

Energy (MeV)	Square Eq. R_{90} (cm), Field Size (cm x cm)	Circular Eq. R_{90} (cm), Field Diameter (cm)
6	1.83, 4 x 4	1.83, 6
9	2.83, 6 x 6	2.83, 8
12	4.03, 8 x 8	4.03, 8
16	5.26, 8 x 8	5.26, 8
20	5.96, 8 x 8	5.96, 8

2.2.2 Step 2: Reducing Number of Energies

The algorithm was able to restrict the maximum number of energies allowed in the plan from one (defined as a conventional plan) to five energies. It should be noted that restricting the number of energies did not require that number of energies be used, only that that many energies

were allowed to be used. After energies were assigned to each PTV pixel of the BEV of depth, the algorithm determined how many energies were used. If the number of energies used was more than the number allowed (i.e. specified by the user), the algorithm went through an iterative process of replacing energies until the reduced number equaled the allowed number. In order to assure full PTV coverage, lower energies were not allowed to replace higher energies. If only one energy was allowed, the algorithm simply determined the maximum energy used and replaced all other energies with the maximum energy. If five energies were allowed, no energy replacement was necessary. If two to four energies were allowed, the energy replacement procedure, illustrated in Figure 13, was as follows:

1. The fractional volume of the PTV covered by each energy in the BEV of depth was determined.
2. Based on the equilibrium R_{90} depths and the fractional volume of each energy, the additional volume irradiated to 90% was determined for each possible replacement (each energy replaced by the next highest energy remaining in the plan).
3. The replacement that resulted in the least additional irradiated volume was selected.
4. The new number of energies used was determined. If it was still more than the number allowed, the process was repeated, replacing one energy at a time, until the number used equaled the number allowed.

2.2.3 Step 3: Construction of Energy Segments

The next step in field segmentation was drawing of initial segments based on the previous energy selection and distal PTV depth for each pixel of the BEV. For each pixel of the BEV in which the PTV exist, the minimum circular field size such that $R_{90}(E, Ø_{min})$ was greater than the depth to distal surface of the PTV was determined (cf. Appendix B) and drawn around the pixel,

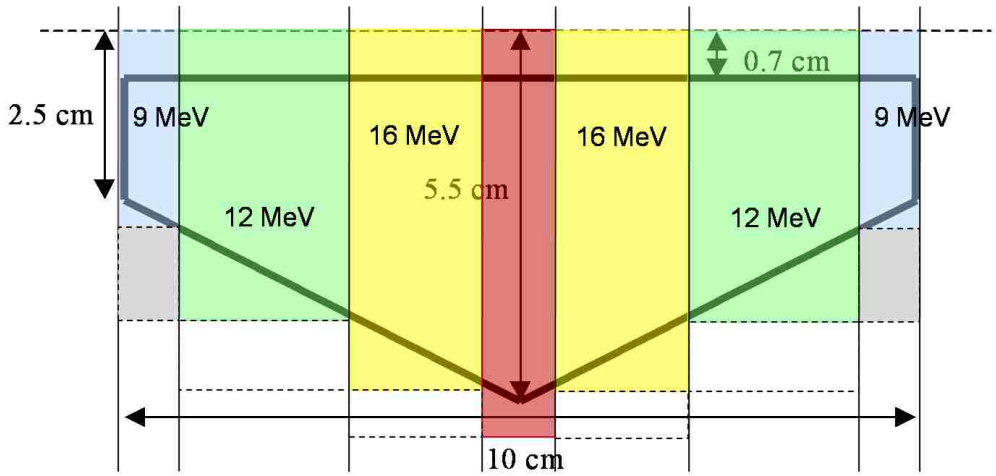

Figure 13: Illustration of energy replacement procedure using the central slice of the pentagon PTV. The dashed box areas represent the additional irradiated volume (shown here as area for illustration purposes) for each possible replacement. If the plan were restricted to allow 3 energies, it's seen that the replacement would be 12 MeV replacing 9 MeV, the shaded box, as it would result in the least additional volume irradiated to 90%.

as illustrated in Figure 14. R_{90} depths in water as a function of circular field diameter are listed for each beam energy for our institution's Varian 21EX in Table 4.

After a circular field was drawn around each pixel, the union of all circular fields of the same energy combined to form a single segment. In areas of overlap, the higher energy segment took precedence. Finally, a process of small segment replacement was executed. Any segments which could not completely contain a 2-cm diameter circle were replaced by the next highest adjacent energy in order to ensure PTV coverage. This was because the smallest measured field size data was from a 2x2 cm^2, and ensured that data would only be interpolated and not extrapolated. In the event that the segment of the highest energy used was too small, the segment was expanded in all directions by one pixel at a time until it was large enough to hold a 2-cm diameter circle. If an expansion occurred, the process started over and continued to execute until there was no change in the segments, as the expansion could have reduced the size of adjacent segments. An example of this process is shown in Figure 15.

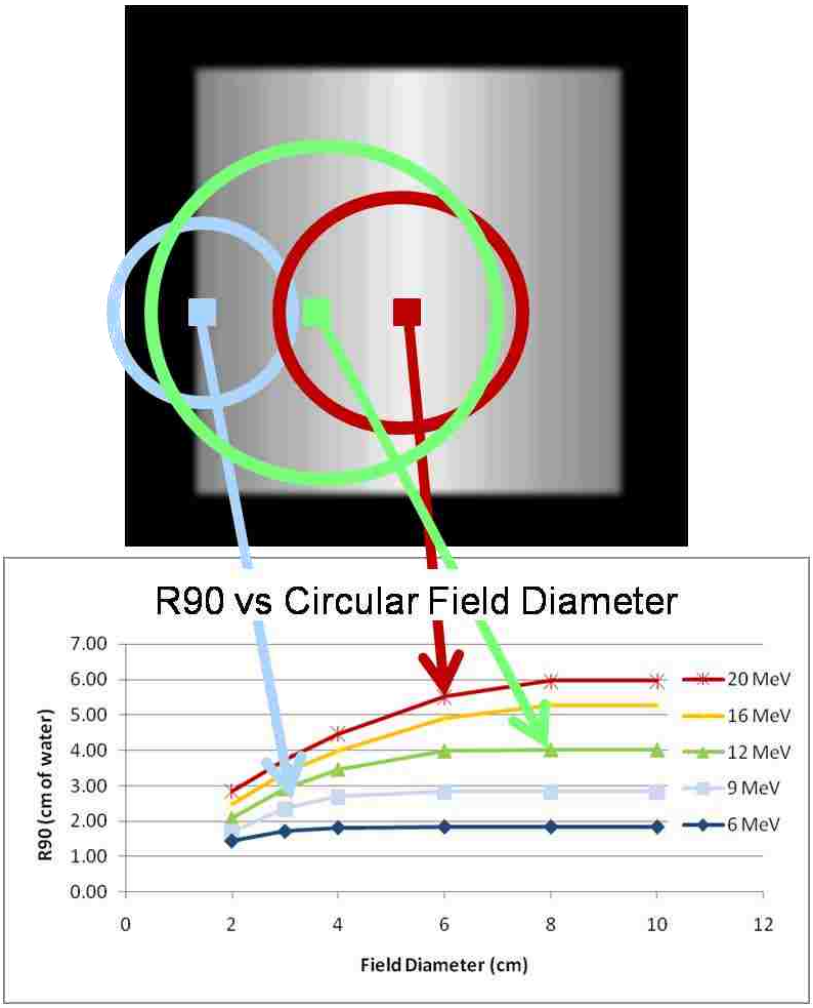

Figure 14: Illustration demonstrating the determination of the minimum circular field size for which R_{90} reaches the distal PTV of each pixel of the BEV. A circular field of the determined diameter is then drawn around the pixel.

Table 4: R_{90} depths in water for all circular field sizes up to 10 cm diameter, converted from measured square data.

R_{90} (cm)	Field Diameter (cm)					
Energy (MeV)	2	3	4	6	8	10
6	1.44	1.70	1.81	1.83	1.83	1.83
9	1.70	2.35	2.69	2.82	2.83	2.83
12	2.08	2.92	3.47	3.99	4.03	4.03
16	2.47	3.37	3.99	4.89	5.26	5.26
20	2.83	3.73	4.46	5.50	5.96	5.96

2.2.4 Step 4: Segment Weighting

Segment weighting was done by energy rather than by individual segments. Since Cerrobend inserts are currently the only available method of SFECT delivery, it was assumed

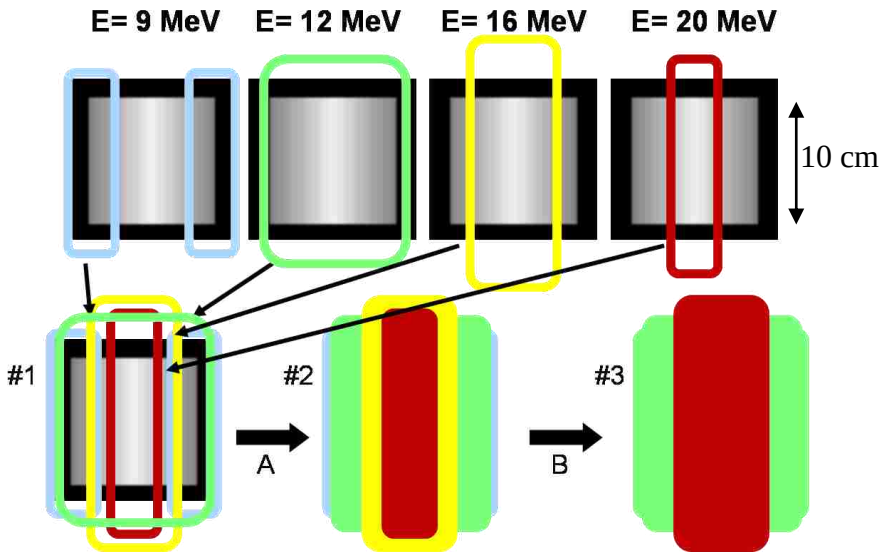

Figure 15: Illustration demonstrating the consolidation of the pixel fields into the final field segmentation. (A) Once the pixel fields for each energy have been combined (#1), the segments for all energies are combined with higher energies taking precedence in areas of overlap (#2). (B) Any segments smaller than 2-cm in diameter are replaced by the next highest adjacent energy.

that they would be used to deliver the plan. In the event that an energy had more than one segment, more than one insert per energy might be required. Extra inserts would lead to longer treatment times, as the radiation therapists would have to enter the room to switch out inserts. Hence, in the present work it has been assumed that all segments of an energy will be treated simultaneously (i.e. mylar base might be required for island blocks). Therefore, segments were weighted by energy rather than individual segments.

Segment weightings were performed both before the calculation of the dose distribution and after. The goal of the weighting (MU) before the dose distribution was calculated was to account for the effect of the OF, determined by the pencil beam algorithm of Aim 1. To achieve this, each segment was assigned MUs equal to 100 times the inverse of its OF. For example, if a segment had an OF of 0.9, delivering 100 MUs would deliver a max dose of only 90 cGy (100*0.9), while delivering 111 MUs (0.9^{-1}*100) would deliver the desired max dose of 100 cGy

(111*0.9). In the case that an energy has multiple segments, the OF of the largest segment was used to assign MUs, even though each segment retained its own OF in the dose calculation.

The goal of the weighting after the dose distribution was calculated was to account for the extra dose from the Pinnacle photon contamination arising from bremsstrahlung (created in the gantry head and Cerrobend insert), which was transmitted through the Cerrobend inserts. During the calculation of the dose distribution, the dose distributions of the individual energies were calculated independently. The point of maximum dose in the dose distribution for each energy was taken as a normalization point. A normalization factor was determined for each energy by normalizing the dose in the composite distributions at the energy's normalization point to 100 cGy. The normalization factor was then applied to the energy's original MUs to get the final MUs for the energy. Finally, rather than recalculate the dose distributions using the new MUs, each normalization factor was applied to its energy's individual dose distributions. The normalized distributions were then added together for the final, composite dose distribution.

2.2.5 Step 5: Optimization

The final segments were larger than the original circular fields drawn around the individual pixels. This resulted in the 90% isodose surface often penetrating deeper than planned. Hence, an iterative optimization algorithm was used to pull the 90% isodose surface closer to the distal PTV surface. The optimization procedure included the following steps:

1. Using the final dose distribution from either the initial plan or the previous iteration of the optimization algorithm, the overshot/undershot of the 90% isodose surface to the distal PTV surface was determined for each pixel of the BEV of distal PTV depth.
2. A virtual PTV (VPTV) was created by subtracting (adding) the overshoot (undershoot) from (to) the PTV for each pixel for the first iteration of the optimization algorithm, as demonstrated in Figure 16. For later iterations, the VPTV

from the previous iteration was modified by the overshoot (undershoot) from the PTV rather than creating a new VPTV. In order to ensure the field goes to the edge of the PTV, the VPTV was not allowed to be less than 1 cm thick. That is, if the VPTV were allowed to shrink to 0 cm thick, then no field would be drawn around the pixel, leaving the PTV untreated.

3. The planning algorithm was repeated starting at Step 3 using the BEV of distal VPTV depth. The optimization algorithm repeated until either the maximum number of iterations (user-defined) was reached or the VPTV no longer changed.

Planning using the VPTV produced smaller (larger) final fields. These fields result in a shallower (deeper) 90% (90 cGy) isodose surface.

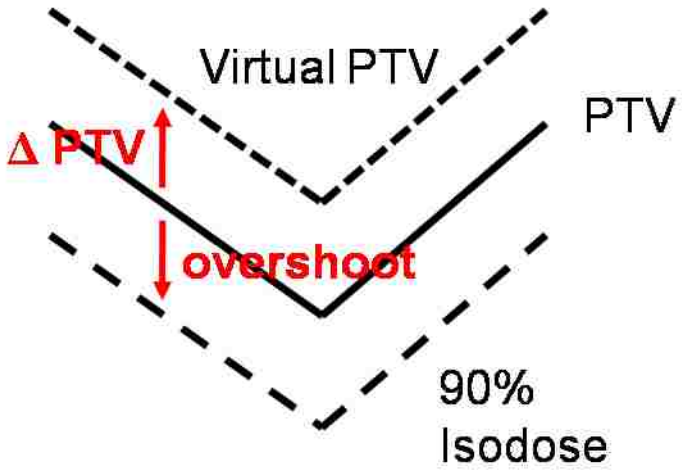

Figure 16: Illustration of creation of the VPTV from the PTV and the 90% isodose. The VPTV (short dashed line) is created by moving the PTV (solid line) opposite of the 90% isodose (long dashed line) by the separation between the PTV and the 90% isodose.

In part 3 of Step 5 the planning algorithm iterated to Step 3 rather than at Step 1 in order to ensure that R_{90} still reached the distal PTV surface. For example, if the distal surface of a PTV were originally 4.5-cm deep, requiring a 16 MeV segment, and the VPTV reduced the distal surface to a depth of 4-cm, repeating the planning algorithm at Step 1 would assign a 12 MeV

segment. The deepest 12 MeV R_{90} is 4.03-cm, and thus a 12 MeV segment would be unable to deliver 90% of the dose to the distal surface of the original PTV. By instead repeating the planning algorithm at Step 3, a smaller 16 MeV segment is used and the 90% isodose is still able to reach the original distal PTV surface.

2.3 Aim 3: Utilization of Algorithm to Compare Impact of Number of Energies

The planning algorithm allowed the planner to choose the number of energies, from 1 to 5, allowed in the plan. Preliminary testing (exemplified in Section 3.2) of the planning algorithm on the hypothetical PTVs described in Section 2.3.1 showed that there was not much, if any, improvement in allowing more than 3 energies. This was because when 4 and 5 energies were allowed, the final plan still only used 3 energies. Allowing more than 3 energies in the plan may be beneficial in cases of PTVs larger than those in the present study, but will likely produce nearly the same fields as the 3 energy plans in the current study. Due to these preliminary tests, and in the interest of shorter treatment times, as more energies require more treatment segments, the plan comparisons were limited to 1, 2, and 3 energies. Therefore, 6 plans were created for each case, 3 using SSCD and 3 using VSCD.

2.3.1 Hypothetical PTVs

In order to assess the planning algorithm's ability to plan SFECT fields in ideal situations, six hypothetical 3D PTVs were created in a flat water phantom. All PTVs were 10-cm wide, began 0.7 cm below the phantom surface, and had depths ranging from 2.5 cm to 5.7 cm. The central slice of each PTV is shown in Figure 17-Figure 22. Figure captions describe the PTVs and the rationale of each.

The four right prism, hypothetical 2D PTVs used by Richert *et al.*(2007) were expanded to 10-cm total thickness (40 0.25-cm thick slices) in a virtual water phantom (50 x 50 x50 cm^3) with the central slice being 0 cm off axis in the z (slice) direction. These 4 PTVs assessed the

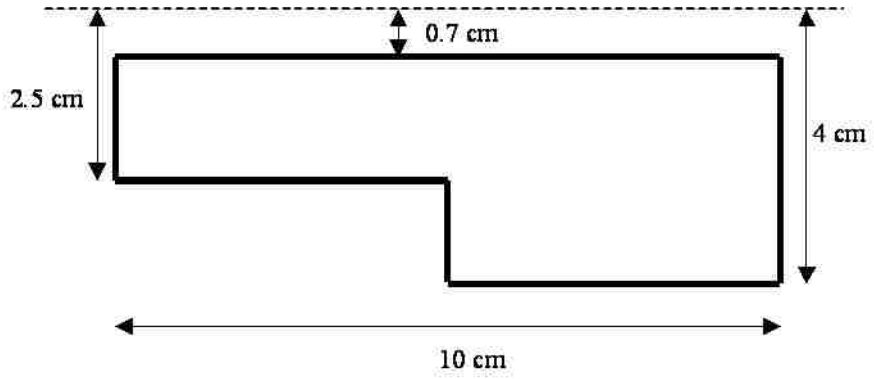

Figure 17: Two-step block PTV. Assesses ability to plan a steep change in depth. PTV approximates a typical post mastectomy treatment volume. Dashed line is phantom surface.

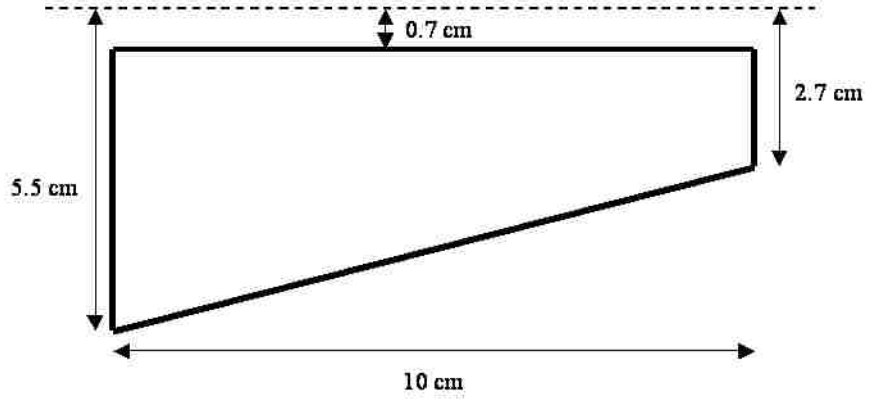

Figure 18: Wedge PTV. Assesses ability to plan a gradual change in depth. Dashed line is phantom surface.

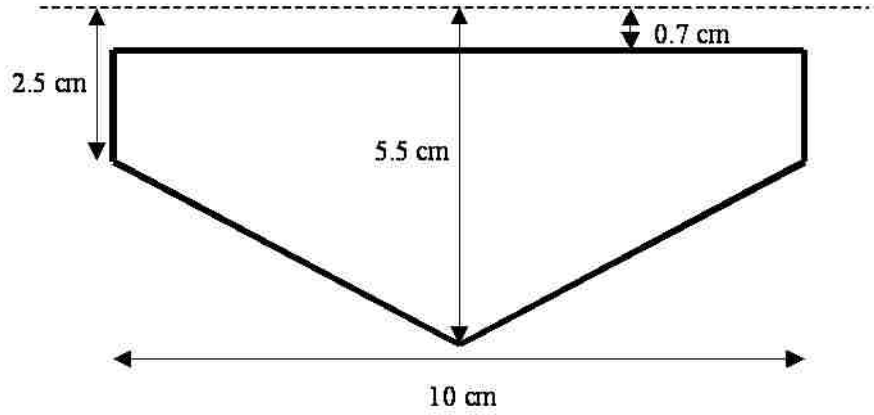

Figure 19: Pentagon PTV. Assesses ability to plan a steep change in depth with the deepest depth in the middle. Dashed line is phantom surface.

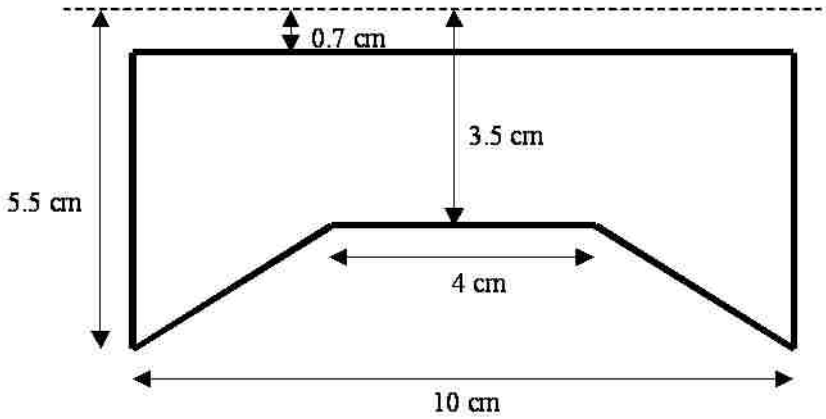

Figure 20: Inverted well PTV. Assesses ability to plan a steep change in depth with the shallowest depth in the middle. Dashed line is phantom surface.

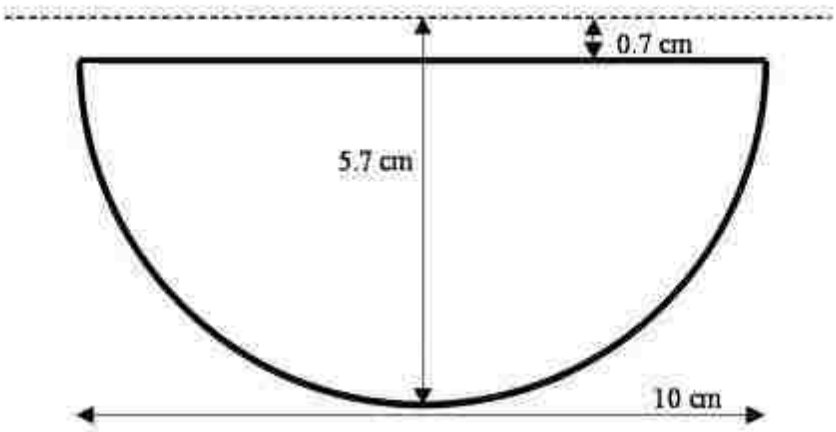

Figure 21: Hemisphere PTV. Assesses ability to plan both gradual and steep changes in depth in two dimensions. Dashed line is phantom surface.

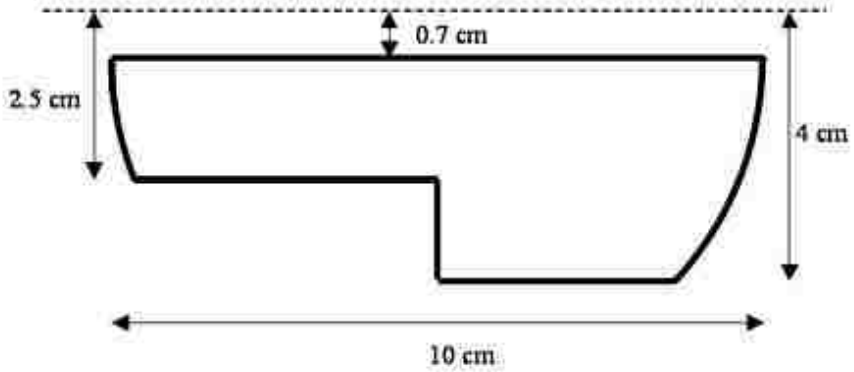

Figure 22: Two-step hemisphere PTV. Assesses ability to plan gradual and steep changes in depth in two dimensions over a more realistic target volume. Dashed line is phantom surface.

algorithm's ability to plan fields based on PTVs with both gradually and steeply changing depths.

Additionally, two "true" 3D PTVs (i.e., not right prisms) were created to assess the algorithm's ability to plan more realistic changes in PTV depth. The first 3D PTV was a hemisphere of 5-cm radius located 0.7 cm below the surface. The second was the intersection of the hemisphere PTV and the two-step block PTV used by Richert *et al.* (2007).

2.3.2 Plan Comparison Metrics

Dose distributions for all plans for each PTV were compared using a variety of metrics. A coverage ratio (CR), sparing ratio (SR), and conformity index (CI) were used to compare how well the dose distributions conform to the PTV. The CR was defined as the fraction of PTV receiving at least 90% of the prescribed dose,

$$CR = \frac{PTV_{90}}{PTV}. \tag{20}$$

The CR could range from 0.0 to 1.0. The CR was ideally 1.0, indicating the entire PTV received at least 90% of the prescribed dose. The SR was defined as the ratio of non-PTV receiving at least 90% of the prescribed dose to the total volume, both PTV and non-PTV, receiving at least 90% of the prescribed dose,

$$SR = \frac{(Non-PTV)_{90}}{(Non-PTV)_{90}+PTV_{90}}. \tag{21}$$

The SR can range from 0.0 to 1.0. The SR was ideally 0.0, indicating that no non-PTV received at least 90% of the prescribed dose. Paddick (2000) defined the CI as

$$CI = \frac{PTV_{90}}{PTV} * \frac{PTV_{90}}{(Non-PTV)_{90}+PTV_{90}}, \tag{22}$$

which was the same as

$$CI = CR * (1 - SR). \tag{23}$$

The CI could range from 0.0 to 1.0. The CI was ideally 1.0, indicating that the entire PTV, and only the PTV, received at least 90% of the prescribed dose. The multi-energy SSCD plans were compared to the single-energy SSCD plan, and the multi-energy VSCD plans were compared to the single-energy VSCD plan, for improvement to conformity. Improved conformity was defined as having a CI that was closer to 1.0.

The spread in the minimum and maximum doses (max-min) to the PTV, the standard deviation of the dose distribution in the PTV, and the difference in dose received by 10% and 90% of the PTV (D_{90-10}), were used to compare dose homogeneity inside the PTV. The VSCD plans were compared to the SSCD plans for improvement to dose homogeneity.

2.4 Aim 4: Demonstrate Use of Algorithm on Patient Data

Two head and neck patients, one previously treated with electrons at MBPCC and one previously treated with IMRT, were selected to assess the planning algorithm's potential to plan SFECT fields to non-flat, heterogeneous targets. As with the hypothetical PTVs, 3 SSCD plans and 3 VSCD plans were generated for each patient case. The multiple-energy allowed plans and the single-energy plan were compared, including comparison for improved dose conformity and dose to critical structures.

2.4.1 Patient Case A

The patient case previously treated with electrons was a squamous cell carcinoma of the left parotid gland. Following excision of the lesion, the patient's left neck was treated in 25 fractions to a total dose of 51.25 Gy using a 12 MeV electron beam. The radiation oncologist contoured the PTV over 14.75 cm (59 2.5-mm slices). A digitally reconstructed radiograph (DRR) of the patient showing the location of the PTV, along with several CT slices demonstrating the changing shape of the PTV, is show in Figure 23. The PTV extended from the skin surface to a minimum depth of about 0.25 cm and a maximum depth of about 4.25 cm. The

spinal cord was contoured as an organ at risk, and the middle left ear and vocal cord were contoured as regions of interest in order to monitor their dose. Because the PTV extended to the skin surface, 0.5 cm of constant thickness bolus was added by creating a bolus contour and setting its density to 1g cm^{-3} to increase dose to the proximal surface of the PTV. The patient data were HIPAA compliant in accordance with MBPCC guidelines. Specifically, all patient identifiers as related to HIPAA defined protected health information were removed prior to the data being used for research and replaced with an internal research identifier of 08-027.

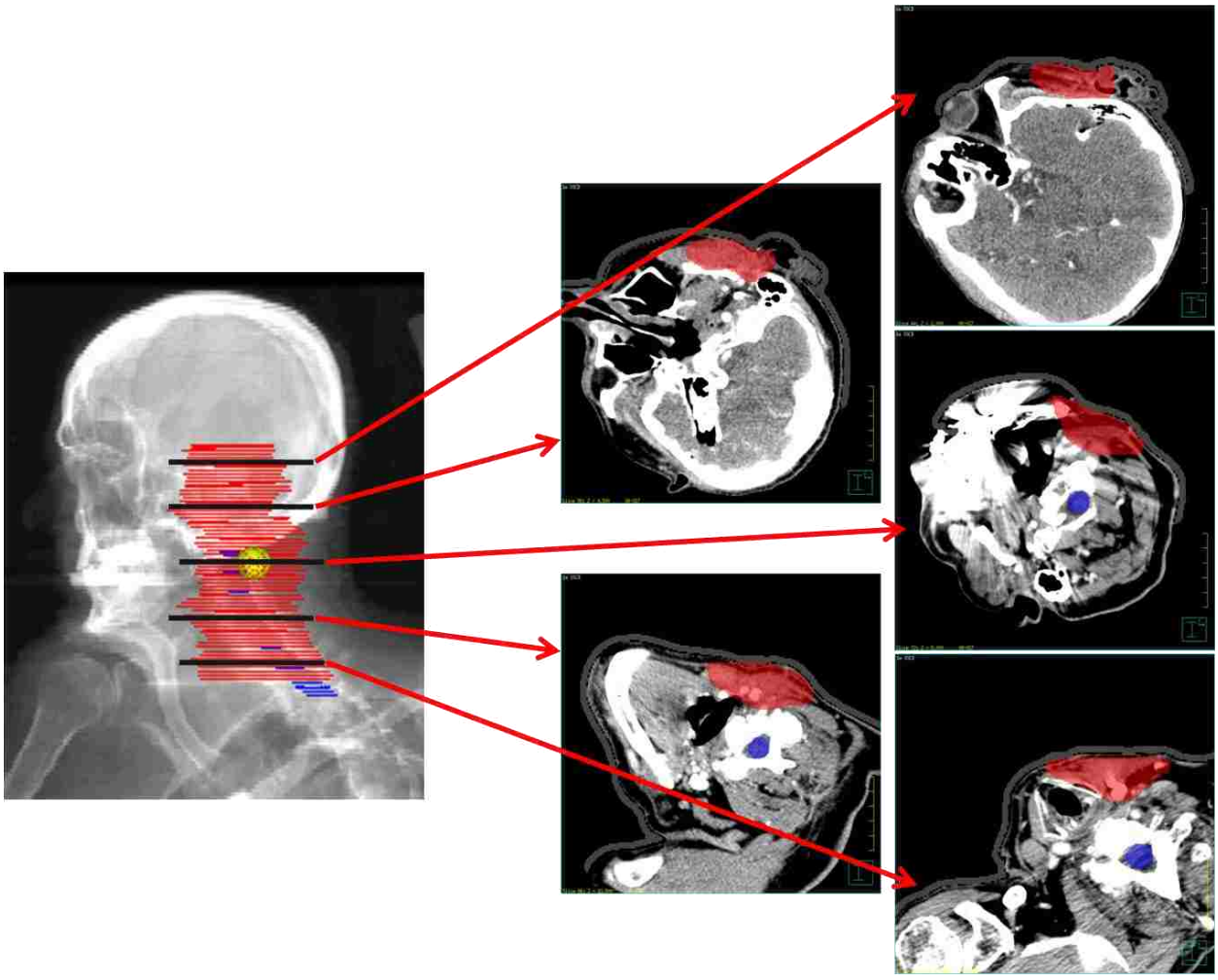

Figure 23: DDR and select transverse CT planes of patient case A. The location of the PTV (shaded red) is seen on the DDR on the left. The spinal cord is shaded blue, and the yellow sphere is the selected isocenter for the patient's plans. The black bars over the PTV indicate the location of the CT planes on the right, which demonstrate the changing shape of the PTV.

2.4.2 Patient Case B

The patient case previously treated with IMRT was a squamous carcinoma in the dermal lymphatic spaces of the right neck. Following excision of the lesion, the patient's right neck was treated to a total dose of 60 Gy in 30 fractions using IMRT. The radiation oncologist contoured the PTV over 12 cm (48 2.5-mm slices). A DRR of the patient showing the location of the PTV, along with several CT slices demonstrating the changing shape of the PTV, is show in Figure 24. The PTV extended from the skin surface to a minimum depth of about 0.25 cm and a maximum depth of about 5.5 cm. The spinal cord and left parotid gland were contoured as organs at risk. The right parotid gland was completely contained inside the PTV and was not a dose limiting structure. Because the PTV extended to the skin surface, 0.5 cm of constant thickness bolus was added by creating a bolus contour and setting its density to 1g cm^{-3} to increase dose to the proximal surface of the PTV. The patient data were HIPAA compliant in accordance with MBPCC guidelines. Specifically, all patient identifiers as related to HIPAA defined protected health information were removed prior to the data being used for research and replaced with an internal research identifier of 08-018.

2.4.3 Patient Treatment Planning

Two copies of each original patient data set were created, and all modifications to the patient data set took place on the copied plans to ensure the original plan remained intact. Pre-algorithm planning took place in the first copy, and post-algorithm steps took place in the second copy. This allowed the contours of possible organs at risk to be removed in the first copy as described below. The contours in the second copy were preserved, allowing the dose to these organs to be determined after the plan was complete.

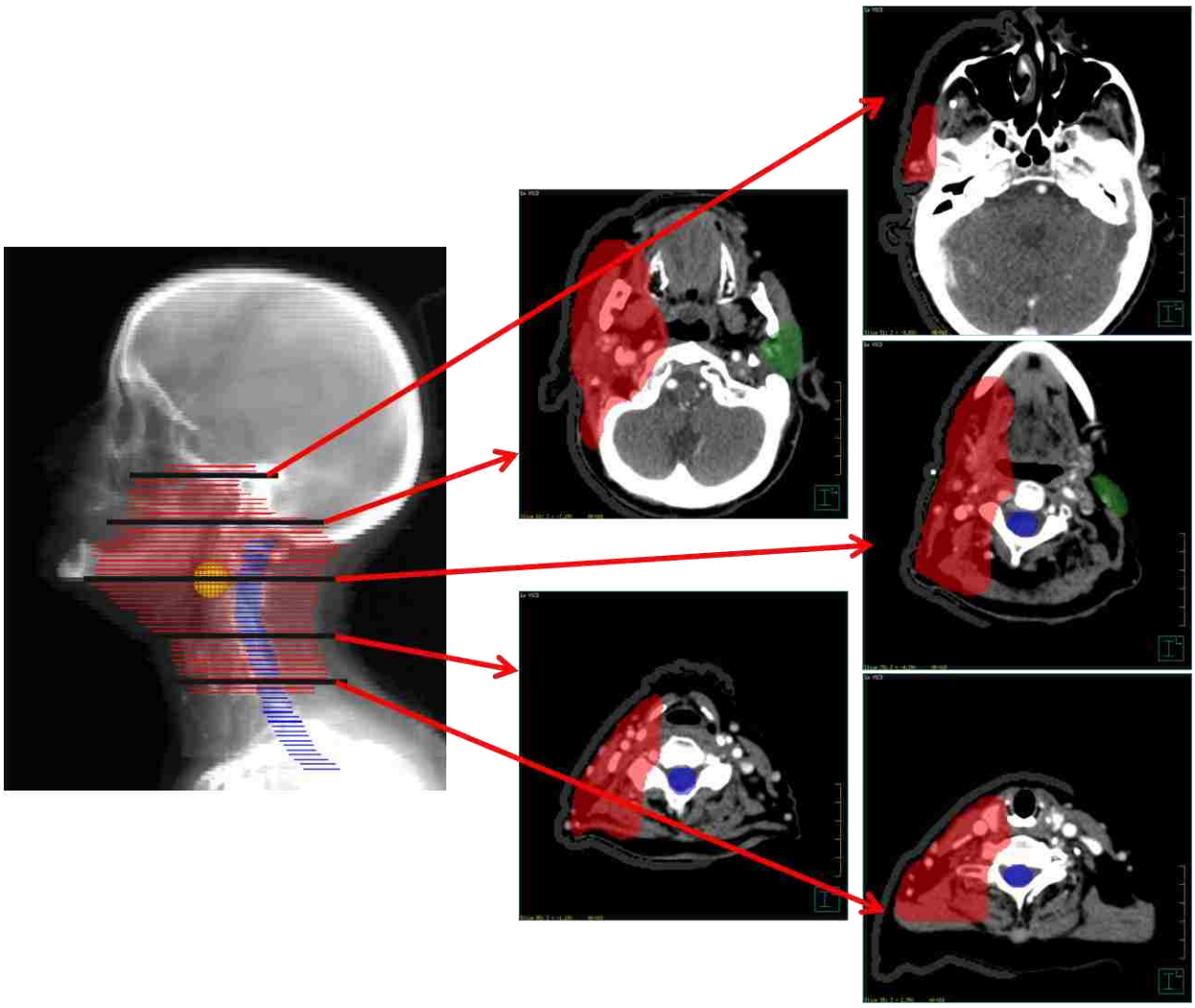

Figure 24: DDR and select transverse CT planes of patient case B. The location of the PTV (shaded red) is seen on the DDR on the left. The spinal cord is shaded blue, and the yellow sphere is the selected isocenter for the patient's plans. The black bars over the PTV indicate the location of the CT planes on the right, which demonstrate the changing shape of the PTV. The left parotid gland (shaded green) is also seen in the CT planes.

2.4.3.1 Pre-Planning Preparation

The patient data required some preparation, performed in Pinnacle v7.4f, before it was able to be used in the external SFECT planning algorithm. The following steps, which took place in the first copy of the patient data set, outline the preplanning process.

1. A new plan trial called "Min Field Trial" was created, and then all other trials were deleted.

2. A “Min Field Iso” point was created, which was placed approximately in the center of the PTV using the Autoplace POI function.
3. A single beam called “Min Field Beam”, with the “Min Field Iso” point as its isocenter, was created.
4. Patient setup parameters, such as gantry angle and couch position, were determined using the beam created in Step 3. These parameters were selected in order that (1) the beam isocenter was at the patient’s surface, i.e. 100-cm SSD, (2) the beam’s central-axis passed near the center of the PTV, and (3) patient’s surface was approximately perpendicular to the beam direction. Once the gantry angle was selected, the SSD of the beam was changed to 100-cm, forcing the isocenter to the patient’s surface.
5. All contours, except for the PTV, were deleted. A “Surface” contour was created around the patient surface for at least each CT slice which contained the PTV. The auto-paint tool was used to quickly contour the surface of each slice, being careful that erroneously auto-contoured air cavities and non-patient items were excluded.
6. After saving the above plan modifications, the plan.points, plan.trial, and plan.roi files were exported from Pinnacle v7.4f into in-house software for processing and planning with the algorithm.

2.4.3.2 Post-Planning Preparation

After the algorithm had planned the SFECT treatment, the created plan was exported into Pinnacle v7.4f for the heterogeneous dose calculation. The plan created by the in-house software was written out in the Pinnacle v7.4f format to an algorithmplan.trial file. The contents of this algorithmplan.trial file were appended to the end of the plan.trial file from the original patient data set. This allowed both the SFECT plan and the original plan to be easily compared in the same data set. The appended original plan.trial and the original plan.points were then imported

back into Pinnacle v7.4f into the second copy of the plan and the plan opened in Pinnacle v7.4f. The plan.roi file that was previously exported from the first copy of the data set was not imported into the second copy in order to preserve the original contours. The following steps describe how the newly created plan was setup in Pinnacle v7.4f for the heterogeneous dose calculation.

1. Changed to the Min Field trial.
2. The beam spreadsheet was opened and the weighting of each individual beam noted.
3. The blocking of each beam was compared to the segments planned by the algorithm. There were several reasons the blocking may have needed to be modified.

3A. If the beam had more than one aperture, Pinnacle v7.4f would not calculate the dose from the beam. As many copies of the beam as needed were created and all but one aperture removed from each copy. The result was as many beams as there were original apertures, with each beam containing one of the original apertures.

3B. If the algorithm planned an aperture with an island block (a ring field), Pinnacle v7.4f partially closed the ring shaped aperture when reading in the block. A copy of the beam was made and the aperture split between the two beams.

4. Calculated the dose distribution of all beams.
5. There were two options for creating a point for use in the dose prescription. One option was to set the weighting of either the beam with the largest open area to 100%, create the prescription point at the location of the max dose, and restore the beam weightings. The second option was used if this point was outside the PTV or near a beam edge. The second option was to place the prescription point at R_{100} near the center of an open area.
6. If additional beams were created from step 3, then the MU/Fraction for each beam in the beam spreadsheet was manually set to 100 times the beam's original weighting.

For example, if the beam had an original weighting of 10.47% and was then split into two beams, each beam had its MUs set to 1047. Once this was done for all beams, the weight of each beam was locked. This ensured that each beam had its correct MUs relative to beams of different energies even after new beams were created.

7. The created "SFECT" prescription was modified to deliver dose to the PTV equivalent to the original IMRT prescription. The prescription was set to "Prescribe Dose" and the "Overall" dose was set to the IMRT prescription divided by 0.9 to 100% of the prescription point. This ensured that the 90% isodose was equal to the original IMRT prescription.
8. If it did not already exist, a "skin" contour was created on each slice within the dose array. A "non-PTV" contour was then created by expanding the skin contour by 0 cm in all directions with the PTV contour as a limiting region of interest (ROI).

Chapter 3. Results and Discussion

3.1 Aim 1: Implementation of a Pencil Beam Algorithm

The equivalency of the coded PBA and the PBA of Pinnacle v7.4f was verified by comparing for each energy the dose distributions calculated by each for several square fields. All field sizes were defined at an isocenter of 100 cm. A 2x2-cm^2 field was calculated at 100-cm SSD to test the coded PBA's ability to calculate the smallest field allowed in the planning algorithm and the smallest field for which Pinnacle v7.4f has measured data. A 4x4-cm^2 field was calculated at 100-cm SSD to test the coded PBA's ability to calculate a mid-sized field for which Pinnacle v7.4f has measured data. A 10x10-cm^2 field was calculated at 100-cm SSD to test the coded PBA's ability to calculate a field larger than the field size required for side-scatter equilibrium. Finally, a 10x10-cm^2 field was calculated at 110-cm SSD to test the coded PBA's ability to calculate dose at an extended SSD. The Pinnacle v7.4f's dose grid [$(0.25\ cm)^3$ voxels] was set to 208x208x56 $pixels^3$ (52x52x14 cm^3) in order to calculate on the same size grid as the coded PBA. The central slice dose distribution was extracted from Pinnacle created RTOG formatted files using in-house software. The central-axis percent depth doses and off-axis profiles for the two systems were compared by overlaying the central slice isodose contour plots of both dose distributions, each normalized to 100% at its central-axis maximum dose. Results at 9 and 20 MeV at 100-cm SSD are shown in Figure 25-Figure 27 and Figure 29-Figure 31, respectively. The results at 9 and 10x10-cm^2 20 MeV field at an extended SSD of 110-cm are shown in Figure 28 and Figure 32, respectively. Additionally, comparison of only the central-axis percent depth doses of the 10x10-cm^2 20 MeV field is shown in Figure 33. Results at 6, 12, and 16 MeV at 100-cm and 110-cm SSD are qualitatively similar and are shown in Appendix C.

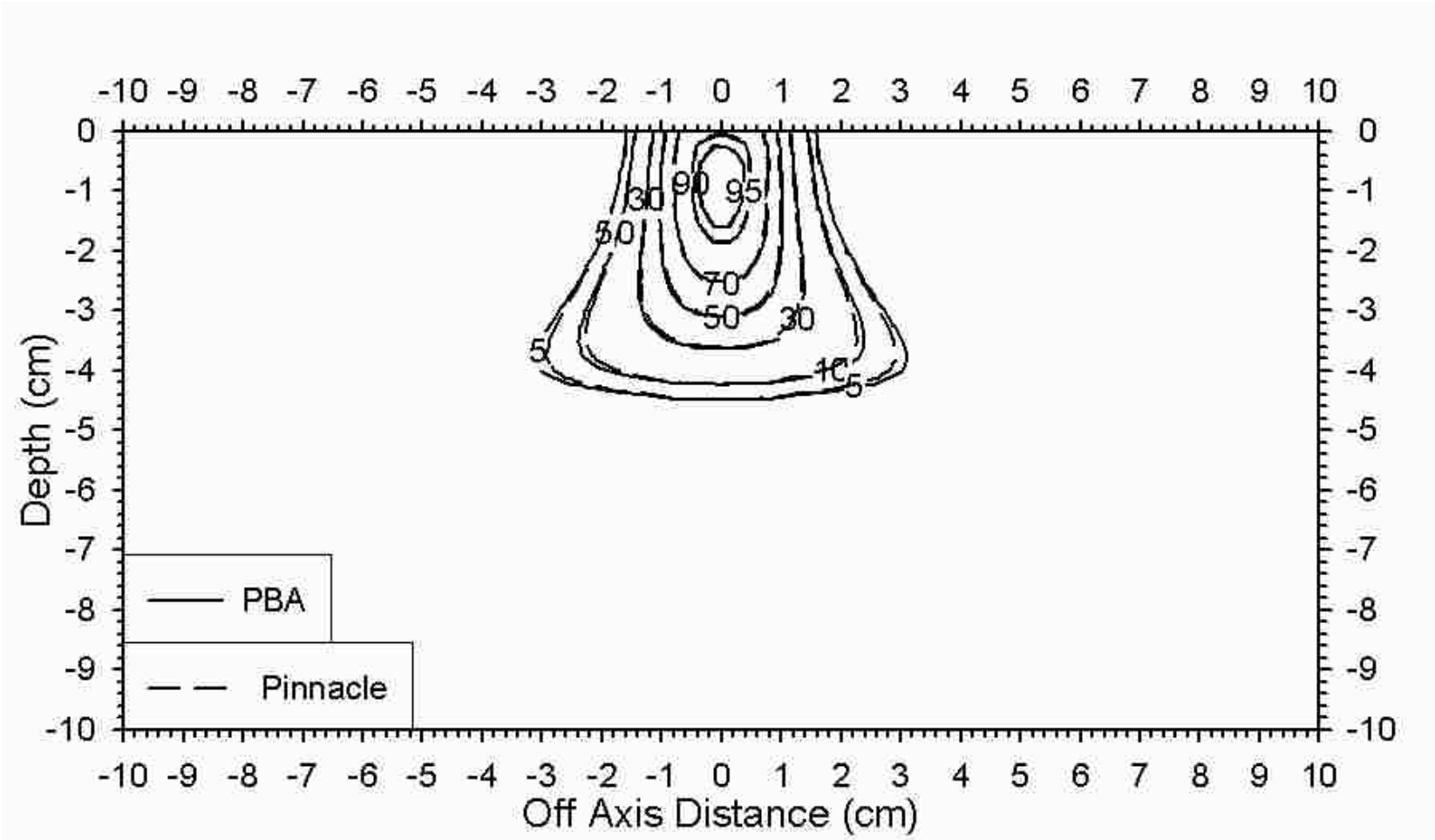

Figure 25: Comparison of dose distributions from a 2x2-cm^2 9 MeV field at 100-cm SSD calculated by the coded PBA (solid line) and Pinnacle (dashed line).

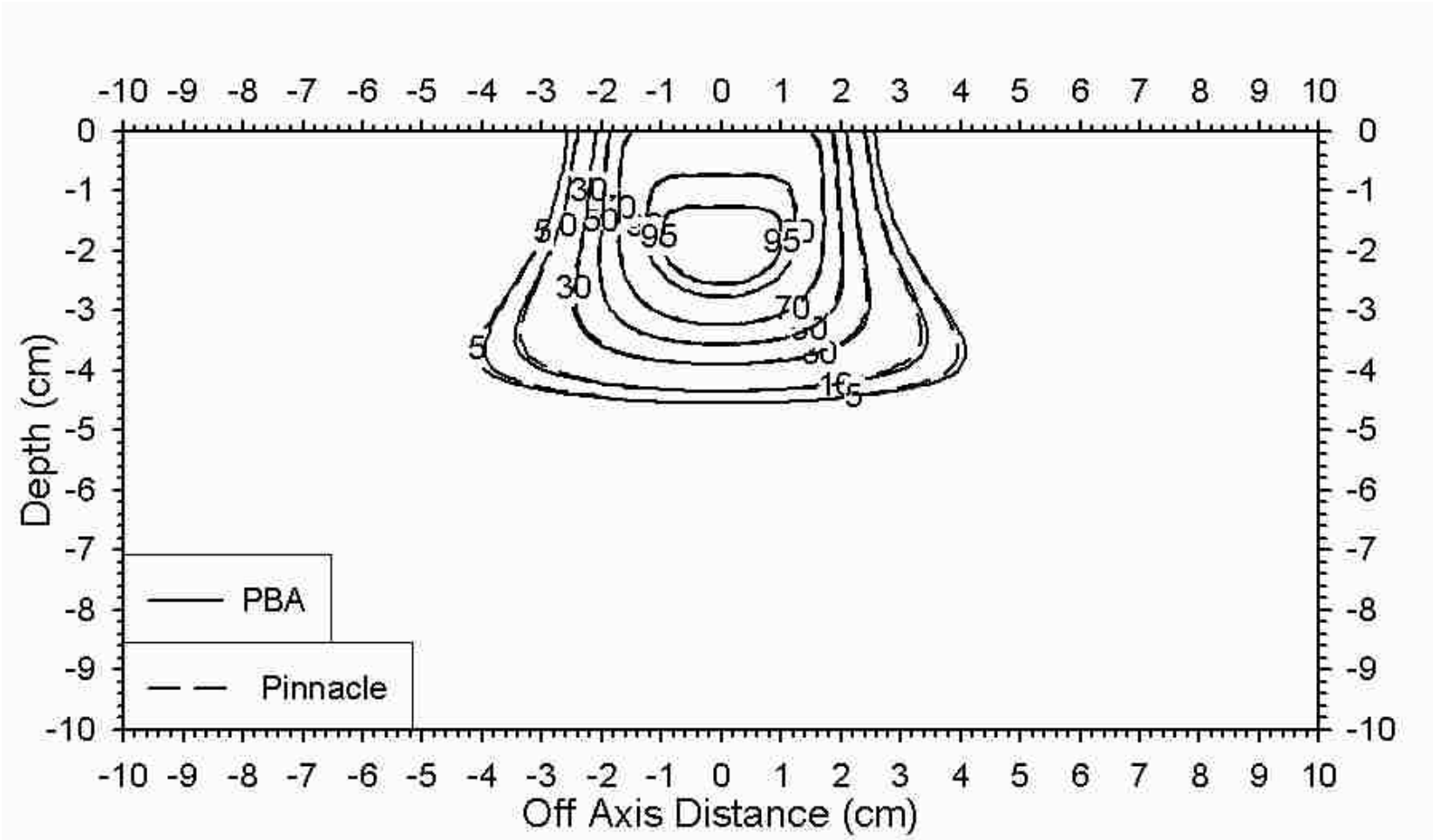

Figure 26: Comparison of dose distributions from a 4x4-cm^2 9 MeV field at 100-cm SSD calculated by the coded PBA (solid line) and Pinnacle (dashed line).

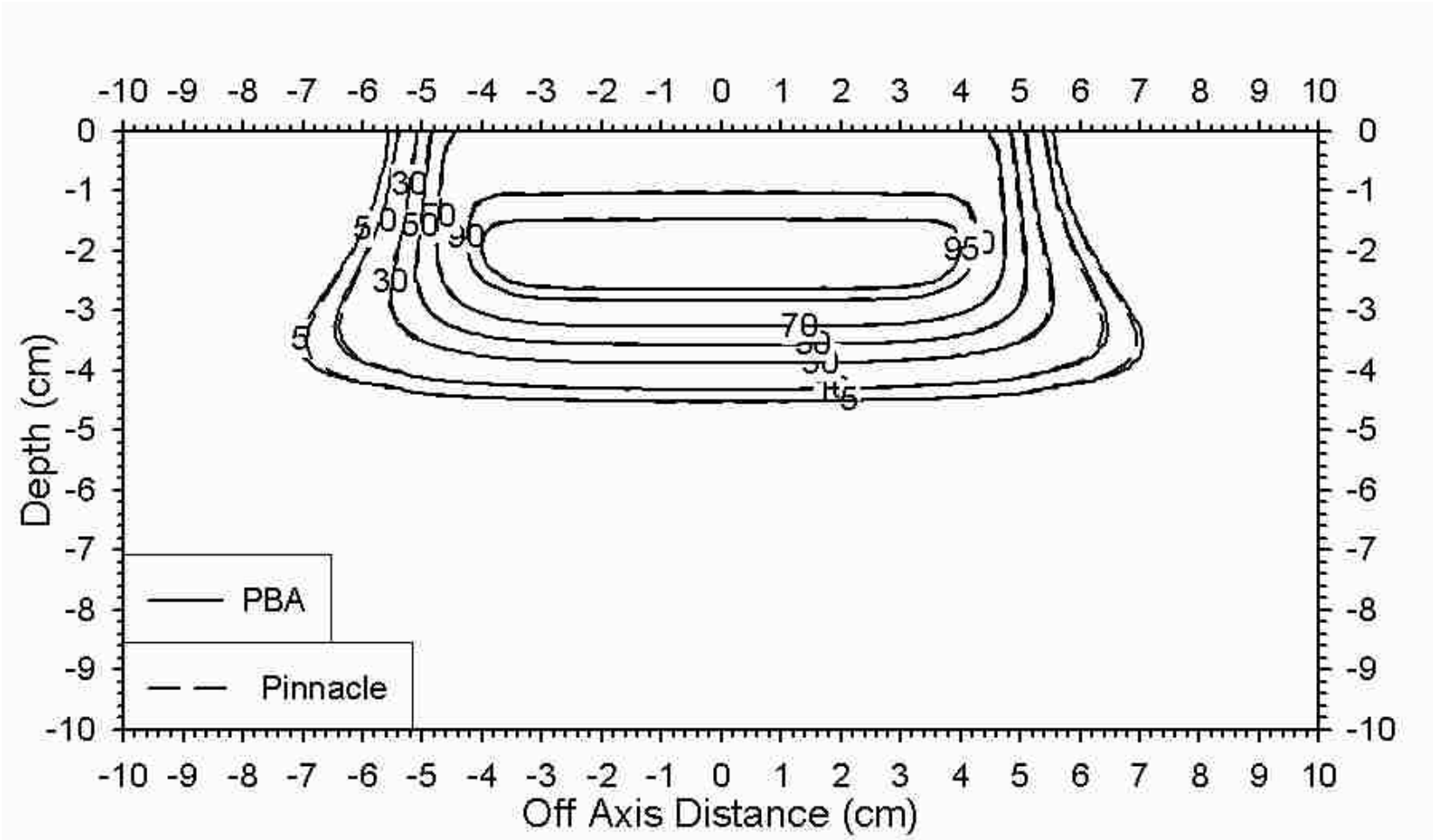

Figure 27: Comparison of dose distributions from a 10x10-cm^2 9 MeV field at 100-cm SSD calculated by the coded PBA (solid line) and Pinnacle (dashed line).

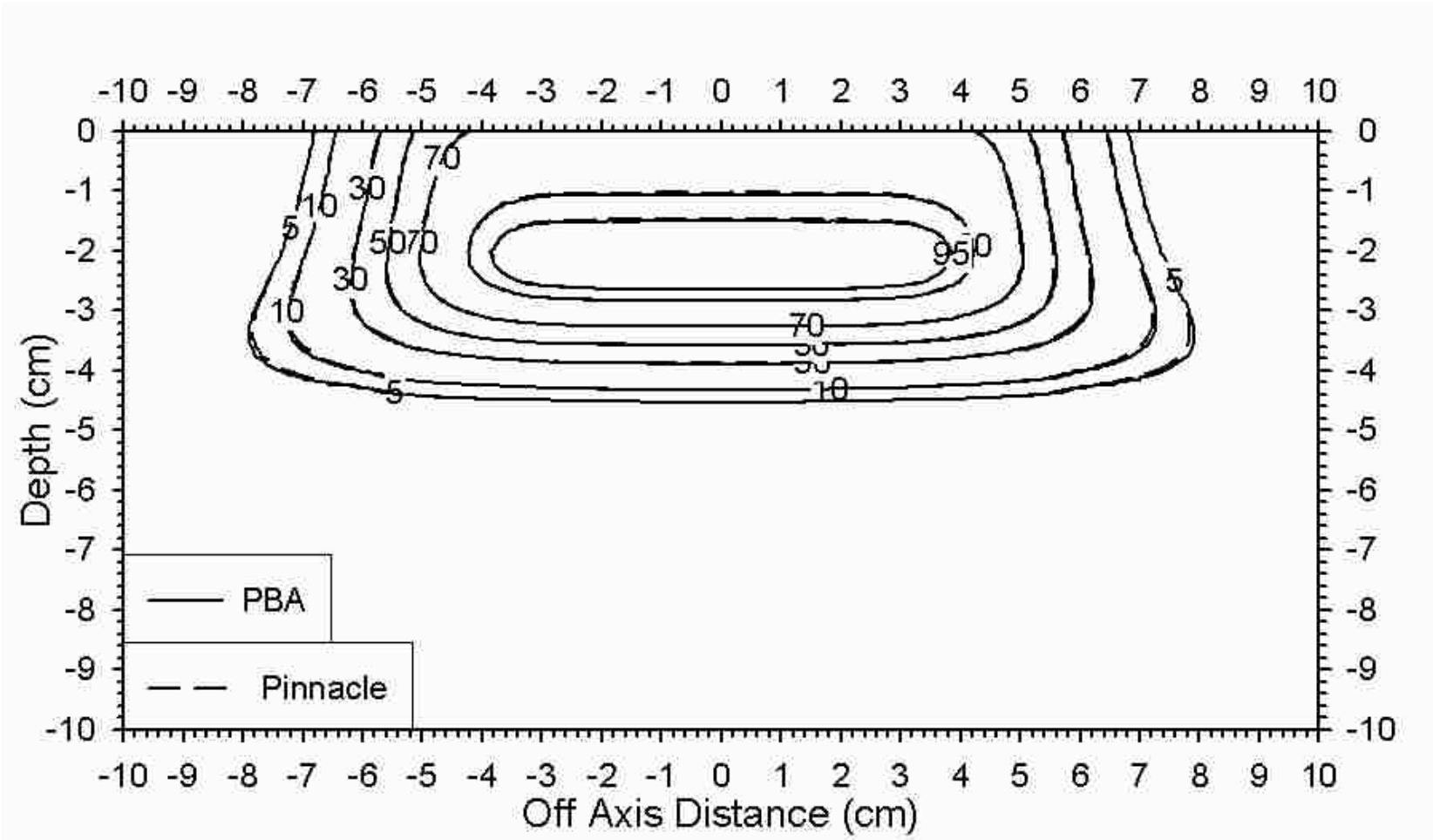

Figure 28: Comparison of dose distributions from a 10x10-cm^2 9 MeV field at 110-cm SSD calculated by the coded PBA (solid line) and Pinnacle (dashed line).

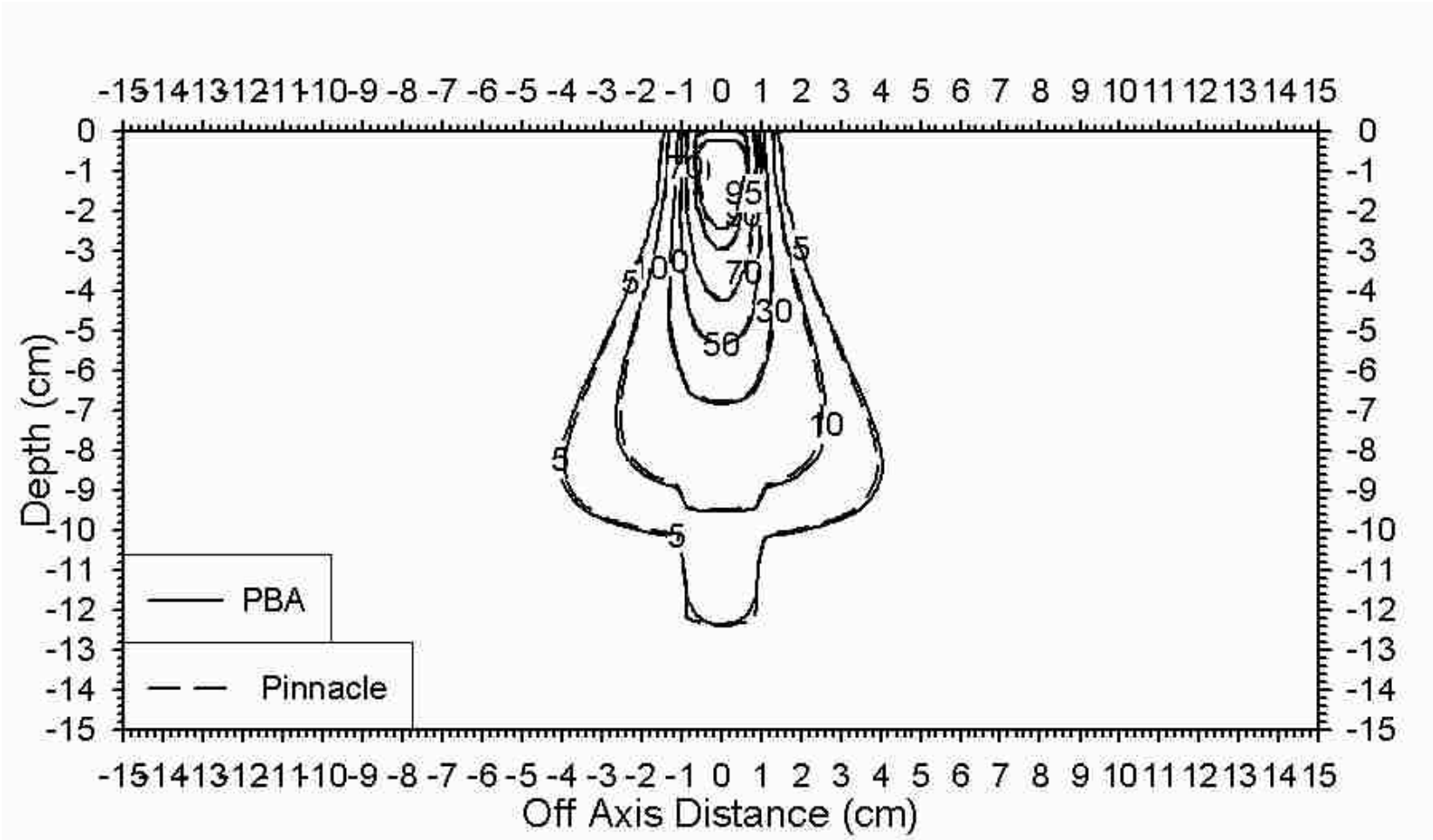

Figure 29: Comparison of dose distributions from a 2x2-cm^2 20 MeV field at 100-cm SSD calculated by the coded PBA (solid line) and Pinnacle (dashed line).

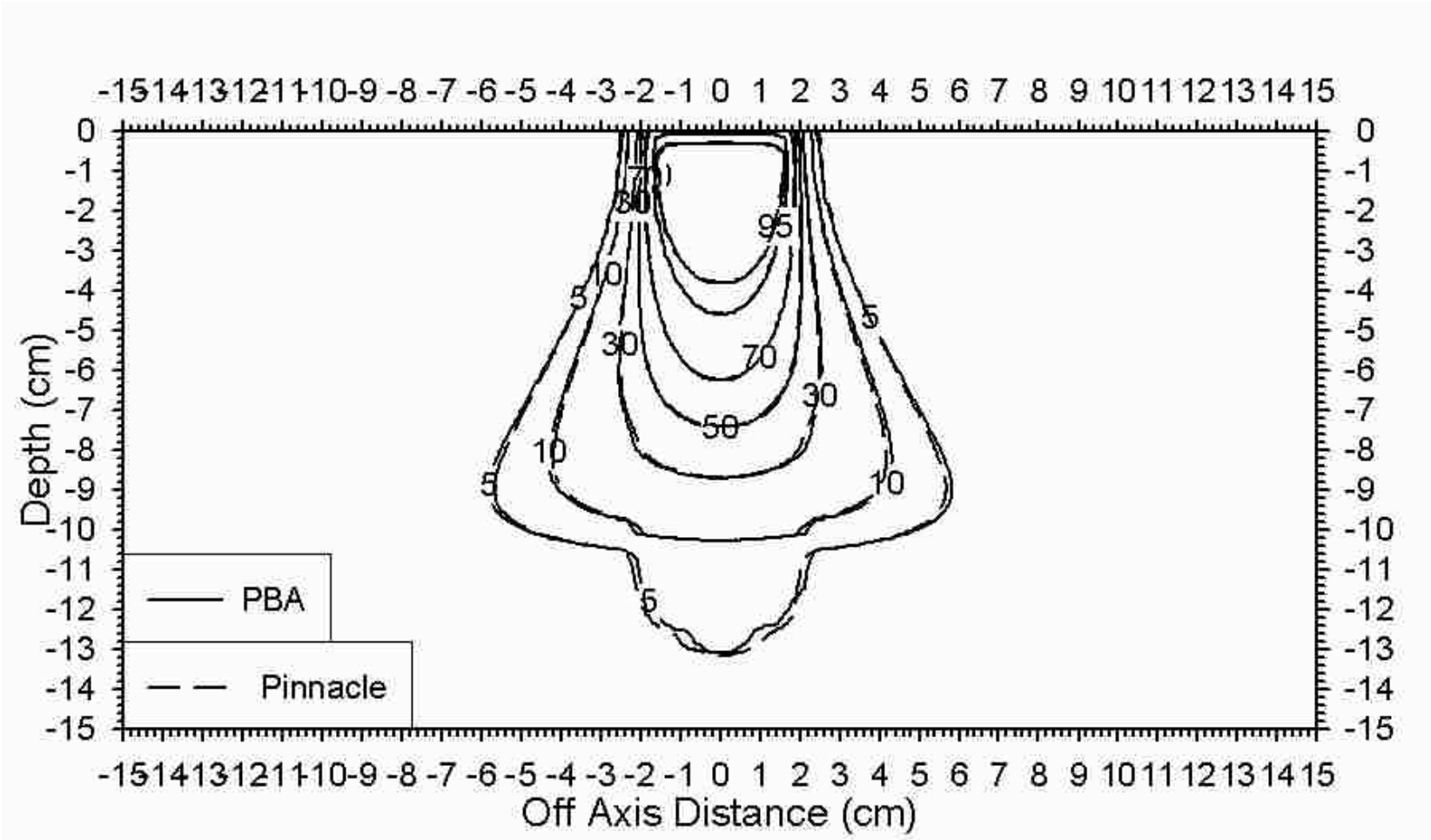

Figure 30: Comparison of dose distributions from a 4x4-cm^2 20 MeV field at 100-cm SSD calculated by the coded PBA (solid line) and Pinnacle (dashed line).

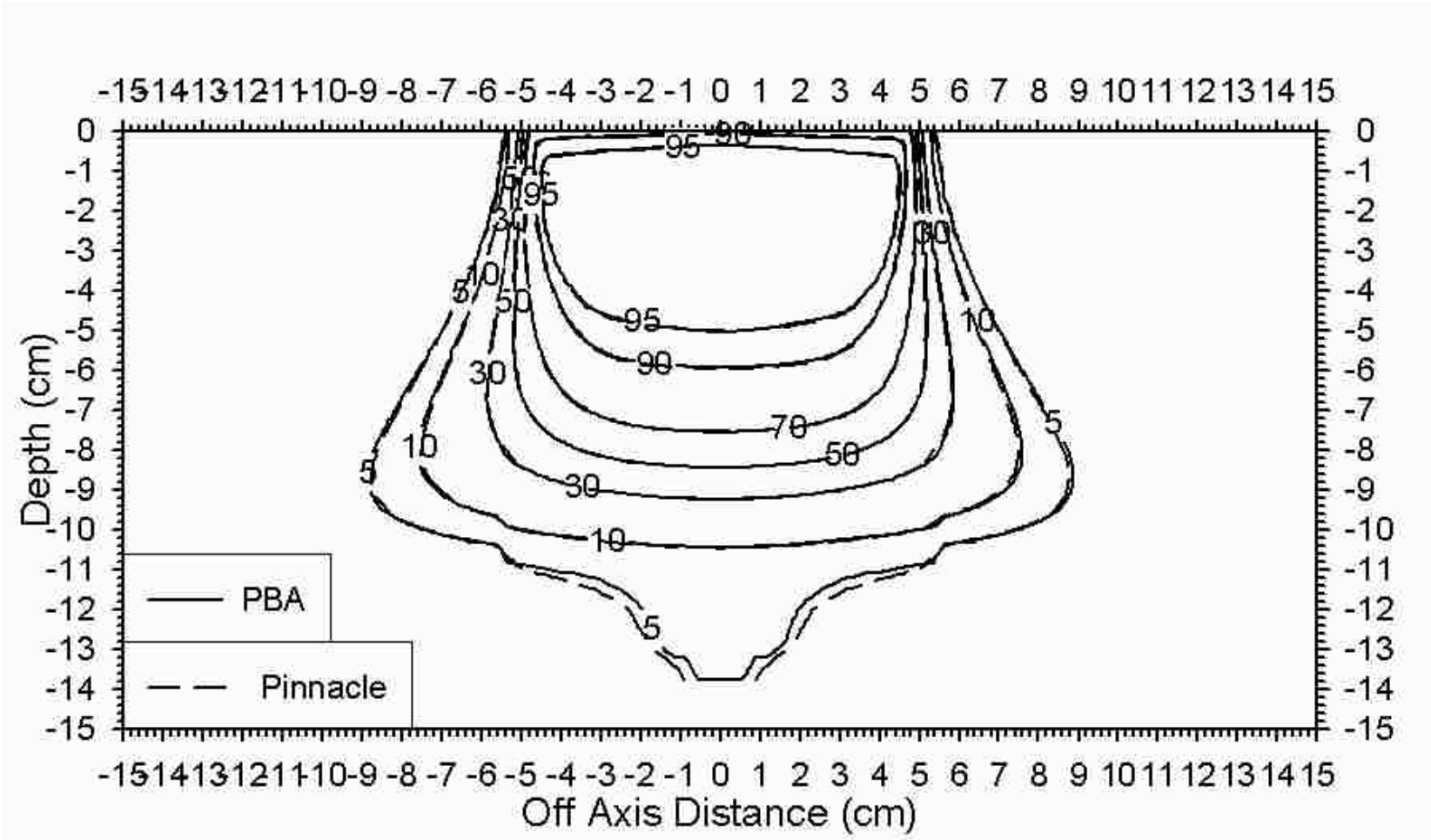

Figure 31: Comparison of dose distributions from a 10x10-cm^2 20 MeV field at 100-cm SSD calculated by the coded PBA (solid line) and Pinnacle (dashed line).

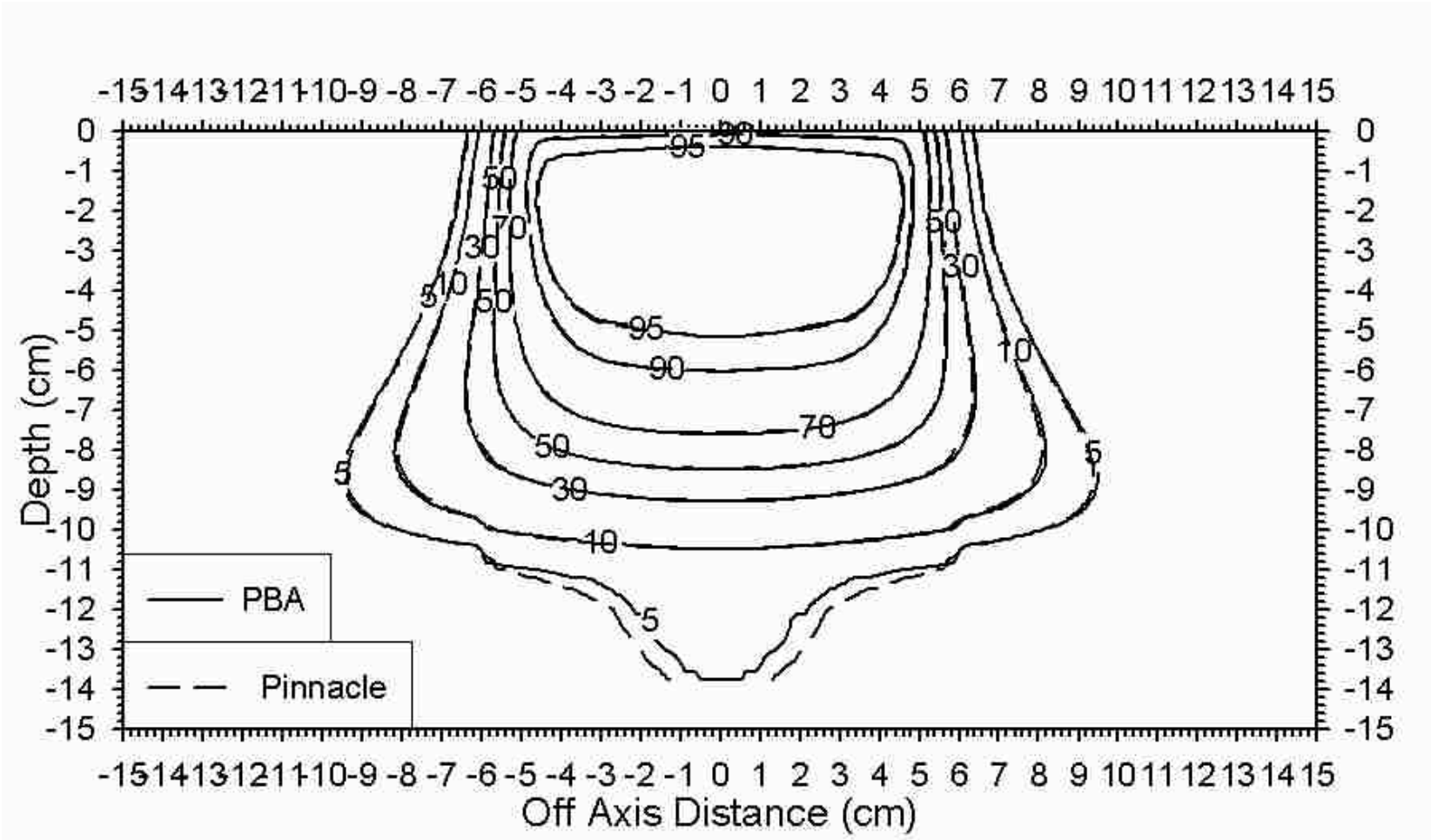

Figure 32: Comparison of dose distributions from a 10x10-cm^2 20 MeV field at 110-cm SSD calculated by the coded PBA (solid line) and Pinnacle (dashed line).

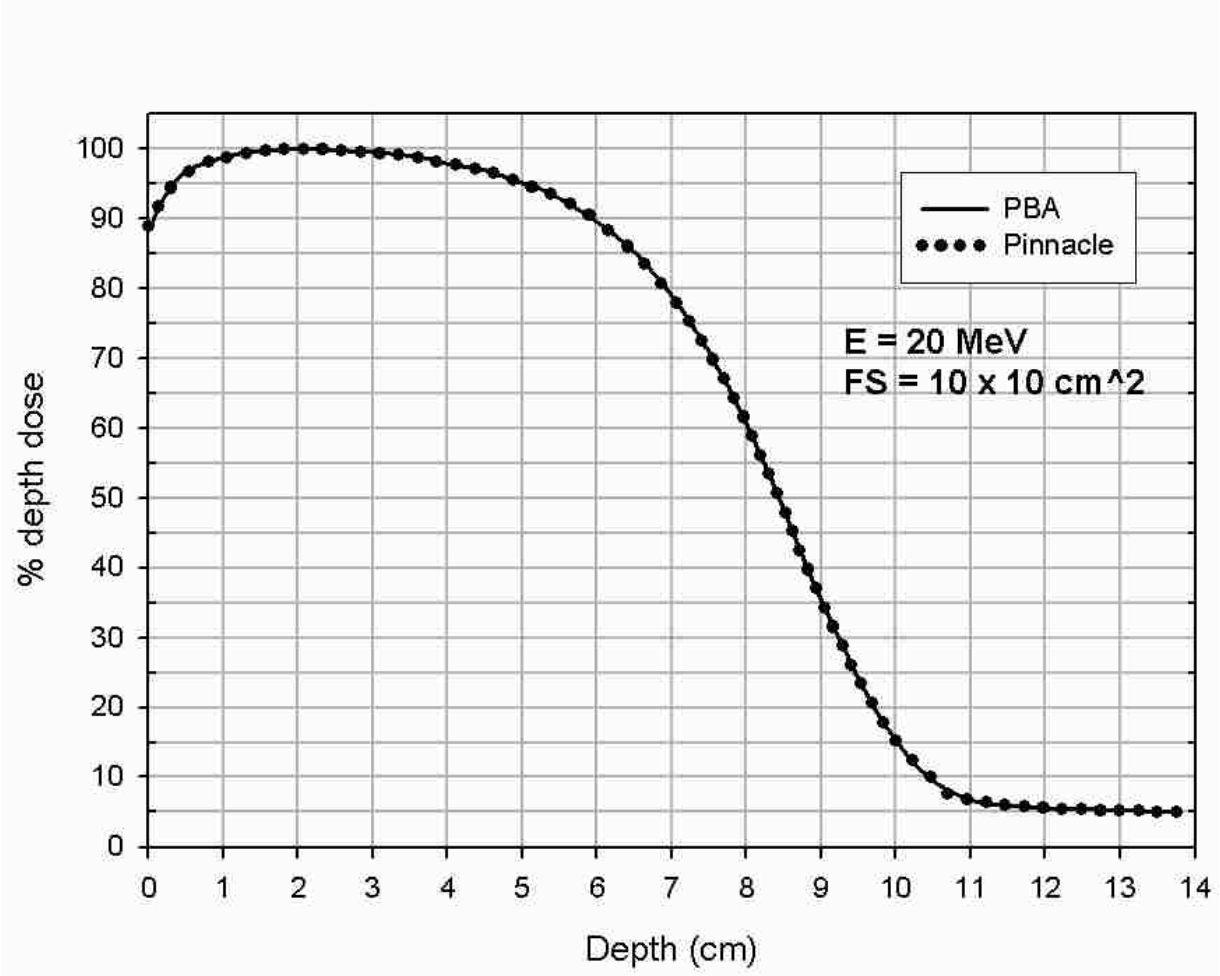

Figure 33: Comparison of central-axis percent depth dose curves from a 10x10-cm^2 20 MeV field at 100-cm SSD calculated by the coded PBA (solid line) and Pinnacle (dotted line).

3.1.1 %DD Comparison

For all fields tested (all combinations of energy, field size, and SSD), good agreement (≤ 1-mm distance to agreement (DTA)) was seen for the central-axis percent depth dose. It appeared in Figure 31 and Figure 32 that the central-axis percent depth doses for the 10x10-cm^2 20 MeV field had a DTA greater than 1 mm near the last calculated depth of 13.75 cm (recall from Section 2.1.6 that dose is only calculated for depths shallower than 14 cm); however this was in a low-dose gradient region and the dose difference at this depth was less than 0.1%, as seen in Figure 33.

3.1.2 Isodose Comparison

For all fields tested, good agreement was seen of the 90% isodose contour and the field width, the latter defined by the location of the 50% isodose contour at R_{100} (depth of 100% central-axis dose).

Good agreement of all in-field isodose contours was seen for all fields tested except the low dose (5%) contours of 20 MeV, in both the 100-cm and 110-cm SSD data, where DTA ranges from 1 mm to nearly 5 mm. The dose at the depth of the 5% isodose contour for these cases is almost entirely due to photon contamination, hence in a low-dose gradient area. In fact, the nearly 5 mm difference seen in Figure 32 corresponds to a dose difference of about 0.25%. This small difference in dose is at a depth far beyond any PTV and therefore is not considered to be a problem. The difference is likely due to a difference in the modeling of the photon dose between the two PBAs.

There was good agreement of isodose contours in the range 10%-90% for the 10x10-cm^2 fields of all energies. However, DTAs ranging from 1 mm to nearly 3 mm (PBA always outside Pinnacle) were seen in the lateral 5% and 10% isodose contours at depths between R_{50} and R_{10} for the 2x2-cm^2 and 4x4-cm^2 fields. This low lateral dose is due to both scattered electrons and photon contamination. The cause of this discrepancy is unknown but is possibly due to slight differences in beam sigma calculation, lateral cutoff distance of dose calculation, and photon contamination models. This discrepancy is at most a 0.75% overestimation (seen in the 3 mm DTA of the 16 MeV fields) of dose on the part of the coded PBA several centimeters off axis from any abutted segment and has little impact on the results and no impact on the conclusions of the current work.

3.2 Aim 2: Develop Field Segmentation Algorithm

In this section the convergence of the algorithm is exemplified for the hemispherical PTV. Results of Step 1, initial energy segmentation, are illustrated in Figure 34. The BEV PTV depth map for the hemispherical PTV (Figure 34A) is shown in Figure 34B. The initial energy segmentation, based on the distal PTV depth and R_{90} for the equilibrium field size, resulted in an energy segmentation requiring 5 energies, shown in Figure 34C. Step 2 was not used in this example because all 5 energies were allowed. In Step 3, due to segment overlap and size restrictions, the number of energies was reduced to 2. The resulting segmentation is shown in Figure 34D. Finally, segment weighting was adjusted in accordance with Step 4. This resulted in the 90% dose contour shown in Figure 35. As normally occurs, due to the merged field segments being larger than the original circular fields drawn around the BEV pixels, the 90% dose contour exceeded the PTV depth. This difference was reduced in Step 5, which modified the PTV and repeated the planning algorithm starting with Step 3. The resulting energy segmentations after 1, 3, 5, and 10 optimization iterations are seen in Figure 36. The corresponding 90% dose contours and comparisons of virtual with original PTVs are seen in Figure 37. Interestingly, the virtual PTV continued to significantly contract with only minor changes in the 90% dose contour. This was because even though the shrinking of the VPTV caused smaller circular pixel fields to be drawn in Step 3, the combination of these fields resulted in field segmentation only slightly smaller than the previous segmentation.

Results for all hypothetical PTVs showed that the planned fields and 90% isodose varied little (and slowly) after a few optimization iterations, due mainly to the shrinking of the VPTV coupled with the minimum 2-cm diameter segments permitted. On the other hand, uncorrectable cold spots (< 90% dose), due to abutting energies differing by more than one energy step (for example, abutting 12 MeV to 20 MeV), in the lower energy side of the abutment edge of some

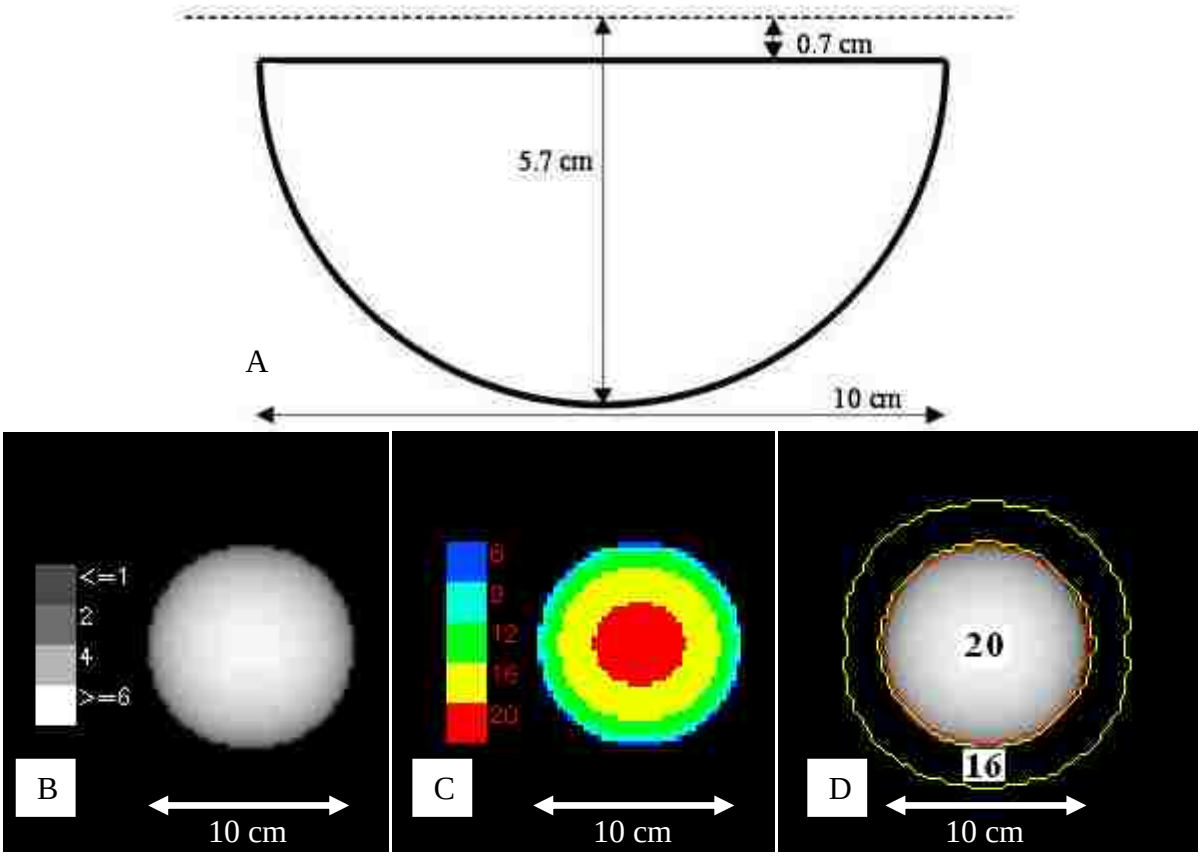

Figure 34: (A) Central cross section of the hemispherical PTV. (B) BEV gray-scale depth map for the hemispherical PTV. (C) BEV of the hemispherical PTV's initial energy selection (dark blue – 6 MeV, light blue – 9 MeV, green – 12 MeV, yellow – 16 MeV, red – 20 MeV). (D) Initial field segmentation of the hemispherical PTV superimposed on the gray-scale depth map. A 16 MeV beam was assigned to the area between the yellow lines, and a 20 MeV beam was assigned to the area inside the red circle.

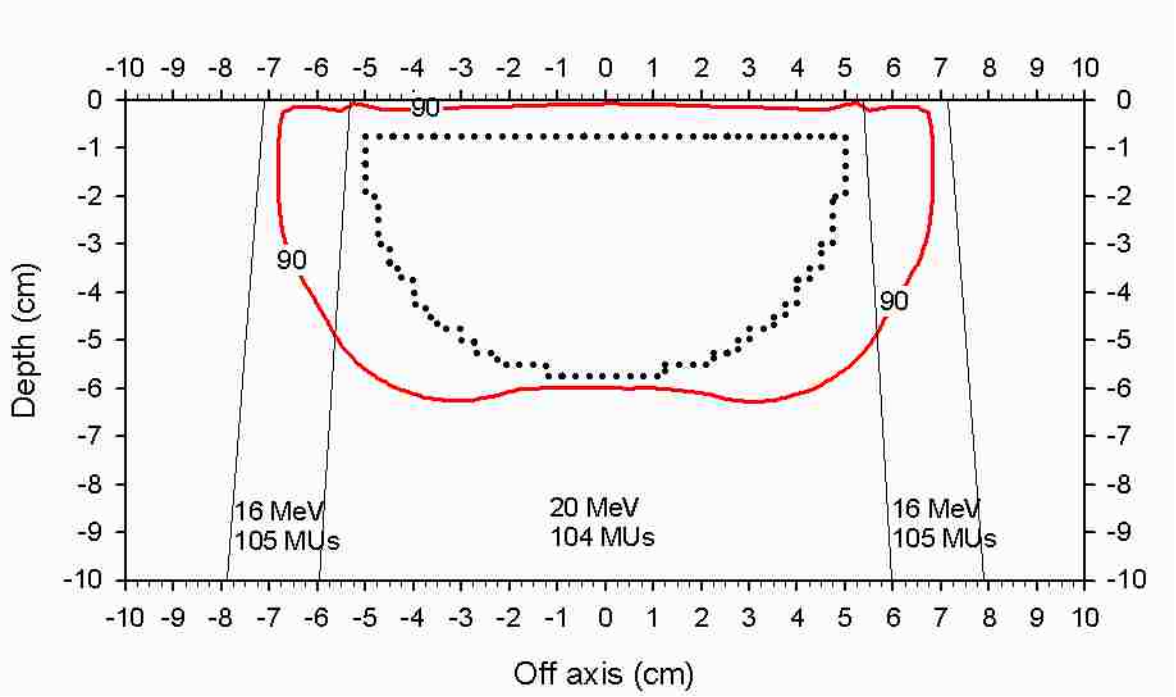

Figure 35: 90% isodose plot of the initial field segmentation (Figure 34D) of the hemispherical PTV. The PTV is represented by the dotted line. A VPTV is not present because it does not exist for the initial segmentation.

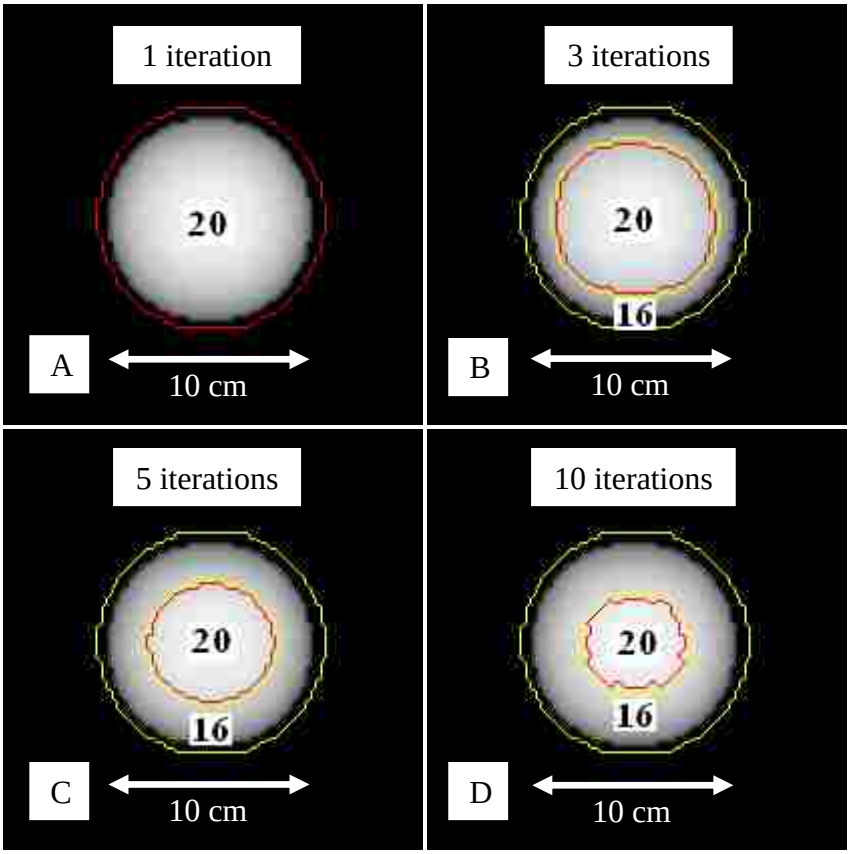

Figure 36: (A) Field segmentation of the hemispherical PTV after one optimization iteration. A 20 MeV beam was assigned to the area inside the red circle. (B) Field segmentation of the hemispherical PTV after three optimization iterations. A 16 MeV beam was assigned to the area between the yellow lines, and a 20 MeV beam was assigned to the area inside the red circle. (C) Field segmentation of the hemispherical PTV after five optimization iterations. A 16 MeV beam was assigned to the area between the yellow lines, and a 20 MeV beam was assigned to the area inside the red circle. (D) Field segmentation of the hemispherical PTV after ten optimization iterations. A 16 MeV beam was assigned to the area between the yellow lines, and a 20 MeV beam was assigned to the area inside the red circle.

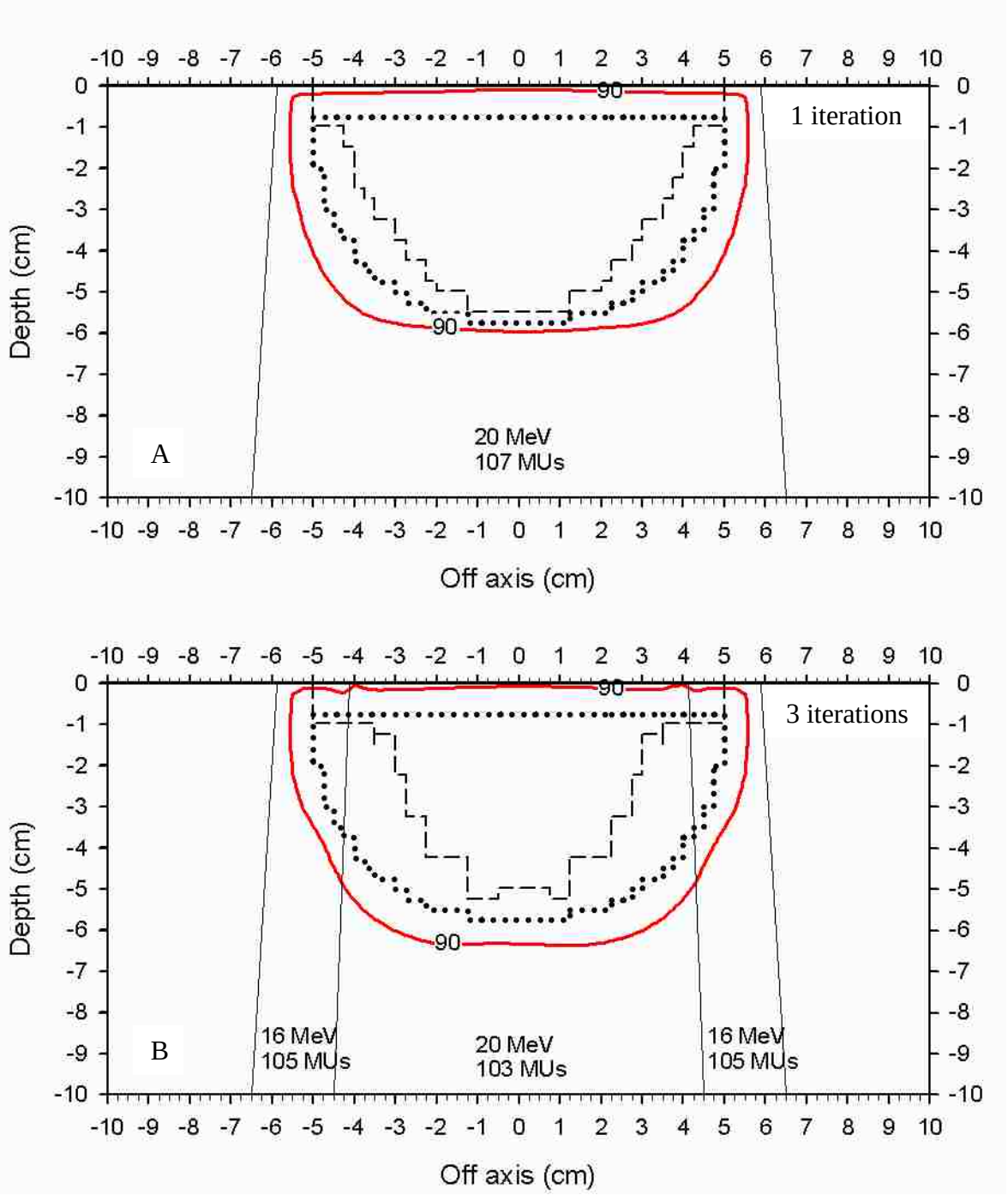

Figure 37: 90% isodose plots resulting from the field segments shown in Figure 36. The PTV is represented by the dotted line. The VPTV that produced the field segmentation is shown by dashed line. (A) 90% isodose after one optimization iteration (Figure 36A). (B) 90% isodose after three optimization iterations (Figure 36B). (C) 90% isodose after five optimization iterations (Figure 36C). (D) 90% isodose after ten optimization iterations (Figure 36D).

Figure 37 (cont.)

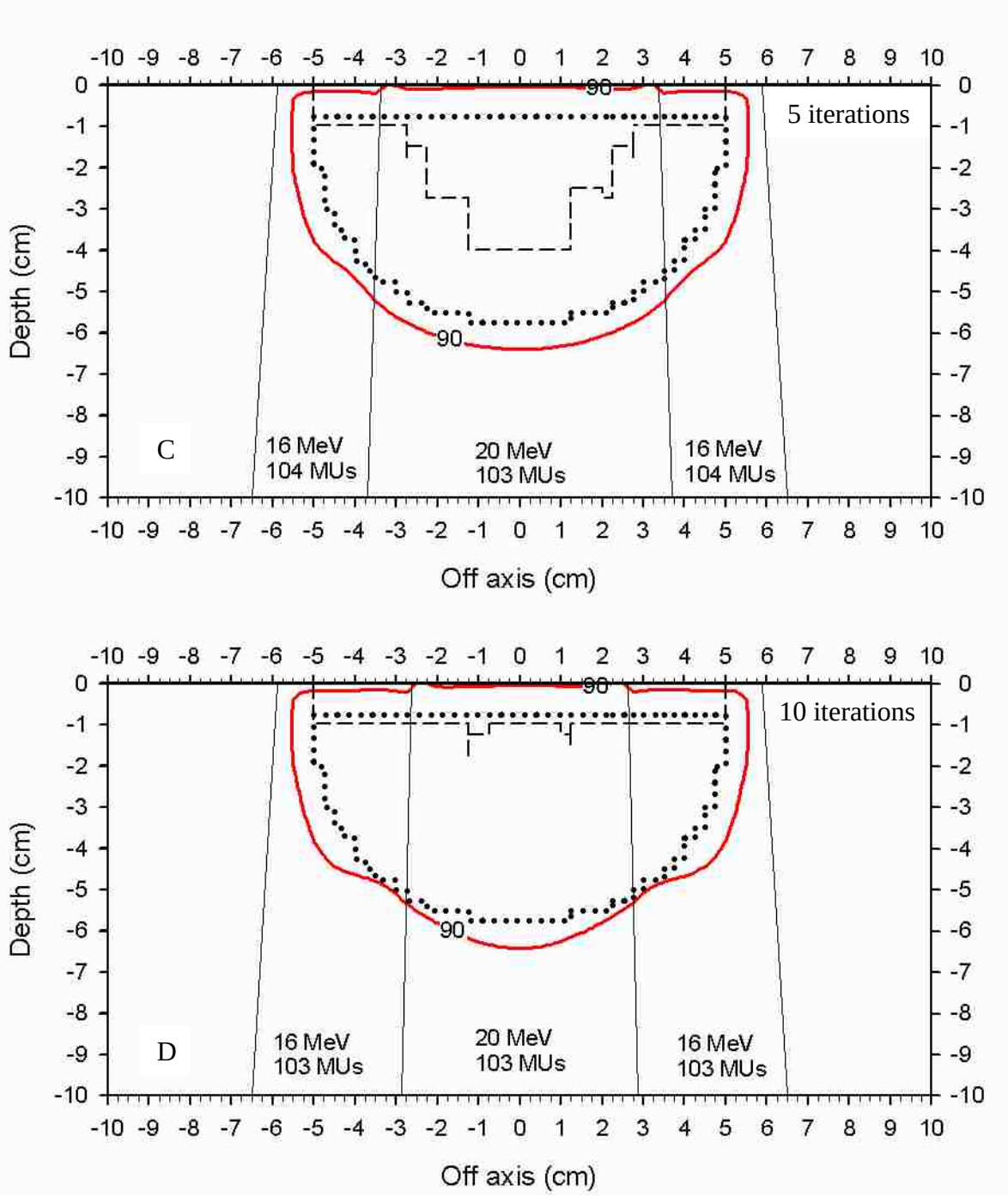

PTVs caused the VPTV to continuously increase in thickness. If allowed to run for many re-planning iterations, the increasing thickness of the VPTV eventually resulted in drawing the maximum 8-cm diameter fields around the pixels in Step 3. Therefore, the default number of

optimization iterations used in the algorithm was 3. As previously mentioned, extra iterations could easily be added if the planner desired.

Even though 5 energies were allowed in the plan and 5 energies were used in the initial energy selection, only 2 energies were used in the final field due to the segments overlapping each other and segment size restrictions. This was typical of all the tested PTVs. Except for possibly when treating PTVs larger than those in the present study, there is little to no plan improvement by allowing more than 3 energies in the plan. Therefore, as mentioned in Section 2.3, the plan comparisons of Aim 3 were limited to 1, 2, and 3 allowed energies.

3.3 Aim 3: Utilization of Algorithm to Compare Impact of Number of Energies

The planning algorithm was used to create plans using 1, 2, and 3 energies for the standard SCD (SSCD = 95 cm) and for the variable SCD (VSCD = 95, 92.5, 88.5, 82.5, and 80.5 cm for 6, 9, 12, 16, 20 MeV, respectively) for the six hypothetical PTVs. The SFECT algorithm was allowed to run for 3 optimization iterations after the initial field segmentation for each plan. Shown for each PTV are selected results of the SSCD and VSCD plans. These include results for the single energy and the best (having the highest CI) two- or three-energy plan. Results for each plan include (1) a BEV of the field segmentation, (2) isodose plots, (3) cumulative dose volume histograms (DVHs) of the PTV and non-PTV, which compare DVHs of the single energy plans with the best multi-energy plans used to determine the comparison metrics, and (4) a table summarizing the statistics of all the plans. For the purpose of the DVHs, non-PTV is defined as all non-PTV within ±10-cm off-axis on both the X and Y axes and within 10-cm depth.

3.3.1 Two-Step Block PTV

The two-step block PTV had two distinct sections, and so even if three energies were allowed, only two energies would ever be used. Therefore, a plan allowing three energies was

not performed for this PTV. The resulting fields and dose distributions for the single-energy SSCD and two-energy SSCD plans are seen in Figure 38 and Figure 39, respectively, and the SSCD plans' DVHs are compared in Figure 40. The resulting fields and dose distributions for the single-energy VSCD and two-energy VSCD plans are seen in Figure 41 and Figure 42, respectively, and the VSCD plans' DVHs are compared in Figure 43. The comparison metrics for all plans are listed in Table 5.

Compared to the single-energy SSCD plan, the two-energy SSCD plan had a reduced CR (0.969 versus 0.998) due to the cold spot at the proximal PTV surface caused by the abutment of the 9 MeV segment to the 12 MeV segment and had an improved SR (0.510 versus 0.521). The reduction in CR was large enough to negate the reduction in SR, causing the two-energy plan to be slightly less conformal than the single-energy plan (CI of 0.475 versus 0.478). Compared to the single-energy VSCD plan, the two-energy VSCD plan had a reduced CR (0.985 versus 0.993), again due to the shallowness of the proximal PTV surface in the area of the 9 MeV segment, had an improved SR (0.494 versus 0.502), and was slightly more conformal (CI of 0.498 versus 0.494).

The edges of the 12 MeV segments are several cm away from the PTV edge because the equilibrium R_{90} of a 12 MeV beam (4.03 cm) was just slightly deeper than the distal PTV surface. This resulted in circular fields of near equilibrium size being required at the edge of the PTV in order for the 90% isodose contour to be deeper than the PTV. As the PTV edges are vertical, a large amount of non-PTV lateral to the PTV was within the 90% isodose. Because the hypothetical PTVs are only 10 cm x 10 cm in BEV, the non-PTV lateral to the PTV within the 90% isodose was comparable in volume to the PTV. This resulted in the high SRs of greater than 0.5, which were typical of all of the hypothetical PTVs. Though such sharp edges are unlikely in patient PTVs, a possible solution to this problem will be discussed later.

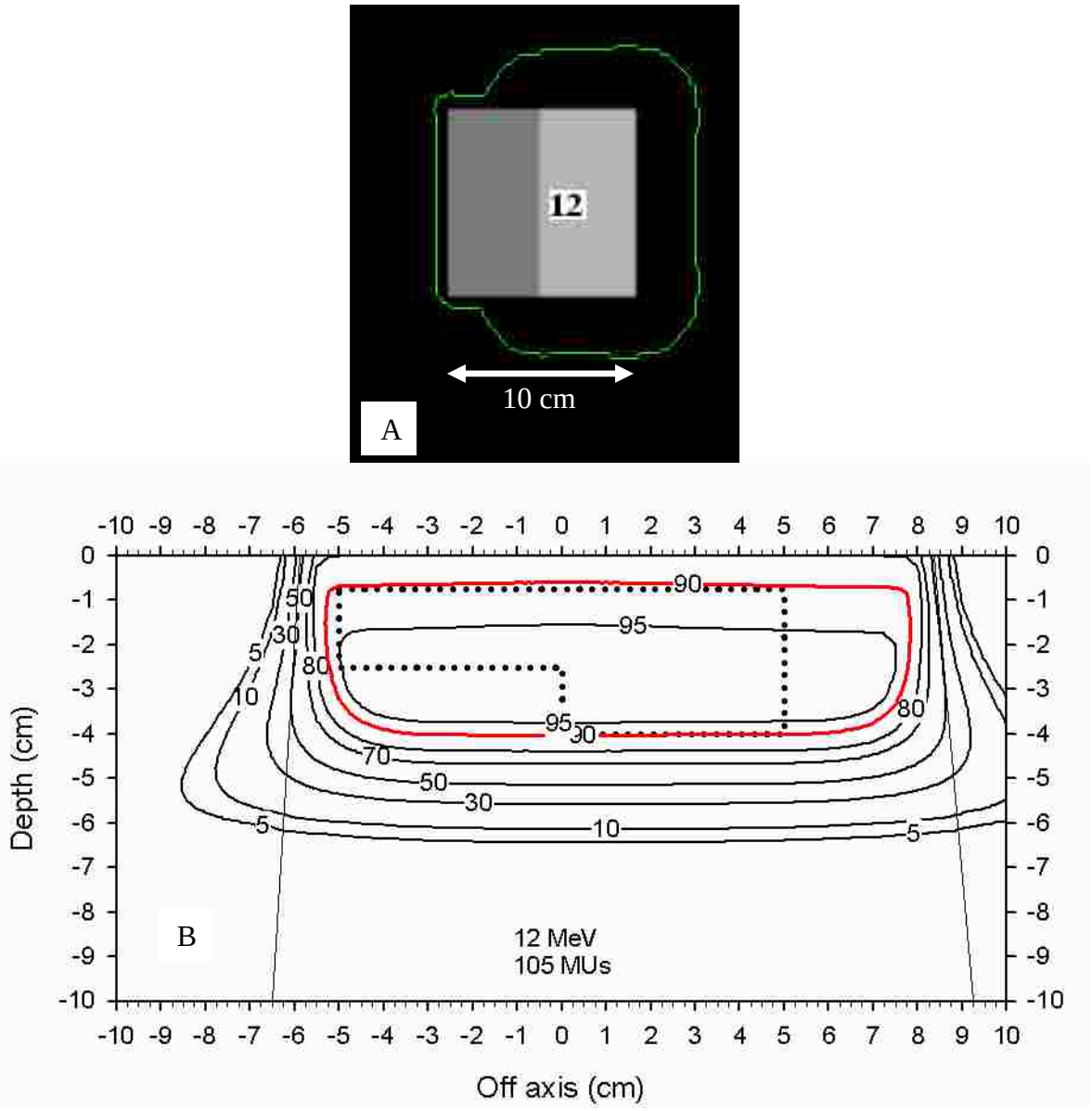

Figure 38: (A) Field segmentation after three optimization iterations for the two-step block PTV using the single-energy SSCD plan. Gray-scale plot is BEV depth map of PTV. View is scaled to isocenter. A single 12 MeV segment (green line) is used. (B) PBA calculated dose distribution for the two-step block PTV using the single-energy SSCD plan. The PTV is the dotted contour; the 90% dose contour is in red.

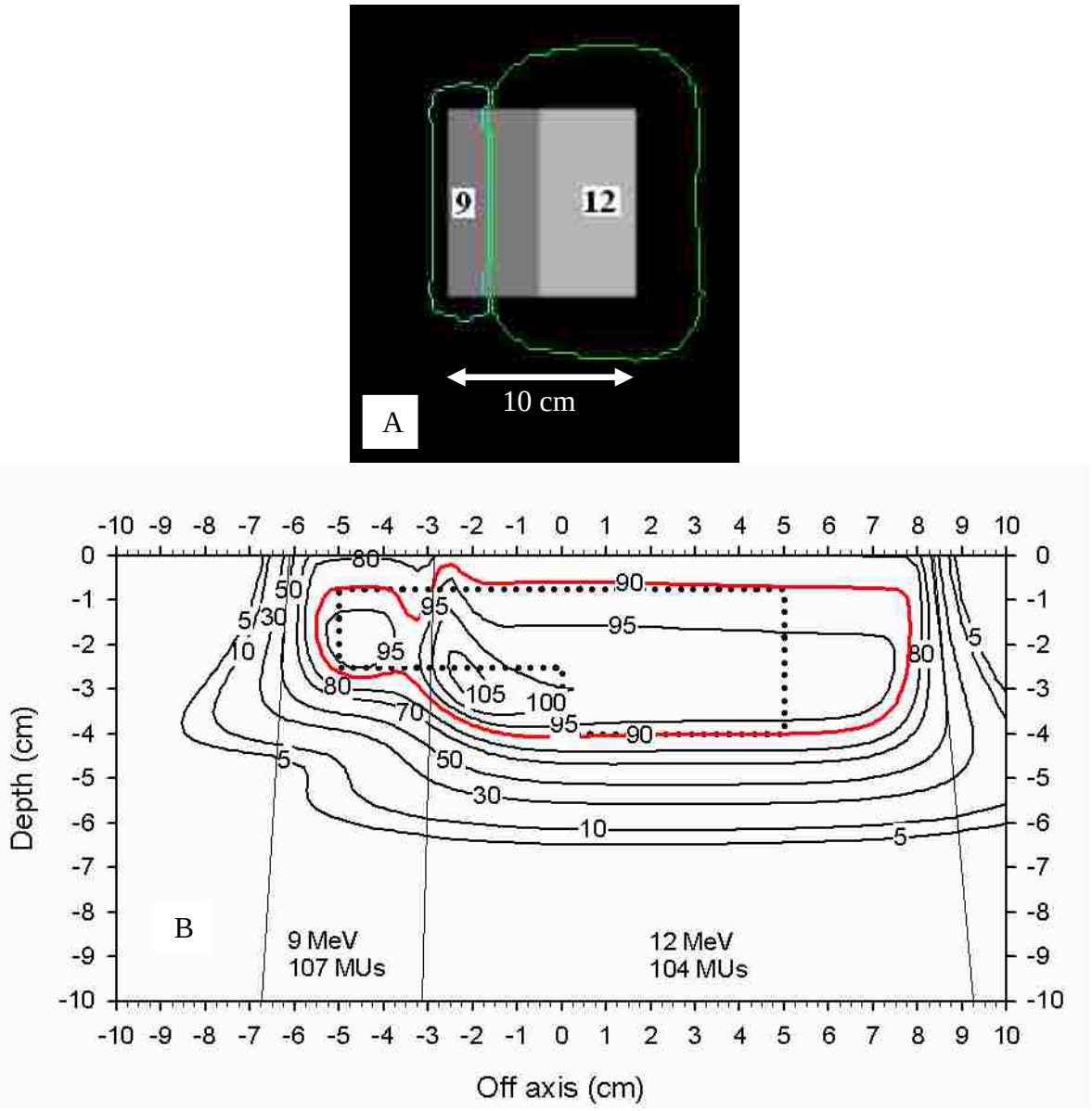

Figure 39: (A) Field segmentation after three optimization iterations for the two-step block PTV using the two-energy SSCD plan. Gray-scale plot is BEV depth map of PTV. View is scaled to isocenter. The left region is a 9 MeV segment (light-blue line) while the right region is a 12 MeV segment (green line). (B) PBA calculated dose distribution for the two-step block PTV using the two-energy SSCD plan. The PTV is the dotted contour; the 90% dose contour is in red.

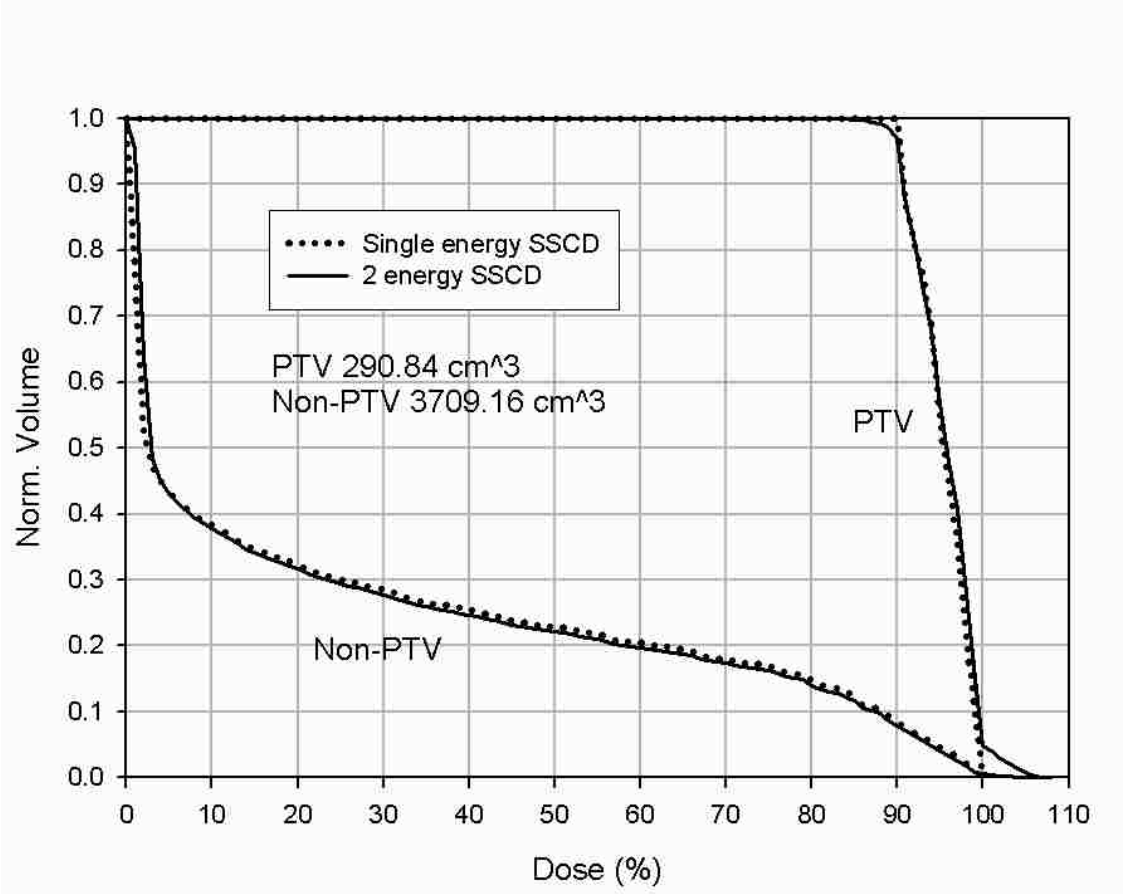

Figure 40: DVHs for the two-step block PTV showing PTV and non-PTV ROIs. The single-energy SSCD plan is shown by the dotted lines and the two-energy SSCD plan by the solid lines.

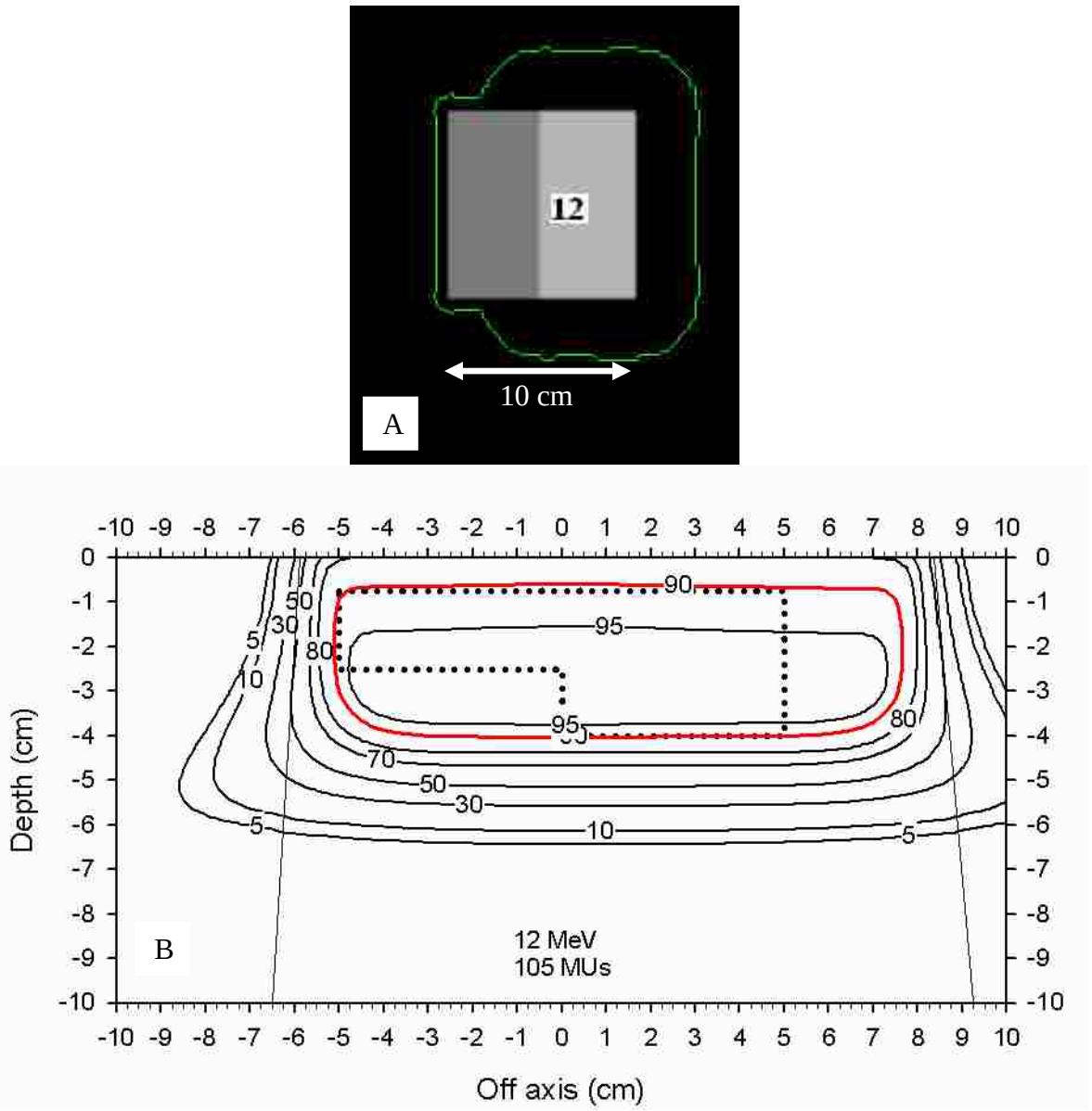

Figure 41: (A) Field segmentation after three optimization iterations for the two-step block PTV using the single-energy VSCD plan. Gray-scale plot is BEV depth map of PTV. View is scaled to isocenter. A single 12 MeV segment (green line) is used. (B) PBA calculated dose distribution for the two-step block PTV using the single-energy VSCD plan. The PTV is the dotted contour; the 90% dose contour is in red.

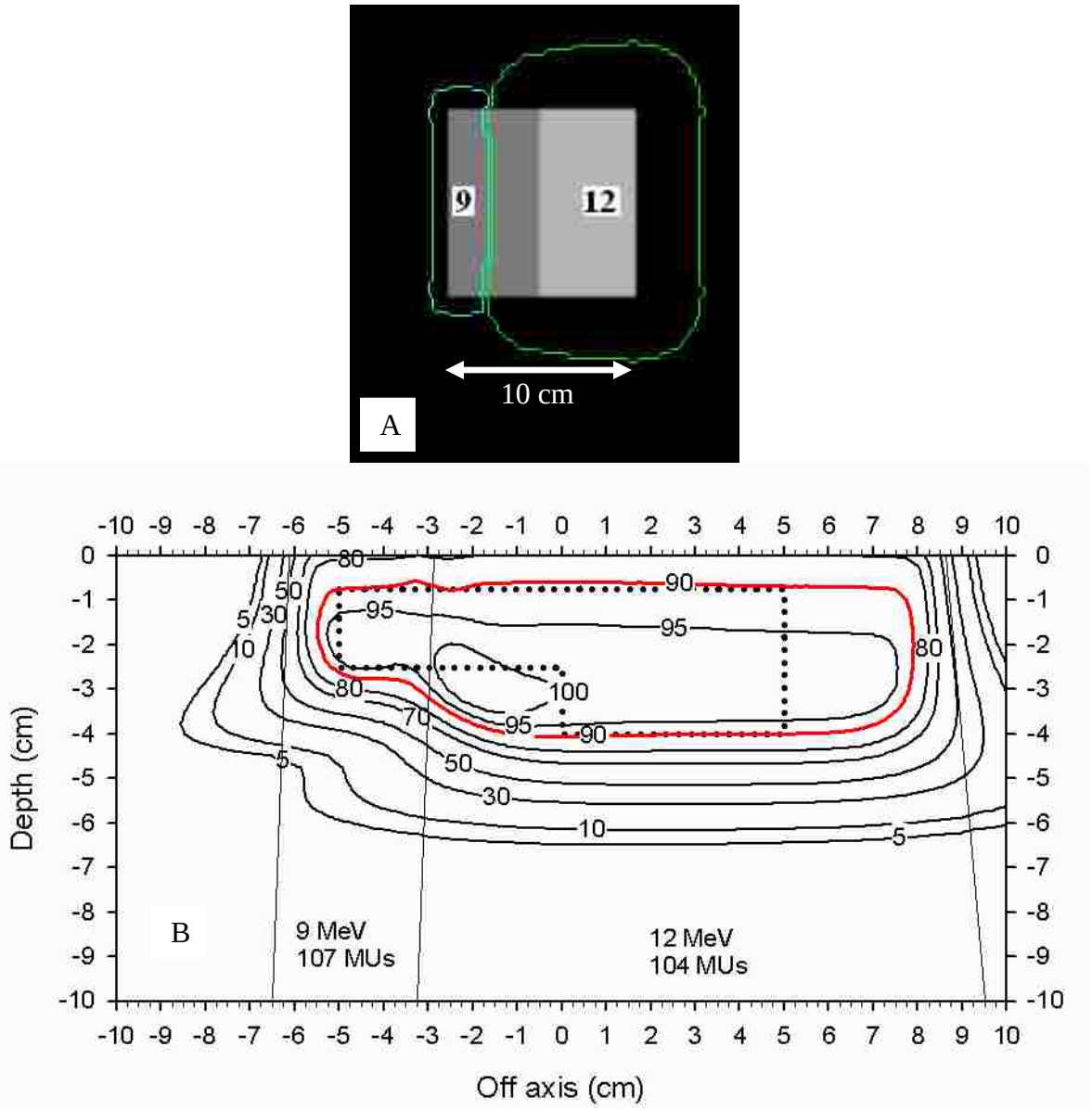

Figure 42: (A) Field segmentation after three optimization iterations for the two-step block PTV using the two-energy VSCD plan. Gray-scale plot is BEV depth map of PTV. View is scaled to isocenter. The left region is a 9 MeV segment (light-blue line) while the right region is a 12 MeV segment (green line). (B) PBA calculated dose distribution for the two-step block PTV using the two-energy VSCD plan. The PTV is the dotted contour; the 90% dose contour is in red.

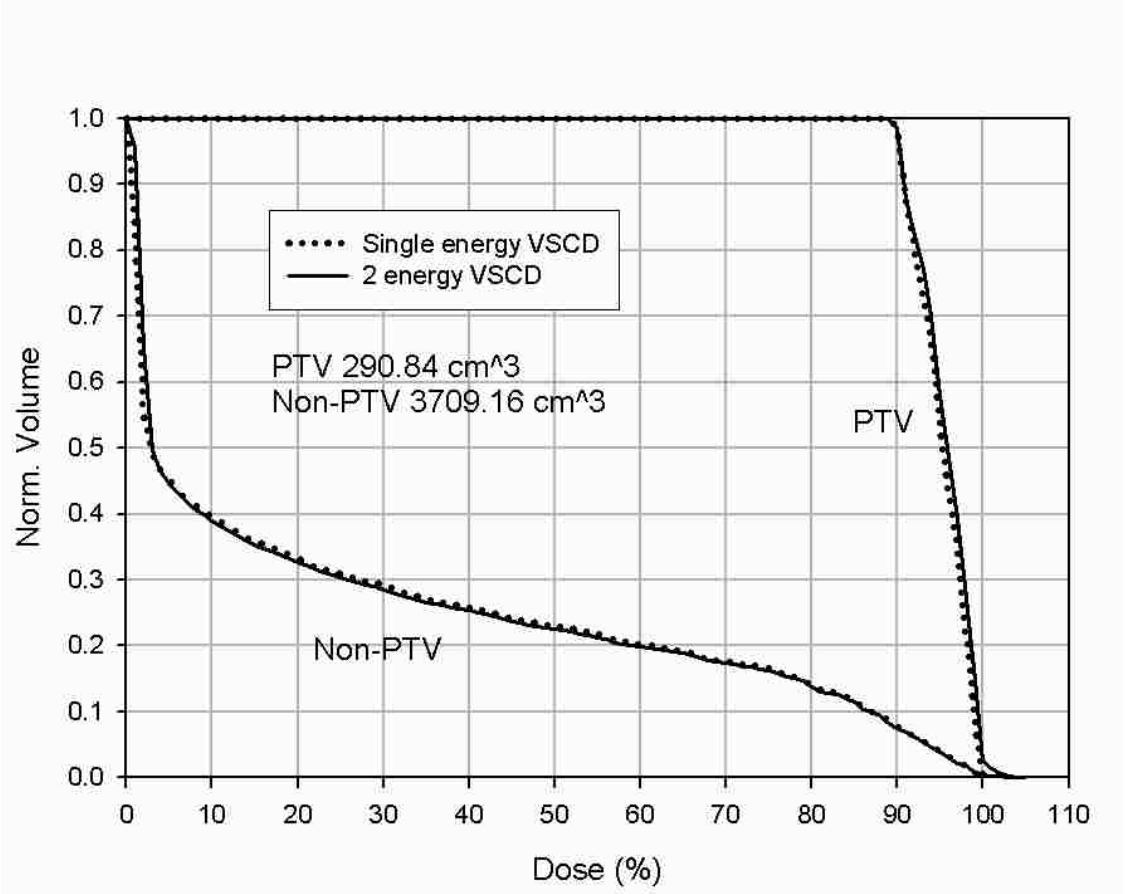

Figure 43: DVHs for the two-step block PTV showing PTV and non-PTV ROIs. The single-energy VSCD plan is shown by the dotted lines and the two-energy VSCD plan by the solid lines.

Table 5: Summary of planning results for the two-step block PTV.

		Conformity			Homogeneity				
Energies	SCD	CR	SR	CI	Min (%)	Max (%)	Max-Min (%)	Std. Dev. (%)	D_{90-10} (%)
1	SSCD	0.998	0.521	0.478	88.0	100.0	12.0	2.9	8.3
2	SSCD	0.969	0.510	0.475	82.8	107.1	24.3	3.5	8.8
1	VSCD	0.993	0.502	0.494	86.8	100.0	13.2	2.9	8.5
2	VSCD	0.985	0.494	0.498	89.0	103.4	14.4	3.1	8.6

The two-energy VSCD plan was slightly more homogenous than the two-energy SSCD plan, as indicated by its reduced max-min (14.4% versus 24.3%), standard deviation (3.1% versus 3.5%), and D_{90-10} (8.6% versus 8.8%). The standard deviation and D_{90-10} are only slightly improved because the hot spot in the 12 MeV segment due to abutment to the 9 MeV segment is mostly outside of the PTV. Richert *et. al.* (2007) also found the VSCD plan to have reduced

max-min (17% versus 30.5%), standard deviation (3.2% versus 4.2%), and D_{90-10} (7.7% versus 10.3%) compared to the SSCD plan for this PTV.

3.3.2 Wedge PTV

The resulting fields and dose distributions for the single-energy SSCD and three-energy SSCD plans are seen in Figure 44 and Figure 45, respectively, and the SSCD plans' DVHs are compared in Figure 46. The resulting fields and dose distributions for the single-energy VSCD and three-energy VSCD plans are seen in Figure 47 and Figure 48, respectively, and the VSCD plans' DVHs are compared in Figure 49. The comparison metrics for all plans are listed in Table 6.

The three-energy SSCD plan had a slightly lower CR (0.992 versus 0.996), an improved SR (0.455 versus 0.493), and was more conformal (CI of 0.540 versus 0.505) compared to the single-energy SSCD plan. The three-energy VSCD plan had a better CR (0.999 versus 0.983), an improved SR (0.383 versus 0.486), and was more conformal (CI of 0.616 versus 0.505) compared to the single-energy VSCD plan. The three-energy plans were more conformal than the two-energy plans, for both SSCD and VSCD, seen by their improved CR (0.992 versus 0.959 for SSCD, 0.999 versus 0.990 for VSCD), SR (0.455 versus 0.521 for SSCD, 0.383 versus 0.418 for VSCD), and CI (0.540 versus 0.460 for SSCD, 0.616 versus 0.576 for VSCD). The drop in CR of the two-energy plans compared to the three-energy plans were due to the cold spots in the PTV at the edge of abutment of the 12 MeV and 20 MeV segments, which were more pronounced than the cold spots created by abutting 12 MeV to 16 MeV and abutting 16 MeV to 20 MeV in the three-energy plans. Additionally, the increase of the two-energy SSCD plan's SR compared to the single-energy SSCD plan was due to the two-energy plan's 12 MeV segment needing to balloon out at the edges, similar to the two-step block PTV, in order to push the 90%

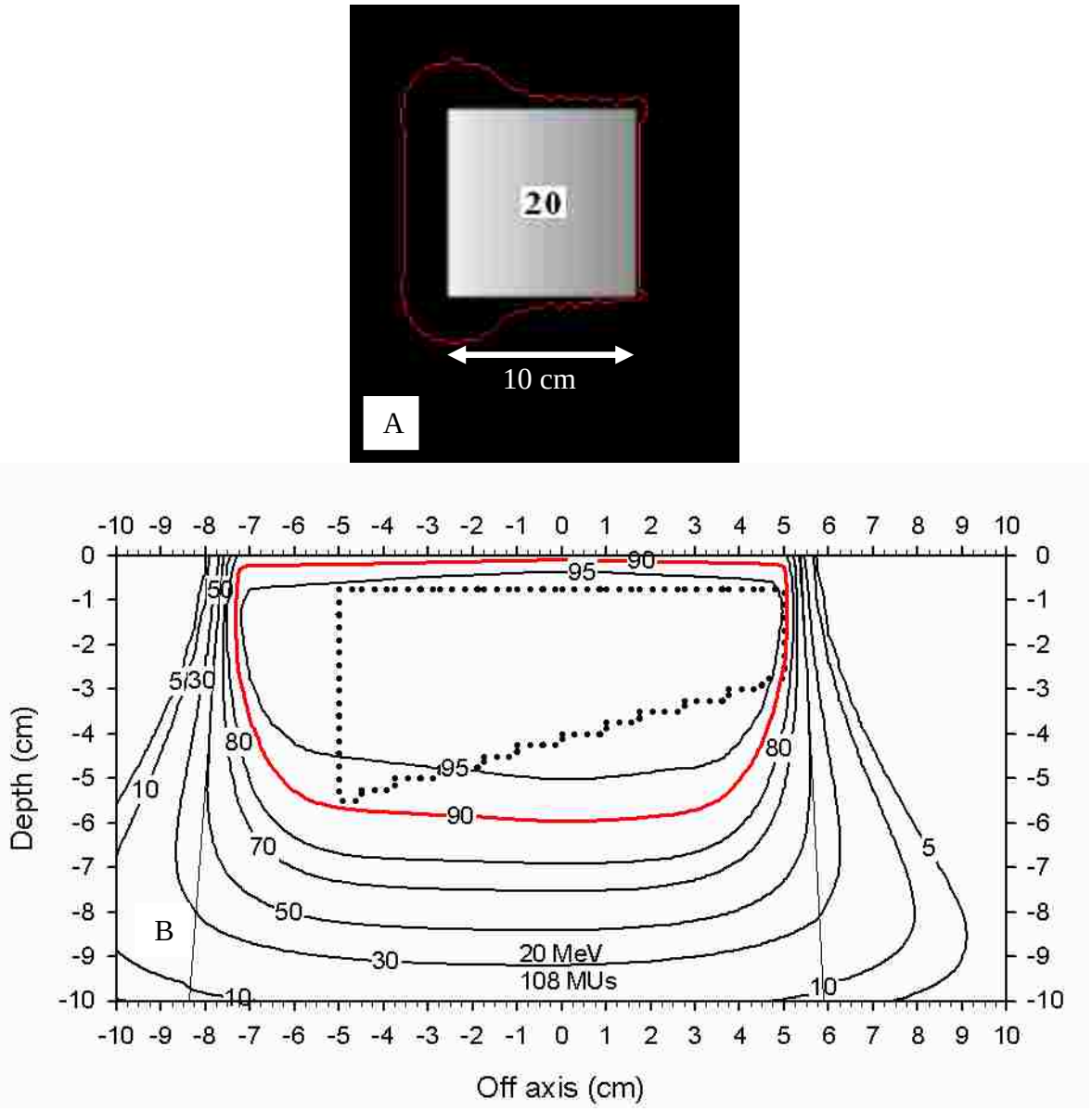

Figure 44: (A) Field segmentation after three optimization iterations for the wedge PTV using the single-energy SSCD plan. Gray-scale plot is BEV depth map of PTV. View is scaled to isocenter. A single 20 MeV segment (red line) is used. (B) PBA calculated dose distribution for the wedge PTV using the single-energy SSCD plan. The PTV is the dotted contour; the 90% dose contour is in red.

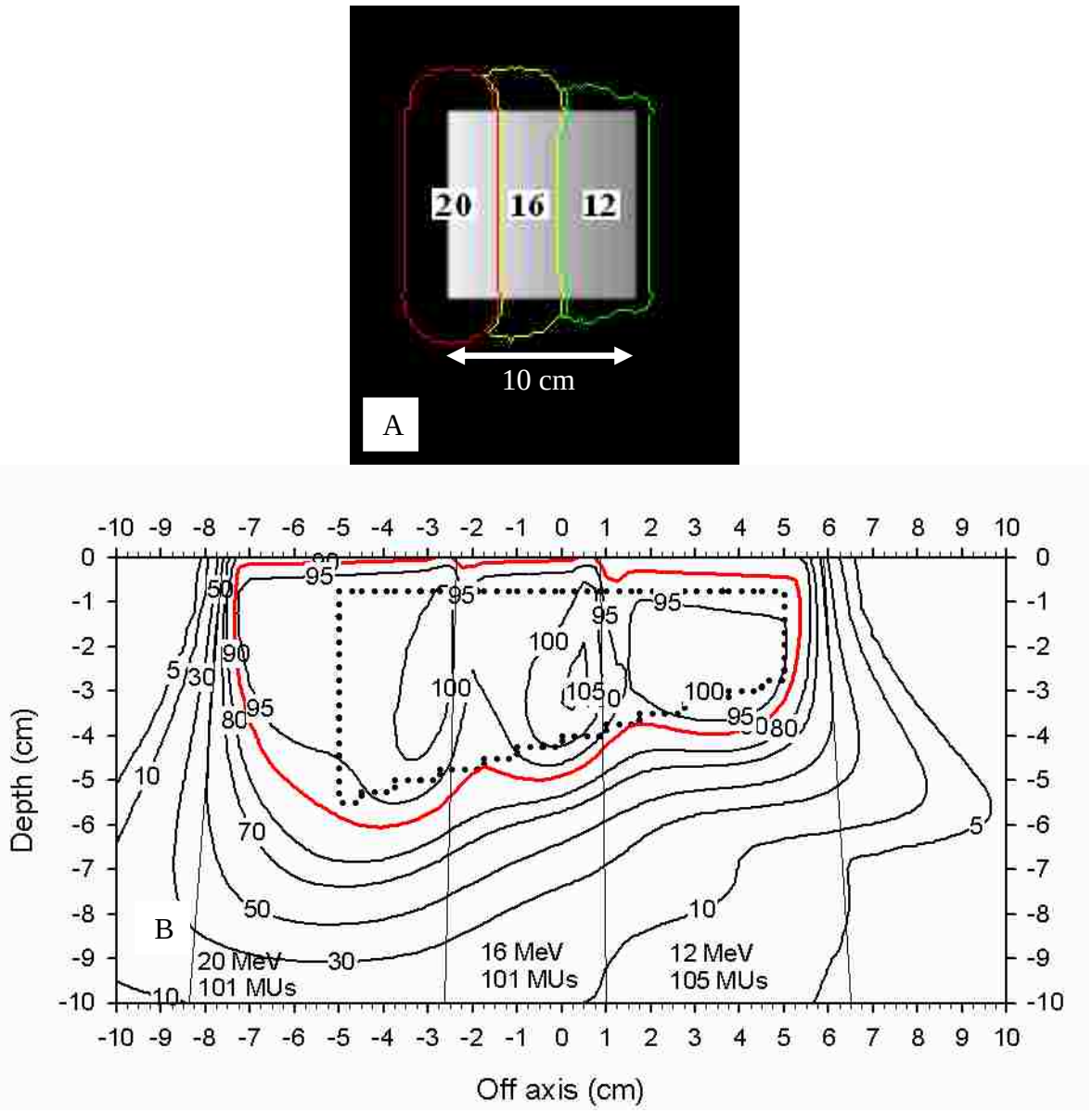

Figure 45: (A) Field segmentation after three optimization iterations for the wedge PTV using the three-energy SSCD plan. Gray-scale plot is BEV depth map of PTV. View is scaled to isocenter. The leftmost segment is 20 MeV (red line), the middle segment is 16 MeV (yellow line), and the rightmost segment is 12 MeV (green line). (B) PBA calculated dose distribution for the wedge PTV using the three-energy SSCD plan. The PTV is the dotted contour; the 90% dose contour is in red.

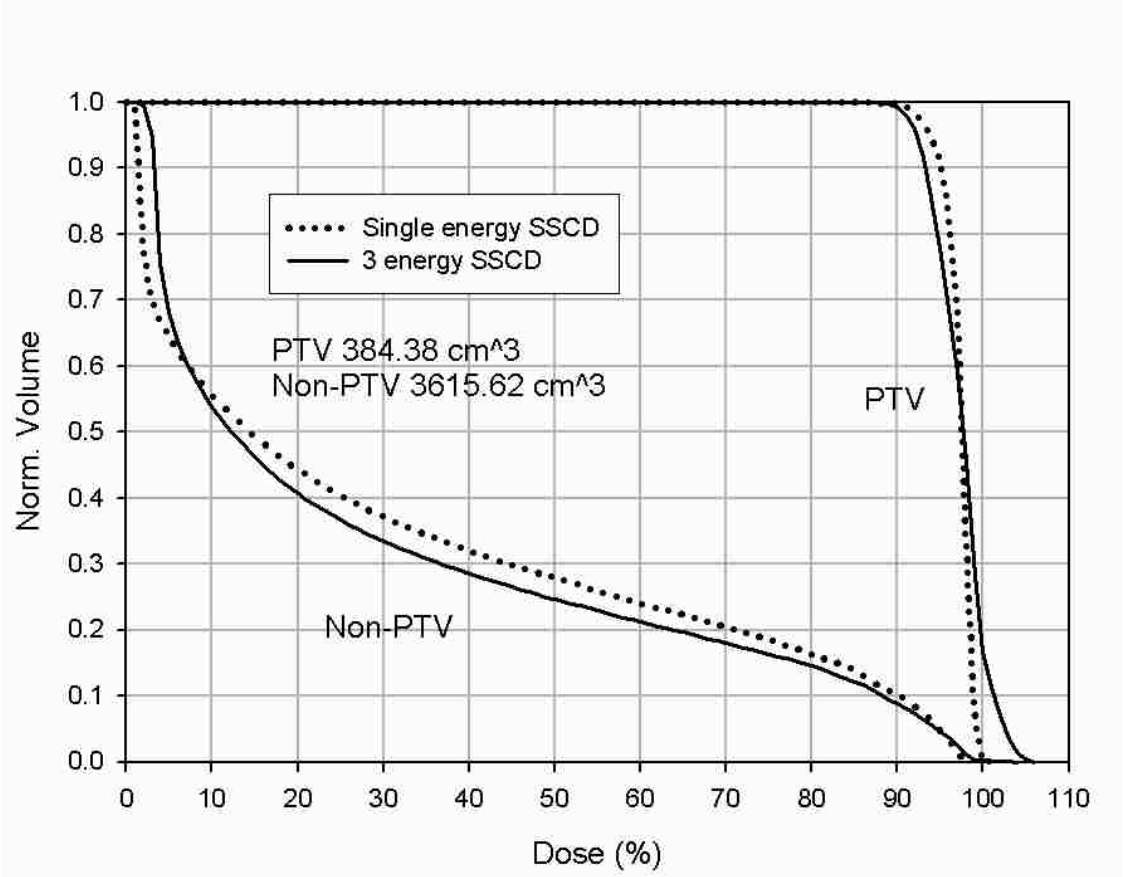

Figure 46: DVHs for the wedge PTV showing PTV and non-PTV ROIs. The single-energy SSCD plan is shown by the dotted lines and the three-energy SSCD plan by the solid lines.

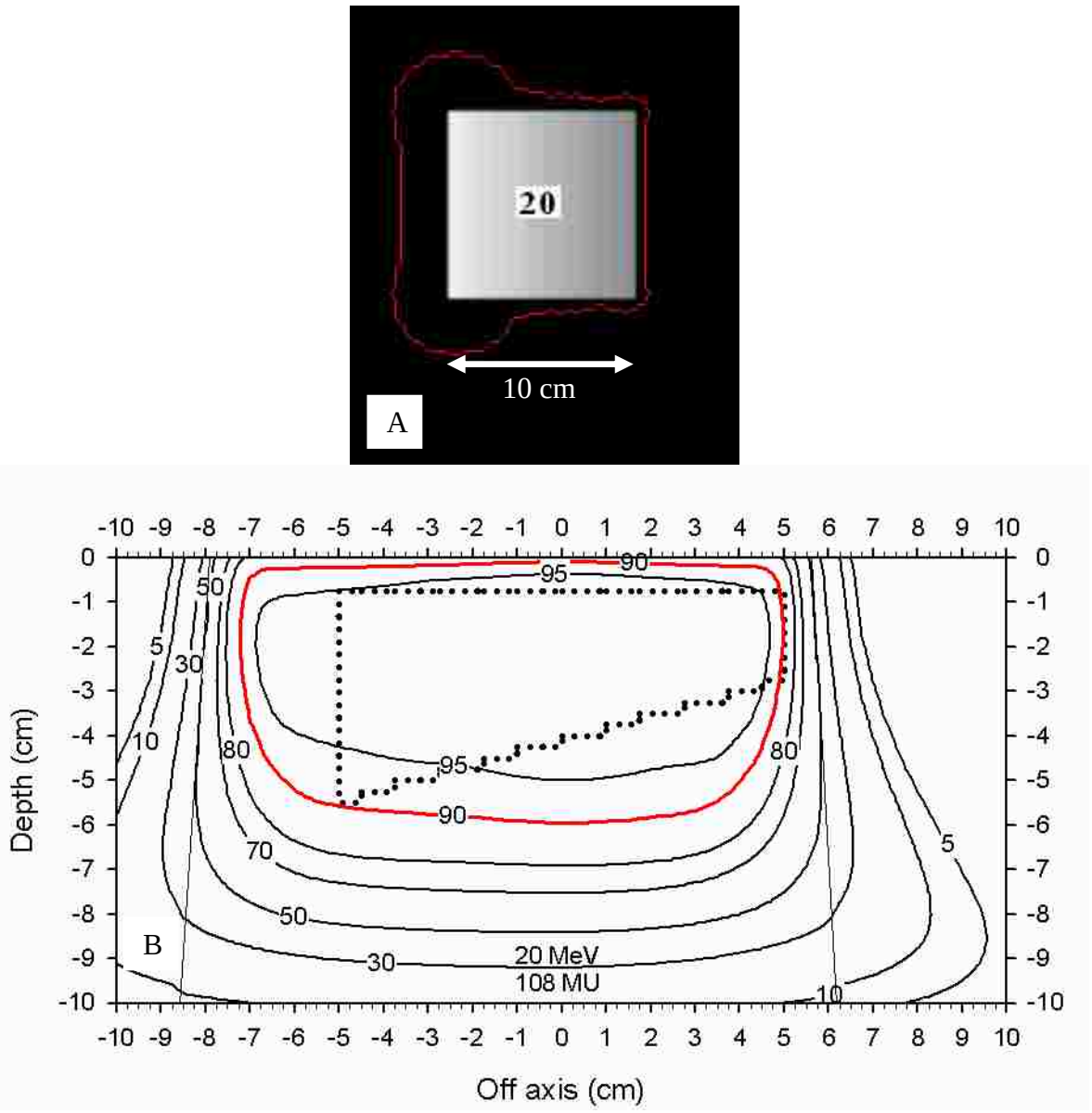

Figure 47: (A) Field segmentation after three optimization iterations for the wedge PTV using the single-energy VSCD plan. Gray-scale plot is BEV depth map of PTV. View is scaled to isocenter. A single 20 MeV segment (red line) is used. (B) PBA calculated dose distribution for the wedge PTV using the single-energy VSCD plan. The PTV is the dotted contour; the 90% dose contour is in red.

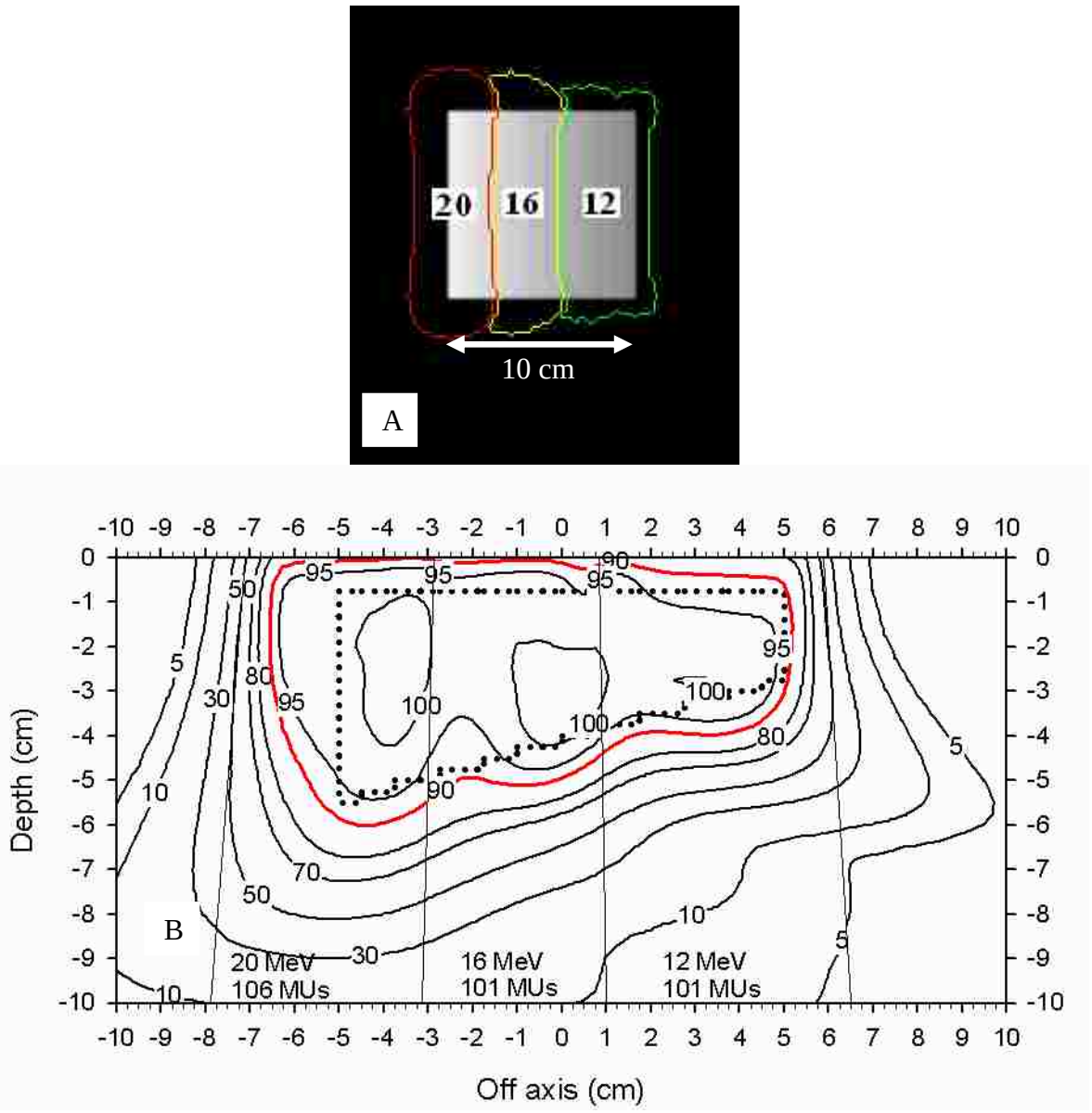

Figure 48: (A) Field segmentation after three optimization iterations for the wedge PTV using the three-energy VSCD plan. Gray-scale plot is BEV depth map of PTV. View is scaled to isocenter. The leftmost segment is 20 MeV (red line), the middle segment is 16 MeV (yellow line), and the rightmost segment is 12 MeV (green line). (B) PBA calculated dose distribution for the wedge PTV using the three-energy VSCD plan. The PTV is the dotted contour; the 90% dose contour is in red.

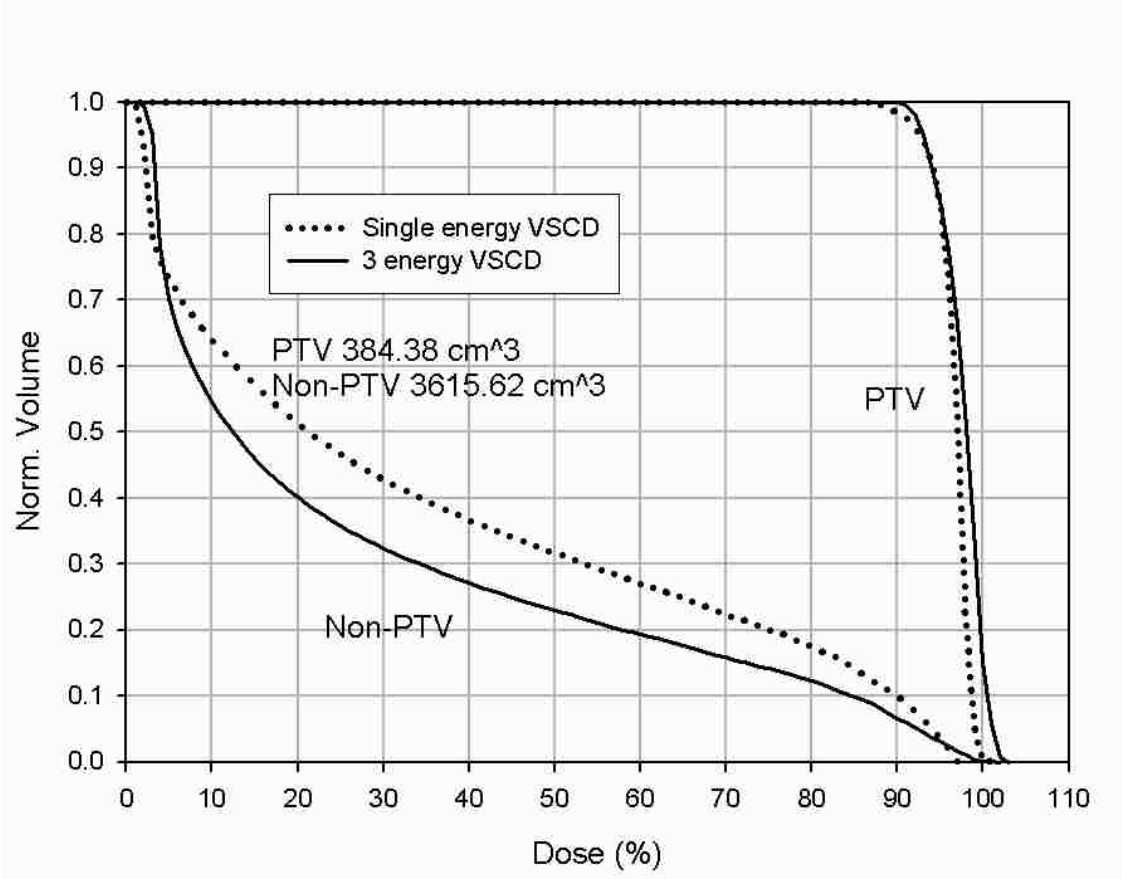

Figure 49: DVHs for the wedge PTV showing PTV and non-PTV ROIs. The single-energy VSCD plan is shown by the dotted lines and the three-energy VSCD plan by the solid lines.

Table 6: Summary of planning results for the wedge PTV.

		Conformity			Homogeneity				
Energies	SCD	CR	SR	CI	Min (%)	Max (%)	Max-Min (%)	Std. Dev. (%)	D_{90-10} (%)
1	SSCD	0.996	0.493	0.505	83.1	100.0	16.9	1.6	3.7
2	SSCD	0.959	0.521	0.460	81.8	114.2	32.4	4.2	10.3
3	SSCD	0.992	0.455	0.540	86.7	105.9	19.2	3.0	8.1
1	VSCD	0.983	0.486	0.505	83.9	100.0	16.1	2.0	4.5
2	VSCD	0.990	0.418	0.576	85.0	105.9	20.9	2.8	6.7
3	VSCD	0.999	0.383	0.616	87.5	102.9	15.4	2.4	6.5

isodose deeper than the distal PTV, resulting in a large amount of non-PTV being irradiated lateral to the PTV.

The three-energy VSCD was also more uniform than the three-energy SSCD plan, evidenced by its smaller max-min (15.4% versus 19.2%), standard deviation (2.4% versus 3.0%),

and D_{90-10} (6.5% versus 8.1%). Richert *et. al.* (2007) had similar VSCD versus SSCD results with reduced max-min (13.4% versus 15.3%), standard deviation (2.4% versus 2.8%), and D_{90-10} (6.1% versus 7.4%).

3.3.3 Pentagon PTV

The resulting fields and dose distributions for the single-energy SSCD and two-energy SSCD plans are seen in Figure 50 and Figure 51, respectively, and the SSCD plans' DVHs are compared in Figure 52. The resulting fields and dose distributions for the single-energy VSCD and two-energy VSCD plans are seen in Figure 53 and Figure 54, respectively, and the VSCD plans' DVHs are compared in Figure 55. The comparison metrics for all plans are listed in Table 7.

Compared to the single-energy SSCD plan, the two-energy SSCD plan had a reduced CR (0.959 versus 0.998) due to cold spots in the 12 MeV segments at the edge of abutment with the 20 MeV segment, improved SR (0.338 versus 0.389), and was more conformal (CI of 0.643 versus 0.609). The two-energy VSCD plan had a better CR (0.997 versus 0.981), a better SR (0.280 versus 0.382), and was more conformal (CI of 0.719 versus 0.606) compared to the single-energy VSCD plan. The two-energy plans had a little better normal tissue sparing than the three-energy plans, for both SSCD and VSCD, seen by their slightly improved SR (0.328 versus 0.338 for SSCD, 0.280 versus 0.296 for VSCD) and were more conformal (CIs of 0.645 versus 0.643 for SSCD, 0.719 versus 0.703 for VSCD).

The two-energy plans outperformed the three-energy plans because the three-energy plans only used two energies in their final segmentation due to their 16 MeV segments being too small. This caused the 16 MeV segments to be merged into the 20 MeV segments in Step 3B (illustrated in Figure 15) of the planning algorithm (Section 2.2.3), irradiating extra non-PTV. As illustrated by this case, because the planning algorithm deals with segments that are too small

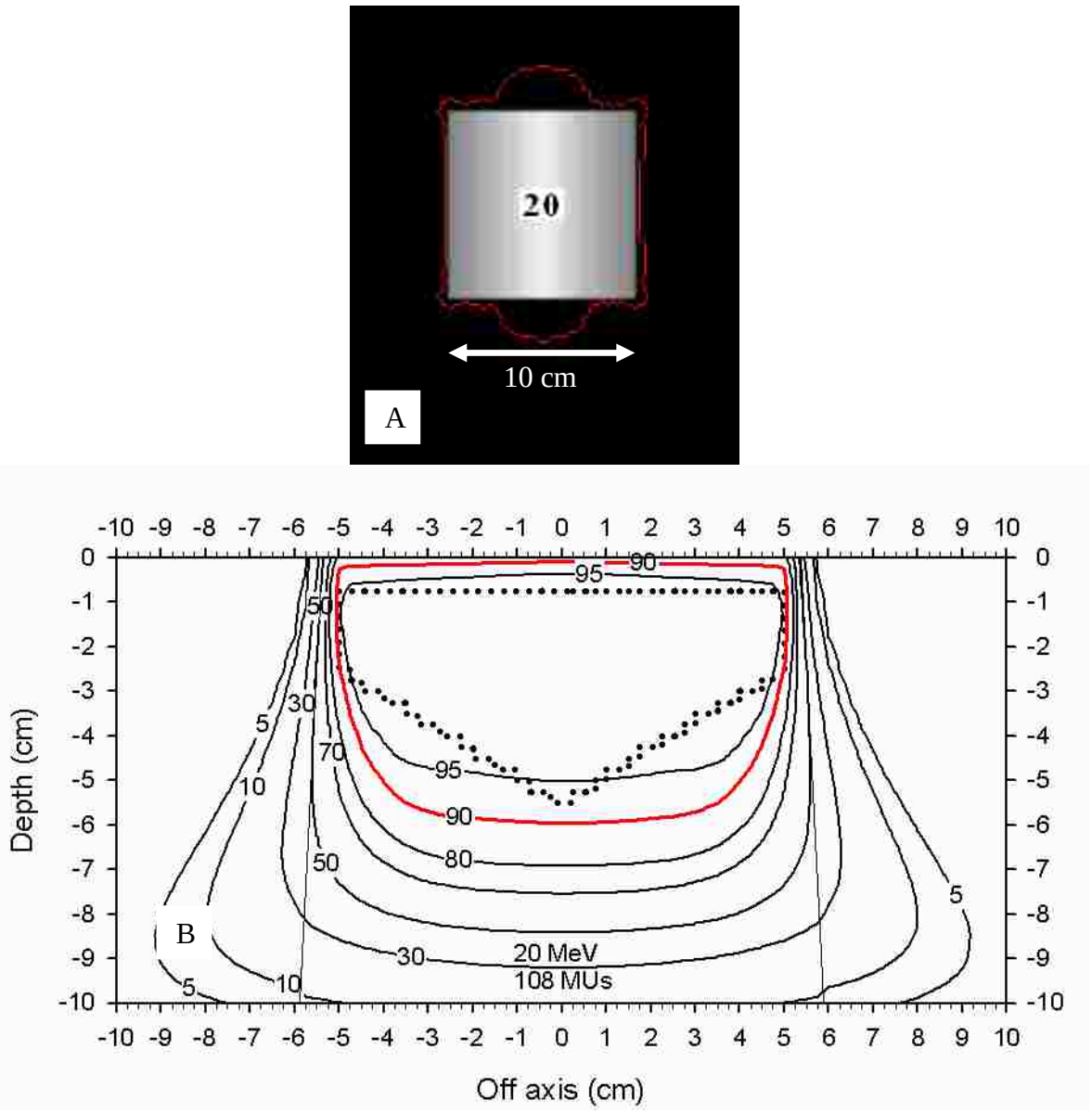

Figure 50: (A) Field segmentation after three optimization iterations for the pentagon PTV using the single-energy SSCD plan. Gray-scale plot is BEV depth map of PTV. View is scaled to isocenter. A single 20 MeV segment (red line) is used. (B) PBA calculated dose distribution for the pentagon PTV using the single-energy SSCD plan. The PTV is the dotted contour; the 90% dose contour is in red.

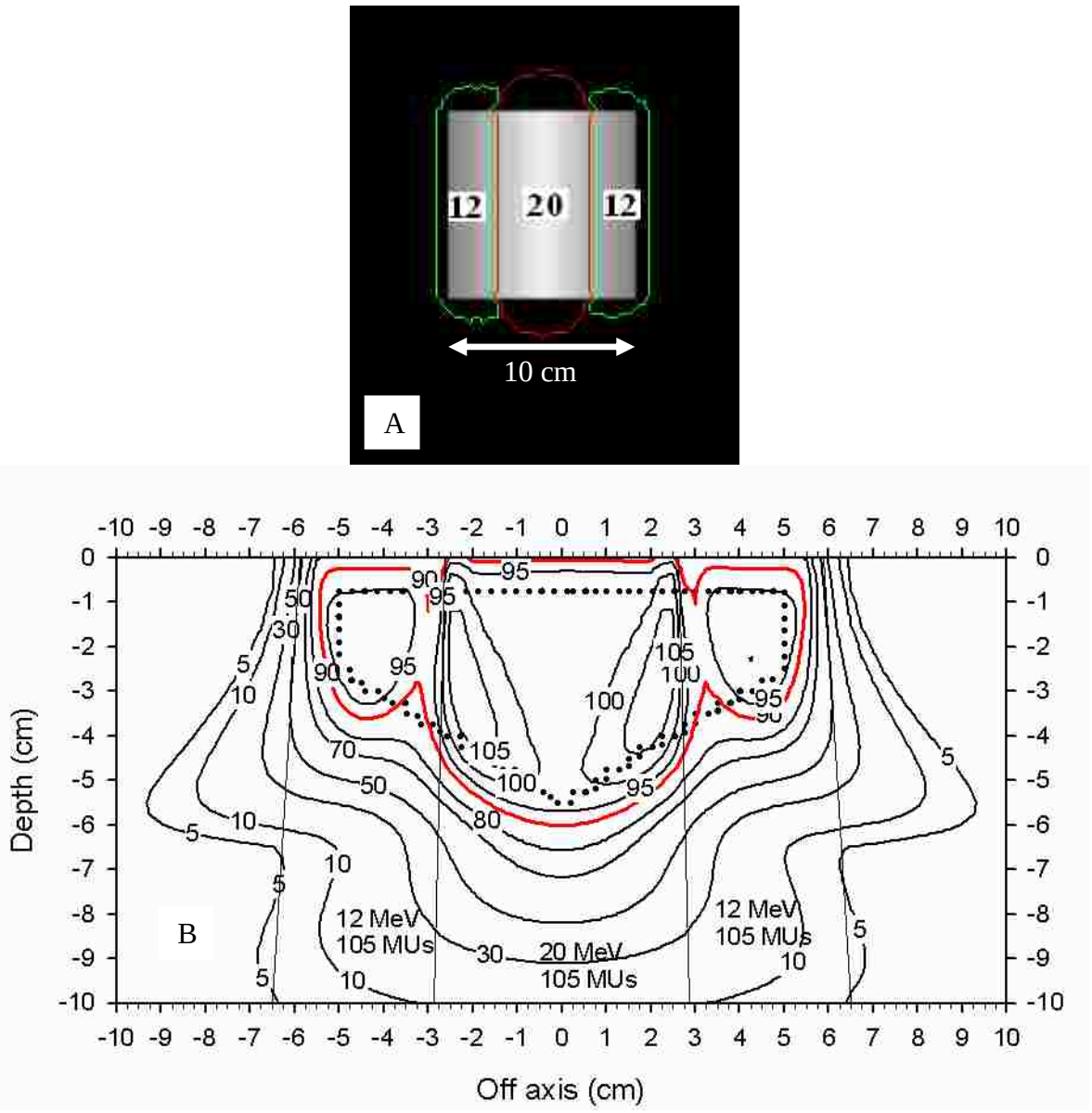

Figure 51: (A) Field segmentation after three optimization iterations for the pentagon PTV using the two-energy SSCD plan. Gray-scale plot is BEV depth map of PTV. View is scaled to isocenter. The outer segments are 12 MeV (green lines) and the inner segment is 20 MeV (red line). (B) PBA calculated dose distribution for the pentagon PTV using the two-energy SSCD plan. The PTV is the dotted contour; the 90% dose contour is in red.

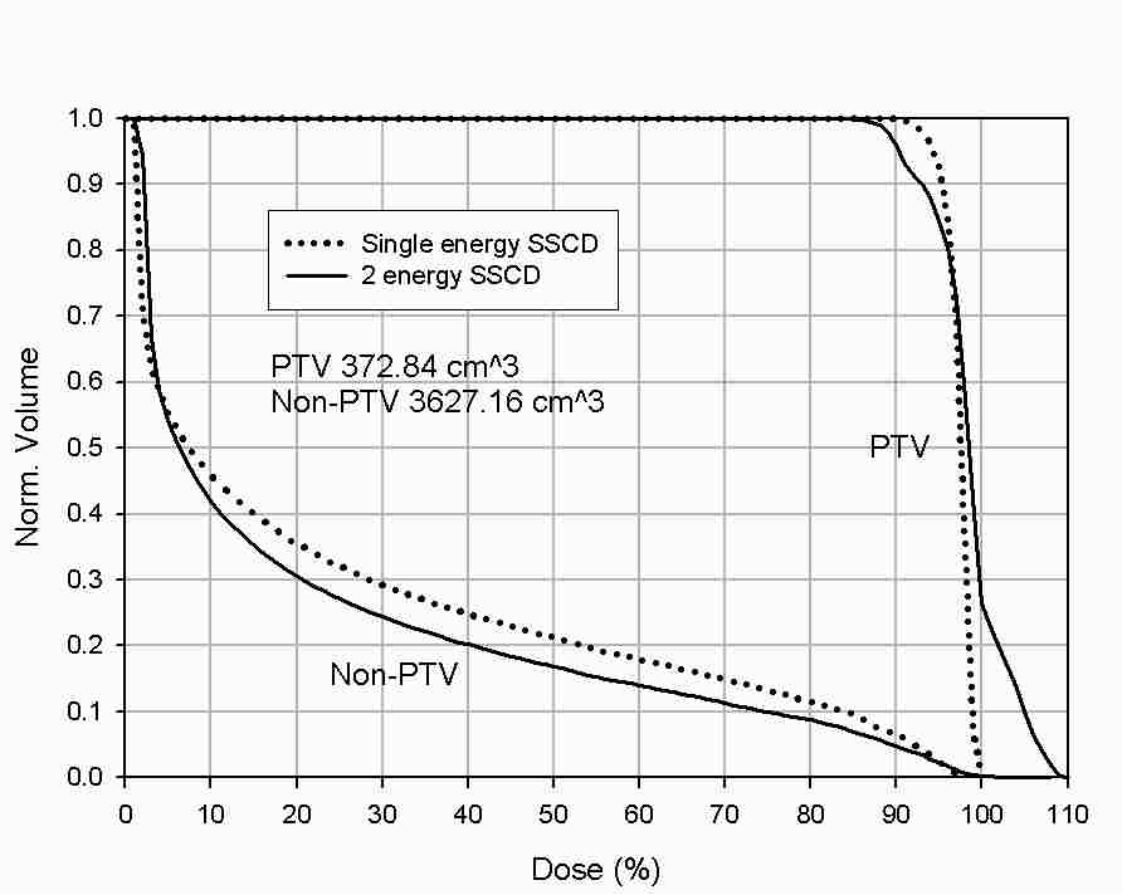

Figure 52: DVHs for the pentagon PTV showing PTV and non-PTV ROIs. The single-energy SSCD plan is shown by the dotted lines and the two-energy SSCD plan by the solid lines.

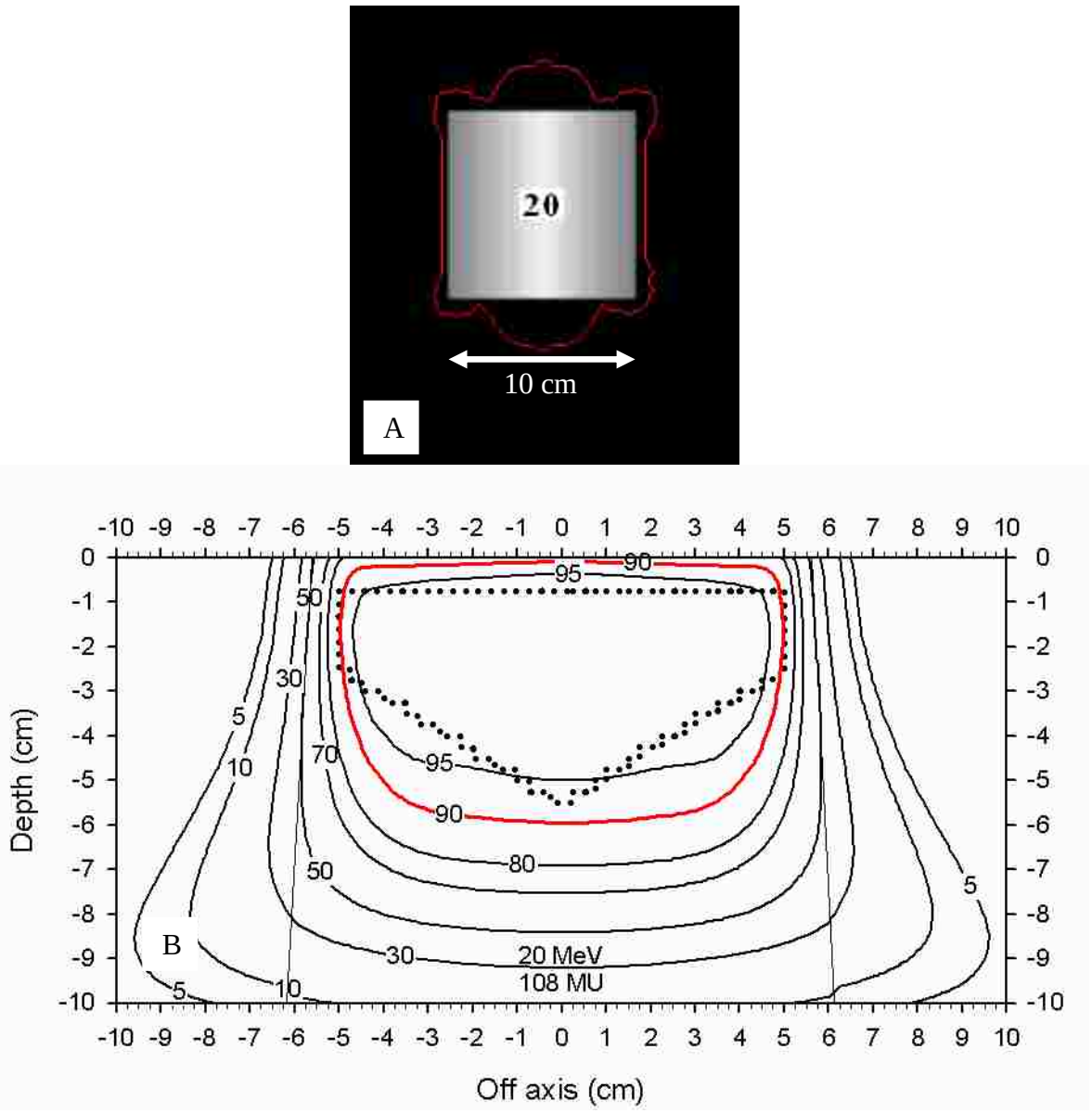

Figure 53: (A) Field segmentation after three optimization iterations for the pentagon PTV using the single-energy VSCD plan. Gray-scale plot is BEV depth map of PTV. View is scaled to isocenter. A single 20 MeV segment (red line) is used. (B) PBA calculated dose distribution for the pentagon PTV using the single-energy VSCD plan. The PTV is the dotted contour; the 90% dose contour is in red.

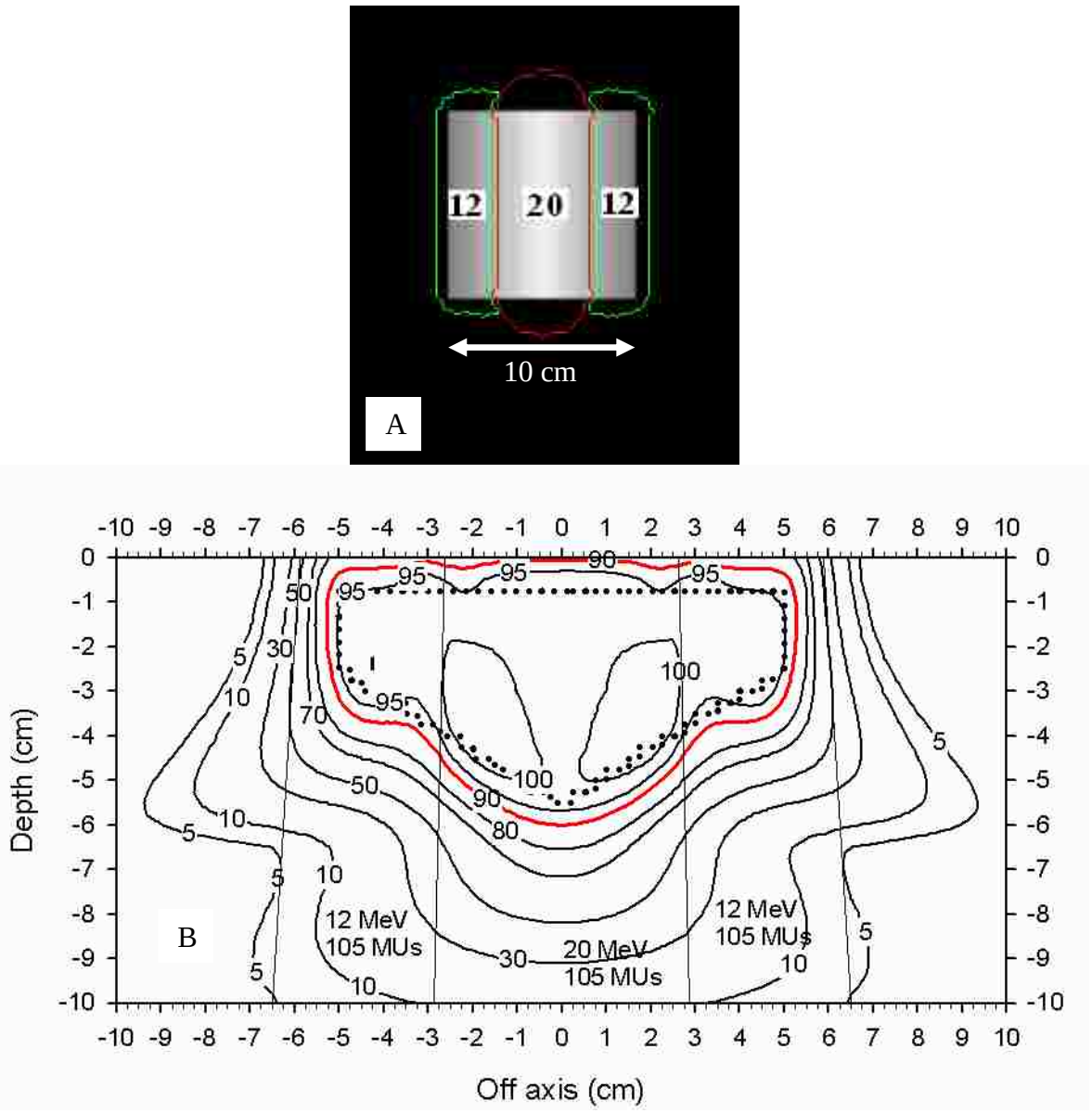

Figure 54: (A) Field segmentation after three optimization iterations for the pentagon PTV using the two-energy VSCD plan. Gray-scale plot is BEV depth map of PTV. View is scaled to isocenter. The outer segments are 12 MeV (green lines) and the inner segment is 20 MeV (red line). (B) PBA calculated dose distribution for the pentagon PTV using the two-energy VSCD plan. The PTV is the dotted contour; the 90% dose contour is in red.

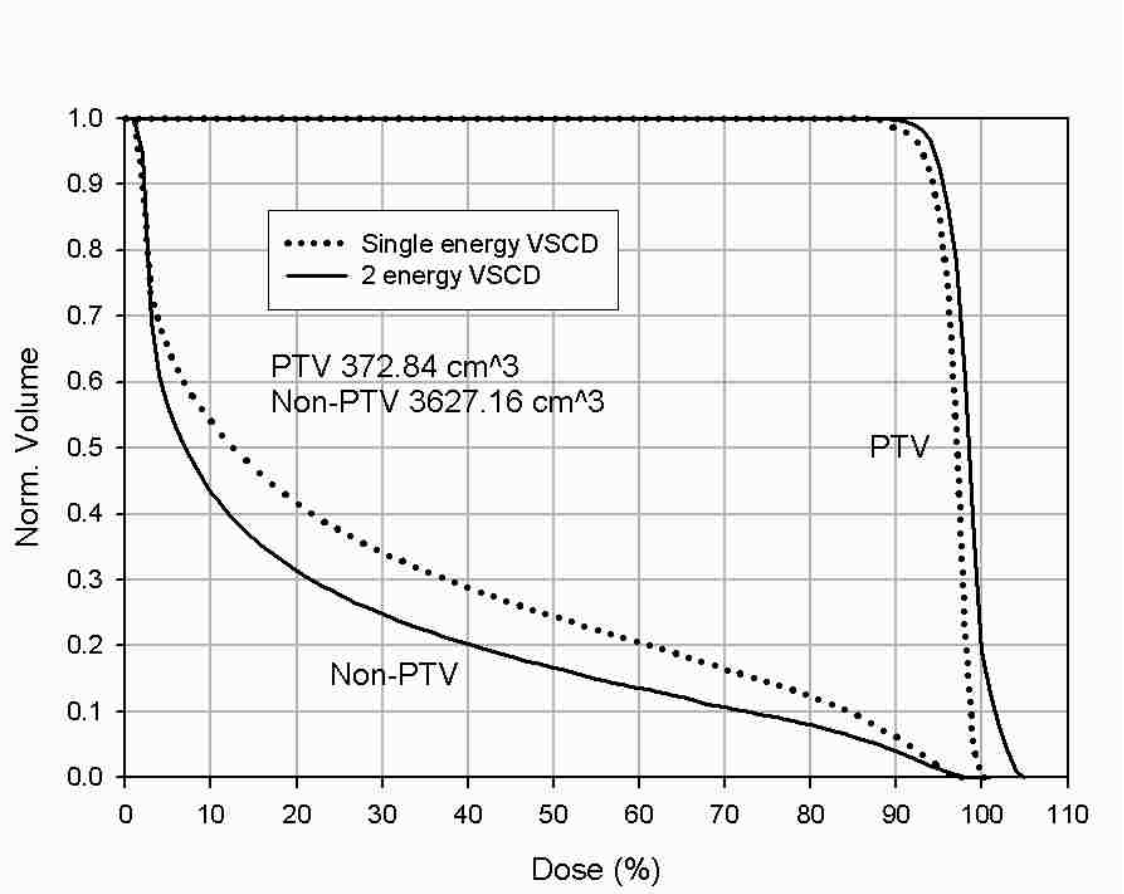

Figure 55: DVHs for the pentagon PTV showing PTV and non-PTV ROIs. The single-energy VSCD plan is shown by the dotted lines and the two-energy VSCD plan by the solid lines.

Table 7: Summary of planning results for the pentagon PTV.

		Conformity			Homogeneity				
Energies	SCD	CR	SR	CI	Min (%)	Max (%)	Max-Min (%)	Std. Dev. (%)	D_{90-10} (%)
1	SSCD	0.998	0.389	0.609	87.7	100.0	12.3	1.5	3.6
2	SSCD	0.959	0.328	0.645	82.4	109.2	26.8	4.4	12.0
3	SSCD	0.971	0.338	0.643	83.5	110.0	26.5	4.2	11.4
1	VSCD	0.981	0.382	0.606	87.6	100.0	12.4	1.9	4.4
2	VSCD	0.997	0.280	0.719	84.1	104.7	20.6	2.3	6.1
3	VSCD	0.998	0.296	0.703	84.9	104.7	19.8	2.2	5.6

by simply merging them with the adjacent segment of the next highest energy in Step 3 (Section 2.2.3) instead of returning to Step 2 (Section 2.2.2), merging the energy segmentation, and then repeating Step 3, one should not expect the segmentation of a three-energy plan that uses only two energies to be the same as the segmentation of a two-energy plan using two energies.

The two-energy VSCD was more homogeneous than the two-energy SSCD plan, evidenced by its smaller max-min (20.6% versus 26.8%), standard deviation (2.3% versus 4.4%), and nearly halved D_{90-10} (6.1% versus 12.0%). Richert *et. al.* (2007) also had reduced max-min (14.4% versus 21.2%), standard deviation (2.2% versus 3.6%), and D_{90-10} (5.8% versus 8.8%) for the VSCD plan compared to the SSCD plan for this PTV.

3.3.4 Inverted Well PTV

The resulting fields and dose distributions for the single-energy SSCD and three-energy SSCD plans are seen in Figure 56 and Figure 57, respectively, and the SSCD plans' DVHs are compared in Figure 58. The resulting fields and dose distributions for the single-energy VSCD and three-energy VSCD plans are seen in Figure 59 and Figure 60, respectively, and the VSCD plans' DVHs are compared in Figure 61. The comparison metrics for all plans are listed in Table 8. Only 2 energies were used in the final field segmentation of the three-energy plans. Again, as discussed in Section 3.3.3, one should not expect the two-energy and three-energy plans to converge to the same final segmentation simply because both plans used the same number of energies in final segmentation.

The three-energy SSCD plan compared to the single-energy SSCD plan had a reduced CR (0.928 versus 0.999) due to the cold spots in the 12 MeV segment just inside the edge of abutment to the 20 MeV segments, an improved SR (0.542 versus 0.587), and was more conformal (CI of 0.425 versus 0.412). The three-energy VSCD plan compared to the single-energy VSCD had a slightly smaller CR (0.997 versus 1.000), a better SR (0.450 versus 0.565), and was more conformal (CI of 0.548 versus 0.435). Similar to the pentagon PTV, the three-energy plans used only two energies in the final segmentation because the 16 MeV segments were too small and thus were replaced by the 20 MeV segment. However, in this case, the segment replacement resulted in the three-energy plans having a slightly better SR (0.542 versus

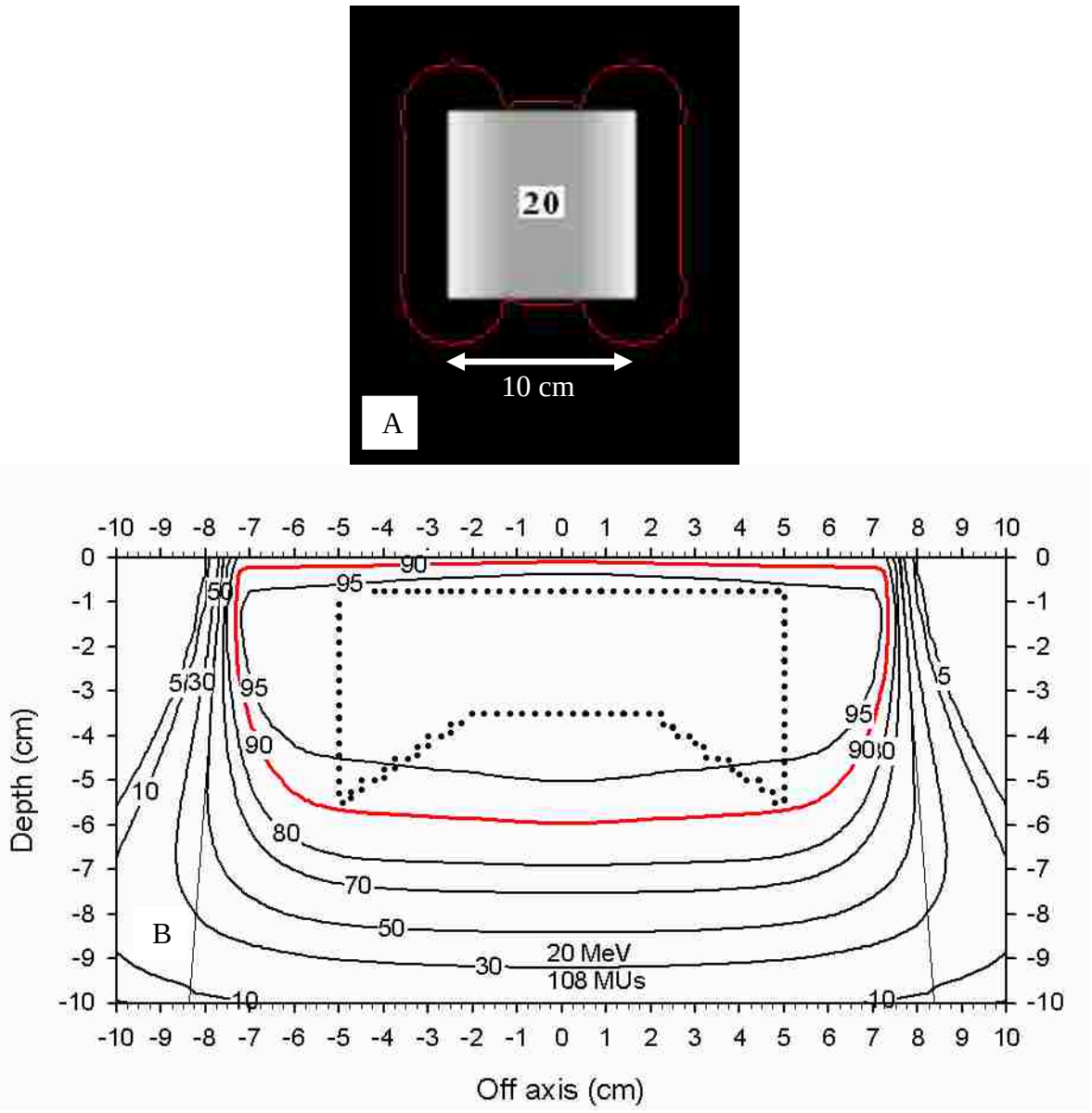

Figure 56: (A) Field segmentation after three optimization iterations for the inverted well PTV using the single-energy SSCD plan. Gray-scale plot is BEV depth map of PTV. View is scaled to isocenter. A single 20 MeV segment (red line) is used. (B) PBA calculated dose distribution for the inverted well PTV using the single-energy SSCD plan. The PTV is the dotted contour; the 90% dose contour is in red.

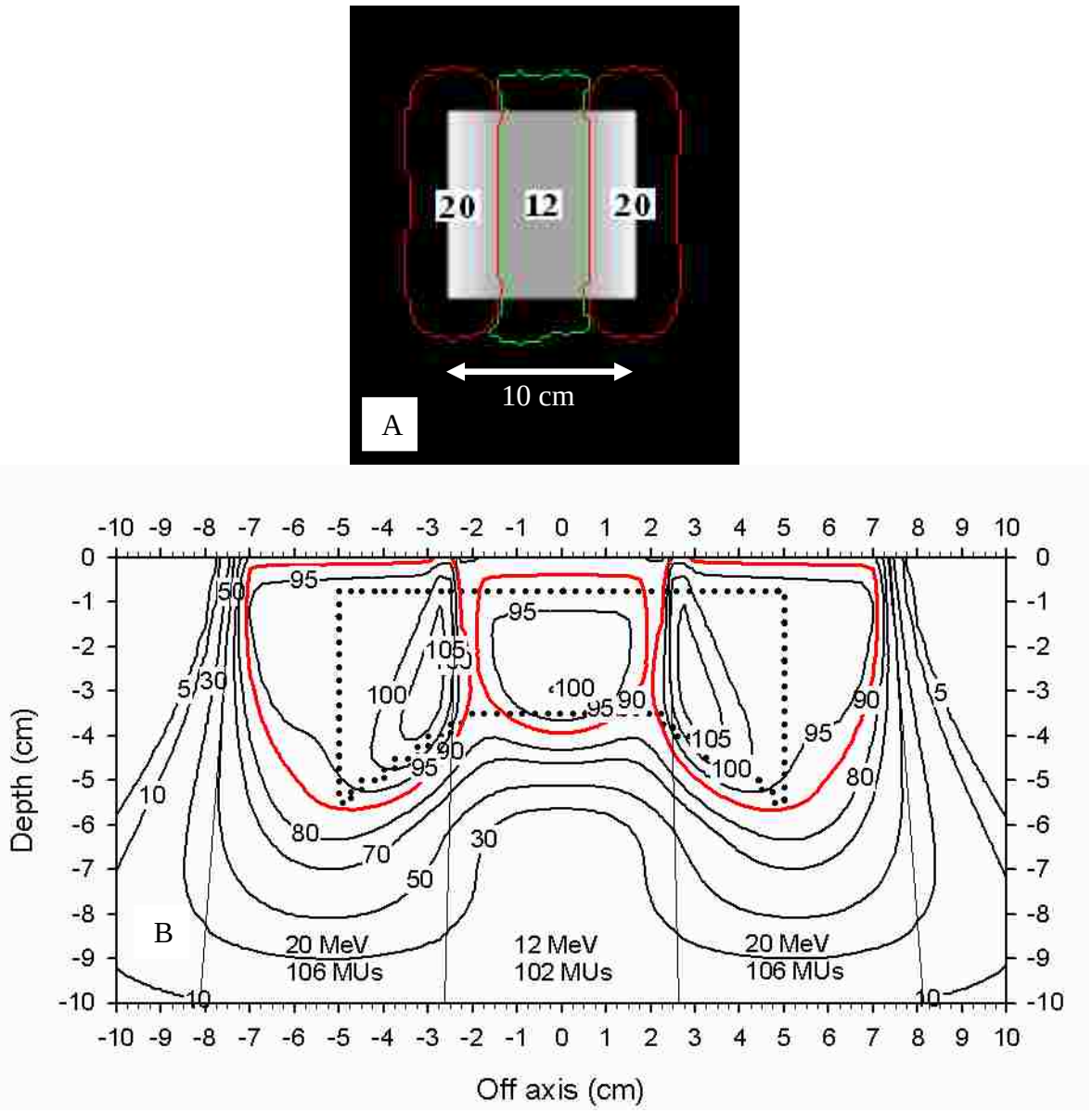

Figure 57: (A) Field segmentation after three optimization iterations for the inverted well PTV using the three-energy SSCD plan. Gray-scale plot is BEV depth map of PTV. View is scaled to isocenter. Only two energies are used in the plan, though three energies were allowed. The outer segments are 20 MeV (red lines) and the inner segment is 12 MeV (green line). (B) PBA calculated dose distribution for the inverted well PTV using the three-energy SSCD plan. The PTV is the dotted contour; the 90% dose contour is in red.

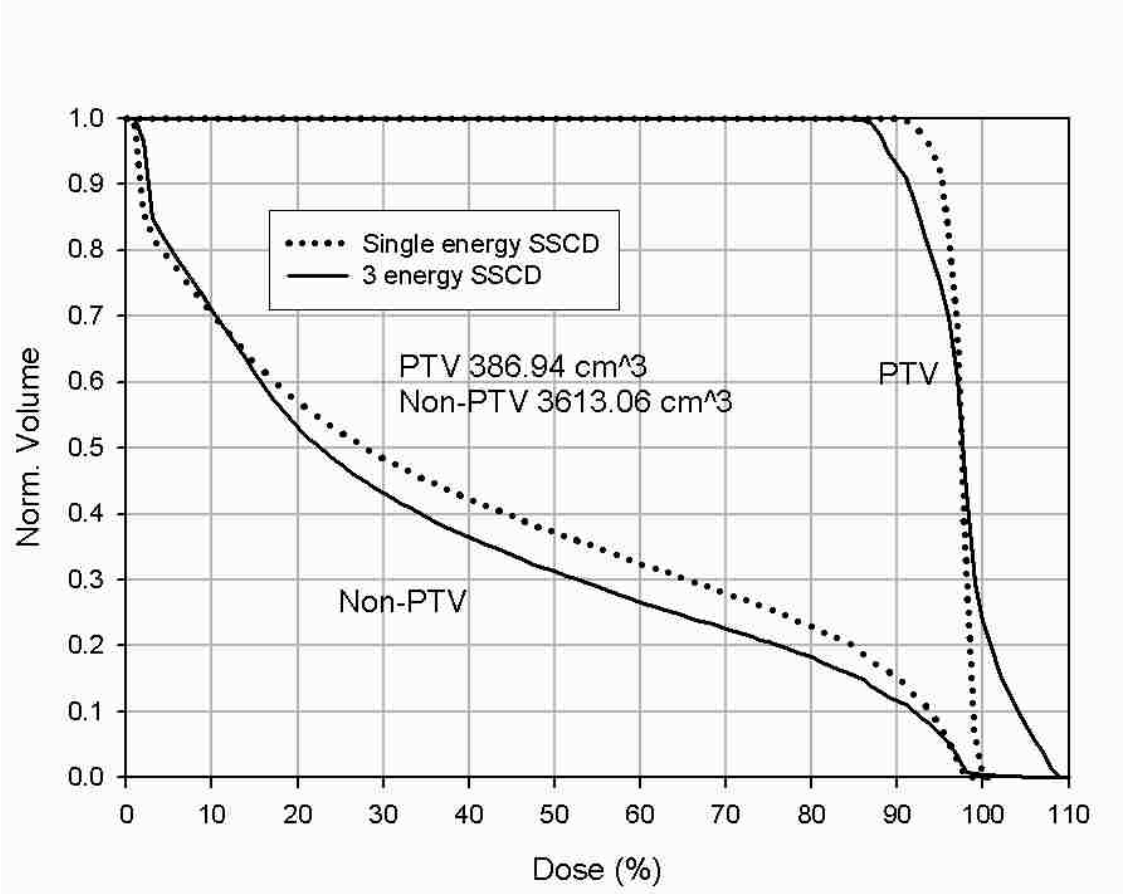

Figure 58: DVHs for the inverted well PTV showing PTV and non-PTV ROIs. The single-energy SSCD plan is shown by the dotted lines and the three-energy SSCD plan by the solid lines.

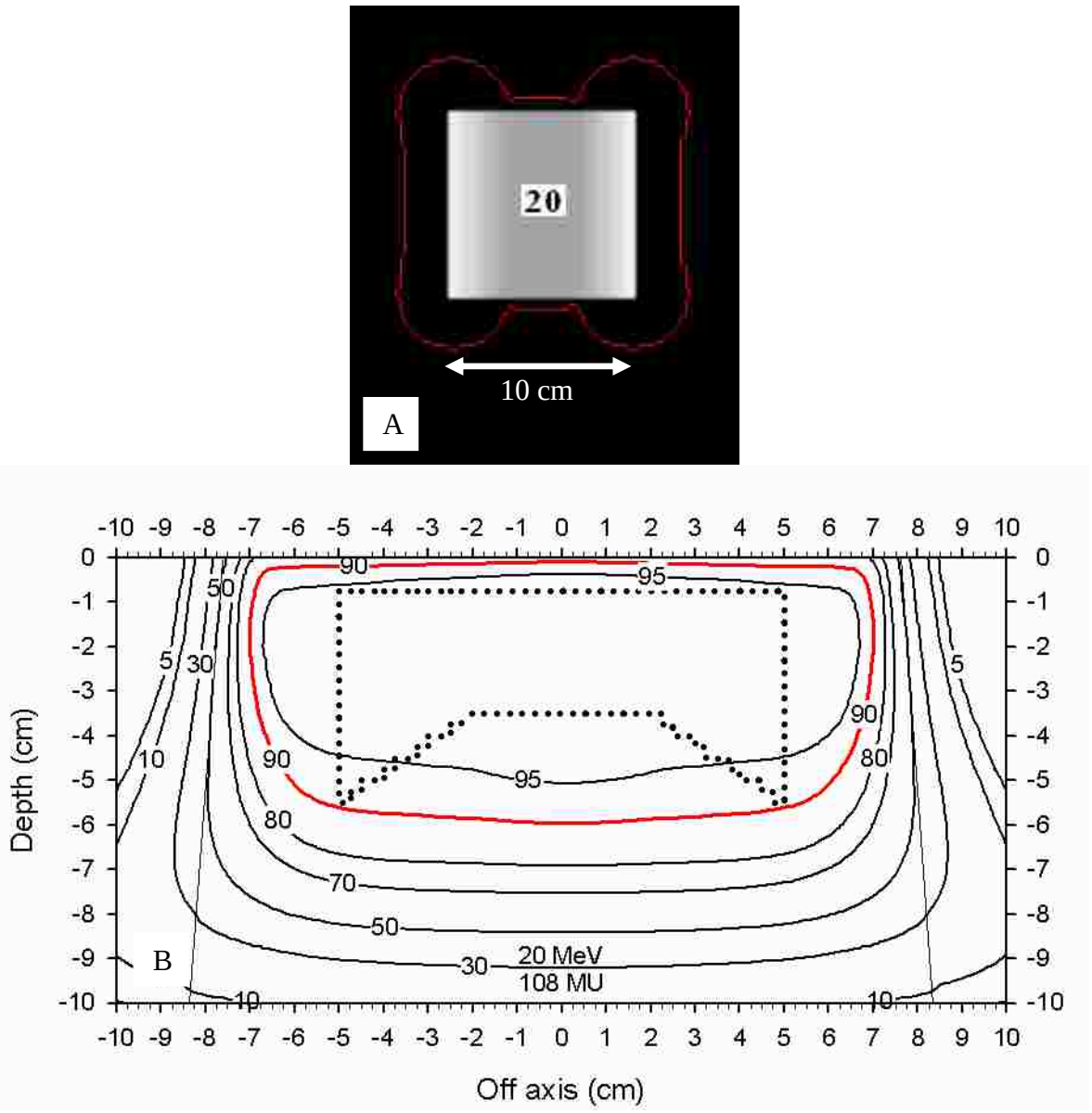

Figure 59: (A) Field segmentation after three optimization iterations for the inverted well PTV using the single-energy VSCD plan. Gray-scale plot is BEV depth map of PTV. View is scaled to isocenter. A single 20 MeV segment (red line) is used. (B) PBA calculated dose distribution for the inverted well PTV using the single-energy VSCD plan. The PTV is the dotted contour; the 90% dose contour is in red.

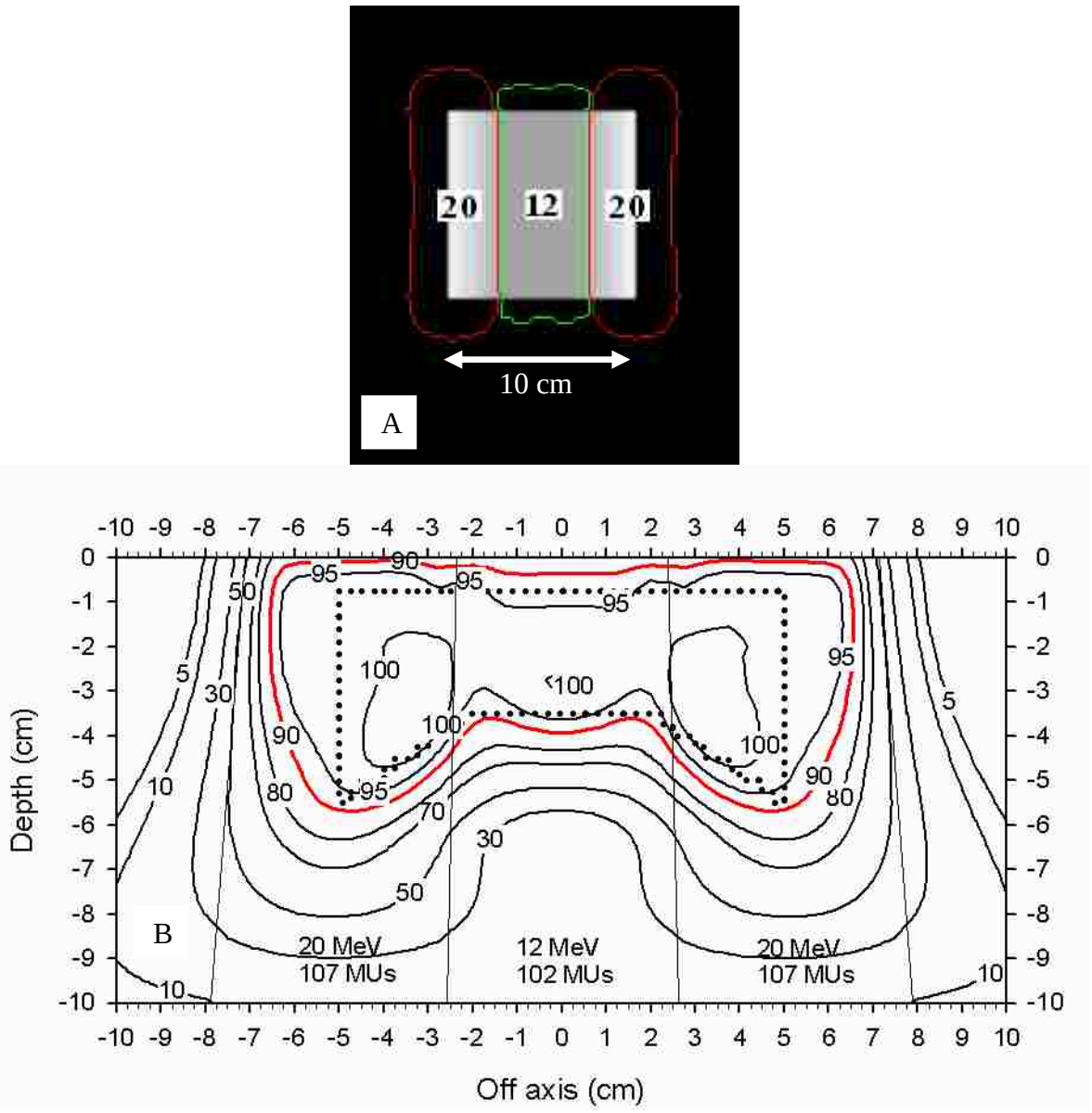

Figure 60: (A) Field segmentation after three optimization iterations for the inverted well PTV using the three-energy VSCD plan. Gray-scale plot is BEV depth map of PTV. View is scaled to isocenter. Only two energies are used in the plan, though three energies were allowed. The outer segments are 20 MeV (red lines) and the inner segment is 12 MeV (green line). (B) PBA calculated dose distribution for the inverted well PTV using the three-energy VSCD plan. The PTV is the dotted contour; the 90% dose contour is in red.

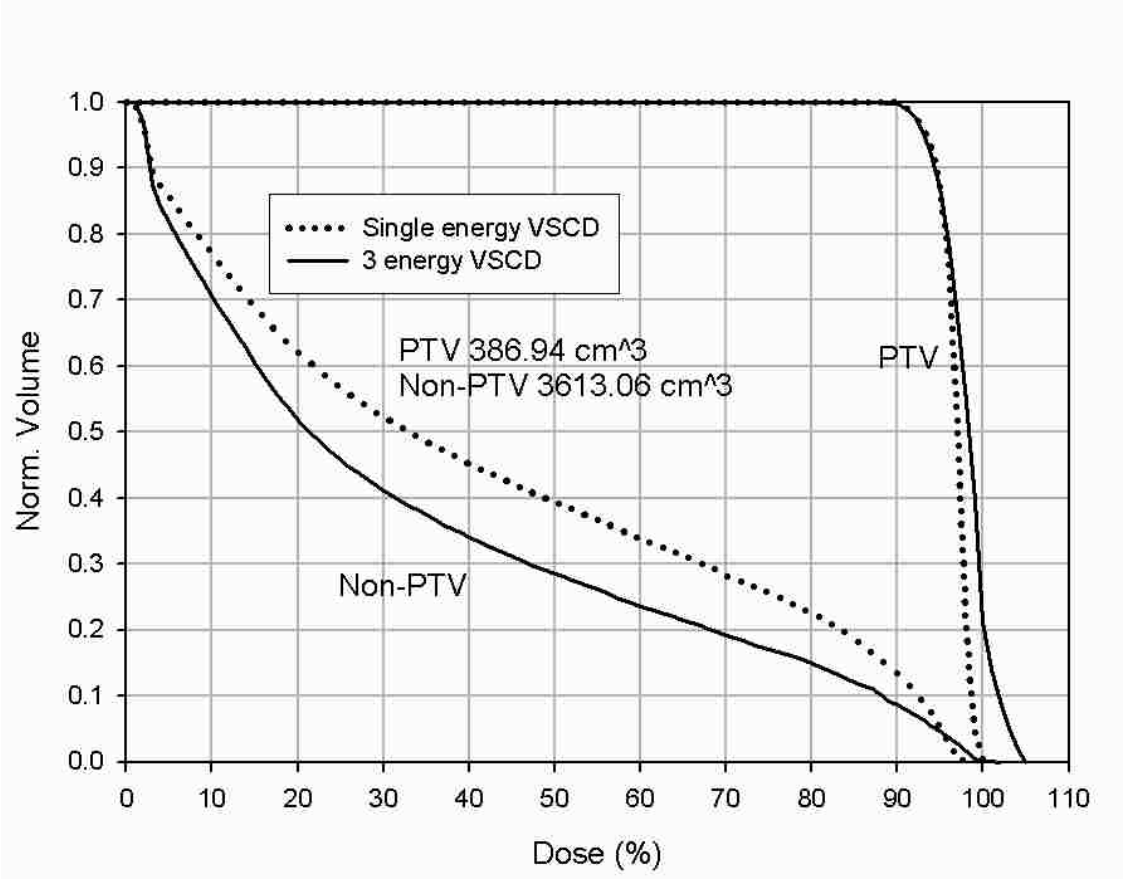

Figure 61: DVHs for the inverted well PTV showing PTV and non-PTV ROIs. The single-energy VSCD plan is shown by the dotted lines and the three-energy VSCD plan by the solid lines.

Table 8: Summary of planning results for the inverted well PTV.

		Conformity			Homogeneity				
Energies	SCD	CR	SR	CI	Min (%)	Max (%)	Max-Min (%)	Std. Dev. (%)	D_{90-10} (%)
1	SSCD	0.999	0.587	0.412	87.6	100.0	12.4	1.6	3.6
2	SSCD	0.930	0.552	0.417	84.9	110.1	25.2	4.7	12.8
3	SSCD	0.928	0.542	0.425	85.0	110.0	25.0	4.7	12.9
1	VSCD	1.000	0.565	0.435	89.9	100.0	10.1	1.6	3.8
2	VSCD	0.995	0.467	0.530	87.7	104.9	17.2	2.9	7.6
3	VSCD	0.997	0.450	0.548	86.6	104.9	18.3	2.8	7.4

0.552 for SSCD, 0.450 versus 0.467 for VSCD) than the two-energy plans, instead of slightly worse as with the pentagon PTV. The three-energy SSCD plan had a slightly worse CR (0.928 versus 0.930) than the two-energy SSCD plan, while the three-energy VSCD plan had a slightly better CR (0.997 versus 0.995) than the two-energy VSCD plan. The three-energy plans were

more conformal than the two-energy plans (CIs of 0.425 versus 0.417 for SSCD, 0.548 versus 0.530 for VSCD).

The three-energy VSCD has a visually more uniform dose distribution than the three-energy SSCD plan, evidenced by its smaller max-min (18.3% versus 25.0%), standard deviation (2.8% versus 4.7%), and greatly reduced $D_{90\text{-}10}$ (7.4 % versus 12.9%). Richert *et. al.* (2007) had similar results for this PTV, finding the VSCD plan to have a reduced max-min (16.2% versus 23.4%), standard deviation (3.0% versus 4.6%), and $D_{90\text{-}10}$ (7.9% versus 13.8%) compared to the SSCD plan.

3.3.5 Hemisphere PTV

The resulting fields and dose distributions for the single-energy SSCD and three-energy SSCD plans are seen in Figure 62 and Figure 63, respectively, and the SSCD plans' DVHs are compared in Figure 64. The resulting fields and dose distributions for the single-energy VSCD and two-energy VSCD plans are seen in Figure 65 and Figure 66, respectively, and the VSCD plans' DVHs are compared in Figure 67. The comparison metrics for all plans are listed in Table 9. Only 2 energies were used in the final field segmentation of the three-energy SSCD plan, and only 1 energy was used in the final field segmentation of the two-energy VSCD plan. As discussed in Section 3.3.3, one should not expect these plans to converge to the same segmentation as the plans with lower allowed energies.

The three-energy SSCD plan had an improved CR (1.000 versus 0.993), a worse SR (0.332 versus 0.204), and was less conformal (CI of 0.668 versus 0.790) when compared to the single-energy SSCD plan. Similarly, the two-energy VSCD plan compared to the single-energy VSCD plan had a better CR (1.000 versus 0.937), an increased SR (0.251 versus 0.170), and was less conformal (CI of 0.712 versus 0.778). The increased SR of the multiple energy plans was due to the 90% isodose of the single-energy SSCD plan naturally being nearly the same shape as

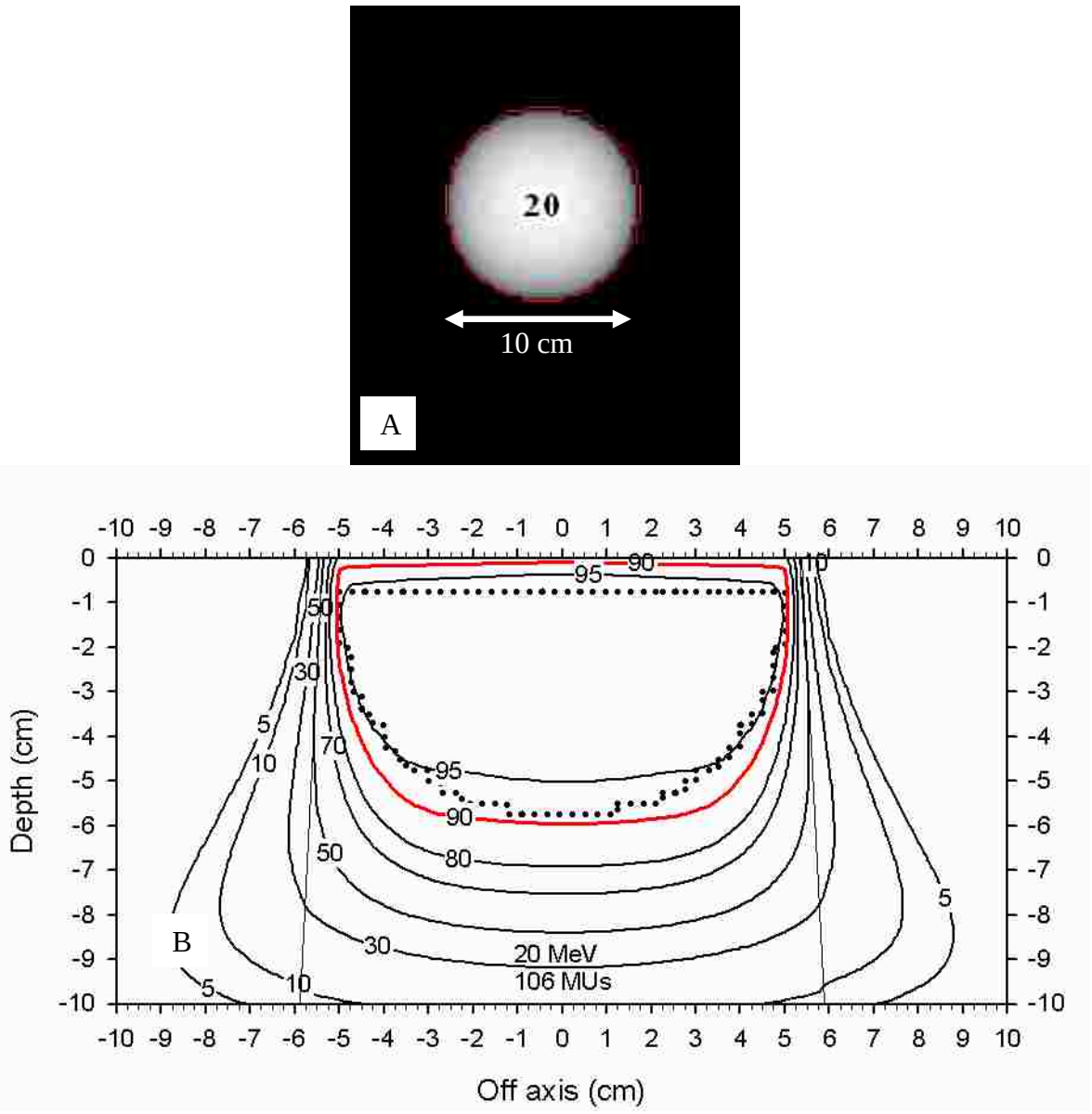

Figure 62: (A) Field segmentation after three optimization iterations for the hemisphere PTV using the single-energy SSCD plan. Gray-scale plot is BEV depth map of PTV. View is scaled to isocenter. A single 20 MeV segment (red line) is used. (B) PBA calculated dose distribution for the hemisphere PTV using the single-energy SSCD plan. The PTV is the dotted contour; the 90% dose contour is in red.

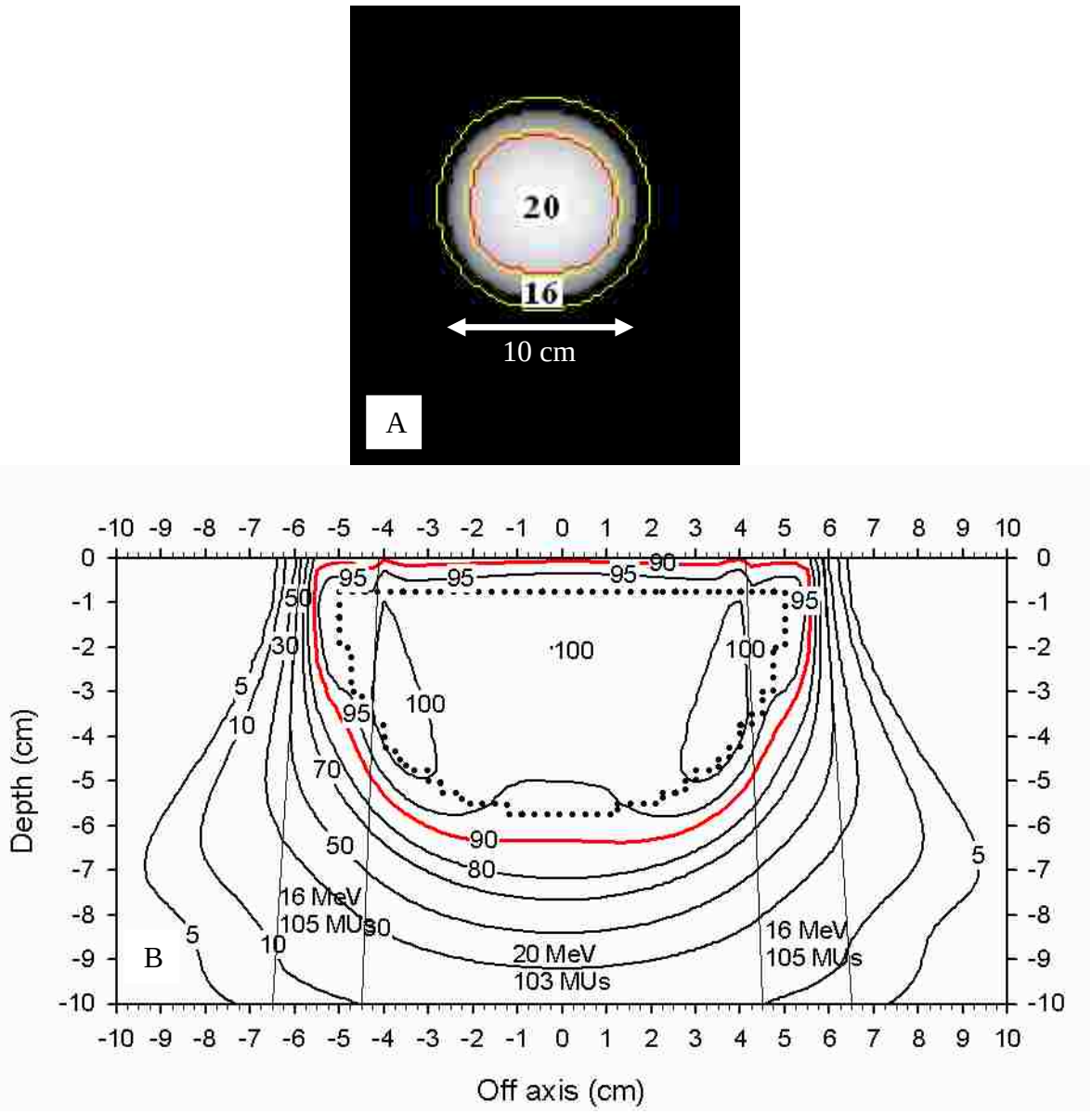

Figure 63: (A) Field segmentation after three optimization iterations for the hemisphere PTV using the three-energy SSCD plan. Gray-scale plot is BEV depth map of PTV. View is scaled to isocenter. Only two energies are used in the plan, though three energies were allowed. The outer ring segment is 16 MeV (yellow line) and the inner segment is 20 MeV (red line). (B) PBA calculated dose distribution for the hemisphere PTV using the three-energy SSCD plan. The PTV is the dotted contour; the 90% dose contour is in red.

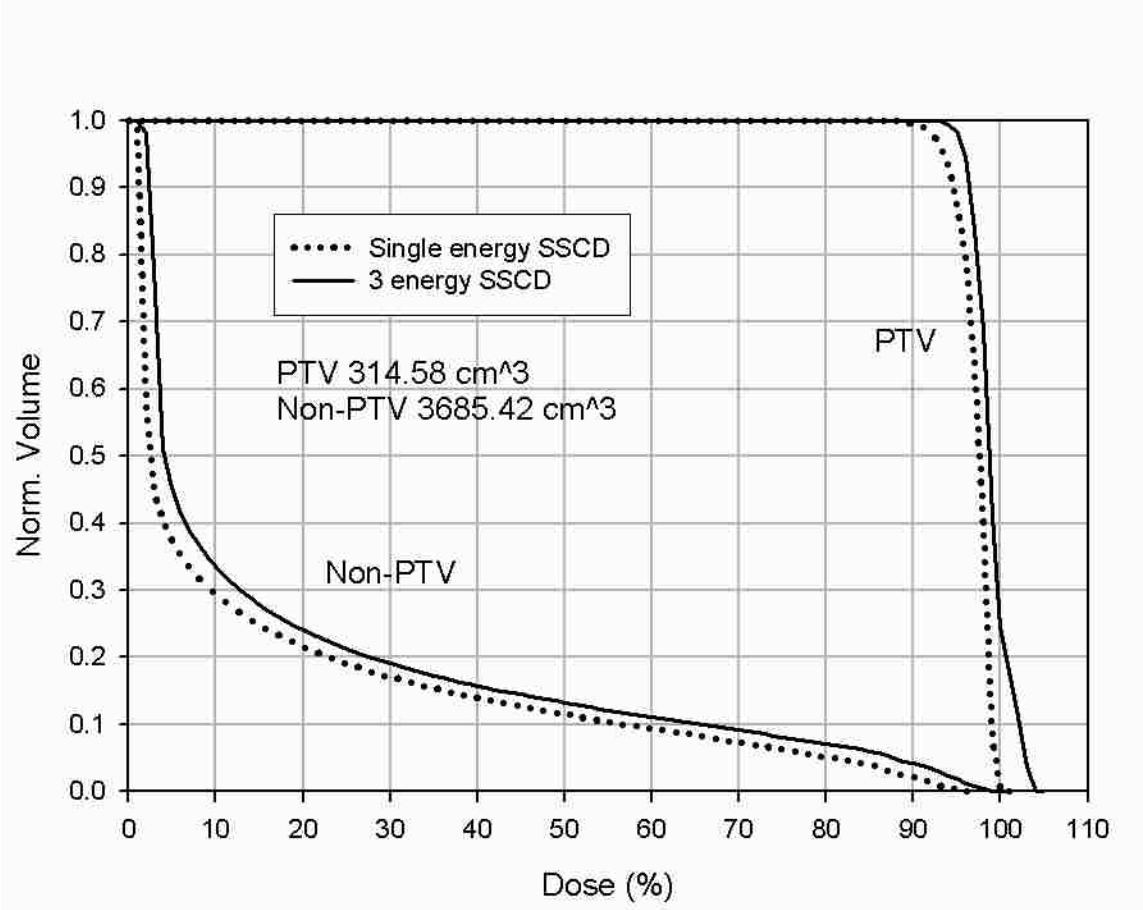

Figure 64: DVHs for the hemisphere PTV showing PTV and non-PTV ROIs. The single-energy SSCD plan is shown by the dotted lines and the three-energy SSCD plan by the solid lines.

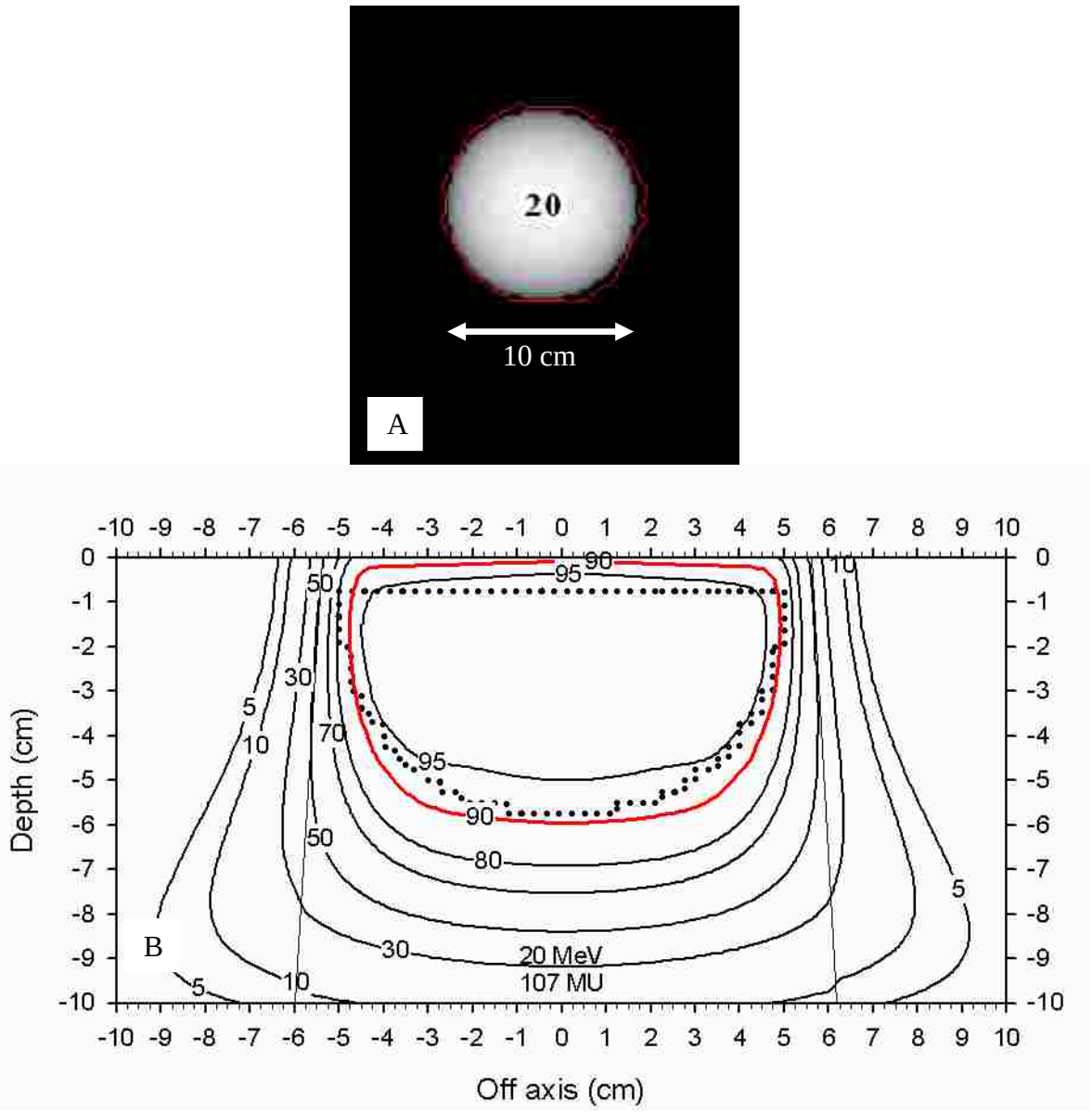

Figure 65: (A) Field segmentation after three optimization iterations for the hemisphere PTV using the single-energy VSCD plan. Gray-scale plot is BEV depth map of PTV. View is scaled to isocenter. A single 20 MeV segment (red line) is used. (B) PBA calculated dose distribution for the hemisphere PTV using the single-energy VSCD plan. The PTV is the dotted contour; the 90% dose contour is in red.

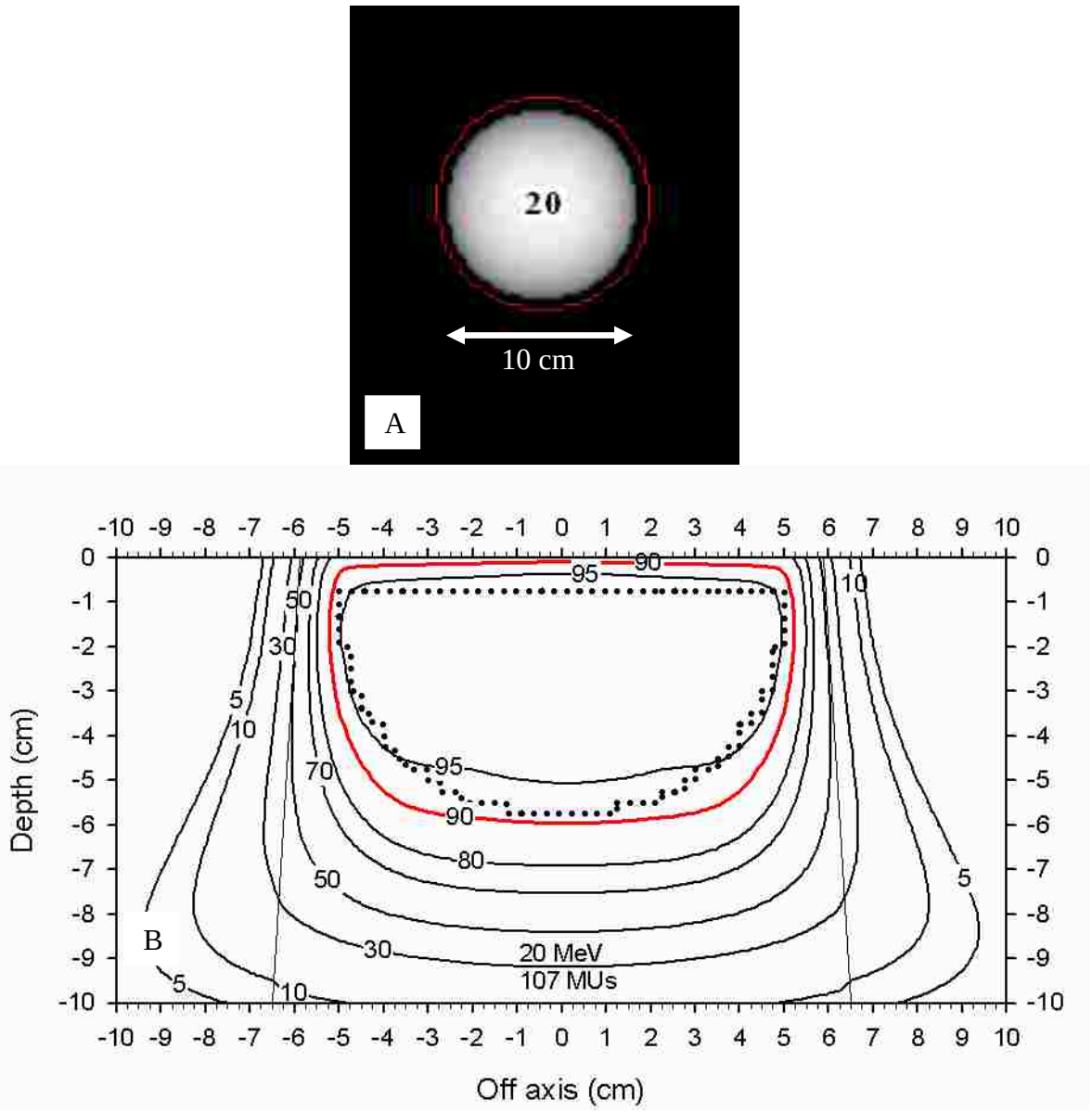

Figure 66: (A) Field segmentation after three optimization iterations for the hemisphere PTV using the two-energy VSCD plan. Gray-scale plot is BEV depth map of PTV. View is scaled to isocenter. Although two energies were allowed in the plan, a single 20 MeV segment (red line) is used. (B) PBA calculated dose distribution for the hemisphere PTV using the two-energy VSCD plan. The PTV is the dotted contour; the 90% dose contour is in red.

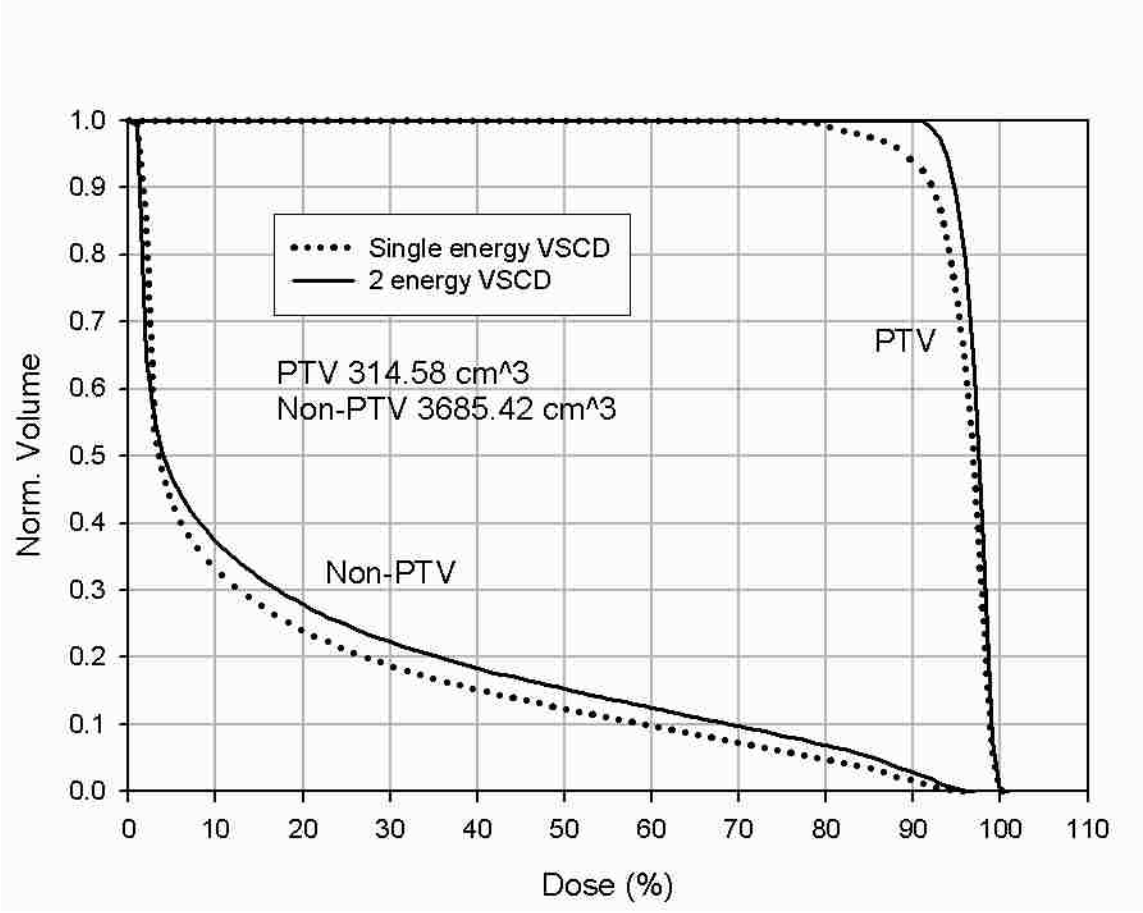

Figure 67: DVHs for the hemisphere PTV showing PTV and non-PTV ROIs. The single-energy VSCD plan is shown by the dotted lines and the two-energy VSCD plan by the solid lines.

Table 9: Summary of planning results for the hemisphere PTV.

		Conformity			Homogeneity				
Energies	SCD	CR	SR	CI	Min (%)	Max (%)	Max-Min (%)	Std. Dev. (%)	D_{90-10} (%)
1	SSCD	0.993	0.204	0.790	88.1	100.0	11.9	1.8	4.4
2	SSCD	1.000	0.342	0.658	91.0	100.0	9.0	1.4	3.4
3	SSCD	1.000	0.332	0.668	92.6	104.2	11.6	2.0	5.7
1	VSCD	0.937	0.170	0.778	71.7	100.0	28.3	3.6	6.6
2	VSCD	1.000	0.251	0.749	90.3	100.0	9.7	1.7	4.2
3	VSCD	1.000	0.288	0.712	93.6	103.4	9.8	1.7	4.5

the PTV. In the case of the three-energy SSCD plan, the 16 MeV segment edges are further away from the edge of the PTV than the edges of the 20 MeV segment used in single-energy SSCD plan and the scatter dose from the 16 MeV segments pushes the 90% isodose of the 20 MeV segment deeper, irradiating more non-PTV and increasing the SR. For the two-energy

VSCD plan, the 20 MeV segment replaces the 16 MeV segment, resulting in a larger 20 MeV segment than used in the single-energy SSCD plan, again increasing the SR. The three-energy SSCD plan was better than the two-energy SSCD plan; both plans had a CR of 1.000, but the three-energy SSCD plan had a better SR (0.332 versus 0.342) than the two-energy SSCD plan, making it more conformal (CI of 0.668 versus 0.658). The two-energy VSCD plan was more conformal (CI of 0.749 versus 0.712) than the three-energy VSCD plan, having a lower SR (0.251 versus 0.288) while both plans had a CR of 1.000.

The three-energy VSCD plan (2 energies used) was slightly more homogenous than the presented three-energy SSCD plan, evidenced by its reduced max-min (9.8% versus 11.6%), standard deviation (1.7% versus 2.0%), and D_{90-10} (4.5% versus 5.7%).

3.3.6 Two-Step Hemisphere PTV

The two-step hemisphere PTV did not have the vertical edges that made three-energy plans unnecessary for the two-step block PTV, and so three-energy plans were performed. However, the three-energy plans only used two energies in their final segmentation, and the two and three-energy plans were nearly identical for both SSCD and VSCD in this case, as opposed to the above cases, due to the still rather steep edges of the PTV. The steep edges caused the 9 MeV and 12 MeV segments to completely overlap the outer 6 MeV segments. This meant that a 6 MeV segment was not present after the combining of the pixel fields in Step 3A (illustrated in Figure 15) of the planning algorithm (Section 2.2.3), and thus Step 3B was not required, resulting in nearly identical field segmentations for the two- and three-energy plans. The resulting fields and dose distributions for the single-energy SSCD and two-energy SSCD plans are seen in Figure 68 and Figure 69, respectively, and the SSCD plans' DVHs are compared in Figure 70. Resulting fields and dose distributions for the single-energy VSCD and two-energy

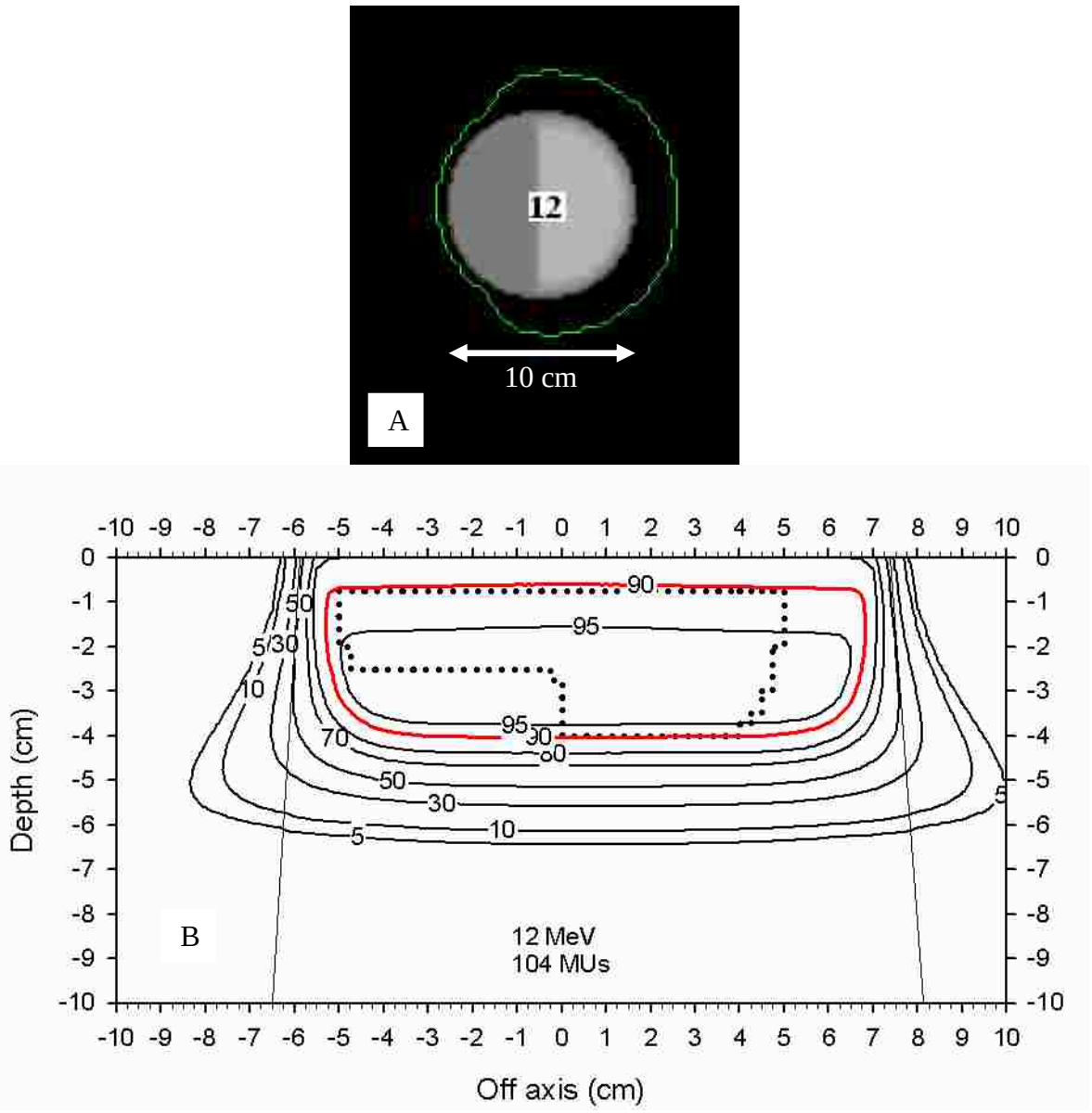

Figure 68: (A) Field segmentation after three optimization iterations for the two-step hemisphere PTV using the single-energy SSCD plan. Gray-scale plot is BEV depth map of PTV. View is scaled to isocenter. A single 12 MeV segment (green line) is used. (B) PBA calculated dose distribution for the two-step hemisphere PTV using the single-energy SSCD plan. The PTV is the dotted contour; the 90% dose contour is in red.

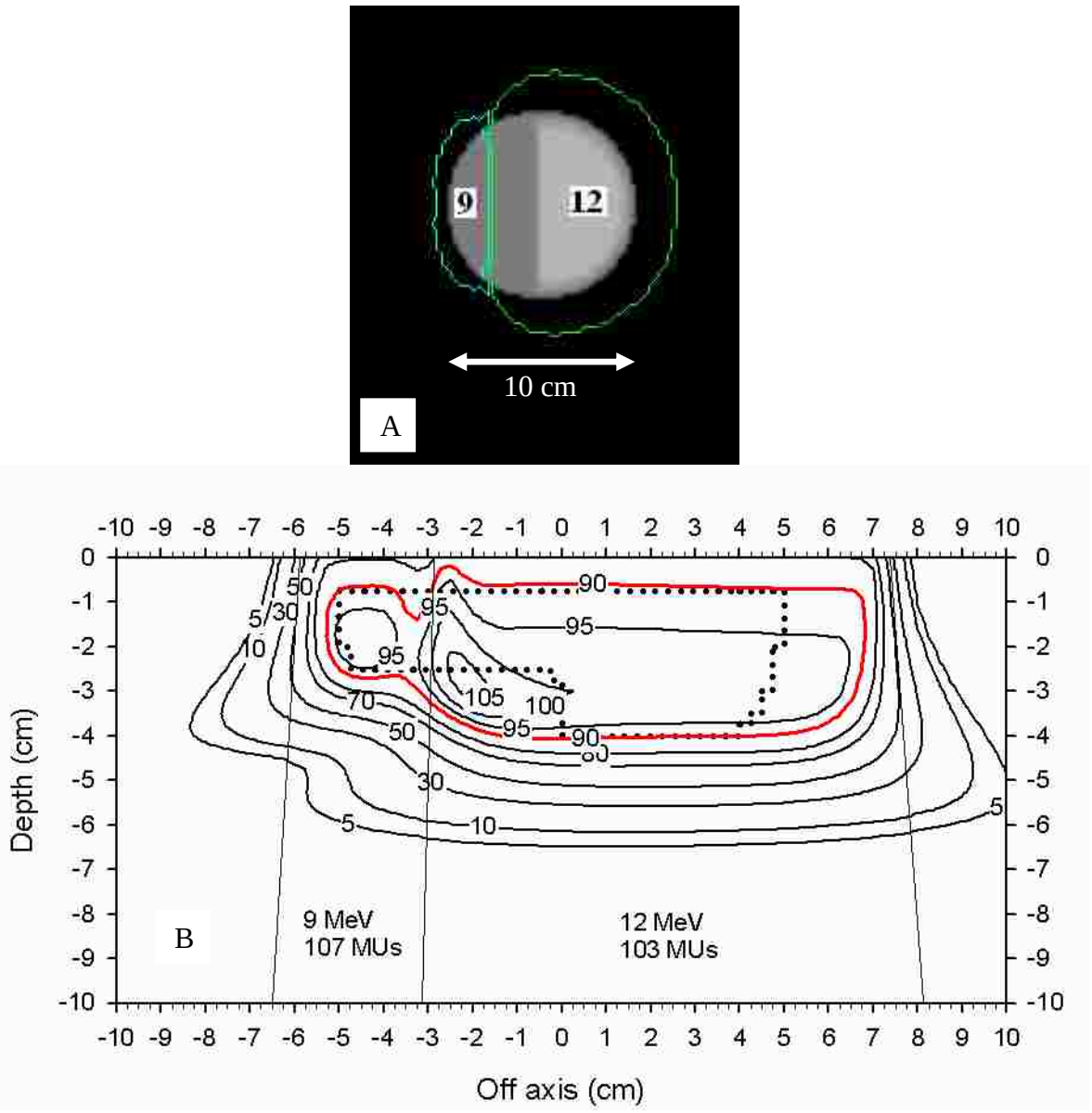

Figure 69: (A) Field segmentation after three optimization iterations for the two-step hemisphere PTV using the two-energy SSCD plan. Gray-scale plot is BEV depth map of PTV. View is scaled to isocenter. The left region is a 9 MeV segment (light-blue line) while the right region is a 12 MeV segment (green line). (B) PBA calculated dose distribution for the two-step hemisphere PTV using the two-energy SSCD plan. The PTV is the dotted contour; the 90% dose contour is in red.

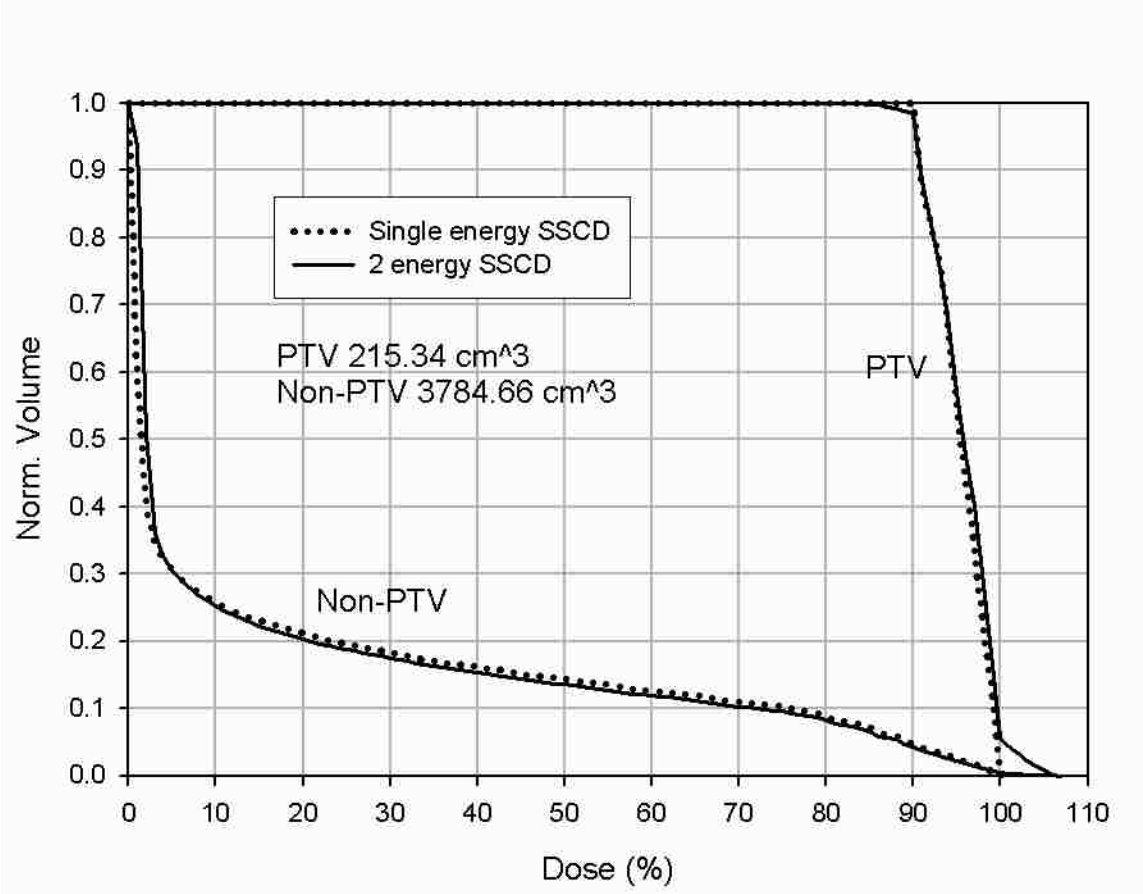

Figure 70: DVHs for the two-step hemisphere PTV showing PTV and non-PTV ROIs. The single-energy SSCD plan is shown by the dotted lines and the two-energy SSCD plan by the solid lines.

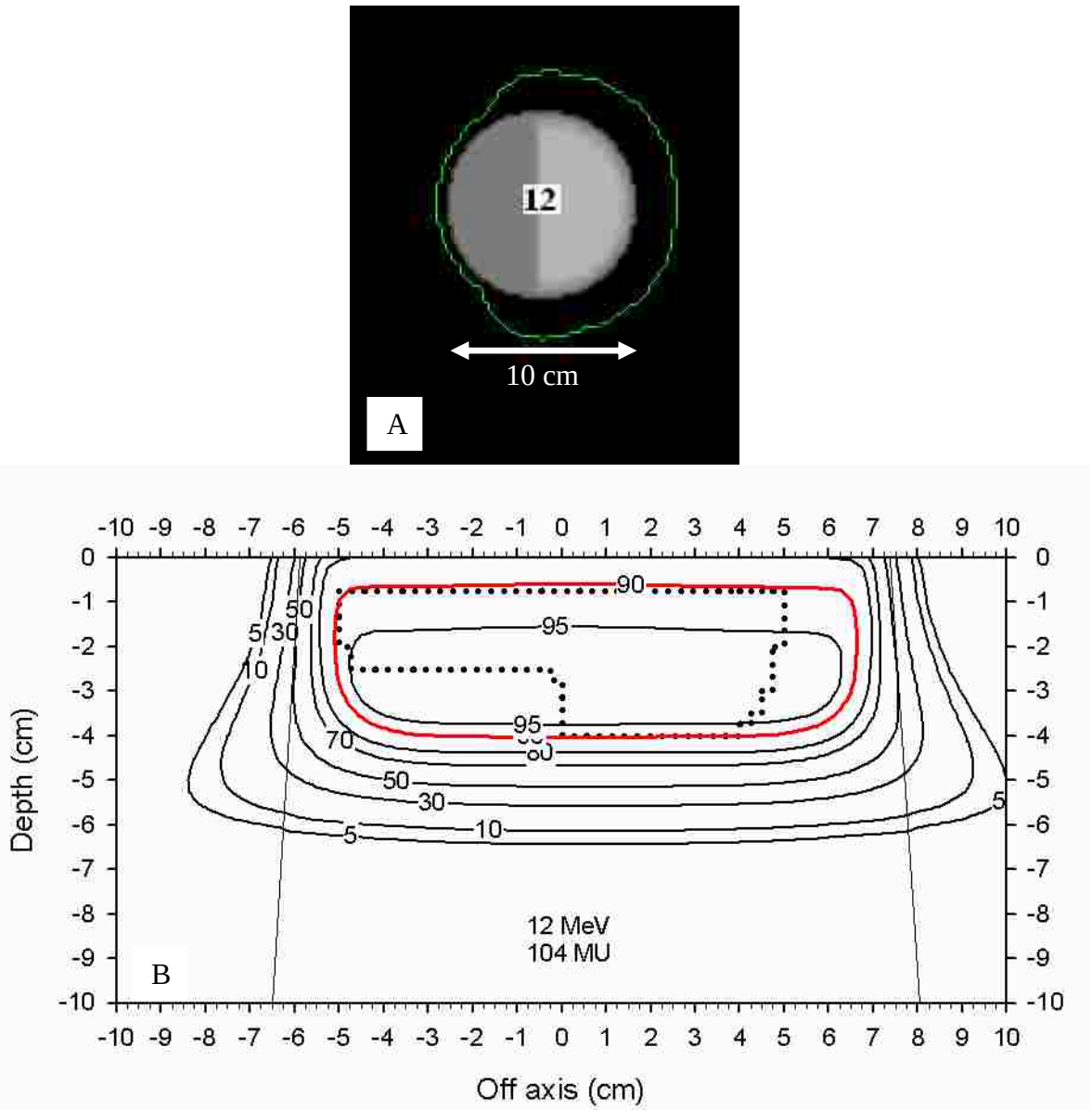

Figure 71: (A) Field segmentation after three optimization iterations for the two-step hemisphere PTV using the single-energy VSCD plan. Gray-scale plot is BEV depth map of PTV. View is scaled to isocenter. A single 12 MeV segment (green line) is used. (B) PBA calculated dose distribution for the two-step hemisphere PTV using the single-energy VSCD plan. The PTV is the dotted contour; the 90% dose contour is in red.

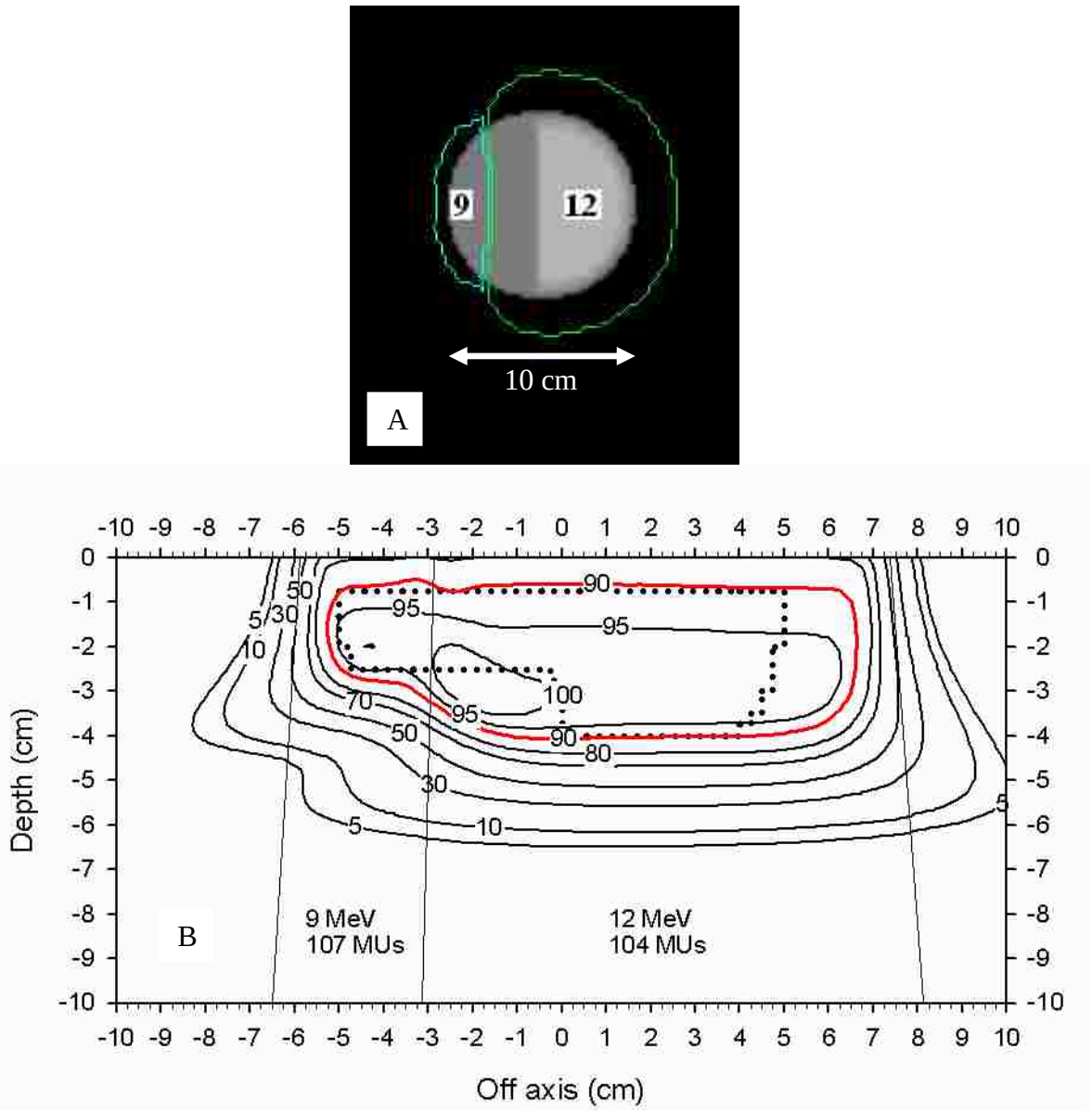

Figure 72: (A) Field segmentation after three optimization iterations for the two-step hemisphere PTV using the two-energy VSCD plan. Gray-scale plot is BEV depth map of PTV. View is scaled to isocenter. The left region is a 9 MeV segment (light-blue line) while the right region is a 12 MeV segment (green line). (B) PBA calculated dose distribution for the two-step hemisphere PTV using the two-energy VSCD plan. The PTV is the dotted contour; the 90% dose contour is in red.

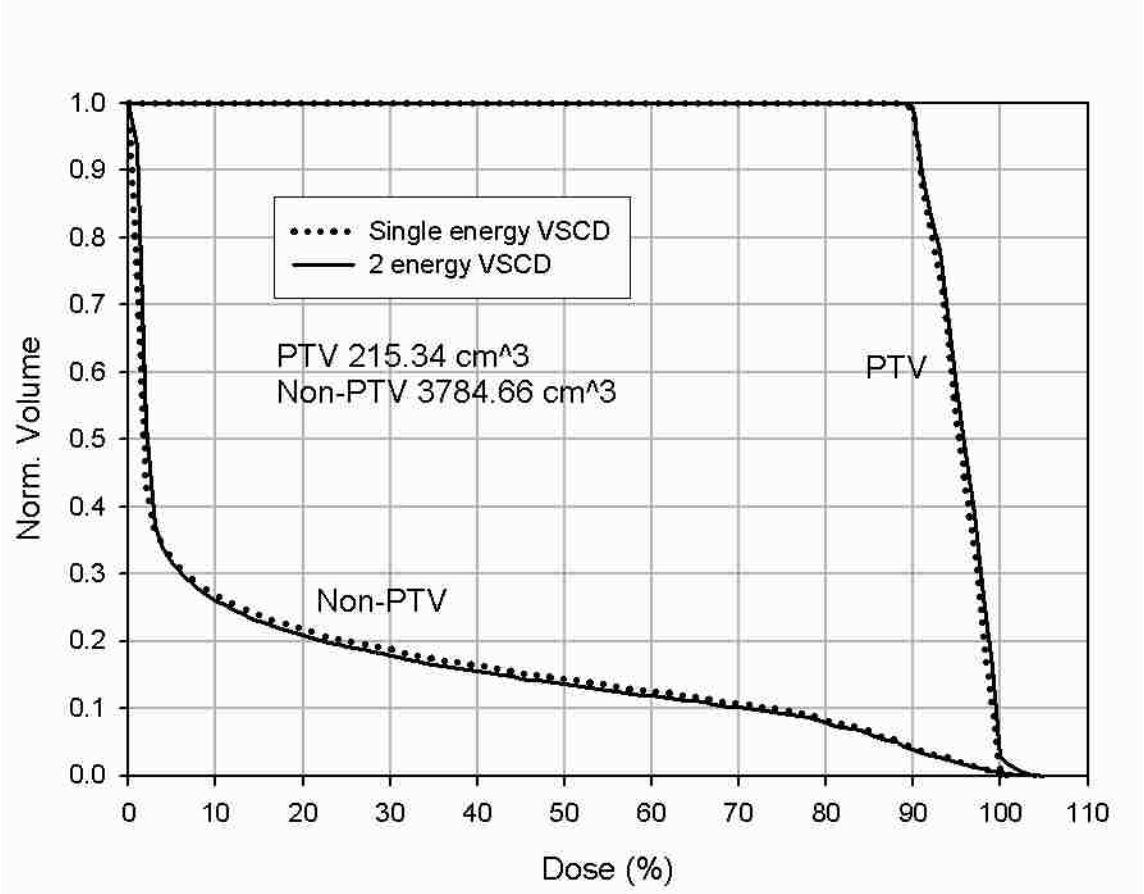

Figure 73: DVHs for the two-step hemisphere PTV showing PTV and non-PTV ROIs. The single-energy VSCD plan is shown by the dotted lines and the two-energy VSCD plan by the solid lines.

Table 10: Summary of planning results for the two-step hemisphere PTV.

		Conformity			Homogeneity				
Energies	SCD	CR	SR	CI	Min (%)	Max (%)	Max-Min (%)	Std. Dev. (%)	D_{90-10} (%)
1	SSCD	1.000	0.449	0.551	90.0	100.0	10.0	2.9	8.4
2	SSCD	0.984	0.428	0.563	83.5	106.5	23.0	3.4	8.8
3	SSCD	0.984	0.428	0.563	83.4	106.5	23.1	3.4	8.8
1	VSCD	0.993	0.424	0.572	87.1	100.0	12.9	2.9	8.6
2	VSCD	0.994	0.403	0.594	88.3	103.6	15.3	3.0	8.5
3	VSCD	0.994	0.403	0.594	88.3	103.6	15.3	3.0	8.5

VSCD plans are seen in Figure 71 and Figure 72, respectively, and the VSCD plans' DVHs are compared in Figure 73. The comparison metrics for all plans are listed in Table 10.

The two-energy SSCD plan had a reduced CR (0.984 versus 1.000) due to the proximal PTV surface being more shallow than the proximal 90% isodose contour of the 9 MeV segment,

had an improved SR (0.428 versus 0.449), and was more conformal (CI of 0.563 versus 0.551) compared to the single-energy SSCD plan. The two-energy VSCD plan had a slightly improved CR (0.994 versus 0.993), had an improved SR (0.403 versus 0.424), and was more conformal (CI of 0.594 versus 0.572) compared to the single-energy VSCD plan.

Similar to the two-step block PTV, the two-energy VSCD plan was only slightly more homogeneous than the two-energy SSCD plan due to the hot spot being located outside the PTV. This was indicated by the two-energy VSCD plan's reduced max-min (15.3% versus 23.0%) and only slightly reduced standard deviation (3.0% versus 3.4%) and $D_{90\text{-}10}$ (8.5% versus 8.8%) compared to the two-energy SSCD plan.

3.3.7 Summary of Planning Results

The results of the single-energy SSCD plan and the best SSCD plan are shown in Table 11 for all PTVs. The results of the single-energy VSCD plan and the best VSCD plan are shown in Table 12 for all PTVs. Also shown are the average change of the best multiple-energy plans compared to the single-energy plans for all PTVs excluding the hemispherical PTV. This was omitted due to its unique shape being so close to the 90% dose contour for the single 20 MeV beam.

In summary of the conformity statistics of the SSCD plans, the CR decreased 3.2% (σ=2.6%), due mostly to cold spots at the abutment edges extending into the PTVs. The 7.6% (σ=5.1%) decrease in the non-PTV treated to 90%, along with the visually more conformal 90% isodose contours, indicated that the planning algorithm was successful in reducing the non-PTV treated. With the exception of the hemispherical PTV, the multiple-energy plans had better sparing of non-PTV. Overall, there was a 3.5% (σ=3.0%) increase in CI, supporting the hypothesis that conformity will increase as multiple energies are allowed.

Table 11: Summary of SSCD planning results for the six hypothetical PTVs.

SSCD Plans							
		Conformity			Homogeneity		
PTV	Energies	CR	SR	CI	Max-Min (%)	Std. Dev. (%)	D_{90-10} (%)
2-step block	1	0.998	0.521	0.478	12.0	2.9	8.3
2-step block	2	0.969	0.510	0.475	24.3	3.5	8.8
Change		-2.9%	-2.1%	-0.6%	+102.5%	+20.7%	+6.0%
Wedge	1	0.996	0.493	0.505	16.9	1.6	3.7
Wedge	3	0.992	0.455	0.540	19.2	3.0	8.1
Change		-0.4%	-7.7%	+6.9%	+13.6%	+87.5%	+118.9%
Pentagon	1	0.998	0.389	0.609	12.3	1.5	3.6
Pentagon	2	0.959	0.328	0.645	26.8	4.4	12.0
Change		-3.9%	-15.7%	+5.9%	+117.9%	+193.3%	+233.3%
Inv. well	1	0.999	0.587	0.412	12.4	1.6	3.6
Inv. well	3	0.928	0.542	0.425	25.0	4.7	12.9
Change		-7.1%	-7.7%	+3.2%	+101.6%	+193.8%	+258.3%
2-step hemi	1	1.000	0.449	0.551	10.0	2.9	8.4
2-step hemi	2	0.984	0.428	0.562	23.0	3.4	8.8
Change		-1.6%	-4.7%	+2.0%	+130.0%	+17.2%	+4.8%
Average Change ± σ		-3.2% ±2.6	-7.6% ±5.1	+3.5% ±3.0	+93.1% ±46.0	+102.5% ±87.7	+124.3% ±120.6
Hemisphere	1	0.993	0.204	0.790	11.9	1.8	4.4
Hemisphere	3	1.000	0.332	0.668	11.6	2.0	5.7
Change		+0.7%	+62.7%	-15.4%	-2.5%	+11.1%	+29.5%

In summary of the conformity statistics of the VSCD plans, the slightly increased CR of 0.5% (σ=1.1%), due to the reduction of cold spots at the abutment edges, was not as statistically significant as the decrease seen in the SSCD plans. The 15% (σ=11%) decrease in the non-PTV treated to 90% indicated that using the VSCD method was slightly more effective than the SSCD method in reducing the non-PTV treated. The improved CR and SR combined to give a 14.3% (σ=11.3%) increase in CI, again supporting the hypothesis that conformity will increase as multiple energies are allowed and indicating that the VSCD method should be used if available.

Dose homogeneity decreased for the multi-energy plans compared to the single-energy plans, for both the SSCD and VSCD plans. As expected from the results of Richert *et. al.* (2007), the VSCD method reduced hot and cold spots at the abutment edges, resulting in

Table 12: Summary of VSCD planning results for the six hypothetical PTVs.

VSCD Plans							
		Conformity			Homogeneity		
PTV	Energies	CR	SR	CI	Max-Min (%)	Std. Dev. (%)	D_{90-10} (%)
2-step block	1	0.993	0.502	0.494	13.2	2.9	8.5
2-step block	2	0.985	0.494	0.498	14.4	3.1	8.6
Change		-0.8%	-1.6%	+0.8%	+8.7%	+4.4%	+1.1%
Wedge	1	0.983	0.486	0.505	16.1	2.0	4.5
Wedge	3	0.999	0.383	0.616	15.4	2.4	6.5
Change		+1.6%	-21.2%	+22.0%	-4.8%	+21.4%	+42.5%
Pentagon	1	0.981	0.382	0.606	12.4	1.9	4.4
Pentagon	2	0.997	0.280	0.719	20.5	2.3	6.1
Change		+1.6%	-26.9%	+18.6%	+65.4%	+22.3%	+37.2%
Inv. well	1	1.000	0.565	0.435	10.1	1.6	3.8
Inv. well	3	0.997	0.450	0.548	18.3	2.8	7.4
Change		-0.3%	-20.4%	+26.2%	+81.7%	+79.6%	+97.8%
2-step hemi	1	0.993	0.424	0.572	12.9	2.9	8.6
2-step hemi	2	0.994	0.403	0.594	15.3	3.0	8.5
Change		+0.1%	-5.0%	+3.8%	+18.6%	+3.7%	-0.9%
Average Change ± σ		+0.5% ±1.1	-15.0% ±11.0	+14.3% ±11.3	+33.9% ±37.6	+26.3% ±31.1	+35.5% ±40.1
Hemisphere	1	0.937	0.170	0.778	28.3	3.6	6.6
Hemisphere	2	1.000	0.251	0.749	9.7	1.7	4.2
Change		+6.7%	+48.1%	-3.8%	-65.8%	-53.6%	-36.8%

improved, compared to multi-energy SSCD plans: max-min, 33.9% (σ=37.6%) versus 93.1% (σ=46.0%), standard deviation of dose within the PTV, 26.3% (σ=31.1%) versus 102.5% (σ=87.7%), and D_{90-10}, 35.5% (σ=40.1%) versus 124.3% (σ=120.6%). This improved dose homogeneity further indicates that the VSCD method should be used if available.

The planning algorithm effectively defined the outer edges of the segmentation in order to cause the 90% isodose to barely encompass the edges of the PTV; this was due to the optimization in Step 5 (Section 2.2.5), despite the use of a parallel beam to create the BEV depth map in Step 1 (Section 2.2.1). This was best exemplified by comparing the outer field edges on the central slice of the single-energy SSCD plan of the wedge (Figure 44B) PTV. The distal depth of the positive off-axis outer edge (+5 cm off-axis) of the wedge PTV is 2.7 cm (Figure

18) with an outer field edge at +5.375-cm off-axis, 0.375 cm past the edge of the PTV. The distal depth of the negative off-axis outer edge (-5 cm off-axis) of the wedge PTV is 5.5 cm with an outer field edge at -7.625-cm off-axis, 2.625 cm past the edge of the PTV. The algorithm adjusted the positive and negative off-axis field edges independently, pulling the 90% isodose line up to the PTV off-axis edges, as seen in Figure 44B.

As discussed in results of the pentagon PTV (Section 3.3.3), the planning algorithm handled segments that are too small by merging them with the segments of the next highest adjacent energy in Step 3 (Section 2.2.3). The result of this was that three-energy plans using only two energies did not converge to the same segmentation as two-energy plans. In other words, different starting points led to different end points even though the same energies were used in the end points. It was hypothesized that perhaps it would be better to deal with small segments by returning to Step 2 (Section 2.2.2) and merge the offending energy's segmentation with that of the next highest adjacent energy and then repeat Step 3, which would cause the three-energy plan to converge to the same solution as the two-energy plan. However, this approach would only be better if the two-energy plans always outperformed the three-energy plans that use two energies. While this was the case with the pentagon PTV, in the case of the inverted-well PTV the three-energy plans using two energies had lower SIs than the two-energy plans (0.542 versus 0.552 for SSCD, 0.450 versus 0.467 for VSCD). This indicated that there is some merit in allowing the different starting points to come to different ends.

3.4 Aim 4: Demonstrate Use of Algorithm on Patient Data

The results of the plans developed using the patient cases are presented. The SFECT optimization algorithm was used to create plans using 1, 2, and 3 energies for the SSCD and VSCD methods. The planning algorithm was allowed to run for 3 optimization iterations after the initial field segmentation. The plans (field segmentation, segment weights) were exported to

the Pinnacle v7.4f treatment planning system, where the dose was calculated using a heterogeneous pencil beam calculation with the same size dose grid in the same location for all plans.

3.4.1 Patient Case A

The prescription point of the single-energy SSCD and VSCD plans was placed at a depth of about 3.43 cm (R_{100} of an open 16 MeV beam) along the beam's superior-inferior axis of slice 84. The prescription point for the three-energy SSCD plan was placed at a depth of about 3 cm +2.5 cm off-axis of slice 72. The three-energy VSCD plan was similar to the three-energy SSCD plan and so used the same prescription point. The prescription of all plans was set to deliver 51.25 Gy (the original plan's prescription point dose) to the plan's prescription point, delivering 46.12 Gy to the 90% isodose contour.

The plans for the single-energy and three-energy SSCD and VSCD plans are presented. The field segmentations of the presented plans, along with the locations of the shown CT slices, are shown in Figure 74 for the SSCD plans and Figure 79 for the VSCD plans. The dose distributions of slices 52, 72, and 92 are presented in Figure 75-Figure 77 and Figure 80- Figure 82 for the SSCD and VSCD plans, respectively. DVHs of the presented plans are shown in Figure 78 for the SSCD plans and Figure 83 for the VSCD plans. Table 13 contains the statistics of all the patient plans, including the two-energy plans, which were not discussed in detail.

In summary of the SSCD plans, the DVH in Figure 78 shows that the three-energy plan covered the PTV as well as the single-energy plan, confirmed by its slightly increased CR compared to that of the single-energy plan (0.975 versus 0.973), but had greater dose heterogeneity due to abutting fields of different energies. Both plans kept the spinal cord well under tolerance dose (4500 cGy) with the three-energy plan treating much of the spinal cord to less dose. The three-energy plan treated the vocal cord and middle ear to less dose than the

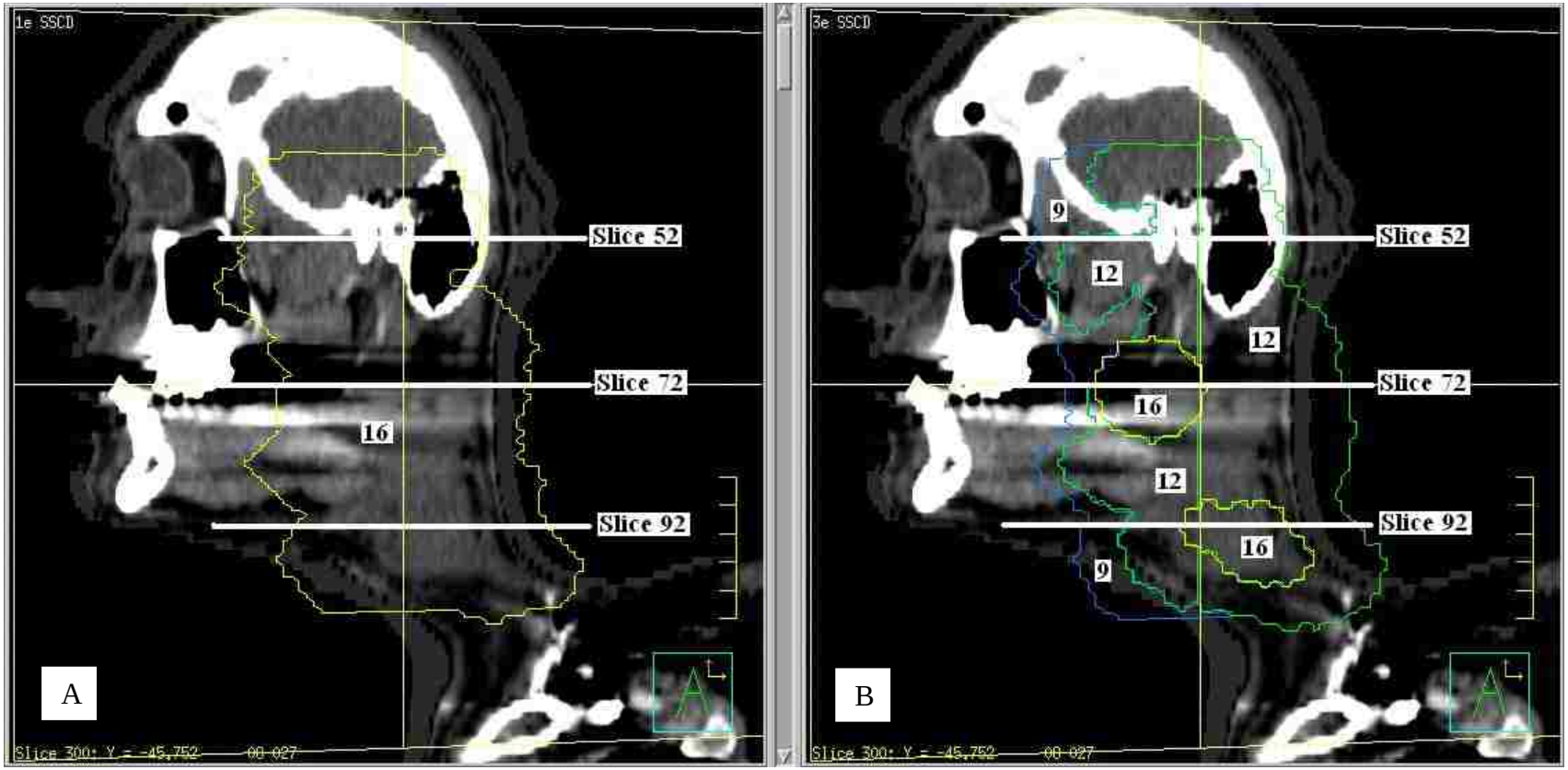

Figure 74: Coronal plane of patient A in the "open neck" treatment position at 2 cm depth, showing the field segmentation for (A) the single-energy SSCD plan and (B) the three-energy SSCD plan. The locations of slices 52, 72, and 92 (z= 3, 8, and 11 cm) are indicated. A BEV of the field segmentation is shown. The single-energy SSCD plan uses a single 16 MeV segment. The three-energy SSCD plan uses a single 9 MeV segment, a single 12 MeV segment, and two 16 MeV segments.

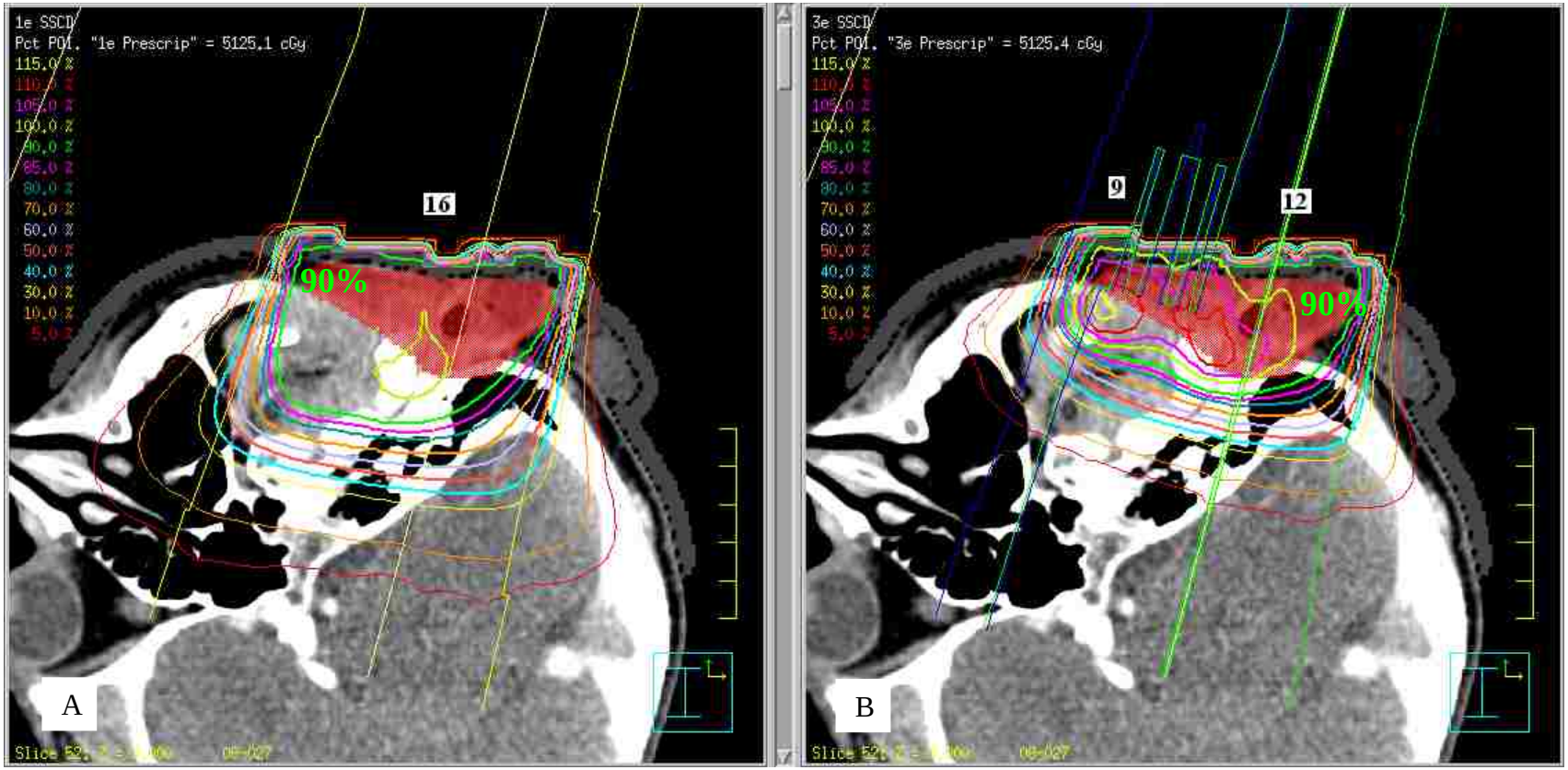

Figure 75: Patient A. Isodose contours in slice 52 for (A) the single-energy SSCD plan and (B) the three-energy SSCD plan. The PTV is shaded red. The 90% dose line is in bright green.

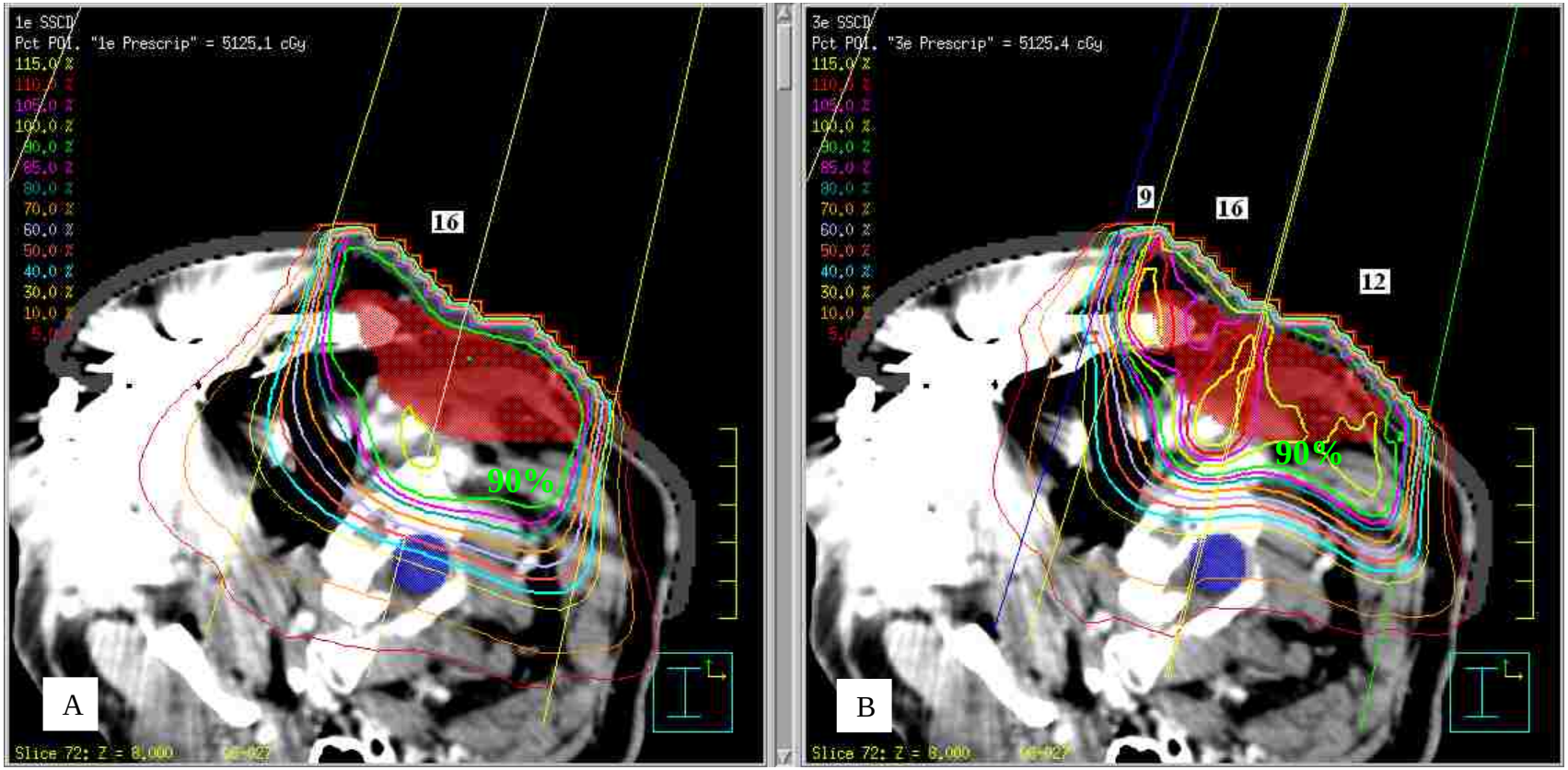

Figure 76: Patient A. Isodose contours in slice 72 for (A) the single-energy SSCD plan and (B) the three-energy SSCD plan. The PTV is shaded red and the spinal cord is dark blue. The 90% dose line is in bright green.

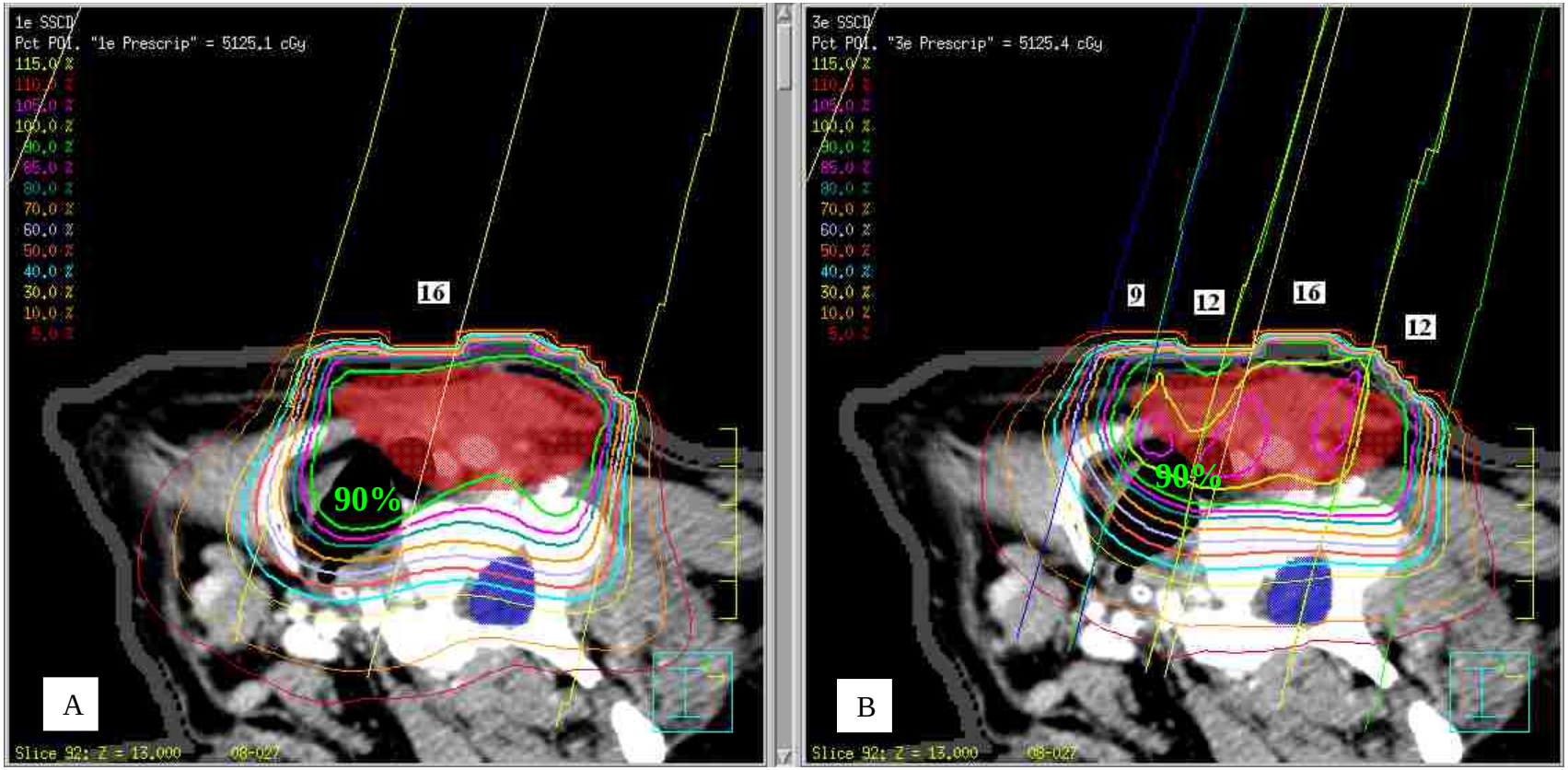

Figure 77: Patient A. Isodose contours in slice 92 for (A) the single-energy SSCD plan and (B) the three-energy SSCD plan. The PTV is shaded red and the spinal cord is dark blue. The 90% dose line is in bright green.

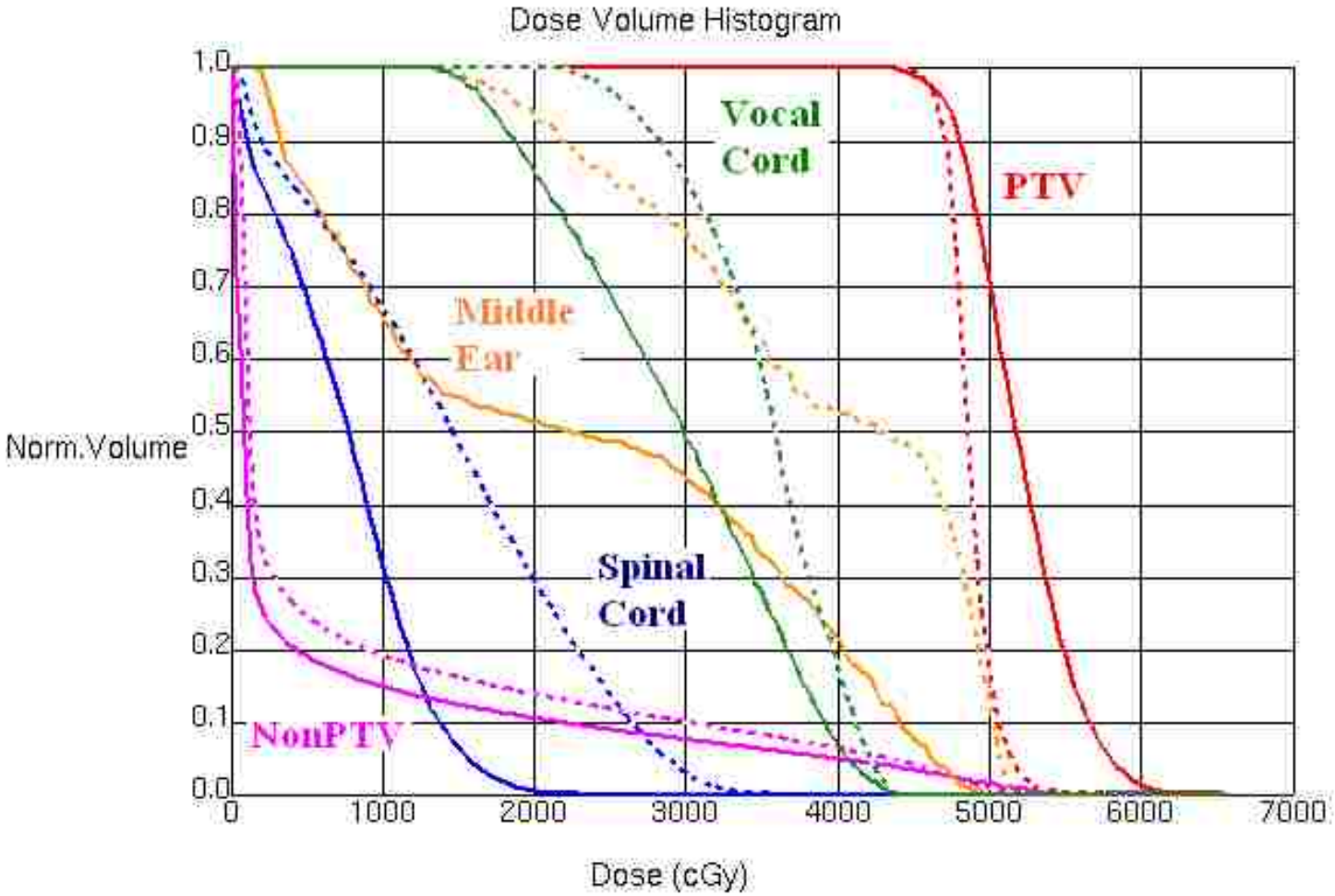

Figure 78: Patient A. Cumulative DVHs for the single-energy SSCD plan (dashed lines) and three-energy SSCD plan (solid lines). Dose to the PTV (red), non-PTV (fuchsia), spinal cord (dark blue), middle left ear (orange), and vocal cord (green) are shown.

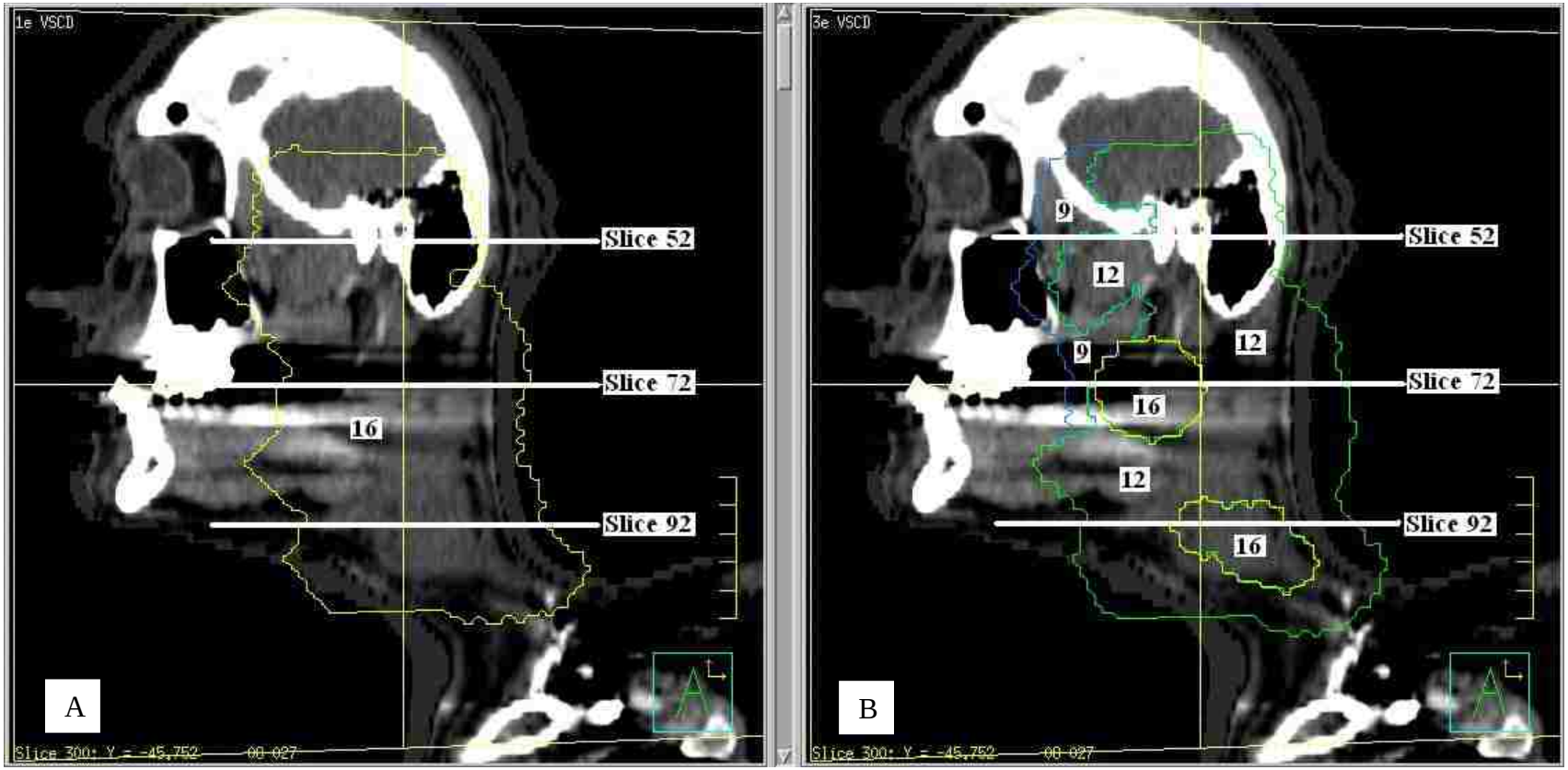

Figure 79: Coronal plane of patient A in the "open neck" treatment position at 2 cm depth, showing the field segmentation for (A) the single-energy VSCD plan and (B) the three-energy VSCD plan The locations of slices 52, 72, and 92 (z= 3, 8, and 11 cm) are indicated. A BEV of the field segmentation is shown. The single-energy VSCD plan uses a single 16 MeV segment. The three-energy VSCD plan uses a single 9 MeV segment, a single 12 MeV segment, and two 16 MeV segments.

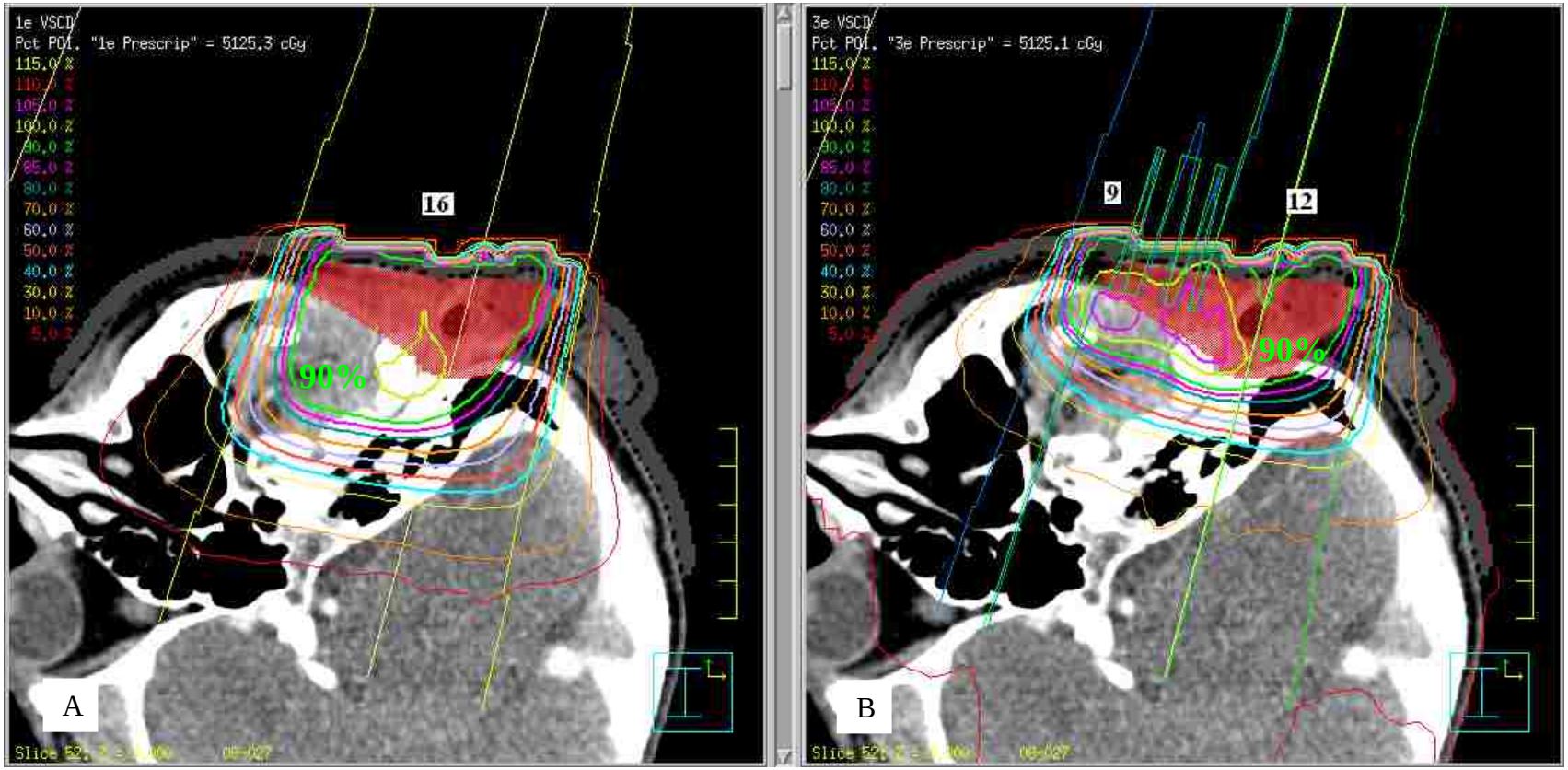

Figure 80: Patient A. Isodose contours in slice 52 for (A) the single-energy VSCD plan and (B) the three-energy VSCD plan. The PTV is shaded red. The 90% dose line is in bright green.

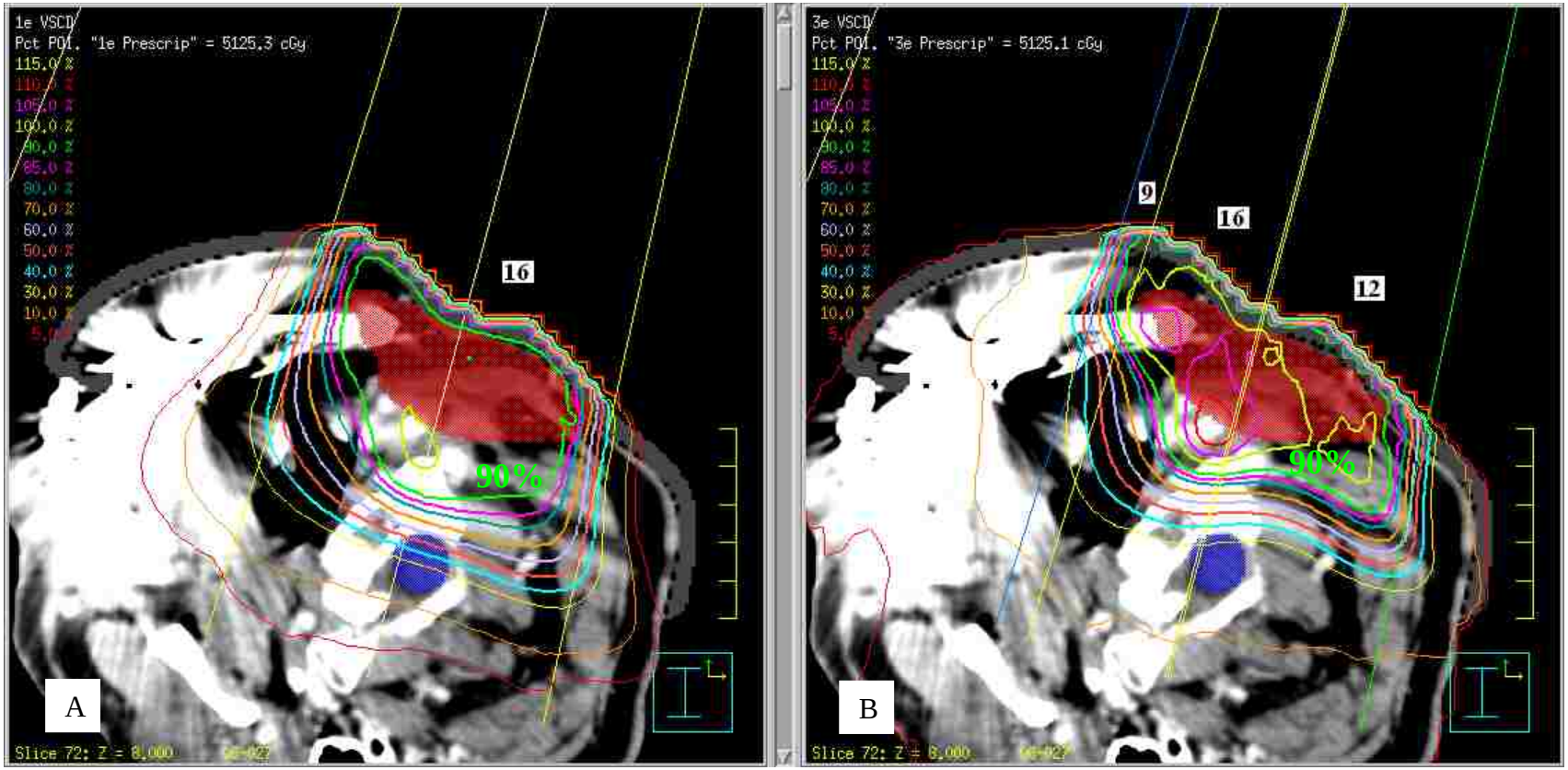

Figure 81: Patient A. Isodose contours in slice 72 for (A) the single-energy VSCD plan and (B) the three-energy VSCD plan. The PTV is shaded red and the spinal cord is dark blue. The 90% dose line is in bright green.

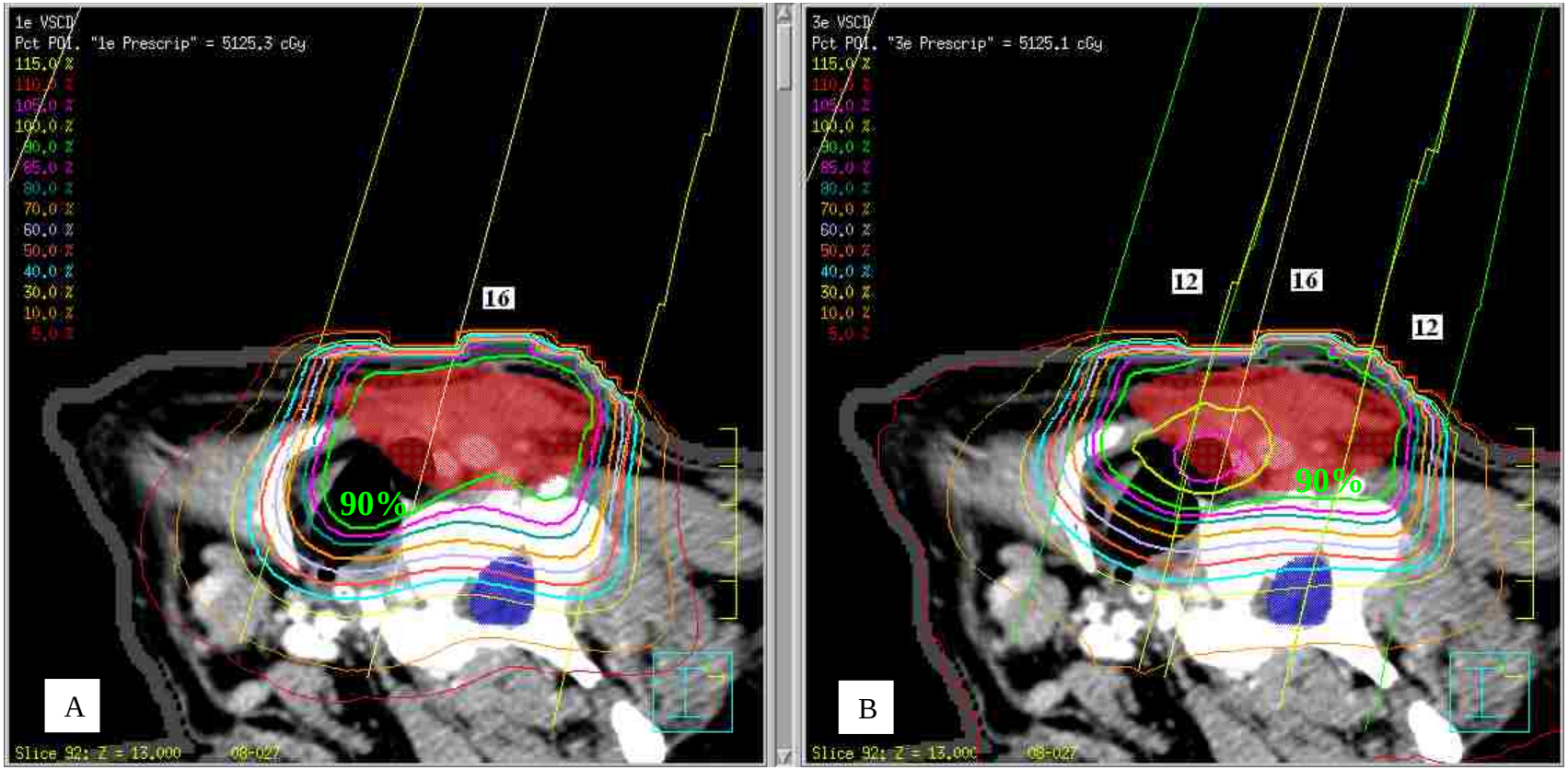

Figure 82: Patient A. Isodose contours in slice 92 for (A) the single-energy VSCD plan and (B) the three-energy VSCD plan. The PTV is shaded red and the spinal cord is dark blue. The 90% dose line is in bright green.

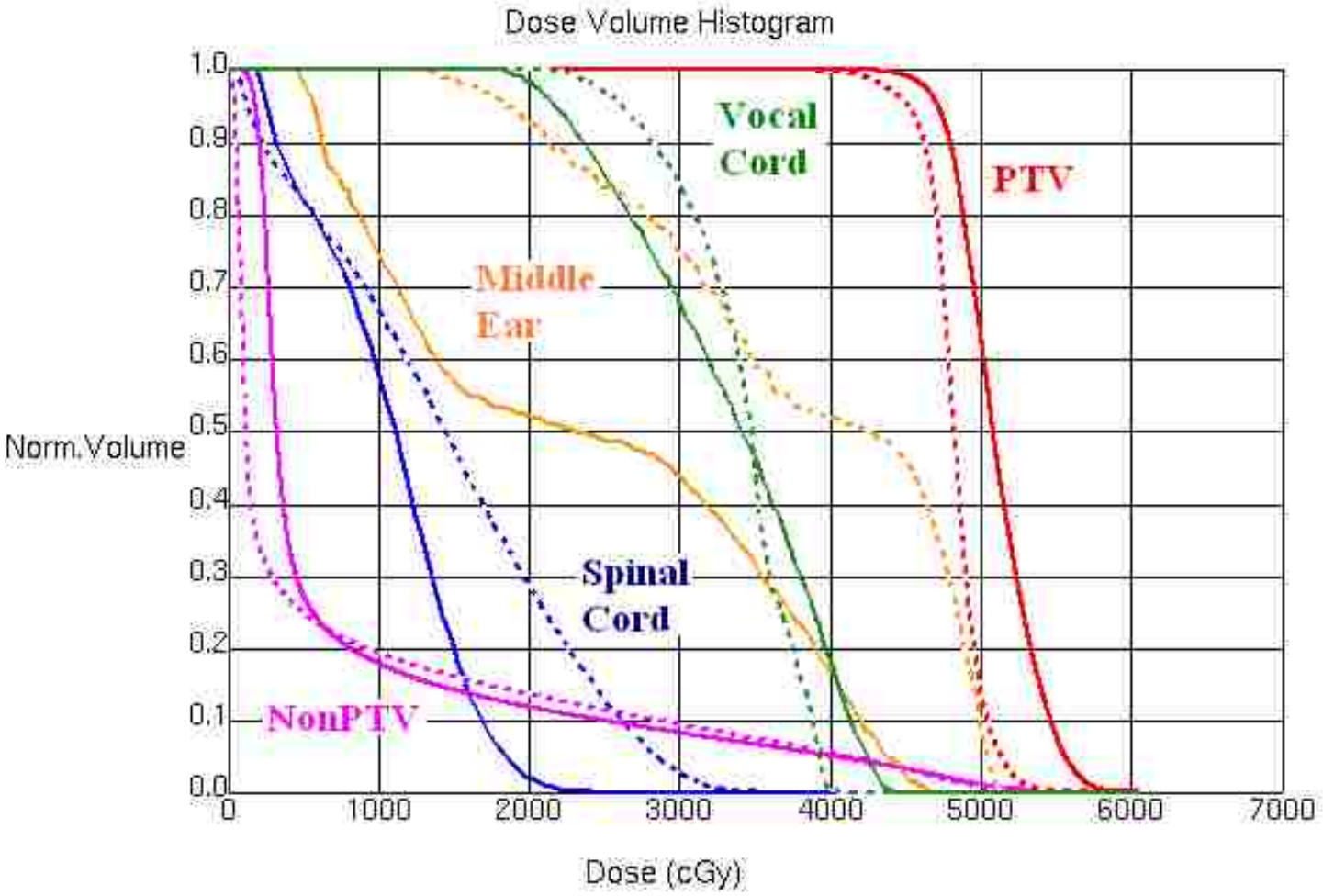

Figure 83: Patient A. Cumulative DVHs for the single-energy VSCD plan (dashed lines) and three-energy VSCD plan (solid lines). Dose to the PTV (red), non-PTV (fuchsia), spinal cord (dark blue), middle left ear (orange), and vocal cord (green) are shown.

Table 13: Summary of planning results for patient case A.

Plan	Dose at Prescription Point (cGy)	Min (%)	Max (%)	Max-Min (%)	Std. Dev. (%)	D_{90-10}	CR	SR	CI
1 SSCD	5125.1	73.3	112.4	39.1	3.0	6.9	0.973	0.448	0.538
2 SSCD	5124.8	73.8	123.6	49.8	4.3	9.9	0.970	0.469	0.515
3 SSCD	5125.4	72.6	126.8	54.1	6.5	16.5	0.975	0.410	0.575
1 VSCD	5125.3	61.6	112.4	50.8	3.8	8.3	0.907	0.393	0.550
2 VSCD	5124.6	73.8	112.4	38.5	3.4	8.0	0.961	0.417	0.560
3 VSCD	5125.1	76.1	117.8	41.7	5.1	13.0	0.978	0.389	0.597

single-energy plan. The three-energy plan also treated non-PTV (defined in Section 2.4.2.2) to less dose, reflected by its reduced SR compared to that of the single-energy plan (0.410 versus 0.448) and seen by the isodose contours in Figure 75-Figure 77. Overall, the three-energy plan was more conformal than the single-energy plan, indicated by its improved CI compared to that of the single-energy plan (0.575 versus 0.538), supporting the hypothesis and indicating that the planning algorithm has the potential to plan SFECT treatments for patient cases.

In summary of the VSCD plans, the DVH in Figure 83 shows that the three-energy plan covered the PTV better than the single-energy plan, confirmed by its better CR compared to that of the single-energy plan (0.978 versus 0.907), but also had greater dose heterogeneity due to abutting fields of different energies. Both plans kept the spinal cord under tolerance, while the three-energy plan treated much less of the cord in the 5-35 Gy region. The three-energy plan treated less of the vocal cord in the 20-35 Gy region than the single-energy SSCD plan, but more in the 35-45 Gy region. The three-energy plan treated the middle ear to less dose than the single-energy plan. The three-energy plan treated more non-PTV than the single-energy plan in the low dose 0-6 Gy region, but less non-PTV in the 6-50 Gy region, seen also by its slightly reduced SR compared to that of the single-energy plan (0.389 versus 0.393). The three-energy plan was more conformal than the single-energy plan, seen by the isodose contours in Figure 80- Figure 82 and by its improved CI compared to that of the single-energy plan (0.597 versus 0.550),

supporting the hypothesis and indicating that the planning algorithm has the potential to plan SFECT treatments for patient cases.

Expected from the results of Richert *et. al.* (2007) and the hypothetical PTVs, the dose homogeneity improved by using the VSCD method. Compared to the three-energy SSCD plan, the three-energy VSCD plan had a smaller max-min dose (41.7% versus 54.1%), standard deviation of dose within the PTV (5.1% versus 6.5%), and $D_{90\text{-}10}$ (13% versus 16.5%). The three-energy VSCD plan was also more conformal than the three-energy SSCD plan (CI of 0.597 versus 0.575), further reinforcing that the VSCD method should be used if available.

3.4.2 Patient Case B

The three-energy SSCD and VSCD plans were similar, using a single 12 MeV segment, a single 16 MeV segment, and two circular 20 MeV segments. All of the plans had a reasonably sized 20 MeV segment in about the same location; therefore all of the plans used the same prescription point, placed along the superior-inferior axis of slice 61 (near the center of the superior 20 MeV segment of the three-energy plans) at a depth of 2.03 cm (R_{100} of an open 20 MeV beam). The prescription of all plans was set to deliver 66.67 Gy to the prescription point, delivering 60 Gy (the original IMRT plan's prescription dose) to the 90% isodose contour.

The plans for the single-energy and three-energy SSCD and VSCD plans are presented. The field segmentations of the presented plans, along with the locations of the shown CT slices, are shown in Figure 84 for the SSCD plans and Figure 89 for the VSCD plans. The dose distributions of slices 61, 73, and 85 are presented in Figure 85-Figure 87 and Figure 90- Figure 92 for the SSCD and VSCD plans, respectively. DVHs of the presented plans are shown in Figure 88 for the SSCD plans and Figure 93 for the VSCD plans. Table 14 contains the statistics of all the patient plans, including the two-energy plans, which were not discussed in detail.

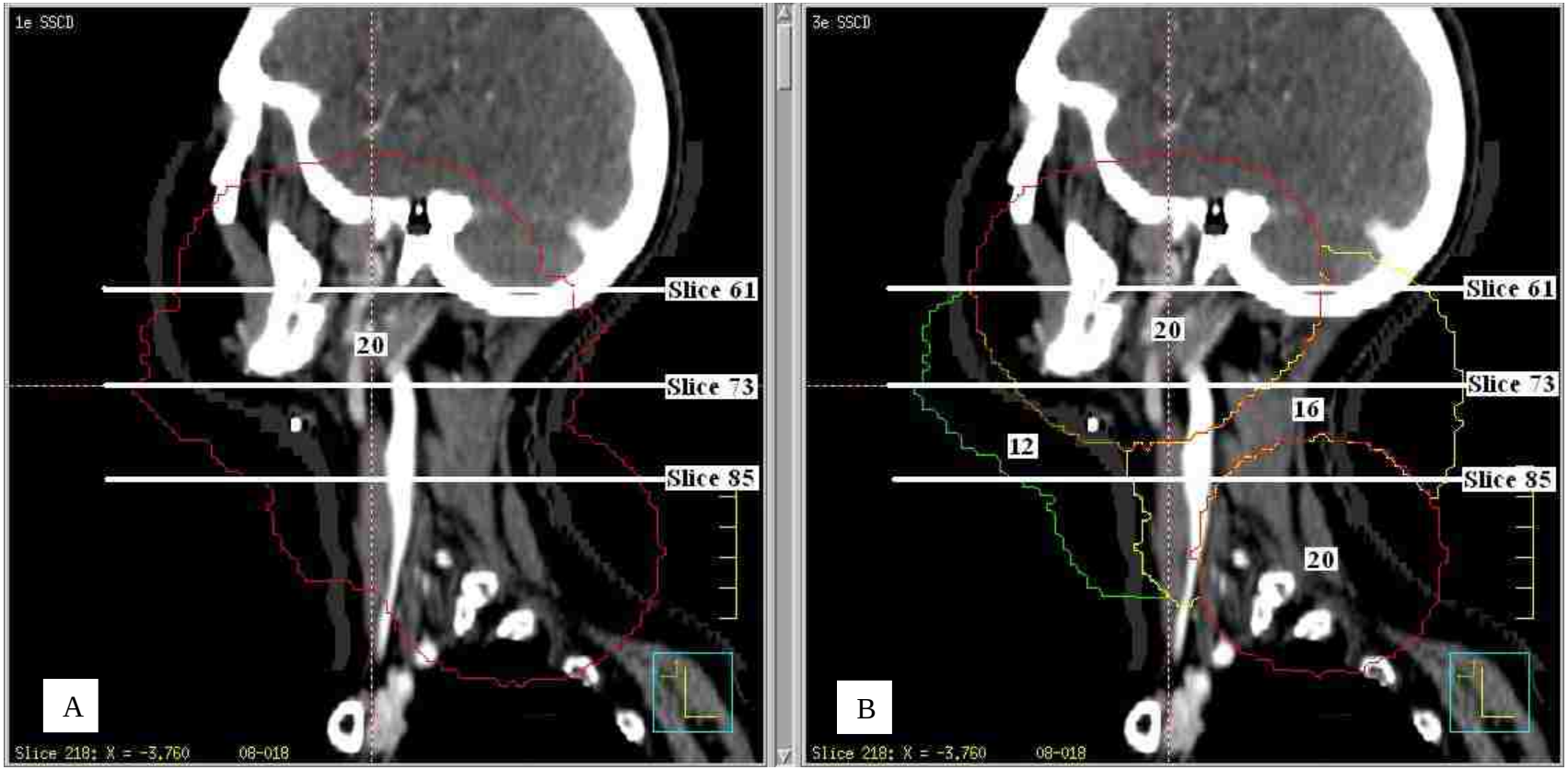

Figure 84: Sagittal plane of patient B at 2 cm depth, showing the field segmentation for (A) the single-energy SSCD plan and (B) the three-energy SSCD plan. The locations of slices 61, 73, and 85 (z= -7.15, -4.15, and -1.15) are indicated. A BEV of the field segmentation is shown. The single-energy SSCD plan uses a single 20 MeV segment. The three-energy SSCD plan uses a single 12 MeV segment, a single 16 MeV segment, and two 20 MeV segments.

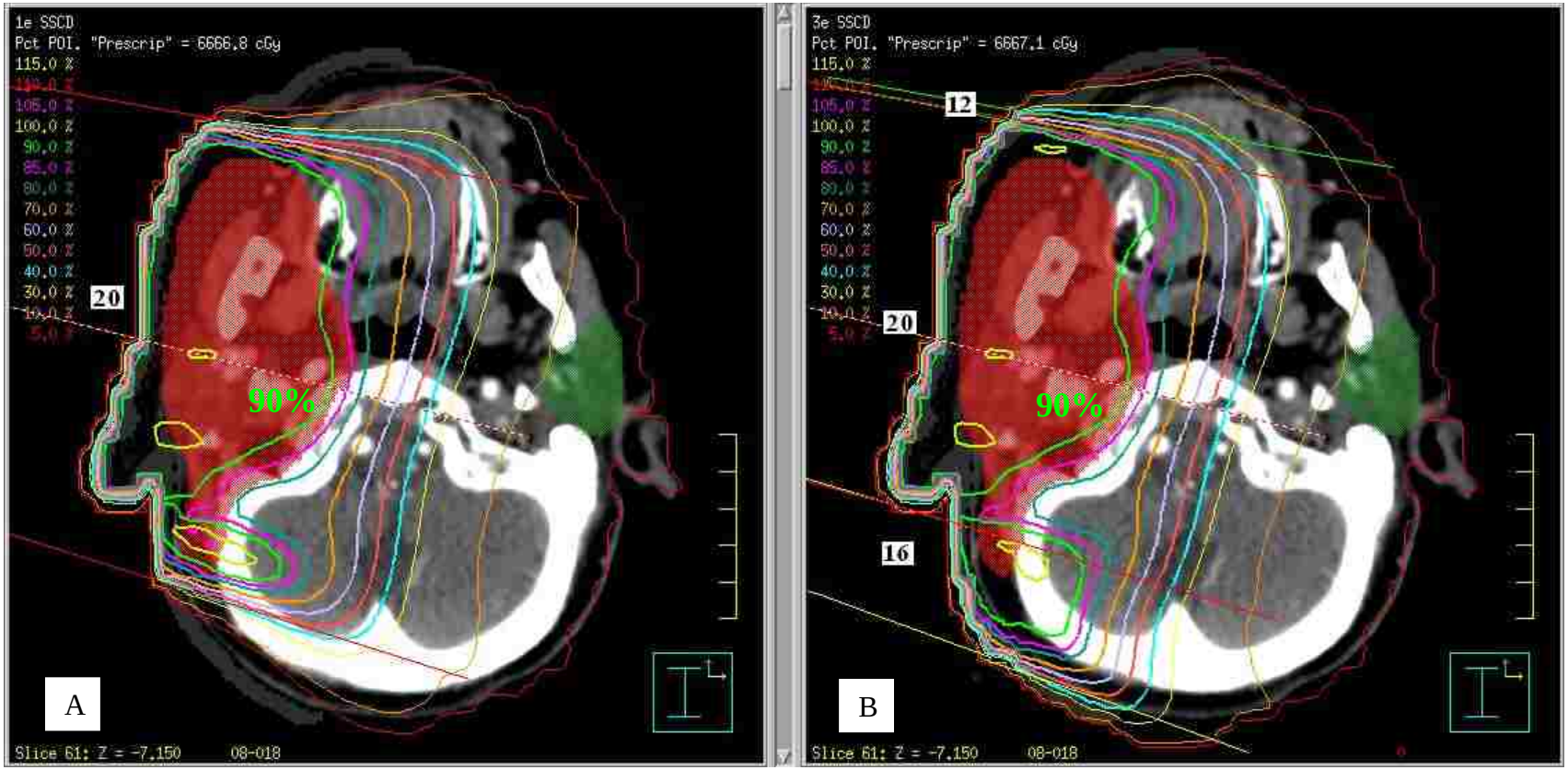

Figure 85: Patient B. Isodose contours in slice 61 for (A) the single-energy SSCD plan and (B) the three-energy SSCD plan. The PTV is shaded red and the left parotid gland is green. The 90% dose line is in bright green. The "bump" of the patient's right ear is the cause for the hot and cold spots seen in both plans.

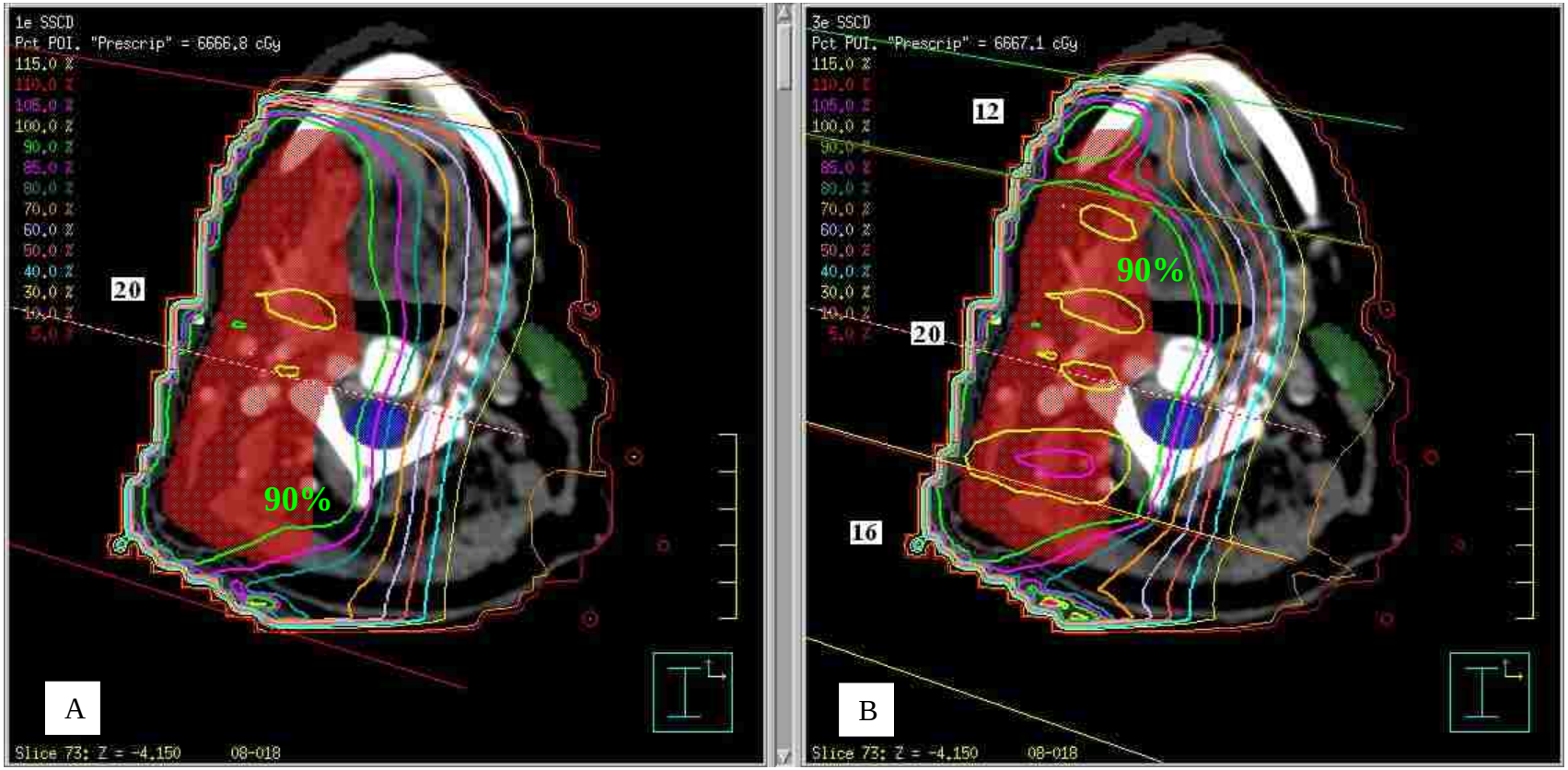

Figure 86: Patient B. Isodose contours in slice 73 for (A) the single-energy SSCD plan and (B) the three-energy SSCD plan. The PTV is shaded red, the spinal cord is dark blue, and the left parotid gland is green. The 90% dose line is in bright green.

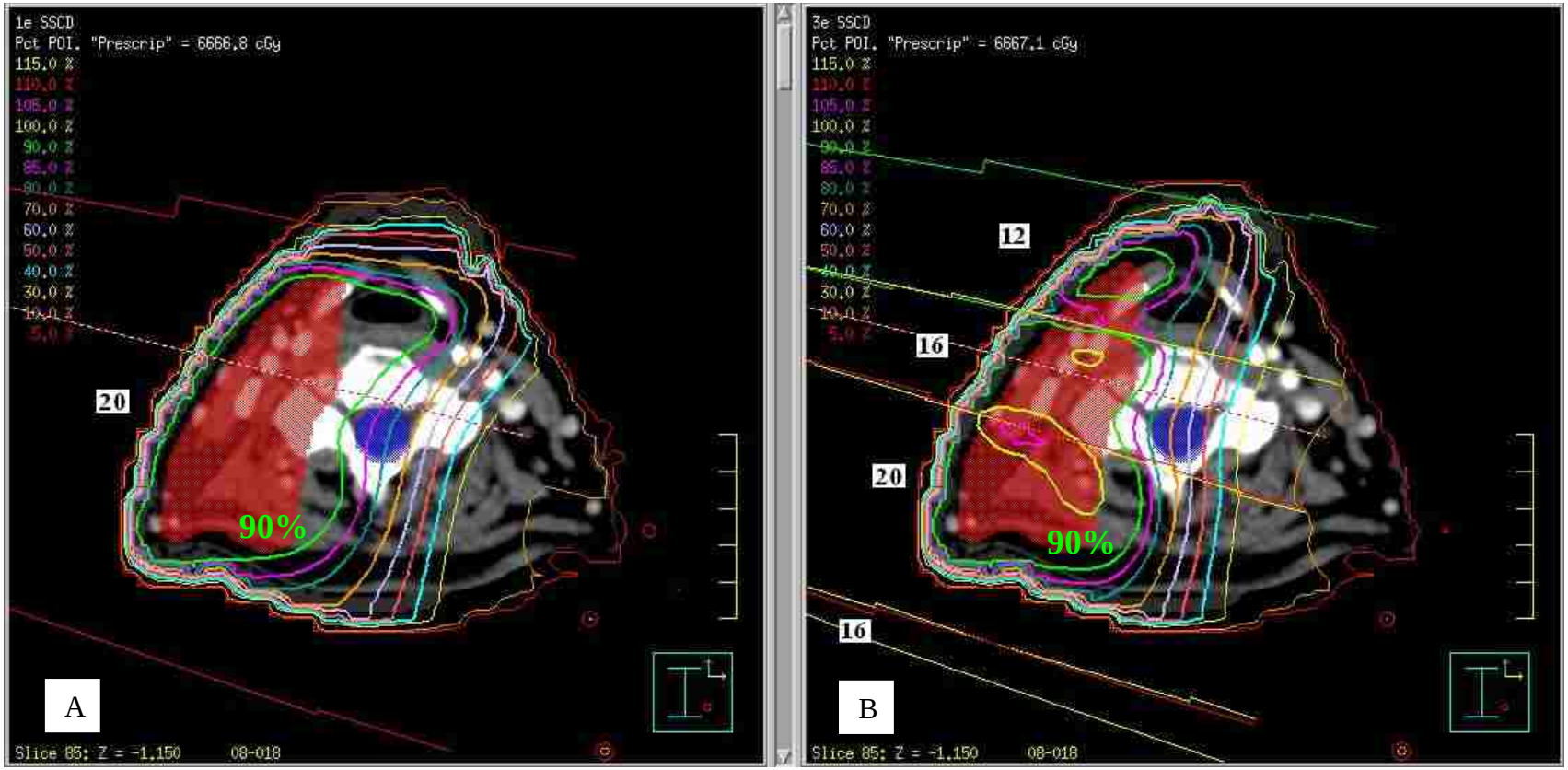

Figure 87: Patient B. Isodose contours in slice 85 for (A) the single-energy SSCD plan and (B) the three-energy SSCD plan. The PTV is shaded red and the spinal cord is dark blue. The 90% dose line is in bright green.

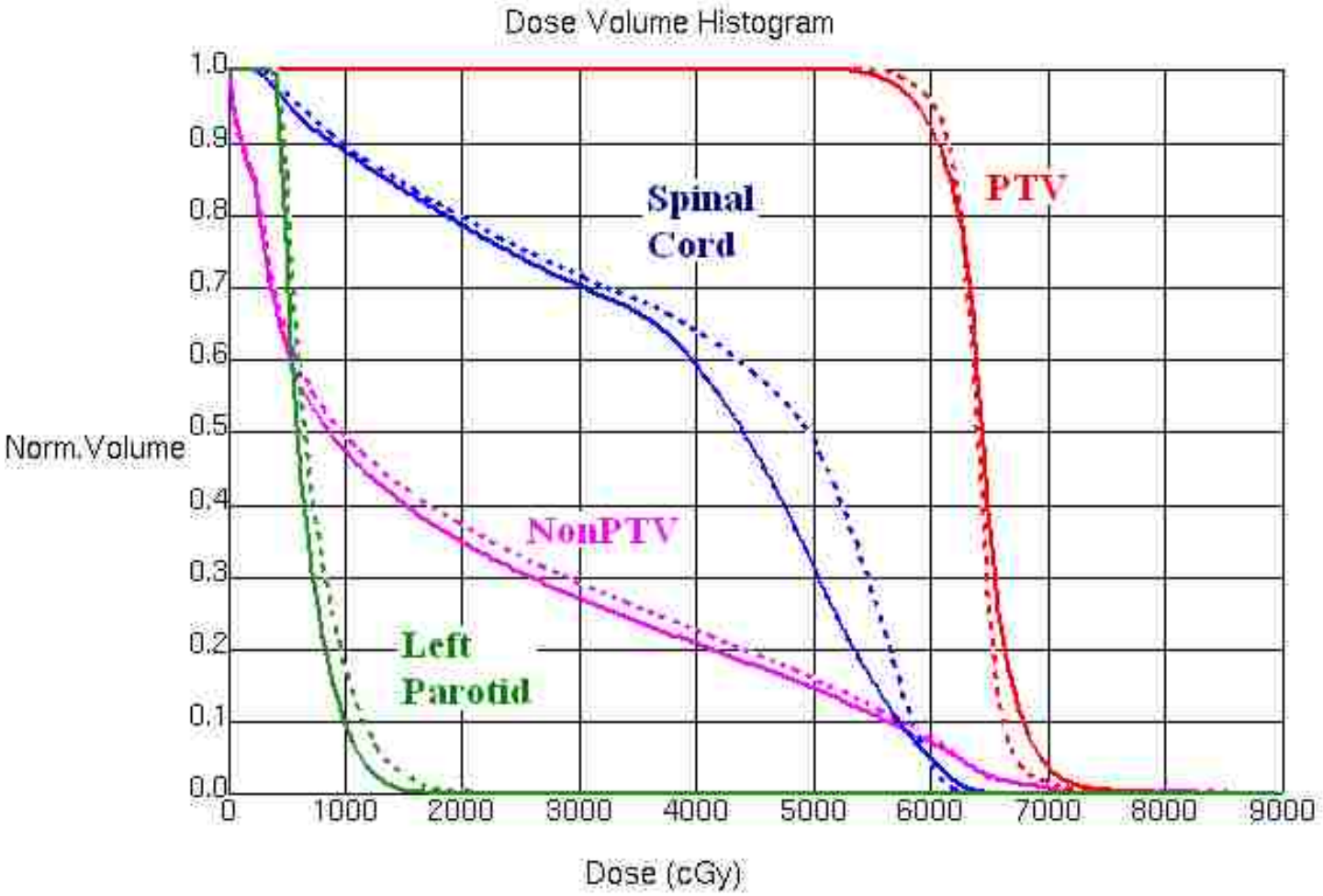

Figure 88: Patient B. Cumulative DVHs for the single-energy SSCD plan (dashed lines) and three-energy SSCD plan (solid lines). Dose to the PTV (red), non-PTV (fuchsia), cord (dark blue), and left parotid gland (green) are shown.

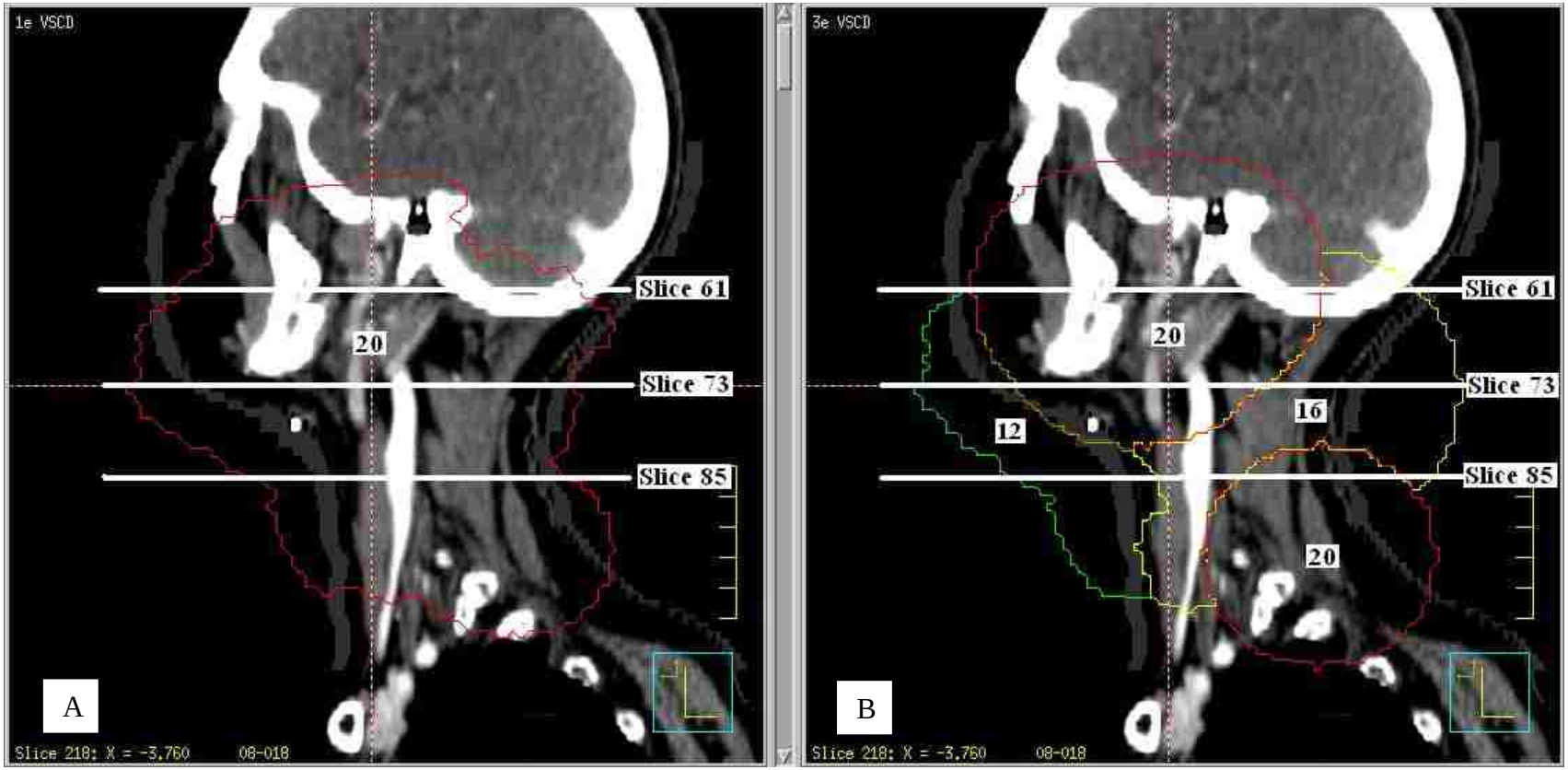

Figure 89: Sagittal plane of patient B at 2 cm depth, showing the field segmentation for (A) the single-energy VSCD plan and (B) the three-energy VSCD plan. The locations of slices 61, 73, and 85 (z= -7.15, -4.15, and -1.15) are indicated. A BEV of the field segmentation is shown. The single-energy VSCD plan uses a single 20 MeV segment. The three-energy VSCD plan uses a single 12 MeV segment, a single 16 MeV segment, and two 20 MeV segments.

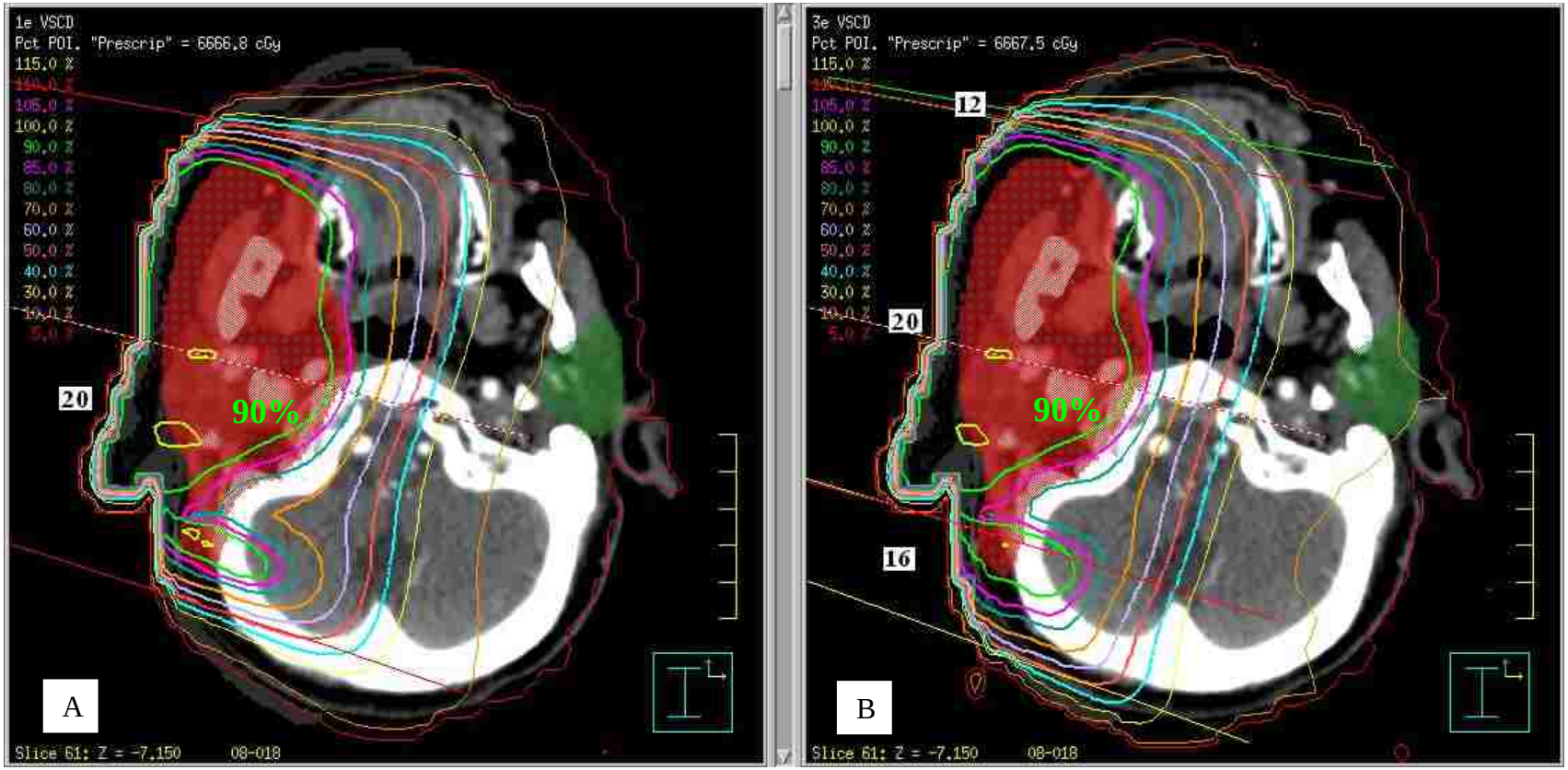

Figure 90: Patient B. Isodose contours in slice 61 for (A) the single-energy VSCD plan and (B) the three-energy VSCD plan. The PTV is shaded red and the left parotid gland is green. The 90% dose line is in bright green. The "bump" of the patient's right ear is the cause for the hot and cold spots seen in both plans.

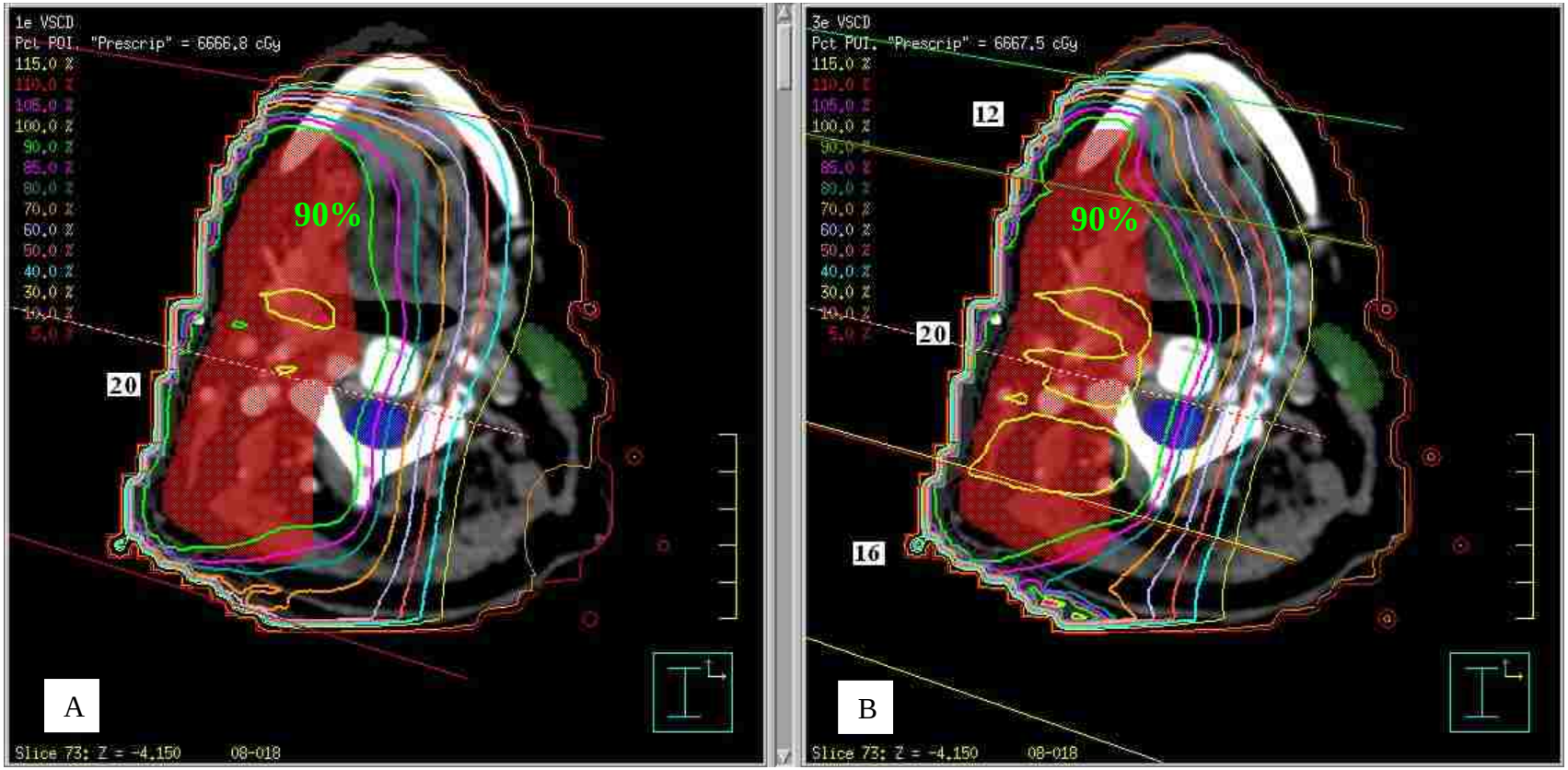

Figure 91: Patient B. Isodose contours in slice 73 for (A) the single-energy VSCD plan and (B) the three-energy VSCD plan. The PTV is shaded red, the spinal cord is dark blue, and the left parotid gland is green. The 90% dose line is in bright green.

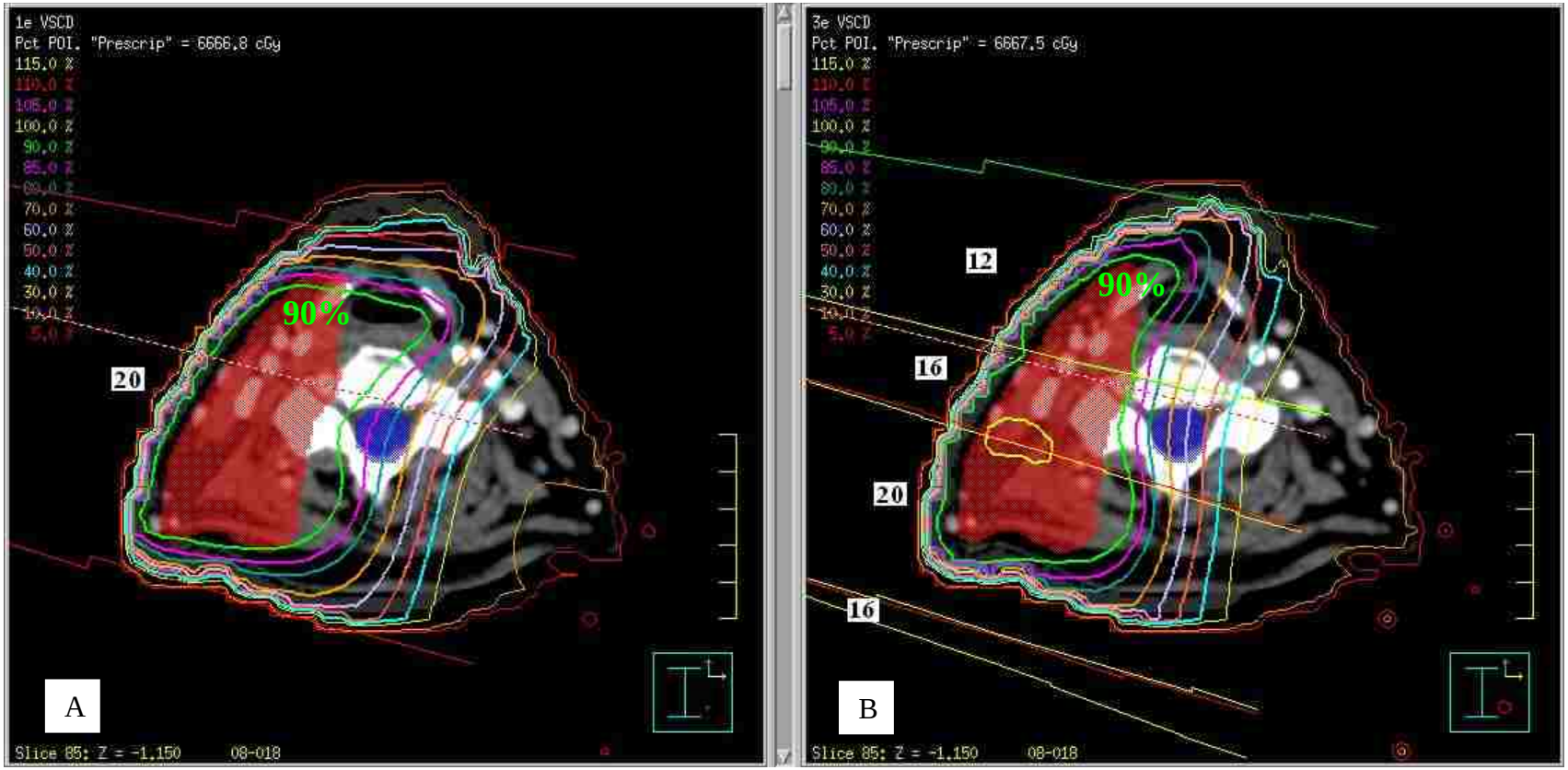

Figure 92: Patient B. Isodose contours in slice 85 for (A) the single-energy VSCD plan and (B) the three-energy VSCD plan. The PTV is shaded red and the spinal cord is dark blue. The 90% dose line is in bright green.

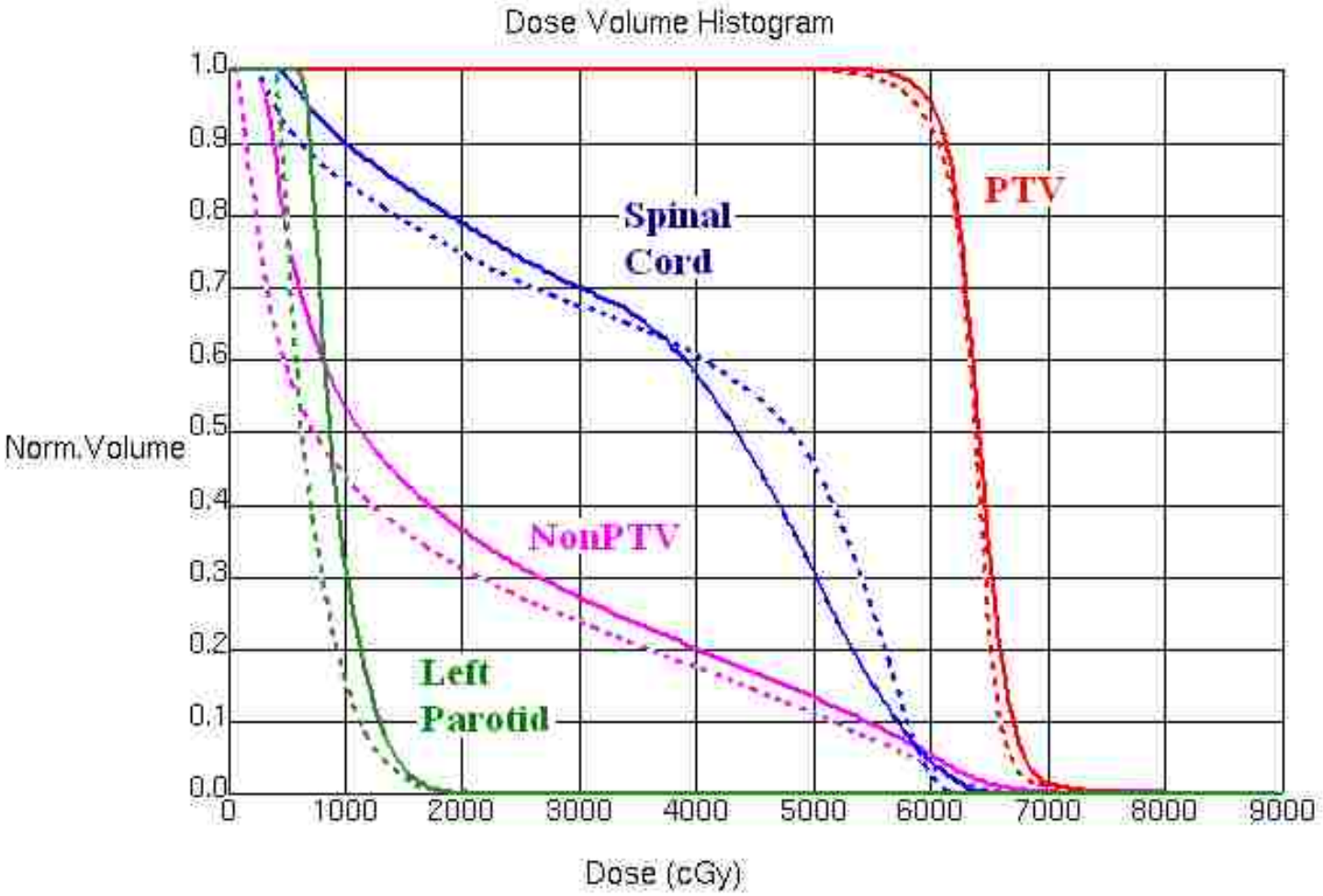

Figure 93: Patient B. Cumulative DVHs for the single-energy VSCD plan (dashed lines) and three-energy VSCD plan (solid lines). Dose to the PTV (red), non-PTV (fuchsia), cord (dark blue), and left parotid gland (green) are shown.

Table 14: Summary of planning results for patient case B.

Plan	Dose at Prescription Point (cGy)	Min (%)	Max (%)	Max-Min (%)	Std. Dev. (%)	D_{90-10}	CR	SR	CI
1 SSCD	6666.8	59.2	119.0	59.8	3.4	7.0	0.954	0.383	0.589
2 SSCD	6667.2	69.4	117.7	48.3	4.7	11.1	0.882	0.400	0.529
3 SSCD	6667.1	67.1	118.2	51.0	4.7	11.0	0.918	0.373	0.576
1 VSCD	6666.8	59.9	115.5	55.6	3.9	8.0	0.921	0.237	0.702
2 VSCD	6667.1	72.8	116.6	43.8	3.6	8.3	0.931	0.341	0.614
3 VSCD	6667.5	74.9	115.0	40.1	3.7	8.6	0.951	0.304	0.662

In summary of the SSCD plans, the DVH in Figure 88 shows that the three-energy plan did not cover the PTV as well as the single-energy plan, seen also by its decreased CR compared to that of the single-energy plan (0.918 versus 0.954), and had greater dose heterogeneity due to abutting fields of different energies. Both plans keep the left parotid gland well under the tolerance level (less than 50% of the volume receives 26 Gy) and with the three-energy plan treating the gland to less dose. Though the three-energy plan treated less of the spinal cord below about 60 Gy than the single-energy plan, neither plan kept the spinal cord under tolerance of a maximum dose of 45 Gy due to the PTV coming within 1 cm of the spinal cord in many of the slices, meaning that neither plan was clinically acceptable. The three-energy plan treated non-PTV (defined in Section 2.4.2.2) to less dose, reflected by its reduced SR compared to that of the single-energy plan (0.373 versus 0.383). The three-energy plan was less conformal than the single-energy plan, seen by its reduced CI compared to that of the single-energy plan (0.576 versus 0.589).

In summary of the VSCD plans, the DVH in Figure 93 shows that the three-energy plan covered the PTV better than the single-energy plan with only slightly increased dose heterogeneity, shown by its improved CR compared to that of the single-energy plan (0.951 versus 0.921). Both plans keep the left parotid gland within tolerance, with the three-energy plan treating the gland to more dose. The three-energy plan treated more of the spinal cord to doses

below 37 Gy and less of the spinal cord to doses from 37 Gy to 60 Gy; however, as for the SSCD, neither plan was clinically acceptable. The three-energy plan treated non-PTV to more dose, reflected by its worse SR compared to that of the single-energy plan (0.304 versus 0.237). As with the SSCD plans, the three-energy plan was less conformal than the single-energy plan, seen by its reduced CI compared to that of the single-energy plan (0.662 versus 0.702).

Expected from the results of Richert *et. al.* (2007) and the hypothetical PTVs, the dose homogeneity improved by using the VSCD method. Compared to the three-energy SSCD plan, the three-energy VSCD plan had a smaller max-min dose (40.1% versus 51.0%), standard deviation of dose within the PTV (3.7% versus 4.7%), and $D_{90\text{-}10}$ (8.6% versus 11.0%). The three-energy VSCD plan was also more conformal than the three-energy SSCD plan (CI of 0.662 versus 0.576), further suggesting that the VSCD method should be used if available.

The results of this patient case did not support the hypothesis. Furthermore, due to the PTV's close proximity to the spinal cord, none of the plans were clinically acceptable. This indicates that this patient was not a candidate for a SFECT treatment alone. However, it is possible that the patient could benefit from mixed beam therapy (SFECT plus IMRT). In the case of a mixed beam plan, the SFECT and IMRT plans would be combined with optimal weighting in order to both reduce the dose to normal tissue (on the part of the SFECT plan) and keep the spinal cord dose within tolerance (on the part of the IMRT plan).

Chapter 4. Conclusions

The hypothesis was tested by completing four specific aims. In Aim 1, the 2D Hogstrom PBA was coded for a flat water phantom to calculate the dose distributions of both SSCD and VSCD plans needed for Aim 2. The coded PBA was found to be sufficiently equivalent to that of the Pinnacle v7.4f treatment planning system.

In Aim 2, an iterative, forward planning algorithm for designing segmented-field ECT fields which allows each segment to have its own energy, shape, size, and weighting was developed. The developed algorithm allows the user to select the number of energies allowed in the plan and whether the plan should be developed using SSCD or VSCD. The algorithm develops an initial plan and then goes through several field optimization iterations, re-planning the fields based on the dose distribution of the previous plan. The plans converged after a few optimizations and if allowed to run indefinitely the fields either changed very little or grew to a maximum size in an attempt to fix un-correctable cold spots caused by abutment of different energies.

In Aim 3, the planning algorithm was tested on six hypothetical PTVs in a flat water phantom. Plans using SSCD and VSCD were developed allowing 1, 2, and 3 energies. The best multiple-energy plan of each method was compared to the method's single-energy plan. The hemispherical PTV was excluded from the summary statistics as its unique shape caused it to be a statistical outlier. On average, the multi-energy SSCD plans' CI improved over that of the single-energy SSCD plans by 3.5% (σ=3.0%) and the multi-energy VSCD plans' CI improved 14.3% (σ=11.3%) compared to the single-energy VSCD plans, supporting the hypothesis. As demonstrated by the results of the pentagon PTV, three-energy plans, including three-energy plans which use only two energies, were not always better than the two-energy plans, indicating that both two- and three-energy plans should be developed and compared for each case. The

results of the inverted well PTV showed that a three-energy plan which uses only two energies can sometimes perform better than a two-energy plan. This indicated that the planning algorithm should iterate at Step 3 and not Step 2, as iterating at Step 2 would cause the three-energy plan using two energies to converge to the same segmentation as the two energy plan. Finally, the VSCD plans were more conformal and had more homogenous dose distributions than the SSCD plans, indicating that VSCD should be used if the technology were available.

In Aim 4, the potential of the algorithm's ability to conform dose to a heterogeneous target and reduce dose to critical structures was studied by using the algorithm on two head and neck patient cases. For patient case A, the planning algorithm was successful in increasing the conformity of the three-energy plan's dose distribution compared to that of the single-energy plan's, supporting the hypothesis and showing that the planning algorithm has the potential to be used to plan SFECT treatments for patient cases. The results of patient case B did not support the hypothesis and showed that SFECT cannot fully replace IMRT in all cases, especially those in which the PTV is located too close to an organ at risk. In such circumstances, SFECT could potentially be used in combination with IMRT for mixed beam therapy to both reduce dose to normal tissue while keeping organs at risk under tolerance doses.

The results of the present work supported the hypothesis that the development of a forward planning algorithm can produce segmented-field ECT fields that improve the dose conformity as the number of beam energies is increased from one to five using the Varian beam set. The hypothesis was only partially confirmed in that dose conformity did improve as the number of energies allowed in the plan was increased from a single energy being allowed, but improved very little or not at all past allowing more than 2 or 3 energies due to the PTVs being relatively small in the BEV. However, the improved conformity came at the expense of dose

homogeneity within the PTV, which could be improved by using the VSCD method if it were available.

4.1 Recommendation – Algorithm Improvements

Based on the results of the hypothetical PTVs, there are several possible improvements to the segmentation optimization (planning). Using divergent beam geometry to produce the BEVs of distal PTV depth might improve the algorithm. In the current work, parallel beam geometry was assumed to generate the BEVs of distal PTV depth, but a divergent beam was used in the calculation of the dose distributions. The use of the virtual PTV seemed to account for the parallel beam geometry reasonably well, but the use of a divergent geometry may produce better results and may require fewer re-planning iterations.

Another possible improvement is "upgrading" the energy of field segments. In areas where the distal PTV is only slightly shallower than an energy's equilibrium R_{90}, it's possible that using the next highest energy may be better. An example of this was seen in the two-step block PTV, in which the edge of the 12 MeV segment extended laterally several cm beyond the PTV edge. If 16 MeV were used instead, the field edge would probably be much closer to the PTV. It's possible that the lateral tissue sparing would negate the extra tissue irradiated below the PTV, resulting in an improved SR and CI.

Using some rules for energy abutment may also improve the algorithm. As seen in the results of the wedge PTV, the hot and cold spots from abutting 12 MeV to 20 MeV were more pronounced than when abutting 12 MeV to 16 MeV and 16 MeV to 20 MeV. It's possible that the improved PTV coverage from reduced cold spots (improved CR) by not allowing abutment of energies differing by more than one energy step could negate the extra tissue irradiated below the PTV by using a higher energy (worse SR), leading to improved conformity.

4.2 Recommendation – PTV Selection

If the previously discussed possible improvements to the planning algorithm or future studies were to be investigated, it is recommended against using the PTVs from this study. They were found to be too small, resulting in only 2 to 3 energies being used in final segmentation even if all 5 energies were allowed. Furthermore, their non-realistic steep edges resulted in field segment edges being too far away from the PTV edge, irradiating a large amount of non-PTV lateral to the PTV. Instead, it is recommended that PTVs from patient plans be transferred onto a flat water phantom to create more realistic situations. It is not recommended that the current planning algorithm be used clinically without further research into the previously mentioned improvements to the planning algorithm and the use of a 3D PBA on the planning of patient cases.

4.3 Future SFECT Studies

One area of future study that could improve dose conformity and worthy of investigation is the use of decreased separation of beam energy steps. Most treatment machines offer electron energies in steps of 3 to 5 MeV, but it's possible that steps of 1 to 2 MeV may improve conformity. An example of the potential improvement can be seen in the two-step block PTV. As previously mentioned, the distal PTV surface was just slightly shallower than the equilibrium R_{90} of 12 MeV and using 16 MeV instead may improve conformity. However, it's also possible using 13 MeV or 14 MeV may provide better conformity than 16 MeV, due to both the lateral tissue sparing from the smaller segments from using an energy greater than 12 MeV and the distal tissue sparing from using an energy lower than 16 MeV. Also, as seen in patient case A (Figure 76), the 90% contour often encloses significant tissue distal to the PTV, not typical of bolus ECT where energy can be continuously modulated.

Another area of future study is investigating an alternative to the VSCD method for the broadening of penumbra. Though the fabrication of the Cerrobend inserts is fairly fast, the switching out of several inserts during treatment would be very time consuming to the radiation therapist, requiring several entries into the room and possible patient realignments for each treatment. Additionally, the electron cone used for the VSCD method is not currently commercially available and is unlikely to be available any time soon. An alternative method is using an eMLC to feather the segment edges to artificially broaden the penumbras. While eMLCs are also not currently commercially available, several eMLCs are under development. Because eMLCs can modulate the beam edge in only one direction (that of leaf motion), additional research of the ability of the eMLC to create the field segments and improve matching through leaf modulation would be integral.

A significant area of future study is improving the planning algorithm's ability to plan patient cases. In the present work, the PBA that calculates the dose distributions used for the optimization iterations was designed to calculate dose for a flat water phantom. It is felt that the planning algorithm's performance with patient cases could be improved if a 3D PBA that takes irregular patient surface and the heterogeneity of patient anatomy into account (as the Pinnacle v7.4f PBA does and as would any treatment planning system that implemented the planning algorithm) were used to calculate the required dose distributions in the segmentation algorithm. It is believed that this improvement could bring the planning algorithm's ability to plan patient cases up to that of its ability to plan the hypothetical cases and make SFECT a viable treatment option for some patients that would presently be treated with IMRT.

Finally, SFECT needs to be compared to other treatment modalities. The current work studied only SFECT compared to conventional electron therapy. SFECT should be compared to bolus ECT for improvement to conformity. As mentioned previously, bolus ECT is a proven

treatment option and may perform better than SFECT in many cases. Additionally, both ECT modalities should be compared to IMRT and to mixed beam therapy, as mixed beam therapy may perform better than either modality alone for some cases.

References

Al-Yahya K, Schwartz M, Shenouda G, Verhaegen F, Freeman C, and Seuntjens J (2005). "Energy modulated electron therapy using a few leaf electron collimator in combination with IMRT and 3D-CRT: Monte Carlo-based planning and dosimetric evaluation" Med. Phys. 32 2976-2986

Ashenafi M S (2006). "Tomotherapy for post-mastectomy radiotherapy (PMRT): Comparison with conventional electron technique," Master's thesis at Louisiana State University

Eyges L (1948). "Multiple scattering with energy loss" Phys. Rev. 74 1534-1535

Gauer T, Albers D, Cremers F, Harmansa R, Pellegrini R, and Schmidt R (2006). "Design of a computer-controlled multileaf collimator for advanced electron radiotherapy" Phys. Med. Biol. 51 5987-6003

Hogstrom K R, Mills M D, and Almond P R (1981). "Electron Beam Dose calculations" Phys. Med. Biol. 26 445-459

Hogstrom K R and Almond P R (1982). "Electron multiple scattering distribution from a point source" Phys. Med. Biol. 27 310-311

Hogstrom K R, Mills M D, Meyer J A, Palta J R, Mellenberg D E, Meoz R T, and Fields R S (1984). "Dosimetric evaluation of a pencil-beam algorithm for electrons employing a two-dimensional heterogeneity correction" Int. J. Rad. Oncol. Biol. Phys. 10 561-569

Hogstrom K R (1987). "Evaluation of electron pencil beam dose calculations" In: J Kereiakes, H Elson and C Born (eds). Radiation Oncology Physics – 1986: Proceedings of the 1986 Summer School of the AAPM, pp. 532-557, New York; American Institute of Physics, 1987

Hogstrom K R and Steadham R S (1996). "Electron Beam Dose Computation" In: J Palta and T R Mackie (eds). Teletherapy: Present and Future – 1996 Proceedings of the Summer School of the AAPM, pp. 137-174, Vancouver: Advanced Medical Publishing, 1996

Hogstrom K R, Antolak J A, Kudchadker, R J, Ma C-M C, and Leavitt D D (2003). "Modulated Electron Therapy" In: J Palta and R Mackie (eds). Intensity Modulated Radiation Therapy, The State of the Art: Proceedings of the 2003 AAPM Summer School, pp. 749-786, Madison: Medical Physics Publishing, Madison, 2003

Hogstrom K R, Boyd R A, Antolak J A , Svatos M M, Faddegon B A, and Rosenman J G (2004). "Dosimetry of retractable eMLC for fixed-beam electron therapy" Medical Physics 31 443-462

International Commission on Radiation Units and Measurements (ICRU) (1984). "Radiation Dosimetry: Electron Beams with Energies Between 1 and 50 MeV" ICRU 35 18-21

Klein E E, Vicic M, Ma C M, Low D A, and Drzymala R E (2008), "Validation of calculations for electrons modulated with conventional photon multileaf collimators" Phys. Med. Biol. 53, 1183-1208

Khan F M, Dopke K P, Hogstrom K R, Kutcher G J, Nath R, Prasad S C, Purdy J A, Rozenfeld M, and Werner B L (1991). "Clinical electron-beam dosimetry: Report of the AAPM radiation therapy committee task group 25" Med. Phys. 18 73-109

Kudchadker R J, Antolak J A, Morrison W H, and Hogstrom K R (2002a). "Conformal head and neck radiotherapy using custom electron bolus" Med. Phys. 29 1337

Kudchadker R J, Hogstrom K R, Garden A S, McNeese M D, Boyd R A, and Antolak J A (2002b). "Electron conformal radiotherapy using bolus and intensity modulation" Int. J. Radiat. Oncol., Biol. Phys. 53 1023-1037

Kudchadker R J, Antolak J A, Morrison W H, Wong P F, and Hogstrom K R (2003). "Utilization of custom electron bolus in head and neck radiotherapy" J Appl. Clin. Med. Phys. 4 321-333

Lee M C, Jiang S B, and Ma C-M (2000). "Monte Carlo and experimental investigations of multileaf collimated electron beams for modulated electron radiation therapy" Med. Phys. 27 2708-2718

Lee M C, Deng J, Li J, Jiang S B, and Ma C M (2001). "Monte Carlo based treatment planning for modulated electron beam radiation therapy" Phys. Med. Biol. 46 2177-2199

Low D A, Starkschall G, Bujnowski S W, Wank L L, and Hogstrom K R (1992). "Electron bolus design for radiotherapy treatment planning: Bolus design algorithms" Med. Phys. 19 115-124

Low D A, Starkschall G, Sherman N E, Bujnowski S W, Ewton J R, and Hogstrom K R (1995). "Computer-aided design and fabrication of an electron bolus for treatment of the paraspinal muscles" Int. J. Radiat. Oncol. Biol. Phys. 33 1127-1138

Ma C M, Pawlicki T, Lee M C, Jiang S B, Li J S, Deng J, Yi B, Mok E, and Boyer A L (2000). "Energy- and intensity-modulated electron beams for radiotherapy" Phys. Med. Biol. 45 2293-2311

Ma C M, Ding M, Li J S, Lee M C, Pawlicki T, and Deng J (2003). "A comparative dosimetric study on tangential photon beams, IMRT and MERT for breast cancer treatment" Phys. Med. Biol. 48 909-924

Mills M D, Hogstrom K R, and Almond P R (1982). "Prediction of electron beam output factors" Med. Phys. 9 60-68

Olofsson L, Mu X, Nill S, Oelfke U, Zackrisson B, and Karlsson M (2004). "Intensity modulated radiation therapy with electrons using algorithm based energy/range selection methods" Radiother. Oncol. 73 223–231

Paddick I I (2000). “A simple scoring ratio to index the conformity of radiosurgical treatment plans. Technical note,” J. Neurosurg. 93 Suppl 3 219-222

Perkins G H, McNeese M D, Antolak J A, Buchholz T A, Strom A E, and Hogstrom K R (2001). “A custom three-dimensional electron bolus technique for optimization of postmastectomy irradiation” Int. J. Radiat. Oncol. Biol. Phys. 51 1142-1151

Ravindran B P, Singh I R R, Brindha S, and Sathyan S (2002). “Manual multi-leaf collimator for electron beam shaping-a feasibility study” Phys. Med. Biol. 47 4389-4396

Richert J, Hogstrom K, Fields R, Matthews K, and Boyd R (2007). “Improvement of field matching in segmented-field electron conformal therapy using a variable-SCD applicator” Phys. Med. Biol. 52 2459–2481

Shiu A S, Tunq S S, Nyerick C E, Ochran T G, Otte V A, Boyer A L, and Hogstrom K R (1994). “Comprehensive analysis of electron beam central-axis dose for a radiotherapy linear accelerator” Med. Phys. 21, 559-566

Starkschall G, Shiu A S, Bujnowski S W, Wang L L, Low D A, and Hogstrom K R (1991). “Effect of dimensionality of heterogeneity corrections on the implementation of a three-dimensional electron pencil-beam algorithm” Phys. Med. Biol. 36 207-227

Starkschall G, Bujnowski S W, Antolak J A, Wang L L, and Hogstrom K R (1994). ‘‘Tools for 3-D electron-beam treatment planning’’ Proceedings of the XIth International Conference on the Use of Computers in Radiation Therapy, Manchester, UK (Handley Printers Limited, Cheshire, 1994), pp. 126–127

Tapley N D (1976). “Clinical Applications of the Electron Beam” New York: John Wiley & Sons

Zackrisson B, and Karlsson M (1996). “Matching of electron beams for conformal therapy of target volumes at moderate depths” Radiother. Oncol. 39 261-270

Appendix A: Derivation of Converting Square-Field to Circular-Field Depth Dose Data

In the present work, we have measured data for square fields but created plans with circular fields. A thorough derivation of the equation used to convert depth dose data from a measured square field of size XxX-cm^2 to that of a circular field of diameter X-cm is presented in this appendix. Note the general integral solution

$$\int x e^{-cx^2} dx = -\frac{1}{2c} e^{-cx^2}$$

and that the error function is defined as

$$\text{erf}(x) = \frac{2}{\sqrt{\pi}} \int_0^x e^{-t^2} dt.$$

From Hogstrom *et al.* (1981), the dose at any point (X, Y, Z) in a phantom is

$$D(X,Y,Z) = \iint_{\substack{Collimator \\ at\ Z}} S(X',Y') d(X'-X, Y'-Y, Z) dX'\, dY', \tag{A1}$$

where S(X′, Y′) is the relative strength of the pencil beam at (X′, Y′) and d(X′-X, Y′-Y, Z) is the dose contribution at (X, Y, Z) from the pencil beam at (X′, Y′). We assume a perpendicularly incident flat beam so S=1.

Next, d can be separated into a central-axis term g(Z) and an off-axis term f(X, Y, Z).

$$d(X,Y,Z) = f(X,Y,Z) g(Z). \tag{A2}$$

From multiple coulomb scattering (Eyges 1948),

$$f(X,Y,Z) = \frac{1}{2\pi\sigma^2} e^{\frac{-(X^2+Y^2)}{2\sigma^2}}, \tag{A3}$$

where σ is the beam sigma, calculated as described in Section 2.1.4.

Combining (A1) - (A3) gives, for a flat water phantom (indicated by the 0 subscripts),

$$D_0(X,Y,Z) = \left(\frac{1}{2\pi\sigma_0^2} \iint_{\substack{Collimator \\ at\ Z}} e^{\frac{-((X-X')^2+(Y-Y')^2)}{2\sigma_0^2}} dX'\, dY' \right) g_0(Z). \tag{A4}$$

If we consider only the central-axis (X=Y=0) dose, then (A4) becomes

$$D_0(Z) = \left(\frac{1}{2\pi\sigma_0^2} \iint_{\substack{Collimator \\ at\ Z}} e^{\frac{-(X'^2+Y'^2)}{2\sigma_0^2}}\, dX'\, dY' \right) g_0(Z). \tag{A5}$$

Since we are no longer concerned with anything other than the central-axis dose, we'll now write X′ as X and Y′ as Y for simplicity. The general equation of central-axis dose in a flat water phantom is then

$$D_0(Z) = \left(\frac{1}{2\pi\sigma_0^2} \iint_{\substack{Collimator \\ at\ Z}} e^{\frac{-(X^2+Y^2)}{2\sigma_0^2}}\, dX\, dY \right) g_0(Z). \tag{A6}$$

Interestingly, solving (A6) for $g_0(Z)$ allows us to equate the central-axis dose of any shaped field to that of any other shaped field. This means that using measured central-axis depth dose data of square fields, we can calculate the central-axis depth dose of any shaped field.

For a square field of side W, (A6) becomes

$$D_0^{WxW}(Z) = \left(\frac{1}{2\pi\sigma_0^2} \int_{\frac{-W}{2}}^{\frac{W}{2}} \int_{\frac{-W}{2}}^{\frac{W}{2}} e^{\frac{-X^2}{2\sigma_0^2}} e^{\frac{-Y^2}{2\sigma_0^2}}\, dX\, dY \right) g_0(Z).$$

Noting that the integration limits are the same for a square field,

$$D_0^{WxW}(Z) = \frac{1}{2\pi\sigma_0^2} \left(\int_{\frac{-W}{2}}^{\frac{W}{2}} e^{\frac{-X^2}{2\sigma_0^2}}\, dX \right)^2 g_0(Z),$$

and then noting that the integral is even,

$$D_0^{WxW}(Z) = \frac{1}{2\pi\sigma_0^2} \left(2 \int_0^{\frac{W}{2}} e^{\frac{-X^2}{2\sigma_0^2}}\, dX \right)^2 g_0(Z). \tag{A7}$$

Substituting

$$\frac{x}{\sqrt{2}\sigma_0} = t,$$

(A7) becomes

$$D_0^{WxW}(Z) = \frac{1}{2\pi\sigma_0^2} \left(2\sqrt{2}\sigma_0 \int_0^{\frac{W}{2\sqrt{2}\sigma_0}} e^{-t^2} dt \right)^2 g_0(Z)$$

$$D_0^{WxW}(Z) = \left(\frac{2}{\sqrt{\pi}} \int_0^{\frac{W}{2\sqrt{2}\sigma_0}} e^{-t^2} dt\right)^2 g_0(Z)$$

$$D_0^{WxW}(Z) = \left(\text{erf}\left(\frac{W}{2\sqrt{2}\sigma_0}\right)\right)^2 g_0(Z). \quad \text{(A8)}$$

For a circular field of radius R, (A6) becomes, converting to cylindrical coordinates,

$$D_0^R(Z) = \left(\frac{1}{2\pi\sigma_0^2} \int_0^R \int_0^{2\pi} e^{\frac{-r^2}{2\sigma_0^2}} r\, dr\, d\theta\right) g_0(Z)$$

$$D_0^R(Z) = \left(\frac{1}{\sigma_0^2} \int_0^R e^{\frac{-r^2}{2\sigma_0^2}} r\, dr\right) g_0(Z)$$

$$D_0^R(Z) = \left[-e^{\frac{-r^2}{2\sigma_0^2}}\right]_0^R g_0(Z)$$

$$D_0^R(Z) = \left(1 - e^{\frac{-R^2}{2\sigma_0^2}}\right) g_0(Z). \quad \text{(A9)}$$

(A8) and (A9) can then be equated by solving each for $g_0(Z)$ and the equality can then be solved for the circular field dose,

$$D_0^R(Z) = D_0^{WxW}(Z) \frac{\left(1 - e^{\frac{-R^2}{2\sigma_0^2}}\right)}{\left(\text{erf}\left(\frac{W}{2\sqrt{2}\sigma_0}\right)\right)^2}. \quad \text{(A10)}$$

(A10) is only correct for parallel beams. For divergent beams, the upper limit of integration changes with Z, so we need only substitute in the correct limit for each Z, which is

$$X(Z) = X(0)\left(\frac{SSD+Z}{SSD}\right) = X(0)\left(1 + \frac{Z}{SSD}\right). \quad \text{(A11)}$$

Combining (A10) and (A11)

$$D_0^R(Z) = D_0^{WxW}(Z) \frac{\left(1 - \exp\left(\frac{-\left(R\left(1+\frac{Z}{SSD}\right)\right)^2}{2\sigma_0^2}\right)\right)}{\left(\text{erf}\left(\frac{W\left(1+\frac{Z}{SSD}\right)}{2\sqrt{2}\sigma_0}\right)\right)^2}. \quad \text{(A12)}$$

(A12) now allows us to convert the measured central-axis depth dose from a square field of any size to that of a circular field of any size. For better accuracy, only fields of R=W/2 were converted.

Appendix B: Determination of Circular Field Size

In order to determine the minimum circular field size such that $R_{90}(E, Ø_{min})$ was greater than the depth to distal surface of the PTV in Section 2.2.3, R_{90} values of all measured field sizes were fit to an equation relating R_{90} to field size for each energy. Measured percent depth dose (%DD) curves from a Varian 21EX for all measured square field sizes up to the equilibrium field (2x2 cm^2, 3x3 cm^2, 4x4 cm^2, 6x6 cm^2, 8x8 cm^2) for all electron energies (6,9,12,16,and 20 MeV) were obtained for this purpose. As in Section 2.2.1, the square field data (Table 15) was converted to circular field data (Table 16) using pencil beam theorem as described in Appendix A.

Table 15: R_{90} depths in water for all measured square field sizes up to 10x10 cm^2.

R_{90} (cm)	Field Size (cm x cm)					
Energy (MeV)	2 x 2	3 x 3	4 x 4	6 x 6	8 x 8	10 x 10
6	1.54	1.77	1.83	1.83	1.83	1.83
9	1.88	2.51	2.78	2.83	2.83	2.83
12	2.30	3.12	3.62	4.02	4.03	4.03
16	2.68	3.56	4.14	4.97	5.26	5.26
20	3.02	3.90	4.61	5.56	5.96	5.96

Table 16: R_{90} depths in water for all circular field sizes up to 10 cm diameter, converted from measured square data.

R_{90} (cm)	Field Diameter (cm)					
Energy (MeV)	2	3	4	6	8	10
6	1.44	1.70	1.81	1.83	1.83	1.83
9	1.70	2.35	2.69	2.82	2.83	2.83
12	2.08	2.92	3.47	3.99	4.03	4.03
16	2.47	3.37	3.99	4.89	5.26	5.26
20	2.83	3.73	4.46	5.50	5.96	5.96

Several fit equations were tested and the equation that provided the best fit was

$$R_{90}(E, Ø) = R_{90}(E, Ø_{eq}) * (1 - e^{a(E) * Ø + b(E)}) + c(E), \text{ for 2-cm} < Ø \leq Ø_{eq}, \quad \text{(B1)}$$

where Ø is the diameter of the circular field, $Ø_{eq}$ is the diameter of the circular field that gives electronic equilibrium, and a, b, and c are energy dependent parameters of the fit. The fit

parameters (Table 17) were determined using Mathematica's FindFit function with QuasiNewton as the set method of fitting. To find the minimum field diameter required, the depth to the distal PTV surface for the pixel was inserted into equation (B1) as $R_{90}(E, Ø)$ and equation (B1) was solved for Ø,

$$Ø = \frac{\ln[R_{90}(E,Ø_{eq}) - R_{90}(E,Ø) + c(E)] - \ln[R_{90}(E,Ø_{eq})] - b(E)}{a(E)} \quad \text{(B2)}$$

Table 17: Energy dependent fit parameters of (B1) and (B2).

Energy (MeV)	a	b	c
6	-0.86	0.33	0.08
9	-0.86	0.83	0.05
12	-0.56	0.45	0.12
16	-0.32	0.17	0.51
20	-0.28	0.14	0.78

Appendix C: Dose Distribution Comparisons

Comparison of calculated dose distributions from the coded PBA and Pinnacle v7.4f for 6, 12, and 16 MeV are presented in this appendix.

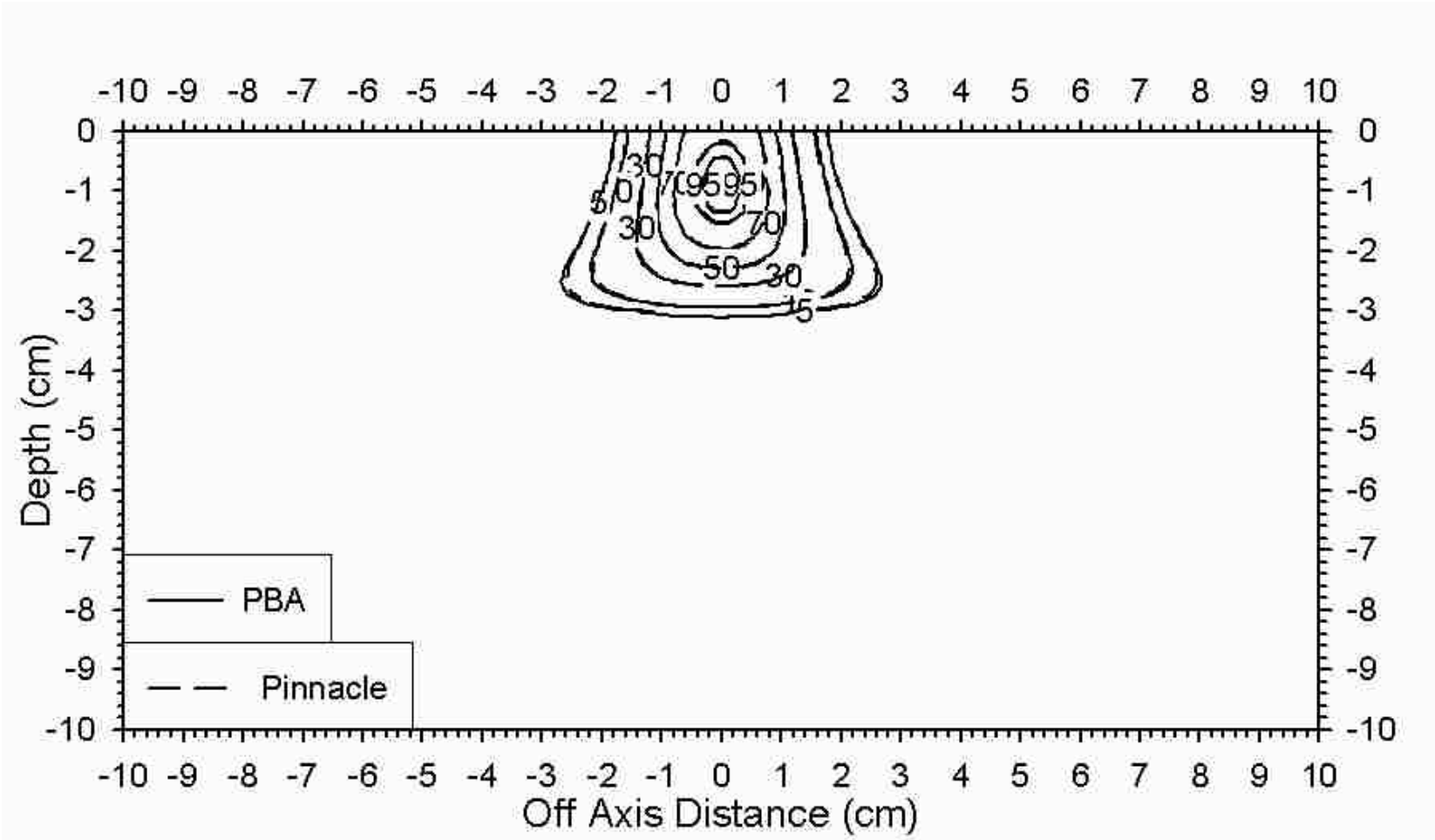

Figure 94: Comparison of dose distributions from a 2x2-cm^2 6 MeV field at 100-cm SSD calculated by the coded PBA (solid line) and Pinnacle (dashed line).

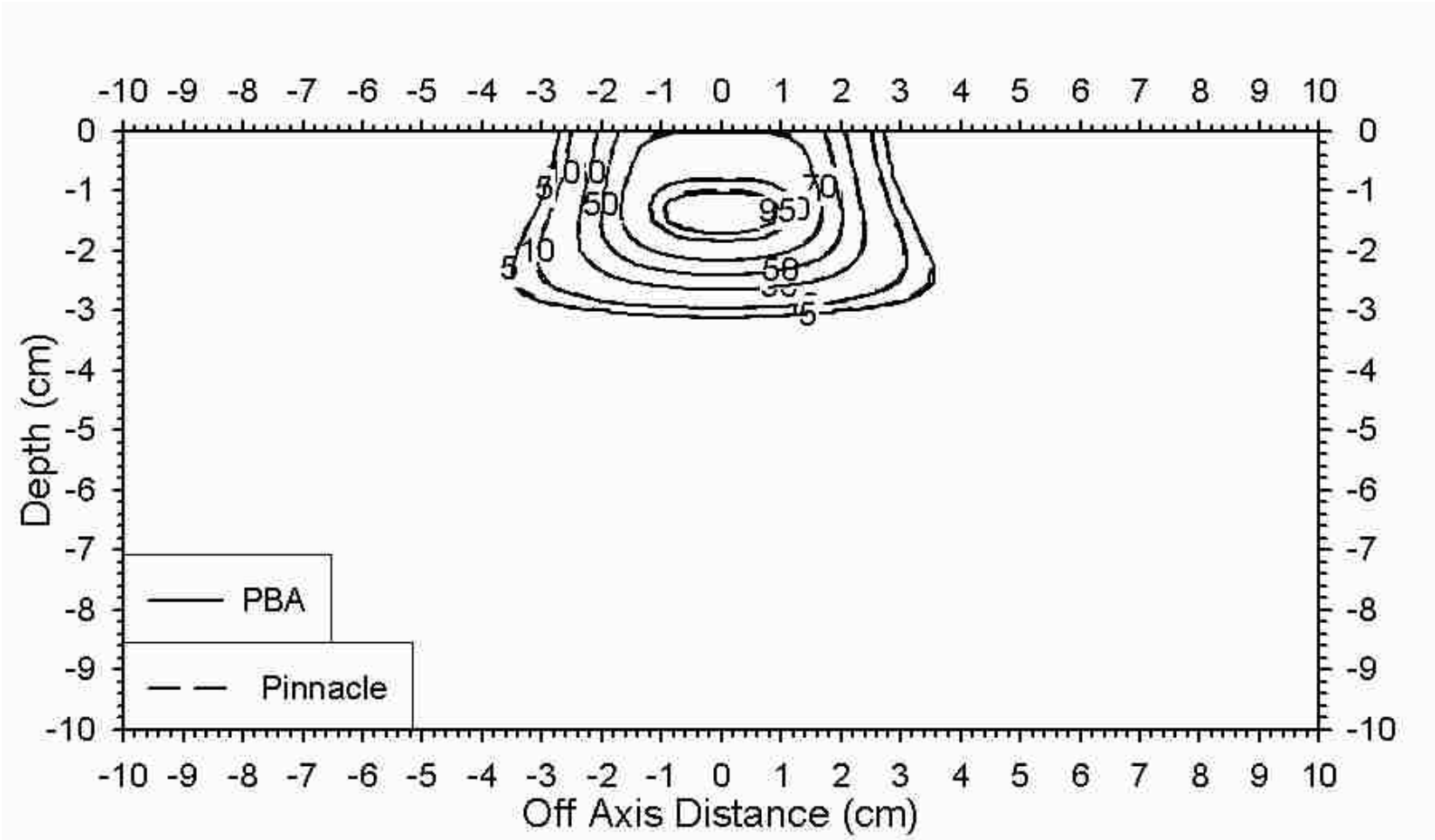

Figure 95: Comparison of dose distributions from a 4x4-cm^2 6 MeV field at 100-cm SSD calculated by the coded PBA (solid line) and Pinnacle (dashed line).

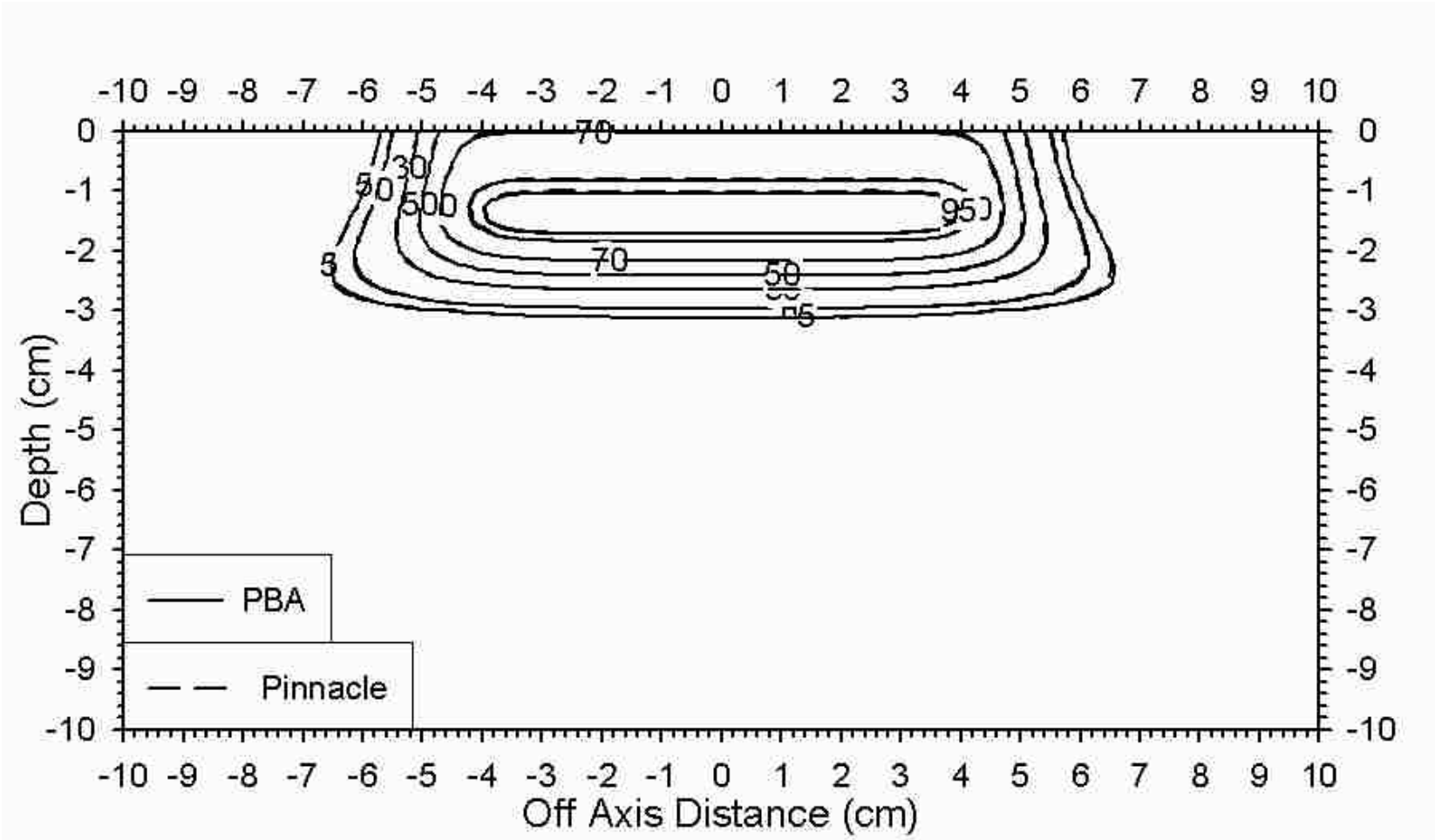

Figure 96: Comparison of dose distributions from a 10x10-cm^2 6 MeV field at 100-cm SSD calculated by the coded PBA (solid line) and Pinnacle (dashed line).

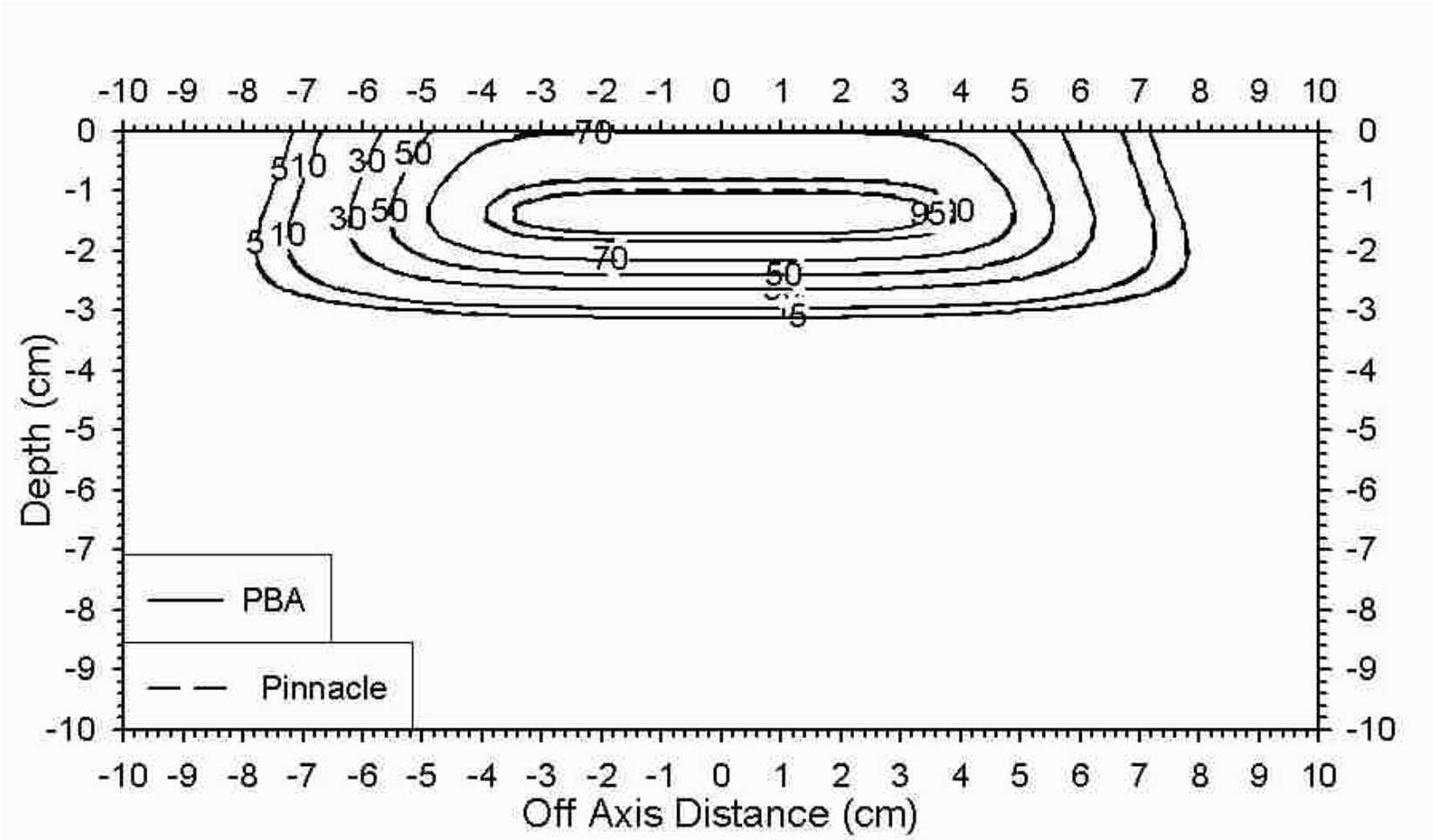

Figure 97: Comparison of dose distributions from a 10x10-cm^2 6 MeV field at 110-cm SSD calculated by the coded PBA (solid line) and Pinnacle (dashed line).

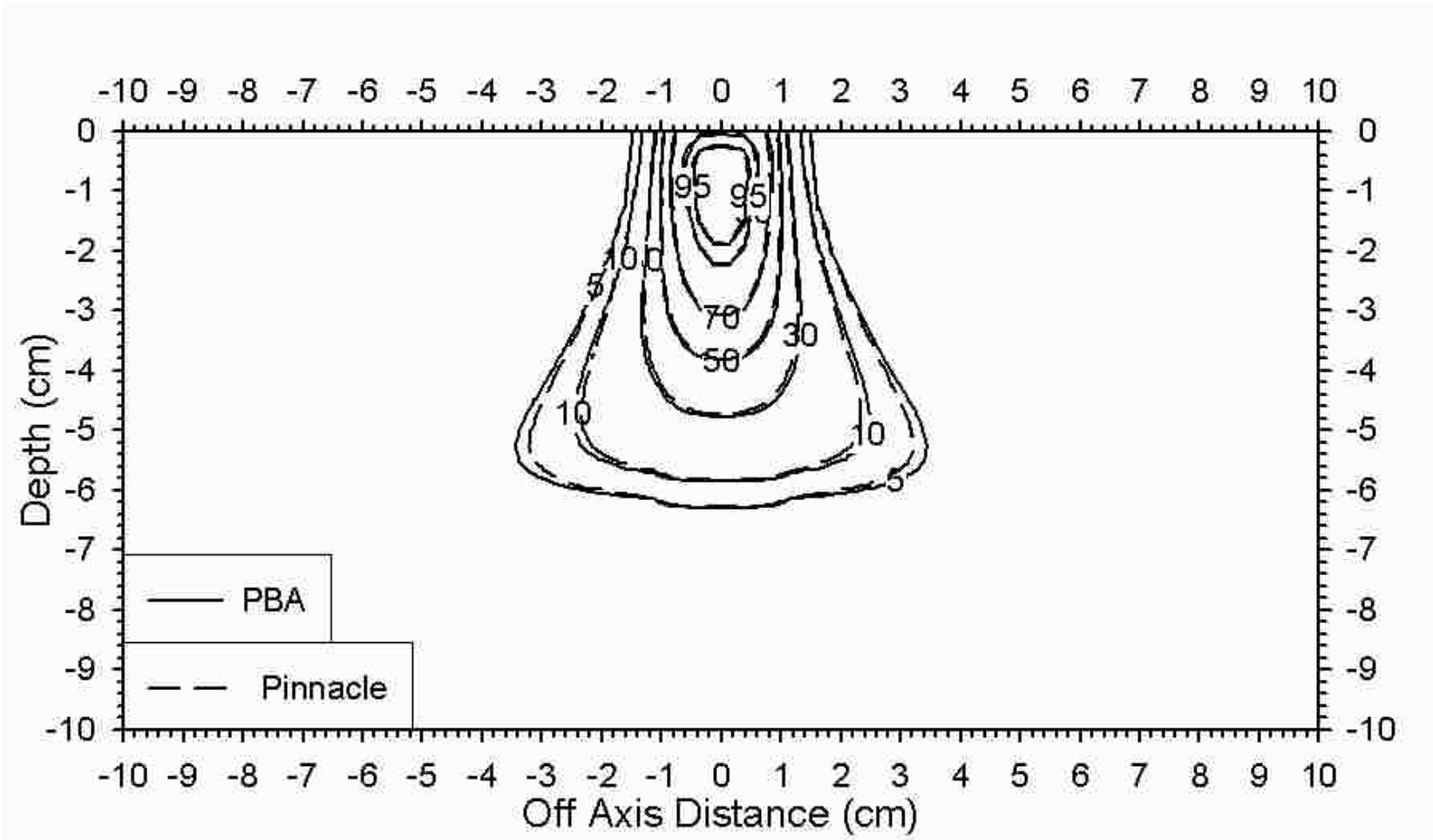

Figure 98: Comparison of dose distributions from a 2x2-cm^2 12 MeV field at 100-cm SSD calculated by the coded PBA (solid line) and Pinnacle (dashed line).

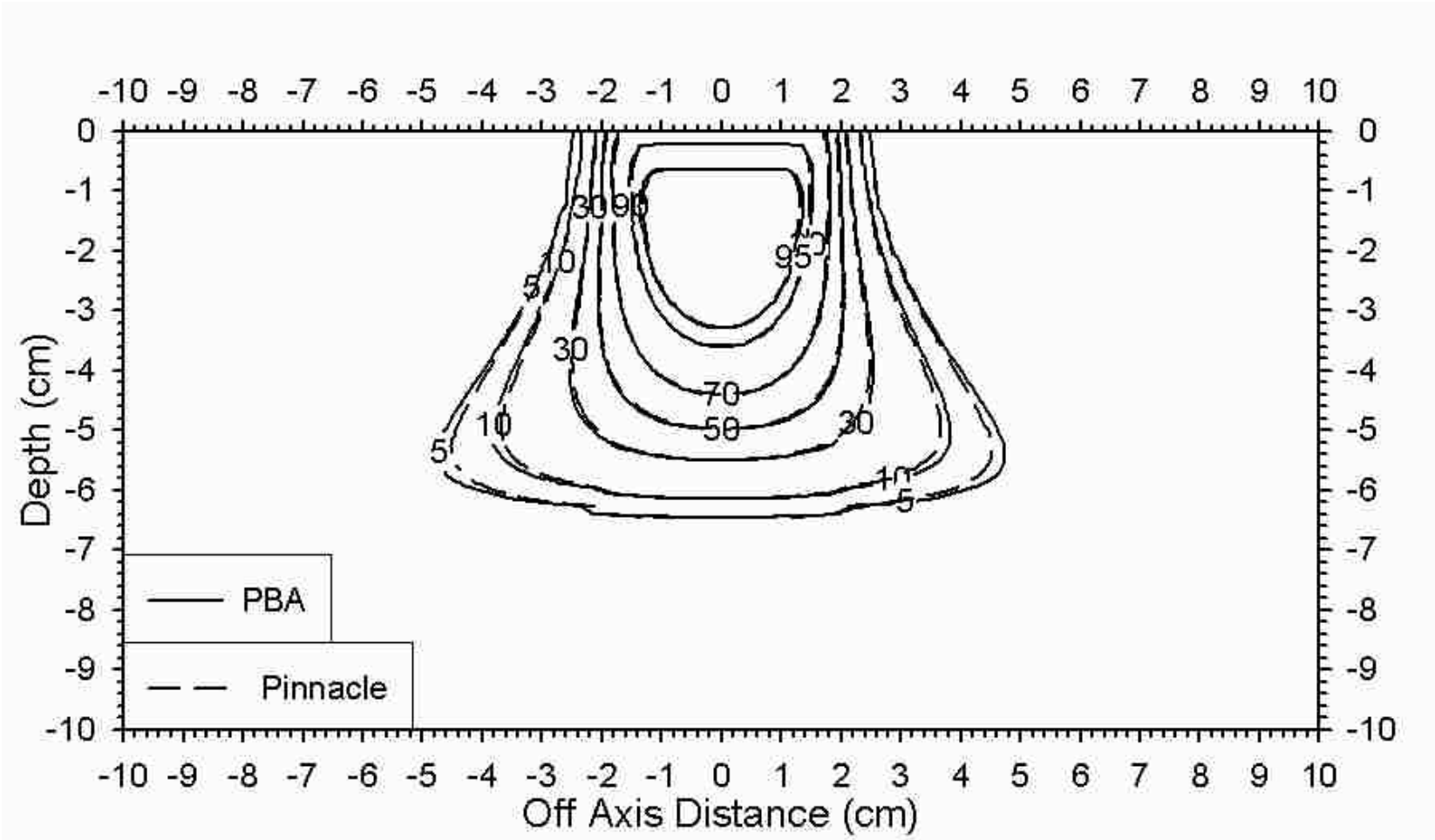

Figure 99: Comparison of dose distributions from a 4x4-cm^2 12 MeV field at 100-cm SSD calculated by the coded PBA (solid line) and Pinnacle (dashed line).

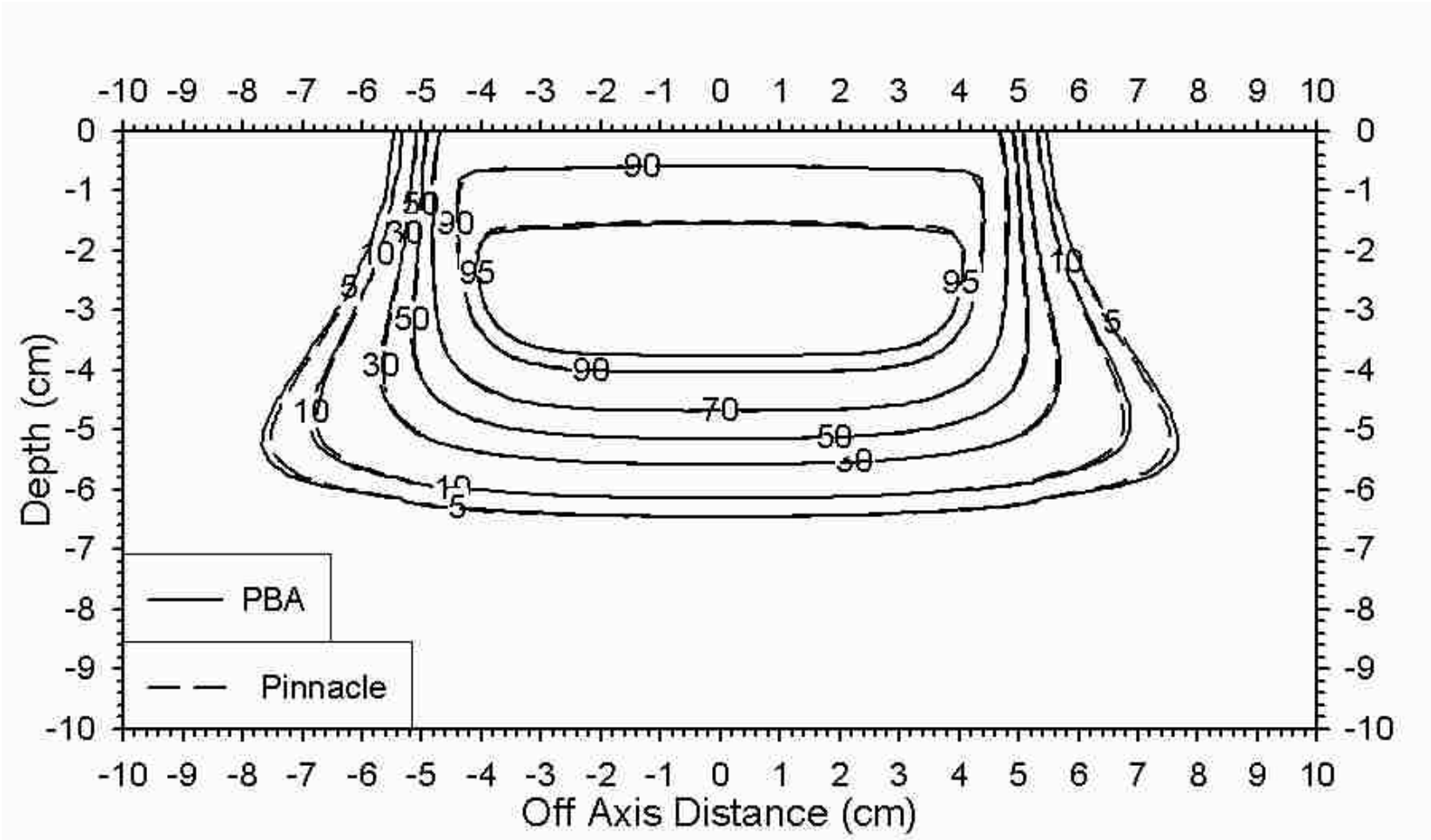

Figure 100: Comparison of dose distributions from a 10x10-cm^2 12 MeV field at 100-cm SSD calculated by the coded PBA (solid line) and Pinnacle (dashed line).

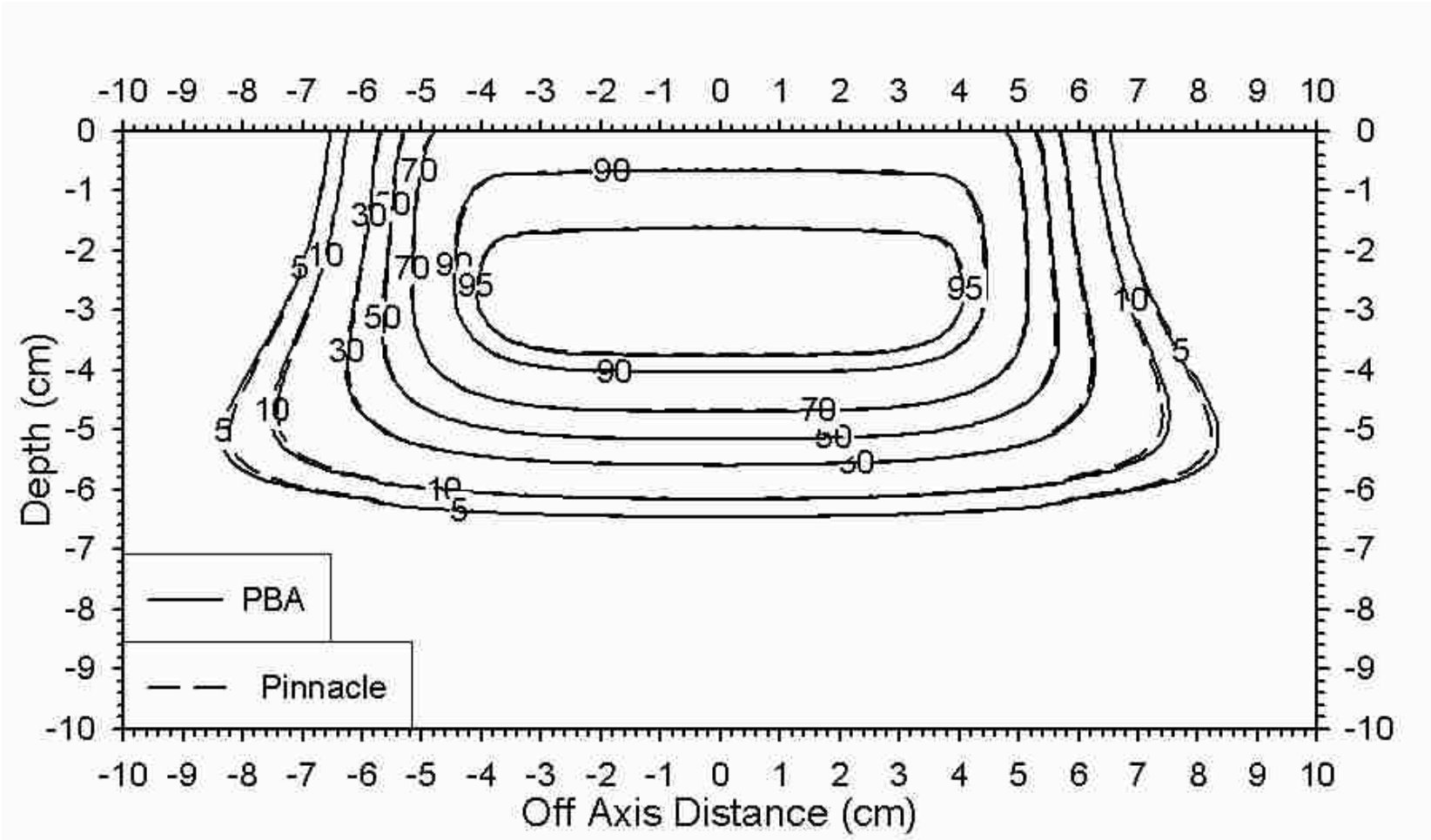

Figure 101: Comparison of dose distributions from a 10x10-cm^2 12 MeV field at 110-cm SSD calculated by the coded PBA (solid line) and Pinnacle (dashed line).

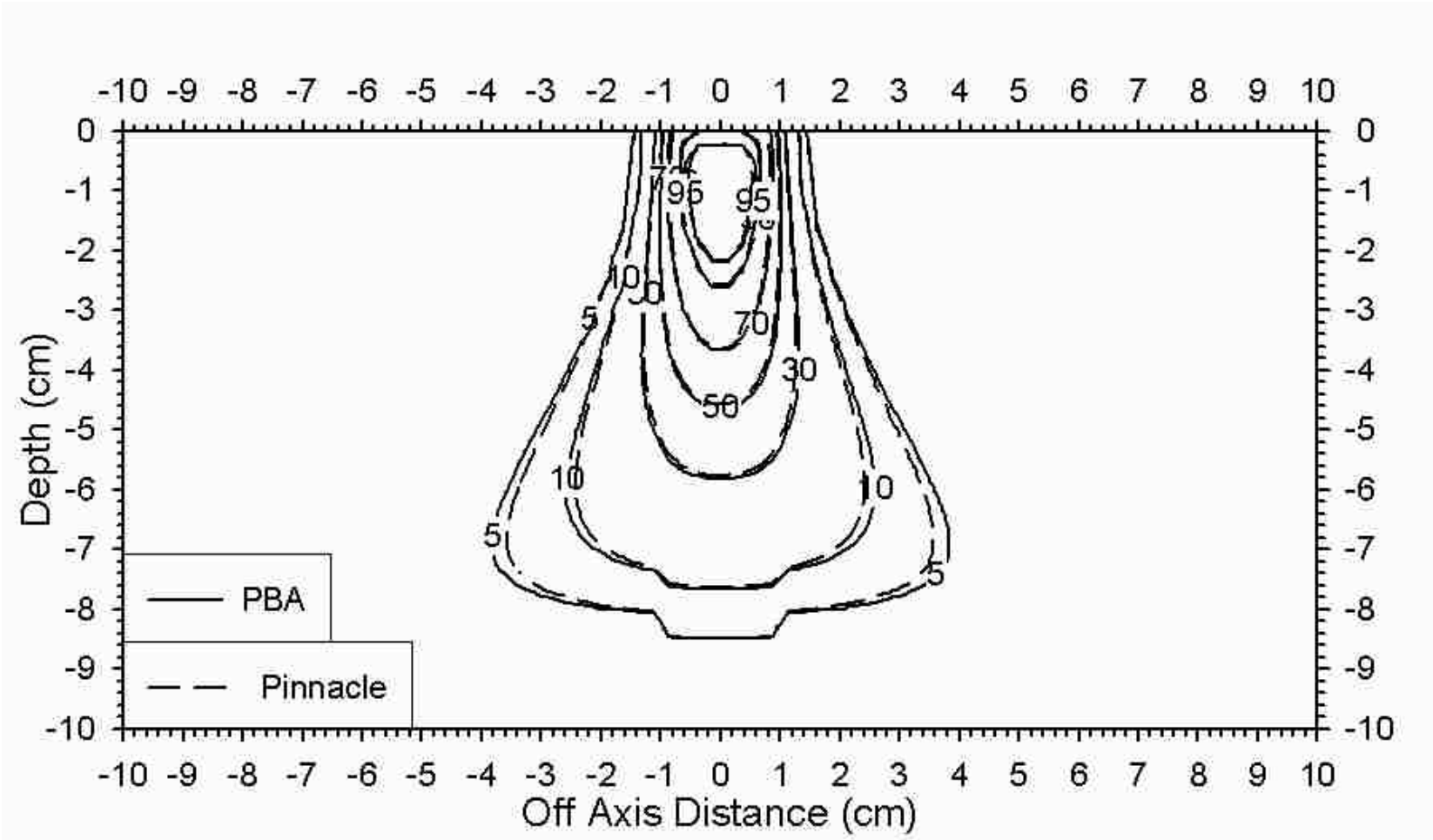

Figure 102: Comparison of dose distributions from a 2x2-cm^2 16 MeV field at 100-cm SSD calculated by the coded PBA (solid line) and Pinnacle (dashed line).

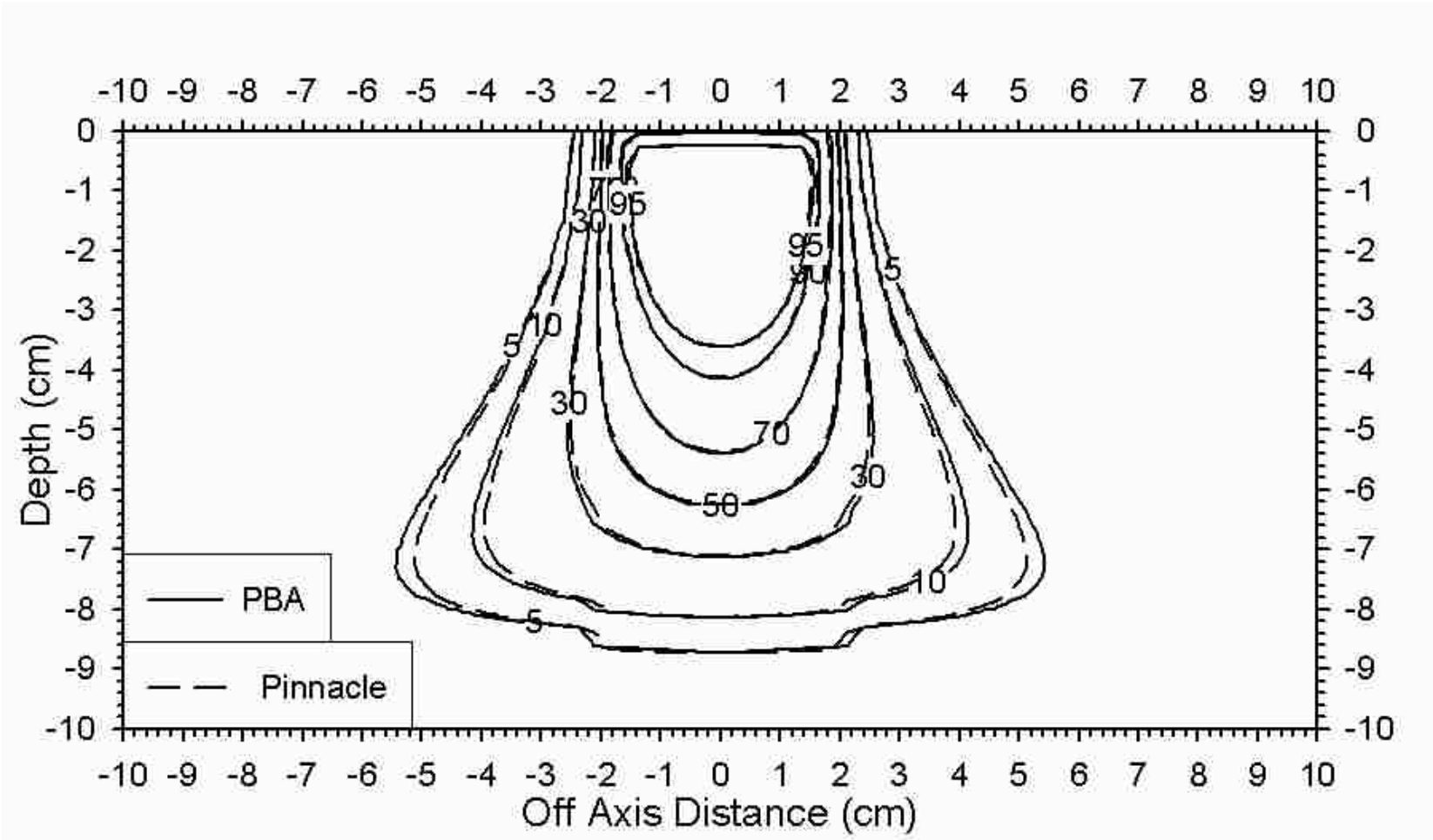

Figure 103: Comparison of dose distributions from a 4x4-cm^2 16 MeV field at 100-cm SSD calculated by the coded PBA (solid line) and Pinnacle (dashed line).

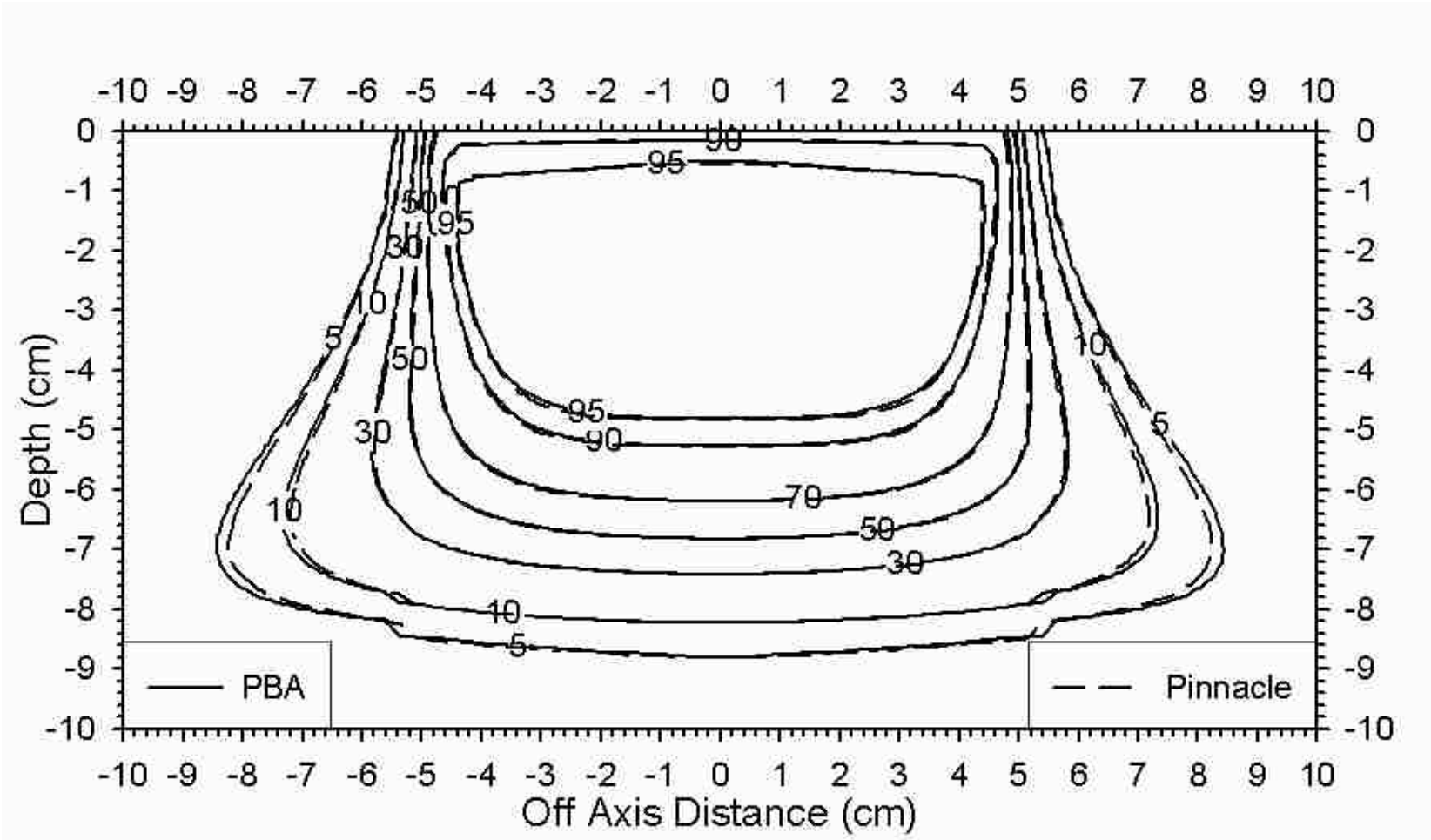

Figure 104: Comparison of dose distributions from a 10x10-cm^2 16 MeV field at 100-cm SSD calculated by the coded PBA (solid line) and Pinnacle (dashed line).

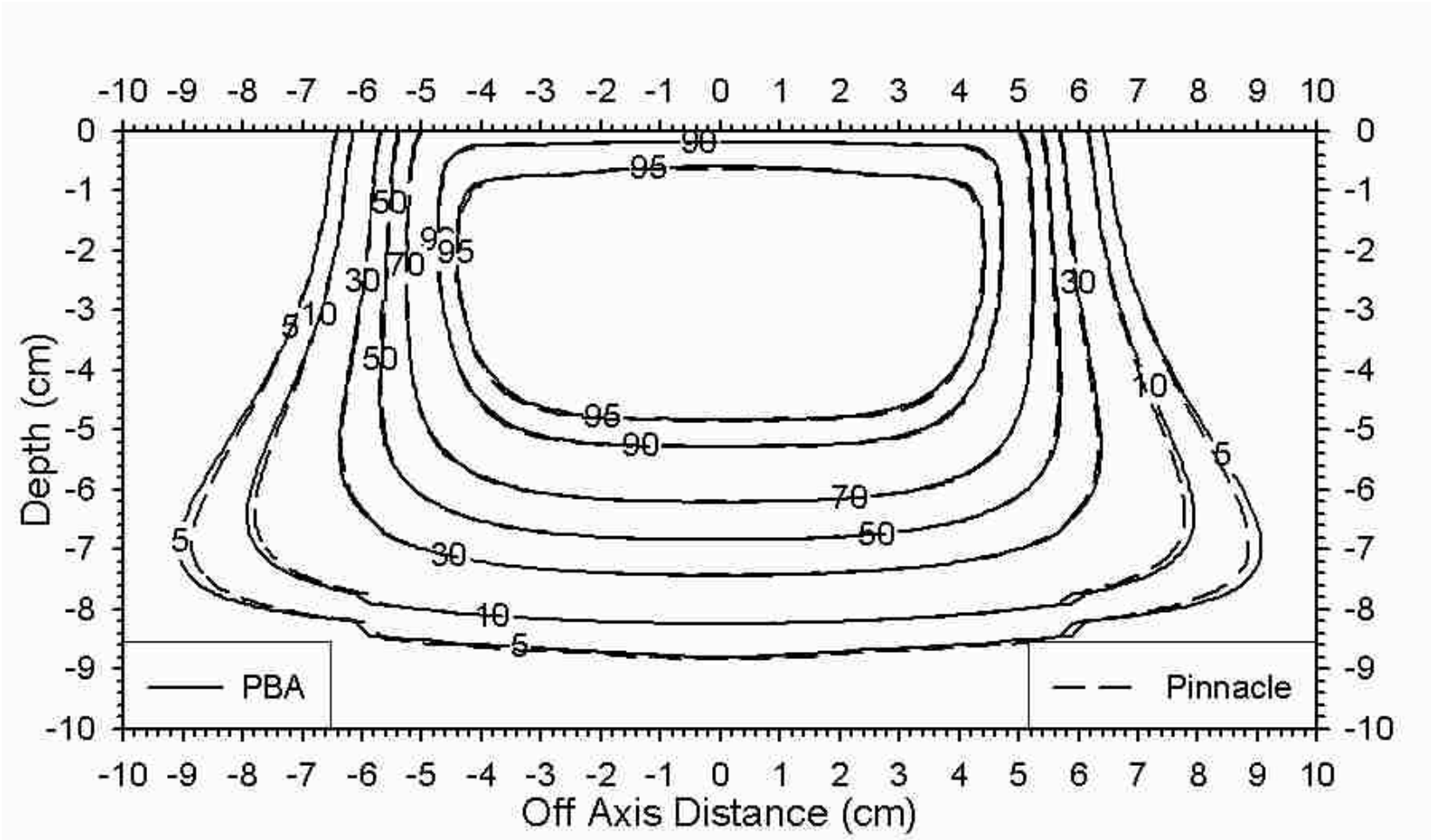

Figure 105: Comparison of dose distributions from a 10x10-cm^2 16 MeV field at 110-cm SSD calculated by the coded PBA (solid line) and Pinnacle (dashed line).

Vita

David Perrin was born in Hammond, Louisiana, in 1981. He grew up in Ponchatoula, Louisiana, where he graduated from Ponchatoula High School in May of 2000. He has lived in Baton Rouge, Louisiana, since then, earning a Bachelor of Science degree in physics with concentration in astronomy in May of 2005 from Louisiana State University. Upon receiving a Master of Science degree in medical physics, he wants to start a career as a clinical medical physicist, preferably somewhere with snow. Soon after, he hopes to marry his soon-to-be fiancée and start a family, assuming she says yes.